

11/18/97
10/18/96
OCIT
C42830

1.50

SEMI-ANNUAL REPORT

(for July - December 1996)

Contract Number NAS5-31363

OCEAN OBSERVATIONS WITH EOS/MODIS:

Algorithm Development and Post Launch Studies

Howard R. Gordon
University of Miami
Department of Physics
Coral Gables, FL 33124

(Submitted January 15, 1997)

Preamble

As in earlier reports, we will continue to break our effort into seven distinct units:

- Atmospheric Correction Algorithm Development
- Whitecap Correction Algorithm
- In-water Radiance Distribution
- Residual Instrument Polarization
- Pre-launch Atmospheric Correction Validation
- Detached Coccolith Algorithm and Post-launch Studies

This separation has been logical thus far; however, as launch of AM-1 approaches, it must be recognized that many of these activities will shift emphasis from algorithm development to validation. For example, the second, third, and fifth bullets will become almost totally validation-focussed activities in the post-launch era, providing the core of our experimental validation effort. Work under the first bullet will continue into the post-launch time frame, but will be driven in part by algorithm deficiencies revealed as a result of validation activities. We will continue to use this format for CY97.

Abstract

Several significant accomplishments were made during the present reporting period.

- We developed a new method for identifying the presence of absorbing aerosols and, simultaneously, performing atmospheric correction. The algorithm consists of optimizing the match between the top-of-atmosphere radiance spectrum and the result of models of both the ocean and aerosol optical properties.
- We developed an algorithm for providing an accurate computation of the diffuse transmittance of the atmosphere given an aerosol model. A module for inclusion into the MODIS atmospheric-correction algorithm was completed.
- We acquired reflectance data for oceanic whitecaps during a cruise on the *RV Ka'imimoana* in the Tropical Pacific (Manzanillo, Mexico to Honolulu, Hawaii). The reflectance spectrum of whitecaps was found to be similar to that for breaking waves in the surf zone measured by *Frouin, Schwindling and Deschamps* [1996]; however, the drop in augmented reflectance from 670 to 860 nm was not as great, and the magnitude of the augmented reflectance was significantly less than expected [*Gordon and Wang*, 1994].
- We developed a method for the approximate correction for the effects of the MODIS polarization sensitivity. The correction, however, requires adequate characterization of the polarization sensitivity of MODIS prior to launch.

1. Atmospheric Correction Algorithm Development.

a. Task Objectives:

During CY 1996 there are four objectives under this task:

(i) Complete development of an algorithm module for removing the effects of stratospheric aerosol and/or cirrus clouds from MODIS imagery over the oceans.

(ii) Conduct research on the effects of strongly absorbing aerosols, and their vertical structure, on the existing atmospheric correction algorithm. Use the results of this research to develop a strategy for their removal.

(iii) Develop a detailed model of the diffuse transmittance of the atmosphere and the manner in which it is influenced by the angular distribution of subsurface upwelling spectral radiance. Add a module for this to the atmospheric correction algorithm.

(iv) Investigate the effects of ignoring the polarization of the atmospheric light field on the performance of the proposed atmospheric correction algorithm.

b. Work Accomplished:

(i) This task was placed on hold to free time to accelerate Major Task #4 below in response to the higher-than-expected MODIS polarization sensitivity in some ocean bands. However, a paper submitted to *Applied Optics* describing our work in this area was accepted for publication (Appendix 2 in the Jan. to June 1996 Semi-Annual Report), and talks with MODIS Science Team Member B.-C. Gao were initiated to coordinate effort for cirrus cloud removal.

(ii) As demonstrated our last Semi-Annual Report (Jan. to June 1996), strongly absorbing aerosols present a serious problem for atmospheric correction. The nature of the problem is two fold: (1) in contrast to weakly-absorbing aerosols, when the aerosol is strongly absorbing its distribution in altitude becomes very important; and (2) the technique of distinguishing aerosol type through examination of the spectral variation of the radiance in the near infrared, used by the MODIS atmospheric-correction algorithm, cannot distinguish between weakly-absorbing and strongly-absorbing aerosols. During this reporting period, we have tested a "spectral matching algorithm" that, although very slow, is capable of distinguishing between weakly- and strongly-absorbing aerosols. It is based on combining an atmospheric model with a water-leaving radiance model for the ocean, and effecting a variation of the relevant parameters until a satisfactory fit to

the MODIS top-of-atmosphere radiance is achieved. We believe that the algorithm is also capable of functioning in the same manner when aerosol vertical structure is an additional parameter. (Note that vertical structure is only important when the aerosol is strongly absorbing.) A report describing this algorithm is attached as Appendix 1.

(iii) The basic correction algorithm yields the product of the diffuse transmittance t and the water-leaving reflectance ρ_w . However, t depends on the angular distribution of ρ_w . If ρ_w were uniform, t would be easy to compute, and this approximation has always been employed in the past. In a series of papers Morel and Gentili [Morel and Gentili, 1991; Morel and Gentili, 1993] studied theoretically the bidirectional effects as a function of the sun-viewing geometry and the pigment concentration. Their simulations suggest that, although the bidirectional effects nearly cancel in the estimation of the pigment concentration using radiance ratios, ρ_w can depend significantly on the solar and viewing angles. (Our major task number 3, a study of the in-water radiance distribution, experimentally addresses this problem.)

In this reporting period, we completed a study to understand the influence of bidirectional effects on the diffuse transmittance t . Through the use of the reciprocity principle, we were able to develop a simplified method of computing t , given the upward radiance distribution with direction just beneath the sea surface. We showed that the difference between t (the correct diffuse transmittance) and t^* (the diffuse transmittance computed by assuming the subsurface upward radiance is uniform) is typically $\lesssim 4\%$, and is a relatively weak function of the aerosol optical thickness. Thus, considering the error likely to result from the removal of the aerosol path radiance, it appears that in the blue t can be replaced by t^* , except in waters with low pigment concentrations, e.g., $\lesssim 0.5 \text{ mg/m}^3$. A paper describing this work has been submitted to *Applied Optics*, and is attached here as Appendix 2.

We have written a software module to accurately compute the diffuse transmittance, and produced the required lookup tables. This module has been delivered to R. Evans for integration into the atmospheric correction software.

(iv) This task was completed as described in the last Semi-Annual Report (Jan. to June 1996).

c. Data/Analysis/Interpretation: See item b above.

d. Anticipated Future Actions:

(i) We must now implement our strategy for adding the cirrus cloud correction into the existing atmospheric correction algorithm. Specific issues include (1) the phase function to be used for

Semi-Annual Report (1 July – 31 December 1996) NAS5-31363

the cirrus clouds, (2) the details of making two passes through the correction algorithm, and (3) preparation of the required tables. These issues will be addressed during CY 1997 with the goal of having a complete implementation ready by the end of CY 1997.

(ii) We will continue the study of the “spectral matching” algorithm with the goal of having an algorithm ready for implementation by the end of CY 1997. As our work has shown that a knowledge of the vertical distribution of the aerosol is critical, if it is strongly absorbing, we have procured a micro pulse lidar (MPL) system for use at sea on validation cruises, and from islands (likely Barbados or the Canary Islands) in the Saharan dust zone, to begin to compile the climatology of the vertical distribution required to adopt candidate distributions for use in this region.

(iii) This task is nearly complete; however, we still need to develop a method to include the effects of the subsurface BRDF for low-pigment waters in the blue.

(iv) Task completed.

Additional tasks for CY97:

(1) We will initiate a study to determine the efficacy of the present atmospheric correction algorithm on removal of the aerosol effect from the measurement of the fluorescence line height (MOD 20).

(2) We will examine methods for efficiently including earth-curvature effects into the atmospheric correction algorithm [*Ding and Gordon, 1994*]. This will most likely be a modification of the look-up tables for the top-of-the-atmosphere contribution from Rayleigh scattering.

(3) We will examine the necessity of implementing our out-of-band correction [*Gordon, 1995*] to MODIS.

e. Problems/Corrective Actions:

(i) None.

(ii) None.

(iii) None.

(iv) None.

Semi-Annual Report (1 July – 31 December 1996) NAS5-31363

(v) None.

f. Publications:

H.R. Gordon, Atmospheric Correction of Ocean Color Imagery in the Earth Observing System Era, *Journal of Geophysical Research, Atmospheres* (Accepted).

H.R. Gordon, T. Zhang, F. He, and K. Ding, Effects of stratospheric aerosols and thin cirrus clouds on atmospheric correction of ocean color imagery: Simulations, *Applied Optics* (In press).

H. Yang and H.R. Gordon, Remote sensing of ocean color: Assessment of the water-leaving radiance bidirectional effects on the atmospheric diffuse transmittance, *Applied Optics* (Submitted).

2. Whitecap Correction Algorithm (with K.J. Voss).

a. Task Objectives:

As described in earlier reports, a whitecap radiometer system has been built and tested to provide a database for developing and validating the whitecap correction algorithm, as well as for providing an estimation of the whitecap contribution to the water-leaving radiance during the post-launch validation phase. The database includes spectral information as well as variables associated with the formation and occurrence of whitecaps such as wind speed and air/sea temperature.

b. Work Accomplished:

The basic design, calibration procedure, operation, and data analysis methods for the whitecap radiometer are described in a paper prepared for submission to the *Jour. Atm. Ocean. Tech.* and attached here as Appendix 3.

From 29 March to 18 April 1996 the whitecap radiometer system was deployed on the NOAA ship *RV Malcolm Baldrige* on a cruise from Miami to a test location in the Gulf of Mexico, approximately 70 miles off shore from Cedar Key (Florida) in the Apalachicola Bay. The location provided relatively warm waters (16°-17°C) with a number of cold fronts moving off the mainland. These fronts usually lasted a couple of days bringing strong winds (sometimes as high as 18 m/s) and lowering the air temperature to about 12°C. The occurrence of an unstable atmosphere and good winds provided an interesting spectral whitewater data set. From 1 to 13 November 1996, the whitecap radiometer was operated on a cruise from Manzanillo, Mexico to Honolulu, Hawaii. This cruise provided whitecap data under conditions of steady winds (the trades) of essentially unlimited duration and fetch. The analysis of these two data sets is provided in a paper prepared for submission to *Jour. Geophys. Res.* and attached here as Appendix 4.

c. Data/Analysis/Interpretation

There have been three significant results from our whitecap research: (1) our measurements confirm the spectral fall off of the augmented reflectance in the NIR, although the reduction at 865 compared to 670 nm was not as large as observed in the surf zone [Frouin, Schwindling and Deschamps, 1996]; (2) whitecaps show significant nonlambertian effects, particularly at large solar zenith angles; and (3) the augmented reflectance of whitecaps appears to be about one-fourth that predicted by recent models [Gordon and Wang, 1994; Koepke, 1984]. The details of these results are provided in Appendix 4.

d. Anticipated Future Actions:

Semi-Annual Report (1 July – 31 December 1996) NAS5–31363

As the basic objectives of this task have been realized, it is being suspended until the validation phase. Karl Moore, the post doctoral associated who was responsible for the operation of the instrument and the data analysis, has accepted a position at the Scripps Institution of Oceanography.

e. Problems/Corrective Actions: None

f. Publications:

K.D. Moore, K.J. Voss, and H.R. Gordon, Whitecaps: Spectral reflectance in the open ocean and their contribution to water-leaving radiance, Ocean Optics XIII, Halifax, Nova Scotia, October 22-25, 1996.

K.D. Moore, K.J. Voss, and H.R. Gordon, Spectral reflectance of whitecaps: Instrumentation, calibration, and performance in coastal waters, *Jour. Atmos. Ocean. Tech.* (Submitted).

K.D. Moore, K.J. Voss, and H.R. Gordon, Spectral reflectance of whitecaps: Fractional coverage and the augmented spectral reflectance contribution to the water-leaving radiance, *Jour. Geophys. Res.* (Submitted).

3. In-water Radiance Distribution (with K.J. Voss).

a. Task Objectives:

The main objective in this task is to obtain upwelling radiance distribution data at sea for a variety of solar zenith angles to understand how the water-leaving radiance varies with viewing angle and sun angle.

b. Work accomplished:

We acquired upwelling radiance distribution data with the RADS camera system during a cruise with Dennis Clark during November. It was very windy during this cruise, but data was acquired in the configuration expected to be used during validation cruises.

c. Data/Analysis/Interpretation: none

We are currently performing the post-cruise calibrations of this instrument, and will be reducing the cruise data when this is completed.

d. Anticipated future actions:

We will be completing the calibrations and reducing data acquired during the cruise. We are also planning on making some minor changes to the instrument to improve its operation at sea. Finally we will be acquiring more data during another cruise with Dennis Clark this spring.

e. Problems/Corrective actions: None.

f. Publications: None.

4. Residual Instrument Polarization.

a. Task Objectives:

The basic question here is: if the MODIS responds to the state of polarization state of the incident radiance, given the polarization-sensitivity characteristics of the sensor, how much will this degrade the performance of the algorithm for atmospheric correction, and how can we correct for these effects?

b. Work Accomplished:

We have developed a formalism [Gordon, 1988] which provides the framework for removal of instrumental polarization-sensitivity effects, and a method for approximately correcting for them. The correction method is presented in a paper submitted for publication in *Applied Optics*, and attached as Appendix 5. The main difficulty that we see now in correcting for the polarization-sensitivity effects is the requirement of an adequate pre-launch characterization of the polarization sensitivity.

c. Data/Analysis/Interpretation:

See Appendix 5.

d. Anticipated Future Actions:

Although this task is now basically complete (a correction algorithm has been developed), we still need to prepare a module for including the polarization-sensitivity correction algorithm in the MODIS atmospheric correction algorithm. Also, as operation of the polarization-sensitivity correction algorithm requires an adequate pre-launch characterization of the polarization sensitivity, we will continue to work with MCST and SBRS to insure that proper characterization is realized.

e. Problems/Corrective Actions: None

f. Publications:

H.R. Gordon, T. Du, and T. Zhang, Atmospheric correction of ocean color sensors: Analysis of the effects of residual instrument polarization sensitivity, *Applied Optics* (Submitted).

5. Pre-launch Atmospheric Correction Validation (with K.J. Voss).

a. Task Objectives:

The long-term objectives of this task are four-fold:

(i) First, we need to study aerosol optical properties over the ocean in order to verify the applicability of the aerosol models used in the atmospheric correction algorithm. Effecting this requires obtaining long-term time series in typical maritime environments. This will be achieved using a CIMEL sun/sky radiometer that can be operated in a remote environment and send data back to the laboratory via a satellite link. These are similar the radiometers used by B. Holben in the AERONET Network. Thus, the first objective is to deploy a CIMEL Automatic Sun Tracking Photometer in a suitable location for studying the optical properties of aerosols over the ocean.

(ii) Second, we must be able to measure the aerosol optical properties from a ship during the initialization/calibration/validation cruises. The CIMEL-type instrumentation cannot be used (due to the motion of the ship) for this purpose. The required instrumentation consists of an all-sky camera (which can measure the entire sky radiance, with the exception of the solar aureole region) from a moving ship, an aureole camera (specifically designed for ship use) and a hand-held sun photometer. We have a suitable sky camera and sun photometer and must construct an aureole camera. Our objective for this calendar year is (1) to assemble, characterize and calibrate the solar aureole camera system, (2) to develop data acquisition software, and (3) to test the system.

In the case of strongly-absorbing aerosols, we have shown that knowledge of the aerosol vertical structure is critical [Gordon, 1996]. Thus, we need to be able to measure the vertical distribution of aerosols during validation exercises. This can be accomplished with ship-borne LIDAR. We have to procure a LIDAR system and modify it for ship operation.

(iii) The third objective is to determine how accurately the radiance at the top of the atmosphere can be determined based on measurements of sky radiance and aerosol optical thickness at the sea surface. This requires a critical examination of the effect of radiative transfer on "vicarious" calibration exercises.

(iv) The forth objective is to utilize data from other sensors that have achieved orbit (OCTS, POLDER, MSX), or are expected to achieve orbit (SeaWiFS) prior to the launch of MODIS, to validate and fine-tune the correction algorithm.

b. Work Accomplished:

Semi-Annual Report (1 July – 31 December 1996) NAS5-31363

(i) During the first part of this period we were operating the CIMEL in its location in the Dry Tortugas. In October this instrument was removed for recalibration. At the same time the AERONET network, run by B. Hobren, decided to upgrade the CIMEL instruments with more stable interference filters and small hardware changes. We will be reinstalling this instrument when it is returned from NASA.

(ii) The sky camera system and aureole system was used on three cruises during this period. The first cruise we participated in occurred during the NASA TARFOX experiment between Bermuda and New York. This cruise took place on a cruise liner, and we participated in all three weeks of the cruise effort. During this time we made measurements with the sky camera (including polarization), aureole camera system (to measure the sky radiance near the sun), and a hand held sunphotometer. In general the weather was not as good as expected (a hurricane when through the area during the cruise) but there were several clear periods during the cruise. The second and third cruises were with Dennis Clark off of Hawaii (during September and November). In the first of these cruises we obtained data with all three systems, but in the third Dennis Clark's group provided the sun photometer data. In addition to participating on the cruises we performed calibrations of all the systems pre and post cruise. We are currently rewriting the data reduction programs for the sky radiance distribution system to allow data reduction to take place on the cruise, to speed this process. In addition this is giving an opportunity to review this process and to perform tests of this data. We have reduced the aureole data from the first two cruises, and are currently evaluating this data.

To address the problem of vertical distribution of aerosols we have acquired a Micro Pulse Lidar from SSEI. This system was delivered at the very end of the period (December 16th), so we have not had a chance to do anything with the system yet.

(iii) As described in our last Semi-Annual Report (Jan. to June 1996), we have completed a study of the accuracy with which one can compute the radiance at the top of the atmosphere from sky radiance measurements made at the sea surface. The results suggest that the bulk of the error is governed by the uncertainty in the sky radiance measurements. Furthermore, it was shown that the largest error in the radiative transfer process was that due to the use of scalar radiative transfer theory, and that improvement would require the use of vector theory, and thus, measurement of the polarization of the sky radiance. We have started to analyze the use of polarization measurements at the surface and it appears that when polarization is included in the sky radiance inversion algorithm, the radiative transfer error can be made very small. Furthermore, we are now examining the extent to which the full linear polarization of the top-of-atmosphere radiance can

Semi-Annual Report (1 July – 31 December 1996) NAS5-31363

be deduced from surface measurements. This may be very important for validating the pre-launch polarization-sensitivity characterization of MODIS.

(iv) We have been in contact with personnel involved with SeaWiFS, OCTS, and MSX to acquire data formats, and satellite data from these instruments to assess the validity of the atmospheric correction algorithm. We have procured an SGI R10000 Workstation (same chip set and operating system as used by MODIS SDST). This will provide the necessary image processing capability for the pre- and post-launch era.

c. Data/Analysis/Interpretation:

(i) The CIMEL instrument was at NASA for most of this period for recalibration and refitting of the interference filters. Thus there has been little data analysis.

(ii) We have been working to reduce the data from the sky camera and aureole camera acquired this period but have not finished this process. Thus there is little to report in terms of analysis or interpretation. We also do not have any data from the LIDAR yet.

d. Anticipated Future Actions:

(i) We will be reinstalling the CIMEL in the Dry Tortugas at the first opportunity after its return from NASA. We are also working on a better method of acquiring the data through NASA. This will enable us to look at the sky radiance data in a more timely manner.

(ii) We will finish the data reduction work with the sky camera system in the next quarter. We are also reworking portions of this system to allow more automation of the data collection, and fix minor problems which developed during the last cruise (specifically overheating of the system computer and corrosion on the computer backplane). The reduced aureole data will be merged with the sky radiance data to provide a complete sky radiance distribution during this next period. We will also finish reducing all of the aureole data during this next period.

Much of our effort in the next several months will be spent learning the new MPL Lidar system, and making the modifications necessary to use the system at sea. We would like to have this system ready for operation during the next cruise opportunity, if possible ready for a field trial in February.

(iii) We will continue development of a sky radiance inversion algorithm that utilizes the full vector radiative transfer equation. This should remove the largest radiative transfer error in predicting the top-of-atmosphere radiance from the bottom-of-atmosphere radiance.

Semi-Annual Report (1 July – 31 December 1996) NAS5-31363

(iv) We will continue to try to obtain ocean color data from other sensors to assess the correction algorithm. Now, OCTS appears to be the most likely candidate. We will install R. Evans' implementation of our atmospheric correction algorithm on the R10000 computer to facilitate fine-tuning the algorithm.

e. Problems/corrective actions: None.

f. Publications:

H.R. Gordon and T. Zhang, How well can radiance reflected from the ocean-atmosphere system be predicted from measurements at the sea surface?, *Applied Optics* **35**, 6527–6543 (1996).

D.K. Clark, H.R. Gordon, K.J. Voss, Y. Ge, W. Broenkow, and C. Trees, Validation of Atmospheric Correction over the Oceans, *Jour. Geophys. Res.* (Accepted).

K.J. Voss and Y. Liu, Polarized radiance distribution measurements of skylight: Part 1, system description and characterization, *Applied Optics* (Submitted).

6. Detached Coccolith Algorithm and Post Launch Studies (W.M. Balch).

During the second half of 1996, we participated in one cruise to the Gulf of Maine, a well known region for mesoscale coccolithophore blooms. We measured coccolithophore abundance, production and optical properties. We also completed a flow cytometer experiment in which we sorted field-derived calcite particles to measure their calcite specific scattering coefficients. A thorough understanding of the relationship between calcite abundance and light scatter, in coccolith-rich and coccolith-poor regions, will provide the basis for a generic suspended calcite algorithm to be used with MODIS data.

a. Task Objectives:

The algorithm for retrieval of the detached coccolith concentration from the coccolithophorid, *E. huxleyi* is described in detail in our ATBD. The key is quantification of the backscattering coefficient of the detached coccoliths. Our earlier studies focussed on laboratory cultures to understand factors affecting the calcite-specific backscattering coefficient. As with algorithms for chlorophyll, and primary productivity, the natural variance between growth related parameters and optical properties needs to be understood before the accuracy of the algorithm can be determined. To this end, the objectives of our coccolith studies have been to define the effect of growth rate on:

- (1) the rate that coccoliths detach from cells (this is also a function of turbulence and physical shear);
- (2) rates of coccolith production;
- (3) morphology of coccoliths; and
- (4) volume scattering and backscatter of coccoliths.

For perspective on the directions of our work, we provide an overview of our previous activities. During 1995, we focussed on all of the above objectives using chemostat cultures (in which algal growth rate is precisely controlled). During the latter half of 1995, our work focused on shipboard measurements of suspended calcite and estimates of optical backscattering as validation of the laboratory measurements. We participated on two month-long cruises to the Arabian sea, measuring coccolithophore abundance, production, and optical properties. During the first half of 1996, we focused again on objectives 2 and 4, during two Gulf of Maine cruises, one in March and one in June. During the second half of 1996, we participated on another cruise to the Gulf of Maine, and further addressed objectives 2 and 4.

b. Work Accomplished:

We have continued data analysis for the Arabian Sea cruises as well as the first two Gulf of Maine cruises of 1996. The current state of the data are as follows:

- (1) We completed our third cruise of 1996 to the Gulf of Maine in November. During this cruise, we sampled for total and calcite-dependent backscattering (continuously), suspended calcite concentrations, calcification rates, chlorophyll concentrations, and coccolithophore and coccolith counts.
- (2) We completed our last set of flow cytometer experiments in which we sorted field-derived calcite particles into vials of pure seawater, measured their volume scattering functions, and measured their calcite concentrations.
- (3) Suspended calcite samples from all Arabian Sea cruises and two cruises to the Gulf of Maine (March and June) have been run in the graphite furnace atomic absorption spectrometer at the University of Maine. We now only have samples from our most recent cruise in November.
- (4) The 400 cell and coccolith counts from the southwest Monsoon cruise (summer '95) have been completed and the data are being hand-entered into spreadsheets at this time. We are currently working on the Arabian Sea Samples from the '95 intermonsoon cruise.
- (5) All calcification data from the Arabian Sea cruise have been processed to units of $\text{gC m}^{-3} \text{ d}^{-1}$ and integrated over the water column at each station and they have been processed into complete sections.
- (6) The Arabian Sea biooptical data is now processed for temperature, salinity, pH, fluorescence and backscatter (with and without calcite) averaged over each kilometer of all trips. All calibration checks have been done for the underway data. Hydrographic plots have been made in which light scattering is plotted as a function of temperature and salinity and the optical and pigment data superimposed.
- (7) We have examined the relationship between the calcite-dependent backscattering (b'_b) and the concentration of suspended calcite or concentration of detached coccoliths for our previous work in the Straits of Florida, Arabian Sea, and North

Semi-Annual Report (1 July – 31 December 1996) NAS5-31363

Atlantic. We have also analyzed these data relevant to our flow cytometer results. This is of major relevance to our MODIS algorithm efforts. Besides actually checking our algorithm, it allows us to define the accuracy and precision of the algorithm. This is exceedingly important for subsequent interpretation. Our results suggest that for the Gordon reflectance model, the algorithm will have a precision of $\pm 25,000$ coccoliths/mL (or in terms of carbon equivalents, $\pm 5 \mu\text{g C}$ as calcite per liter).

c. Data/Analysis/Interpretation:

As expected, calcite-dependent backscattering was low in the Gulf of Maine during March, but it was still measurable. Typically, calcite scattering accounted for 5-10% of total backscattering. A very different picture was observed in June. Acid-labile scattering increased to 30-40% of total backscattering in Wilkinson Basin, a stratified basin in the middle of the Gulf of Maine. Acid-labile scattering dropped over Georges Bank as the predominant populations were diatoms, and values increased again in the Northeast Channel, similar to previous blooms that we have observed. The observations are consistent with the calcite being produced in the more stable Wilkinson Basin with subsequent advection around the NE flank of Georges Bank. We completed another Gulf of Maine cruise at the end of October, and again took the flow-through system. Much of these data are still in the process of being worked-up.

Calcification measurements from the March 1996 cruise were remarkably high, given that this was at the beginning of the Spring bloom. We were finding >10% of the carbon being fixed into coccoliths. This also explains the relatively high fraction of calcite-dependent light scattering seen during this time. Calcification rates are still being processed for the June cruise but preliminary results suggest that they were quite high.

d. Anticipated Future Actions:

Work in CY97 will address several areas:

- (1) Processing of the suspended calcite samples from the November '96 cruise.
- (2) Data will be collated from the Arabian Sea and Gulf of Maine cruises in order to calculate turnover of the calcite particles. This can only occur after step 1 is completed.
- (3) We are continuing analysis of our latest flow cytometer results from the fall '96 experiment. The suspended calcite samples from that last experiment will be run.

Semi-Annual Report (1 July – 31 December 1996) NAS5-31363

- (4) The underway data from the Gulf of Maine will be merged with our calibration measurements (vicarious calibrations are periodically made at sea and these data must be processed to verify whether instrument calibrations changed).
- (5) Hydrographic plots of the Gulf of Maine data will be made in which light scattering and chlorophyll are plotted in temperature salinity space.

e. Problems/Corrective Actions: None

f. Publications:

W. M. Balch, J. J. Fritz, and E. Fernandez, Decoupling of calcification and photosynthesis in the coccolithophore *Emiliana huxleyi* under steady-state light-limited growth. *Marine Ecology Progress Series*, **142** 87-97 (1996).

E. Fernandez, J. J. Fritz and W. M. Balch, Growth-dependent chemical composition of the coccolithophorid *Emiliana huxleyi* in light-limited chemostats, *J. Exp. Mar. Biol. Ecol.* (In press).

J. J. Fritz and W. M. Balch, A coccolith detachment rate determined from chemostat cultures of the coccolithophore *Emiliana huxleyi*, *J. Exp. Mar. Biol. Ecol.* (In press).

K. J. Voss, W. M. Balch, and K. A. Kilpatrick. Scattering and attenuation properties of *Emiliana huxleyi* cells and their detached coccoliths, *Limnol. Oceanogr.* (Submitted).

8. Other Activities.

The bulk of the PI's effort during this reporting period was focused on five activities. The first was the preparation of revisions of the Water-leaving Radiance and Coccolith concentration ATBD's. These revisions were completed and delivered to the EOS Senior Project Scientist on August 15, 1996. The second was a detailed revision of the MOCEAN Validation Plan on behalf of the Group. This occurred after attending the MODIS Ocean Group (MOCEAN) Meeting in July. The third was participation in the MCST audit of progress toward the Level 1B algorithm in the VIS/NIR bands on September 5, 1996. The fourth was participation in the MODIS ATBD review November 20, 1996. The fifth was an intensive effort to assess the effects of the larger-than-expected MODIS polarization sensitivity on MODIS products, and to understand the anomalous polarization-sensitivity characterization tests.

9. Publications, submissions, and abstracts for CY 96.

H.R. Gordon, Atmospheric Correction of Ocean Color Imagery in the Earth Observing System Era, *Journal of Geophysical Research, Atmospheres* (Accepted).

H.R. Gordon, T. Zhang, F. He, and K. Ding, Effects of stratospheric aerosols and thin cirrus clouds on atmospheric correction of ocean color imagery: Simulations, *Applied Optics* (In press).

H.R. Gordon and T. Zhang, How well can radiance reflected from the ocean-atmosphere system be predicted from measurements at the sea surface?, *Applied Optics*, **35**, 6527-6543 (1996).

T. Zhang and H.R. Gordon, Columnar aerosol properties over oceans by combining surface and aircraft measurements: sensitivity analysis, *Applied Optics* (Accepted).

D. K. Clark, H.R. Gordon, K.J. Voss, Y. Ge, W. Broenkow, and C. Trees, Validation of Atmospheric Correction over the Oceans, *Jour. Geophys. Res.* (Accepted).

H. Yang and H.R. Gordon, Remote sensing of ocean color: Assessment of the water-leaving radiance bidirectional effects on the atmospheric diffuse transmittance, *Applied Optics* (Submitted).

H.R. Gordon, T. Du, and T. Zhang, Atmospheric Correction of Ocean Color Sensors: Analysis of the Effects of Residual Instrument Polarization Sensitivity, *Applied Optics* (Submitted).

K.D. Moore, K.J. Voss, and H.R. Gordon, Whitecaps: Spectral reflectance in the open ocean and their contribution to water-leaving radiance. Ocean Optics XIII, Halifax, Nova Scotia, October 22-25, 1996.

K.D. Moore, K.J. Voss, and H.R. Gordon, Spectral reflectance of whitecaps: Instrumentation, calibration, and performance in coastal waters, *Jour. Atmos. Ocean. Tech.* (Submitted).

K.D. Moore, K.J. Voss, and H.R. Gordon, Spectral reflectance of whitecaps: Fractional coverage and the augmented spectral reflectance contribution to the water-leaving radiance, *Jour. Geophys. Res.* (Submitted).

K.J. Voss and Y. Liu, Polarized radiance distribution measurements of skylight: Part 1, system description and characterization, *Applied Optics* (Submitted).

W. M. Balch and K. A. Kilpatrick, Calcification rates in the equatorial Pacific along 140°W, *Deep Sea Research*, **43** 971-993 (1996).

Semi-Annual Report (1 July – 31 December 1996) NAS5-31363

W. M. Balch, J. J. Fritz, and E. Fernandez, Decoupling of calcification and photosynthesis in the coccolithophore *Emiliana huxleyi* under steady-state light-limited growth. *Marine Ecology Progress Series*, **142** 87-97 (1996).

W. M. Balch, K. A. Kilpatrick, P. M. Holligan and C. Trees, The 1991 coccolithophore bloom in the central north Atlantic I- Optical properties and factors affecting their distribution. *Limnology and Oceanography* (In press).

W. M. Balch, K. Kilpatrick, P. M. Holligan, D. Harbour, and E. Fernandez, The 1991 coccolithophore bloom in the central north Atlantic II- Relating optics to coccolith concentration, *Limnology and Oceanography* (In press).

E. Fernandez, J. J. Fritz and W. M. Balch, Growth-dependent chemical composition of the coccolithophorid *Emiliana huxleyi* in light-limited chemostats, *J. Exp. Mar. Biol. Ecol.* (In press).

J. J. Fritz and W. M. Balch, A coccolith detachment rate determined from chemostat cultures of the coccolithophore *Emiliana huxleyi*, *J. Exp. Mar. Biol. Ecol.* (In press).

K. J. Voss, W. M. Balch, and K. A. Kilpatrick. Scattering and attenuation properties of *Emiliana huxleyi* cells and their detached coccoliths, *Limnol. Oceanogr.* (Submitted).

10. References.

- Ding, K. and H. R. Gordon, Atmospheric correction of ocean color sensors: Effects of earth curvature, *Applied Optics*, 33, 7096-7016, 1994.
- Frouin, R., M. Schwindling and P. Y. Deschamps, Spectral reflectance of sea foam in the visible and near-infrared: In-situ measurements and implications for remote sensing of ocean color and aerosols, *Jour. Geophys. Res.*, 101C, 14,361-14,371, 1996.
- Gordon, H. R., Ocean Color Remote Sensing Systems: Radiometric Requirements, *Society of Photo-Optical Instrumentation Engineers, Recent Advances in Sensors, Radiometry, and Data Processing for Remote Sensing*, 924, 151-167, 1988.
- Gordon, H. R., Remote sensing of ocean color: a methodology for dealing with broad spectral bands and significant out-of-band response, *Applied Optics*, 34, 8363-8374, 1995.
- Gordon, H. R., 1996, Atmospheric Correction of Ocean Color Imagery in the Earth Observing System Era, *Jour. Geophys. Res.* (In press).
- Gordon, H. R. and M. Wang, Influence of Oceanic Whitecaps on Atmospheric Correction of SeaWiFS, *Applied Optics*, 33, 7754-7763, 1994.
- Koepke, P., Effective Reflectance of Oceanic Whitecaps, *Applied Optics*, 23, 1816-1824, 1984.
- Morel, A. and B. Gentili, Diffuse reflectance of oceanic waters: its dependence on Sun angle as influenced by the molecular scattering contribution, *Applied Optics*, 30, 4427-4438, 1991.
- Morel, A. and B. Gentili, Diffuse reflectance of oceanic waters. II. Bidirectional aspects, *Applied Optics*, 32, 6864-6879, 1993.

Appendix 1

**A method for atmospheric correction in the
presence of strongly absorbing aerosols**

1. Introduction

The Coastal Zone Color Scanner (CZCS) demonstrated the feasibility of measuring marine phytoplankton concentrations from earth-orbiting sensors.^{1,2} Based the success of the CZCS, several similar instruments with higher radiometric sensitivity and a larger number of spectral bands, e.g., the sea-viewing wide-field-of-view sensor (SeaWiFS),³ the moderate resolution imaging spectroradiometer (MODIS),⁴ etc., will be launched in the near future. These ocean color instruments will actually measure the chlorophyll *a* concentration in the water as a surrogate for the phytoplankton concentration. In fact, the CZCS measured the sum of the concentrations of chlorophyll *a* and its degradation product phaeophytin *a*. This sum was referred to as the pigment concentration, *C*. Phytoplankton pigments have a broad absorption maximum in the blue (~ 435 nm) and a broad absorption minimum in the green (~ 565 nm), and the CZCS algorithms derived *C* from the ratio of the radiances backscattered out of the water (the water-leaving radiance, L_w) near these two wavelengths.^{5,6} Typically, L_w is at most 10% of the total radiance, L_t , exiting the top of the atmosphere (TOA) in the blue and $< 5\%$ in the green. Therefore, it is necessary to extract L_w from L_t to derive *C*. This process is called atmospheric correction.

The atmospheric correction algorithm developed for CZCS⁶⁻¹⁰ is not sufficiently accurate for the new generation of sensors with higher radiometric sensitivity. Atmospheric correction of these sensors requires incorporation of multiple-scattering effects. Gordon and Wang^{11,12} developed such an algorithm for SeaWiFS, and found that the multiple-scattering effects depended on the physical and chemical properties of the aerosol (size distribution and refractive index). Therefore, incorporation of multiple scattering into atmospheric correction required the introduction of aerosol models in the algorithm.

The Gordon and Wang algorithm is very simple to describe. The spectral variation in L_t in the near infrared (NIR) spectral region where $L_w \approx 0$ is used to provide information concerning the aerosol, as L_t there is due principally to Rayleigh scattering (which is known) and to aerosol scattering. The Rayleigh scattering component is then removed, and the resulting spectral variation is compared to that produced by a set of candidate aerosol models in order to determine which two models of the candidate set are most appropriate. These models are then used to estimate

the multiple-scattering effects. Gordon¹² has shown that this algorithm can provide L_w with the desired accuracy as long as the aerosol is weakly absorbing (more accurately, the aerosol must be weakly absorbing and it must follow the relationship between size distribution and refractive index that is implicitly implied in the choice of the candidate aerosol models). Unfortunately, strongly-absorbing aerosols, e.g., aerosols from anthropogenic urban sources or mineral dust transported from desert areas to the ocean, can possess size distributions similar to the weakly-absorbing aerosols typically present over the oceans. As the spectral variation of aerosol scattering depends mostly on the aerosol size distribution, and only weakly on the index of refraction, the spectral variation of scattering in the NIR is not sufficient to distinguish between weakly- and strongly-absorbing aerosols. Furthermore, in the case of mineral dust an additional complication arises: the dust is colored, i.e., its absorption is a function of wavelength.^{13,14} Even if it were possible to estimate the absorption characteristics of mineral dust aerosol in the NIR, one would still not know the extent of absorption in the visible. This is a particularly serious problem, as regions contaminated by mineral dust are often highly productive and thus important from a biogeochemical point of view. In fact, dust deposition may actually be providing nutrients that enable the phytoplankton to bloom.¹⁵

The difficulty in detecting the presence of strongly absorbing aerosols is that the effects of absorption become evident only in the multiple scattering regime. In the single scattering regime, the reflectance of the aerosol is proportional to the product of the single scattering albedo (ω_0) and the aerosol optical thickness (τ_a), i.e., at small τ_a there is no way to distinguish nonabsorbing aerosols ($\omega_0 = 1$) with a given τ_a from absorbing aerosols ($\omega_0 < 1$) and a larger τ_a . Retrieval of information concerning aerosol absorption requires multiple scattering; however, this multiple scattering need not be aerosol multiple scattering — when a low concentration of aerosols exists in the presence of strong Rayleigh scattering, e.g., in the blue, multiple Rayleigh scattering can increase the length of photon paths through the aerosol and enhance the chance of absorption. Also, if distributed vertically in the atmospheric column, the aerosol can reduce the Rayleigh-scattering component, which is otherwise large in the blue. Thus, the possibility of inferring aerosol absorption is increased as one progresses from the NIR into the visible, but unfortunately L_w is not known there (that is why atmospheric correction is required in the first place). The inescapable conclusion is

that the SeaWiFS algorithm¹¹ must fail when the aerosol is strongly absorbing unless the candidate aerosol models are restricted to those with similarly strong absorption properties.¹² Unless one could use a global aerosol climatology, i.e., knowledge of the aerosol expected to be present in a given region and time, to restrict the candidate aerosol models to the appropriate set, an alternate approach is needed.

In addition to atmospheric correction, there is compelling interest in studying the global distribution and transport of aerosols because of their role in climate forcing and biogeochemical cycles.^{16,17} Furthermore, not only is the aerosol concentration required, it is also important to know their absorption properties to understand their climatic effects. There has been continuing interest in measuring aerosol concentration from earth-orbiting sensors.^{18–27} Over the oceans these sensors generally utilize spectral bands for which the ocean can be assumed to be black ($L_w = 0$) or at least to have constant reflectance. By analogy to the atmospheric correction problem above, estimation of aerosol absorption properties from space fails for these sensors. The one exception is the retrieval of spatial distributions of strongly-absorbing aerosols using the Total Ozone Mapping Spectrometer (TOMS) measurements in the ultraviolet.²⁸

In this paper, we describe an alternate approach to the problem of estimating oceanic biophysical properties, and aerosol physical-chemical properties, using space-borne ocean color sensors. The approach is to utilize all of the spectral bands of the sensor. This insures sufficient multiple-scattering (Rayleigh scattering in the blue) to enable identification of aerosol absorption. In order to separate the effects of aerosols from radiance backscattered from beneath the sea surface (L_t), an ocean color model, in which the reflectance is related to the phytoplankton pigment concentration and the scattering properties of the phytoplankton and their associated detrital material, is used. As with the SeaWiFS algorithm, several candidate aerosols models are employed: nonabsorbing, weakly absorbing, and strongly absorbing. Through a systematic variation of the candidate model aerosols, phytoplankton scattering, C , and τ_a , a “best” fit to simulated spectral L_t data is obtained. It is found that the algorithm can successfully discriminate between weakly- and strongly-absorbing aerosols, and can provide estimates of C , τ_a , and ω_0 with an accuracy that is nearly independent of ω_0 . For consistency with earlier work,¹² we specifically examine a situation that would be

encountered off the U.S. East Coast in summer: polluted continental air transported by the winds to the Middle Atlantic Bight. However, this situation is used only as an example to demonstrate the approach, we believe that it could be applied to ocean regions subjected to mineral dust as well as aerosol resulting from biomass burning.

We begin with a discussion of the approach and the modeling of the various quantities required for implementation. Next, we test the efficacy of the algorithm using simulated SeaWiFS³ data. Recall SeaWiFS has 8 spectral bands centered at 412, 443, 490, 510, 555, 670, 765, and 865 nm. Finally, we examine the degradation of the performance of the algorithm in the presence of L_t -measurement error.

2. The algorithm approach and implementation

Neglecting influence of direct sun glitter and whitecaps, the total upwelling reflectance exiting the top of the atmosphere $\rho_t(\lambda)$ consists of the following components:^{11,12} the pure Rayleigh (molecular) scattering contribution $\rho_r(\lambda)$, the pure aerosol scattering contribution $\rho_a(\lambda)$, the contribution due to the interaction effect between air molecules and aerosols $\rho_{ra}(\lambda)$, and the desired water-leaving contribution $t(\lambda)\rho_w(\lambda)$, *i.e.*,

$$\rho_t(\lambda) = \rho_r(\lambda) + \rho_a(\lambda) + \rho_{ra}(\lambda) + t(\lambda)\rho_w(\lambda), \quad (1)$$

where $t(\lambda)$ is the diffuse transmittance of the atmosphere. From the satellite image, we have the spectrum of the upwelling reflectance $\rho_t(\lambda)$. As $\rho_r(\lambda)$ depends only on the surface atmospheric pressure,^{9,29} it is not difficult to remove the pure Rayleigh scattering contribution $\rho_r(\lambda)$ from the total reflectance $\rho_t(\lambda)$,

$$[\rho_t(\lambda) - \rho_r(\lambda)] = [\rho_a(\lambda) + \rho_{ra}(\lambda)] + t(\lambda)\rho_w(\lambda). \quad (2)$$

The known reflectance spectrum of $[\rho_t(\lambda) - \rho_r(\lambda)]$ consists of two parts which are hard to separate, the water-leaving reflectance term $t(\lambda)\rho_w(\lambda)$ and the aerosol contribution $[\rho_a(\lambda) + \rho_{ra}(\lambda)]$ (which includes the interaction term between aerosols and air molecules). The goal of atmospheric correction is to retrieve the water-leaving reflectance $\rho_w(\lambda)$ from the known reflectance $[\rho_t(\lambda) - \rho_r(\lambda)]$.

Because of the high spatial and temporal variability of the physical, chemical, and optical properties of aerosols, it is difficult to estimate the aerosol contribution $[\rho_a(\lambda) + \rho_{ra}(\lambda)]$ to the total upwelling reflectance.

The basic assumption of the proposed algorithm is that for each aerosol and pigment concentration there is a unique and distinctive spectrum characteristic of its upwelling reflectances $[\rho_a(\lambda) + \rho_{ra}(\lambda)]$ and $[t(\lambda)\rho_w(\lambda)]$. In a given sun-viewing geometry, similar (or close) spectra to $[\rho_t(\lambda) - \rho_r(\lambda)]$ can only be obtained from the atmosphere-ocean system by a combination of aerosols having similar optical properties to the actual aerosol, and a pigment concentration similar to that actually present in the ocean. That is, when we estimate $[t(\lambda)\rho_w(\lambda)]$ and $[\rho_a(\lambda) + \rho_{ra}(\lambda)]$ separately and form $[\rho_a(\lambda) + \rho_{ra}(\lambda)]'$ and $[t(\lambda)\rho_w(\lambda)]'$, where here and henceforth the primes will refer to computed or trial estimates, the computed reflectance spectrum

$$[\rho_t(\lambda) - \rho_r(\lambda)]' = [\rho_a(\lambda) + \rho_{ra}(\lambda)]' + [t(\lambda)\rho_w(\lambda)]',$$

will fit the true reflectance spectrum $[\rho_t(\lambda) - \rho_r(\lambda)]$ in the visible and near infrared only if *both* the computed water-leaving reflectance $[t(\lambda)\rho_w(\lambda)]'$ and the computed aerosol contribution $[\rho_a(\lambda) + \rho_{ra}(\lambda)]'$ fit their true values *individually*. In order to implement this idea, we need to be able to obtain estimates of $[t(\lambda)\rho_w(\lambda)]'$ and $[\rho_a(\lambda) + \rho_{ra}(\lambda)]'$. We now describe how the use of this assumption is accomplished.

2.A The water component: $t\rho_w$

The prediction of the water-leaving reflectance, $\rho_w(\lambda)$, is effected using the semi-empirical bio-optical radiance model, developed by Gordon *et al.*³⁰ for Case 1 waters^{5,31}, i.e., waters for which the optical properties are controlled by the water itself and by the concentration of phytoplankton and their decay products. As we use the pigment concentration C as a surrogate for the phytoplankton concentration, one would expect that the absorption and scattering properties of the particles would depend only on C ; however, it is found for such waters that for a given C the total scattering coefficient varies by roughly a factor of two.⁵ Thus, a second scattering-related parameter b^0 which ranges from 0.12 to 0.45 m^{-1} with a mean value of 0.30 m^{-1} (when C has units of mg/m^3)

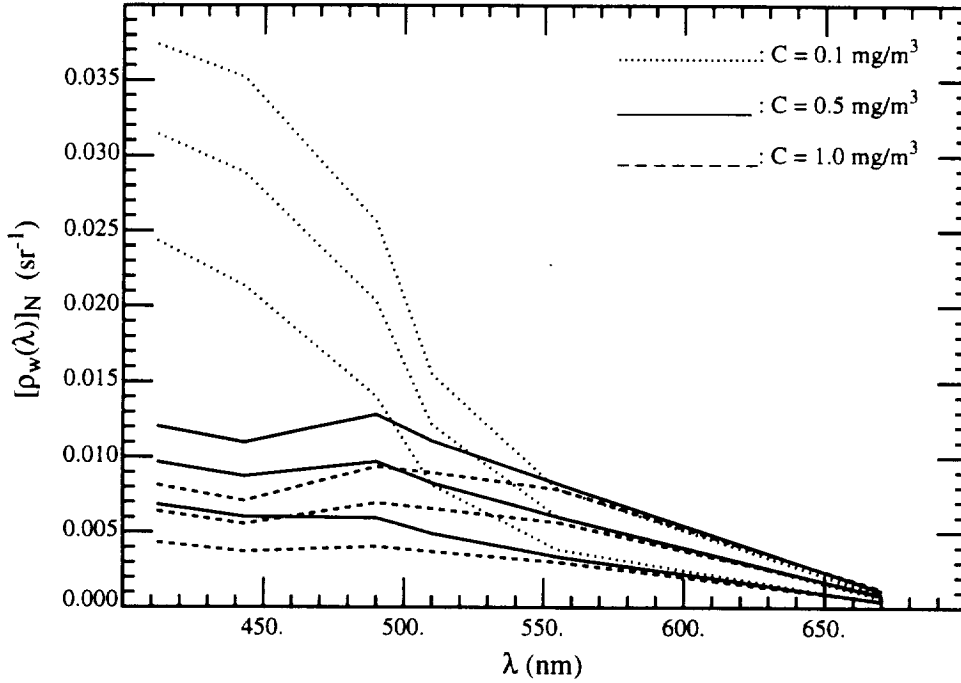


Figure 1 Spectrum of normalized water-leaving reflectance $[\rho_w(\lambda)]_N$ for pigment concentrations of 0.1, 0.5, and 1.0 mg/m^3 . For each pigment concentration, from the upper to the lower curves, the values of coefficient b^0 are 0.45, 0.30, and 0.12 m^{-1} , respectively.

is introduced. Gordon *et al.*³⁰ found that by using such a model, the water-leaving radiance dependence on C in Case 1 waters could be explained. Similar results were also obtained by Bricaud and Morel.³² This bio-optical ocean color model actually provides the *normalized* water-leaving reflectance,^{6,12} $[\rho_w(\lambda)]_N$, defined by

$$[\rho_w(\lambda)]_N \equiv \rho_w \exp[(\tau_r/2 + \tau_{Oz})/\cos \theta_0],$$

where τ_r and τ_{Oz} are the Rayleigh and Ozone optical thicknesses of the atmosphere, respectively, and θ_0 is the solar zenith angle. Sample spectra of $[\rho_w(\lambda)]_N$ as a function of C and b^0 are shown in Figure 1. Clearly, the normalized water-leaving reflectance is very sensitive to the pigment concentration C for short wavelengths (412 and 443 nm) and small pigment concentration ($C \lesssim 0.4 \text{ mg/m}^3$). For longer wavelengths (555 and 670 nm) or large pigment concentrations ($C \gtrsim 0.8 \text{ mg/m}^3$), $[\rho_w(\lambda)]_N$ does not depend significantly on the pigment concentration C . It is taken to be zero at 765 and 865 nm.

It should be noted that the Gordon *et al.*³⁰ reflectance model above does not take into account the bidirectional effects of the sub-surface upwelled spectral radiance, i.e., it assumes that the upwelling radiance beneath the sea surface is totally diffuse. Morel and co-workers^{33–36} have demonstrated that this is not the case; however, as Morel and Gentili³⁶ have shown, bidirectional effects can be easily introduced into the model and described as a function of C .

Once $\rho_w(\lambda)$ is determined, it is necessary to propagate it to the top of the atmosphere (TOA). As mentioned earlier, this is accomplished using the diffuse transmittance $t(\lambda)$. Tanre *et al.*³⁷ and Gordon *et al.*⁶ provided simple expressions for $t(\lambda)$ that include the effects of both aerosol and Rayleigh scattering. Later, Yang and Gordon³⁸ provided a detailed analysis of $t(\lambda)$ based on precise computations. They showed that (1) bidirectional effects play a role in t only in the blue and only at low C , (2) aerosols play a significant effect on t only if they are strongly absorbing, (3) t is independent of the aerosol vertical structure even if the aerosol is strongly absorbing, and (4) given an aerosol model it is simple to predict the correct value of t for any aerosol concentration and viewing geometry. The value of t can be computed precisely given C (to provide bidirectional effects), an aerosol model (to provide the aerosol properties), and the aerosol optical thickness $\tau_a(\lambda)$ (to provide the aerosol concentration). However, for the purposes of this paper, we will approximate t by assuming it is independent of the aerosol. In this case, $t(\lambda)$ is given by

$$t(\lambda) = \exp \left[-(\tau_r(\lambda)/2 + \tau_{Oz}) / \cos \theta_v \right],$$

where θ_v is the angle between the zenith and a line from the sensor to the pixel under consideration. Thus, the simulated $t(\lambda)\rho_w(\lambda)$ is given by

$$t(\lambda)\rho_w(\lambda) = [\rho_w(\lambda)]_N \exp \left[-(\tau_r(\lambda)/2 + \tau_{Oz}) \left(\frac{1}{\cos \theta_0} + \frac{1}{\cos \theta_v} \right) \right]. \quad (3)$$

2.B The aerosol component: $\rho_a + \rho_{ra}$

Gordon and Wang¹¹ have shown that the multiple scattering effects in $\rho_a + \rho_{ra}$ depend significantly on the physical and chemical properties of the aerosol, i.e., their size distribution and refractive index. Thus aerosol models had to be introduced to incorporate multiple scattering effects

in atmospheric correction. Similarly, aerosol models are also required to retrieve aerosol properties from space observations.^{39,40} Gordon and Wang¹¹ used aerosol models that were developed by Shettle and Fenn⁴¹ for LOWTRAN-6⁴². These models consist of particles distributed in size according to combinations of two log-normal distributions, and are described in detail in Ref. 12. Briefly, four models at four different relative humidities are used here. These are the Maritime (M), the Coastal (C), the Tropospheric (T), and the Urban (U). The relative humidities used are 50%, 70%, 90%, and 99%. We denote a particular model by a letter and a number, e.g., M99 refers to the Maritime model at 99% relative humidity. There is an increasing amount of absorption as one progresses through M,C,T, to U. For example, at 865 nm the aerosol single-scattering albedo, ω_0 , is 0.9934, 0.9884, and 0.9528, respectively, for the Maritime, Coastal, and Tropospheric models (RH = 80%), while in contrast, $\omega_0 = 0.7481$ for the Urban model. Here, the Urban model is intended to represent strongly absorbing aerosols that might be present over the oceans near areas with considerable urban pollution, e.g., the Middle Atlantic Bight off the U.S. East Coast in summer.

We employ these sixteen aerosol models as candidates to test the algorithm. For a two-layer atmosphere, with the aerosol confined to the bottom layer, the scalar radiative transfer equation (polarization ignored) was solved for each of the 16 candidate aerosol models (M, C, T, U aerosols with RH = 50%, 70%, 90%, 99%) with eight values of $\tau_a(\lambda)$ in the range of 0.05 to 0.8 at each wavelength λ , for solar zenith angle $\theta_0 = 0^\circ$ to 80° in increments of 2.5° , and for 33 different viewing zenith angles with θ_v in the range of 0° to 90° . As it is difficult to have this large computational set of values of $[\rho_a(\lambda) + \rho_{ra}(\lambda)]$ available for image processing for all of the aerosol candidates, aerosol optical thicknesses, sun-viewing geometries $(\theta_0, \theta_v, \phi_v)$, and spectral bands; in a manner similar to the Gordon and Wang algorithm,¹² lookup tables (LUTs) are used to provide $[\rho_a(\lambda) + \rho_{ra}(\lambda)]$. In the Gordon and Wang algorithm the lookup tables related $[\rho_a(\lambda) + \rho_{ra}(\lambda)]$ to $\rho_{as}(\lambda)$, the single scattered aerosol reflectance. Equivalently, we relate the term $[\rho_a(\lambda) + \rho_{ra}(\lambda)]$ to the aerosol optical thickness τ_a ; our simulated values of $[\rho_a(\lambda) + \rho_{ra}(\lambda)]$ are fit to

$$[\rho_a(\lambda) + \rho_{ra}(\lambda)] = a(\lambda) \tau_a + b(\lambda) \tau_a^2 + c(\lambda) \tau_a^3 + d(\lambda) \tau_a^4 \quad (4)$$

using least-squares. To further reduce storage, coefficients $a(\lambda)$, $b(\lambda)$, $c(\lambda)$ and $d(\lambda)$ were expanded in Fourier series in the azimuth view-angle ϕ_v , and only the Fourier coefficients were stored in

the LUTs. Samples of the fit of $[\rho_a(\lambda) + \rho_{ra}(\lambda)]$ to the aerosol optical thickness are presented in Figure 2 for a sun-viewing geometry with $\theta_0 = 60^\circ$, $\theta_v \approx 46^\circ$, and $\phi_v \approx 93^\circ$. This geometry has relatively large errors in the fits compared to the other geometries used here. It can be seen that the method of using Eq. (4), and Fourier expanding its coefficients, is appropriate for computing $[\rho_a(\lambda) + \rho_{ra}(\lambda)]$ for any candidate aerosol model, at any sun-viewing geometry, aerosol optical thickness, and wavelength. The largest fitting errors occurred at the largest wavelength ($\lambda = 865$ nm) and small aerosol optical thickness ($\tau_a \approx 0.1$). They were of the order of 1% to 2%.

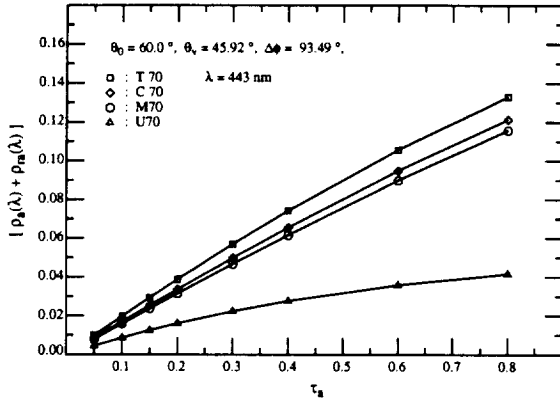


Figure 2(a) Curve fits of $[\rho_a(\lambda) + \rho_{ra}(\lambda)]$ vs. τ_a for aerosol models of M70, C70, T70 and U70 at $\lambda = 443$ nm with $\theta_0 = 60.0^\circ$, $\theta_v = 45.92^\circ$, and $\phi = 93.49^\circ$.

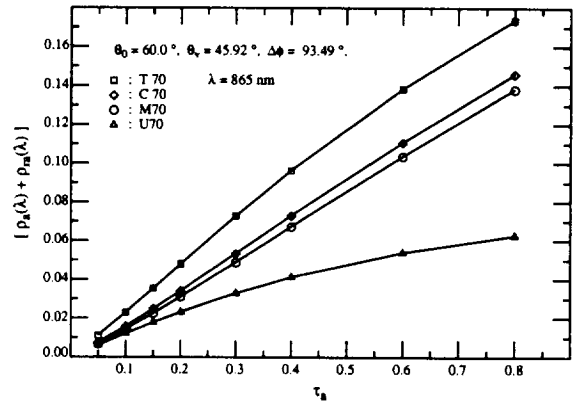


Figure 2(b) Curve fits of $[\rho_a(\lambda) + \rho_{ra}(\lambda)]$ vs. τ_a for aerosol models of M70, C70, T70 and U70 at $\lambda = 865$ nm with $\theta_0 = 60.0^\circ$, $\theta_v = 45.92^\circ$, and $\phi = 93.49^\circ$.

2.C The algorithm implementation

We experimented with several approaches for implementing the algorithm. The one we found most effective is summarized as follows:

First, for the given sun-viewing geometry $(\theta_0, \theta_v, \phi_v)$, we vary the value of aerosol optical thickness at 865 nm, $\tau_a(865)$, for each candidate aerosol model to provide the aerosol component $[\rho_a(\lambda) + \rho_{ra}(\lambda)]'$. We then vary the pigment concentration C and the scattering-related coefficient b^0 to provide the water-leaving reflectance $[t(\lambda)\rho_w(\lambda)]'$. These yield a trial upwelling reflectance $[\rho_t(\lambda) - \rho_r(\lambda)]'$ at each of N bands of the ocean color sensor.

Second, we compute the percent deviation δ' of this simulated spectrum $[\rho_t(\lambda) - \rho_r(\lambda)]'$ from the measured true spectrum $[\rho_t(\lambda) - \rho_r(\lambda)]$ for each test set $(A, \tau_a, C, b^0)'$, where A labels the candidate aerosol model. The percent deviation $\delta(A, \tau_a, C, b^0)'$ is defined in the sense of root-mean-squares,

$$\delta(A, \tau_a, C, b^0)' = \sqrt{\frac{1}{N-1} \sum_{i=1}^N \left[\frac{[\rho_t(\lambda_i) - \rho_r(\lambda_i)] - [\rho_t(\lambda_i) - \rho_r(\lambda_i)]'}{[\rho_t(\lambda_i) - \rho_r(\lambda_i)]} \right]^2}. \quad (5)$$

Third, we sort the deviations $\delta(A, \tau_a, C, b^0)'$ to find 10 best sets of $(A, \tau_a, C, b^0)'$ which yield 10 smallest percent deviations $\delta(A, \tau_a, C, b^0)'$.

Fourth, as the correct aerosol model is unlikely to be identical to one of the candidates, we assume the characteristics of aerosols and pigment concentration can be adequately described by these 10 best sets of parameters $(A, \tau_a, C, b^0)'$. The retrieved single scattering albedo ω'_0 and optical thickness τ'_a of the aerosols, and $b^{0'}$ and the pigment concentration C' in the ocean are then computed by averaging ω'_0 , τ'_a , $b^{0'}$ and C' over the 10 best sets of $(A, \tau_a, C, b^0)'$.

3. The algorithm's performance

In this section, we examine the performance of the spectrum-matching algorithm by applying it to SeaWiFS.³ The sun-viewing geometries are taken as those used in Refs. 11 and 12: viewing at the center of the scan (viewing zenith angle $\theta_v \approx 1^\circ$) for solar zenith angle $\theta_0 = 20^\circ, 40^\circ$ and 60° , and viewing at the edge of the scan ($\theta_v \approx 45^\circ$) near the perpendicular plane for $\theta_0 = 0^\circ, 20^\circ, 40^\circ$ and 60° . These cover much of the range of sun-viewing geometries available to SeaWiFS. Pseudo data are provided by solving the scalar radiative transfer equation for a two-layer atmosphere system with a specified aerosol confined in the lower layer. The pseudo water-leaving reflectance $\rho_w(\lambda)$ was provided for $b^0 = 0.30 \text{ m}^{-1}$ (the mean value for Case 1 waters) and pigment concentrations $C = 0.1, 0.5$, and 1.0 mg/m^3 .

The algorithm attempts to match the pseudo data spectrum of $\rho_t(\lambda)$ by varying the testing aerosol model among its 16 candidates ($N_A = 16$), the aerosol optical thickness $\tau_a(865)$ from 0.01

to 0.40 in increments of 0.01 ($N_\tau = 40$), the pigment concentration from 0.05 to 1.50 mg/m³ in increments of 0.05 mg/m³ ($N_C = 30$), and finally, b^0 from 0.12 to 0.45 m⁻¹ in increments of 0.03 m⁻¹ ($N_b = 12$). The total number of elements in the test set $(A, \tau_a, C, b^0)'$ is $N = N_A \times N_\tau \times N_C \times N_b = 16 \times 40 \times 30 \times 12 = 230400$.

For the first test of the algorithm we examined cases in which the aerosol optical properties of the pseudo atmosphere were included in the candidate aerosol models, i.e., the aerosol optical properties in the atmosphere system were taken from M70, C70, T70 and U70. The optical thickness at 865 nm was taken to be $\tau_a(865) = 0.1, 0.2$ or 0.3 . The main purpose of this was to test the code for implementation of the algorithm. In all cases, for the best set (smallest δ') the correct aerosol model and the correct values of the parameters were chosen. In fact, δ' for the correct set was a small fraction of a percent and ~ 10 to 30 times smaller than the second best set. The residual error was due to small errors in the LUTs. Even the averages over the ten best sets were excellent, providing close values of $\tau_a(865)$, b^0 , and C . As the aerosol single scattering albedo ω_0 is a weak function of wavelength λ , we use its the retrieved value at 865 nm, $\omega_0(865)$, (averaged over the ten best sets) as an indication of the algorithm's ability to distinguish between weakly- and strongly-absorbing aerosols. The derived values of $\omega_0(865)$ showed that weakly and strongly absorbing aerosols are easily recognized by the algorithm.

As it is not likely for the aerosols in the atmosphere will have exactly the same optical properties as any one of candidate aerosol models, we tested more realistic cases in which the aerosol models were similar to, but not the same as, any of the sixteen candidate aerosol models. Following Gordon¹² the aerosol models M80, C80, T80 and U80 (Shettle and Fenn models with relative humidity 80%) were chosen for this purpose. We begin by describing the results obtained from averaging the parameters from the sets with the ten smallest values of δ' . The averaged $\omega'_0(865)$, $\tau'_a(865)$, and C' for a given geometry are taken to be the retrieved values of these parameters. To estimate the performance on a more global scale, i.e., for all sun-viewing geometries, we then average over all seven sun-viewing geometries and compute the mean and the standard deviation in the retrieved parameter values. The mean values of retrieved aerosol single scattering albedo $\omega'_0(865)$ are provided in Table 1 for aerosol models M80, C80, T80 and U80. It can be seen from

Table 1 that the retrieved results for ω_0 are very good for each of four pseudo aerosol models. Large percent deviations (the standard deviation over the seven geometries divided by the mean) in the range of 3% to about 8%, are encountered for the strongly absorbing U80 aerosol model, nevertheless the algorithm can distinguish between the weakly absorbing aerosols (M80, C80, T80) and the strongly absorbing aerosol (U80) without difficulty.

Since the ultimate goal of ocean color remote sensing is to estimate the phytoplankton pigment concentration, we now examine the retrieval of C using the algorithm. Table 2 presents the mean values of retrieved C' , which are averaged over seven sun-viewing geometries and also over the four test aerosol models, M80, C80, T80, and U80 (28 cases in all). It can be observed that the retrieved results of pigment concentration are reasonable for all three tested aerosol optical thicknesses [$\tau_a(865) = 0.1, 0.2$, and 0.3] and all three pigment concentrations [$C = 0.1, 0.5$, and 1.0 mg/m^3]. For the small pigment concentration, $C = 0.1 \text{ mg/m}^3$, or for small aerosol optical thickness, $\tau_a(865) = 0.1$, the spectrum-matching algorithm still works very well. With an increase in either pigment concentration or aerosol concentration, the percent deviations and percent errors in the retrieved C' become larger. For comparison, Table 3 provides similar results for the weakly-absorbing aerosols only, using the Gordon and Wang correction algorithm.¹² Note that the present algorithm behaves as well as the Gordon and Wang algorithm, even when strongly-absorbing aerosols are included. Had strongly-absorbing aerosols been included in Table 3, the results would have been significantly poorer, e.g., in some cases it would have been impossible to even compute C because one or both of the required ρ_w 's would likely be negative.

Detailed retrievals of the pigment concentration C are tabulated in Table 4, which gives percentages of cases with relative error in the retrieval, $|\Delta C|/C$, less than 5%, 10%, 20%, and 30%, respectively. For the smallest pigment concentration, in all of the 84 cases examined (three aerosol optical thicknesses, four aerosol models, and seven sun-viewing geometries), $|\Delta C|/C < 20\%$, and even $< 5\%$ for about 90% of the cases. For a pigment concentration of $C = 0.5 \text{ mg/m}^3$, and for small aerosol optical thickness, $\tau_a(865) = 0.1$, all individual simulations have $|\Delta C|/C < 30\%$, while for $\tau_a(865) = 0.2$ there are about 89% of the cases having $|\Delta C|/C < 30\%$, and for $\tau_a(865) = 0.3$ about 75% of the cases having $|\Delta C|/C < 30\%$. At the highest pigment concentration examined

(1.0 mg/m³), for small aerosol optical thickness the algorithm still performs very well with only one case with $|\Delta C|/C > 30\%$. However, as $\tau_a(865)$ increases, the errors become larger, and about 71% of the cases have $|\Delta C|/C < 30\%$ for $\tau_a(865) = 0.2$, and only about 60% for $\tau_a(865) = 0.3$.

The algorithm clearly works better in estimating C for smaller pigment concentrations. This is explained by the relationship between the (normalized) upwelling water-leaving reflectance and the pigment concentration (see Figures 1 and 2). As we stated in Section 2, the water-leaving reflectance depends strongly on pigment concentration C when C is small ($C \lesssim 0.4$ mg/m³). At small C , a small change in C (0.05 mg/m³ in the algorithm) will result in a significant change in the upwelling water-leaving reflectance. But when pigment concentration is as large as about 1.0 mg/m³, the upwelling water-leaving reflectance is only a weak function of pigment concentration, and a small change of 0.05 mg/m³ in C is not going to result in any significant change in the upwelling water-leaving reflectance. This causes the large percent deviation in C when the algorithm is applied to large pigment concentrations.

Mean values of the retrieved aerosol optical thickness $\tau'_a(865)$ over the seven sun-viewing geometries and four testing aerosol models (M80, C80, T80 and U80) are presented in Table 5. The mean values are close to their corresponding “true” aerosol optical thicknesses, the percent deviations are ranged from about 6% to about 11%.

Figure 3 provides samples of the three best sets (A, τ_a, C, b^0) determined by the algorithm for aerosol models of M80, C80, T80 and U80 with $\tau_a(865) = 0.2$ and $C = 0.5$ mg/m³, for a single sun-viewing geometry ($\theta_0 = 20^\circ$, $\theta_v = 45.92^\circ$, $\phi_v = 90^\circ$). As the pseudo aerosol models (M80, C80, T80 and U80) are similar to the candidate models used in the algorithm, (M, C, T, and U with RH = 50%, 70%, 90% and 99%), but are not identical to any of 16 candidates, there is no correct aerosol model for the algorithm to choose to match the upwelling reflectance $[\rho_a(\lambda) + \rho_{ra}(\lambda) + t(\lambda)\rho_w(\lambda)]$. The figure shows that the aerosol models which have similar optical properties to those of pseudo aerosol models are selected first by the algorithm. Even though there are some errors caused by picking the incorrect aerosol models, the pigment concentration chosen by the algorithm is close to its true value (0.5 mg/m³ in Figure 3). For the four pseudo aerosol models tested, the percent deviations of the best match for whole spectrum $\delta(A, \tau_a, C, b^0)'$ varied from about 0.7% to 1.1%.

Unlike the case when the test aerosol was one of the candidates, there was no significant increase in δ' from the best set to the second best set. For the best 10 sets, the largest percent deviation for $C = 0.5 \text{ mg/m}^3$ is about 1.5%.

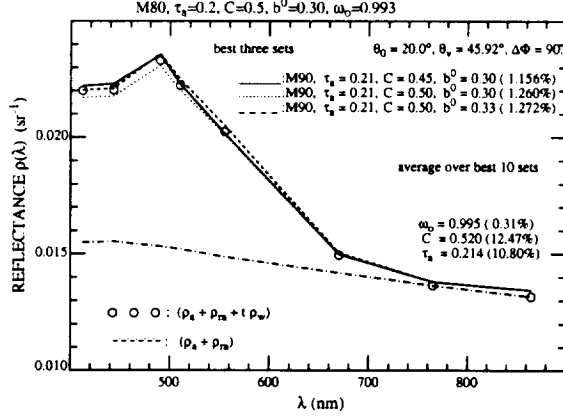


Figure 3(a) Reflectance spectrum matching for aerosol model M80 and pigment concentration $C = 0.50 \text{ mg/m}^3$ with sun-viewing geometry of $\theta_0 = 20.0^\circ$, $\theta_v = 45.92^\circ$, and $\phi = 90.0^\circ$.

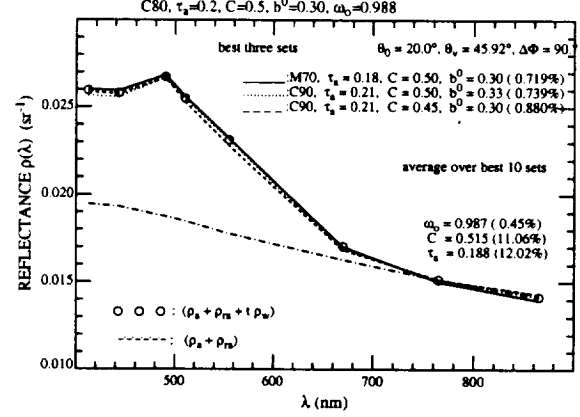


Figure 3(b) Reflectance spectrum matching for aerosol model C80 and pigment concentration $C = 0.50 \text{ mg/m}^3$ with sun-viewing geometry of $\theta_0 = 20.0^\circ$, $\theta_v = 45.92^\circ$, and $\phi = 90.0^\circ$.

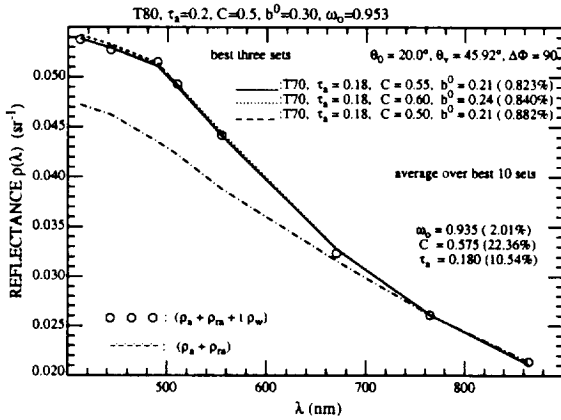


Figure 3(c) Reflectance spectrum matching for aerosol model T80 and pigment concentration $C = 0.50 \text{ mg/m}^3$ with sun-viewing geometry of $\theta_0 = 20.0^\circ$, $\theta_v = 45.92^\circ$, and $\phi = 90.0^\circ$.

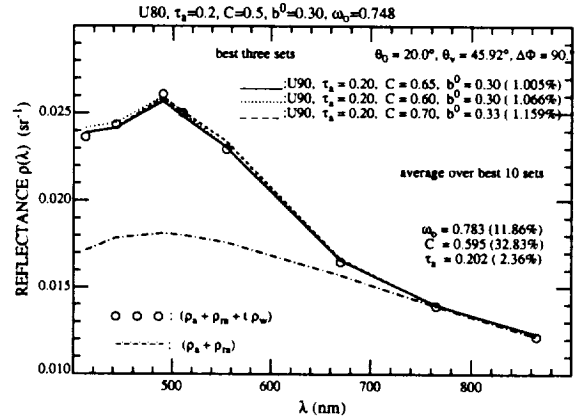


Figure 3(d) Reflectance spectrum matching for aerosol model U80 and pigment concentration $C = 0.50 \text{ mg/m}^3$ with sun-viewing geometry of $\theta_0 = 20.0^\circ$, $\theta_v = 45.92^\circ$, and $\phi = 90.0^\circ$.

From these tests of the algorithm we conclude that it can detect the presence of strongly absorbing aerosols successfully. Whenever the optical properties of aerosol in the atmosphere are the same (or very close) to that of any of the 16 candidate aerosol models employed in the

algorithm, the retrieved pigment concentration C will be excellent, meeting the requirements of SeaWiFS and MODIS. If the optical properties of the aerosol in the atmosphere are similar to that of any candidate aerosol model, the retrieval results for the pigment concentration C will still be good in the presence of small pigment concentration or small aerosol optical thickness. When both large aerosol optical thickness [$\tau_a(865)$ around 0.2 to 0.3] and large pigment concentration [C around 0.5 to 1.0 mg/m³] are present in the atmosphere-ocean system, the performance of the algorithm will be degraded. Still, for the worst scenario examined here, $\tau_a(865) = 0.3$ and $C = 1.0$ mg/m³, about 60% of the individual simulations have $|\Delta C|/C < 30\%$.

These simulations suggest that the success of the algorithm depends on the appropriateness of candidate aerosol models and the bio-optical model employed in the algorithm. Although we will not be able to know the percent errors in the retrieved aerosol single scattering albedo $\omega'_0(865)$ and pigment concentration C' in processing a satellite image, we can compute $\delta(A, \tau_a, C, b^0)'$ over all bands which are used for ocean color remote sensing. Generally, small percent deviations lead to small percent errors, so that the percent deviations for retrieved $\omega'_0(865)$ and C' can also be used to assess the performance of the algorithm.

4. Further tests

Addition tests of this algorithm remain to be completed. As mentioned in Section 1, when the aerosol is strongly absorbing, ρ_t depends significantly on the aerosol's vertical distribution. In the simulations presented here, the correct vertical distribution was assumed, i.e., the pseudo data were created using the same vertical distribution as was assumed for the candidate aerosol models. We believe that the vertical distribution can be introduced into the algorithm simply as new candidate aerosol models, e.g., the U70 model with all of the aerosol in the marine boundary layer and the U70 aerosol model with the aerosol uniformly mixed in the entire atmosphere, would represent distinct candidate aerosol models. This hypothesis will be tested. Also, we need to examine the sensitivity of the algorithm to errors in $\rho_t - \rho_r$.

References

- [1] W. A. Hovis, D. K. Clark, F. Anderson, R. W. Austin, W. H. Wilson, E. T. Baker, D. Ball, H. R. Gordon, J. L. Mueller, S. Y. E. Sayed, B. Strum, R. C. Wrigley and C. S. Yentsch, "Nimbus 7 coastal zone color scanner: system description and initial imagery," *Science* **210**, 60–63 (1980).
- [2] H. R. Gordon, D. K. Clark, J. L. Mueller and W. A. Hovis, "Phytoplankton pigments derived from the Nimbus-7 CZCS: initial comparisons with surface measurements," *Science* **210**, 63–66 (1980).
- [3] S. B. Hooker, W. E. Esaias, G. C. Feldman, W. W. Gregg and C. R. McClain, *SeaWiFS Technical Report Series: Volume 1, An Overview of SeaWiFS and Ocean Color* (NASA, Greenbelt, MD, Technical Memorandum 104566, July 1992).
- [4] V. V. Salomonson, W. L. Barnes, P. W. Maymon, H. E. Montgomery and H. Ostrow, "MODIS: Advanced Facility Instrument for Studies of the Earth as a System," *IEEE Geosci. Rem. Sens.* **27**, 145–152 (1989).
- [5] H. R. Gordon and A. Y. Morel, *Remote Assessment of Ocean Color for Interpretation of Satellite Visible Imagery: A Review* (Springer-Verlag, New York, 1983), 114 pp.
- [6] H. R. Gordon, D. K. Clark, J. W. Brown, O. B. Brown, R. H. Evans and W. W. Broenkow, "Phytoplankton pigment concentrations in the Middle Atlantic Bight: comparison between ship determinations and Coastal Zone Color Scanner estimates," *Applied Optics* **22**, 20–36 (1983).
- [7] H. R. Gordon, "Removal of Atmospheric Effects from Satellite Imagery of the Oceans," *Applied Optics* **17**, 1631–1636 (1978).

- [8] H. R. Gordon and D. K. Clark, "Atmospheric effects in the remote sensing of phytoplankton pigments," *Boundary-Layer Meteorology* **18**, 299–313 (1980).
- [9] H. R. Gordon, J. W. Brown and R. H. Evans, "Exact Rayleigh Scattering Calculations for use with the Nimbus-7 Coastal Zone Color Scanner," *Applied Optics* **27**, 862–871 (1988).
- [10] R. H. Evans and H. R. Gordon, "CZCS 'System Calibration:' A retrospective examination," *Jour. Geophys. Res.* **99C**, 7293–7307 (1994).
- [11] H. R. Gordon and M. Wang, "Retrieval of water-leaving radiance and aerosol optical thickness over the oceans with SeaWiFS: A preliminary algorithm," *Applied Optics* **33**, 443–452 (1994).
- [12] H. R. Gordon, 1996, Atmospheric Correction of Ocean Color Imagery in the Earth Observing System Era, *Jour. Geophys. Res.* (In press).
- [13] G. A. d'Almeida, P. Koepke and E. P. Shettle, *Atmospheric Aerosols — Global Climatology and Radiative Characteristics* (A. Deepak Publishing, Hampton, VA, 1991).
- [14] T. Nakajima, M. Tanaka, M. Yamano, M. Shiobara, K. Arao and Y. Nakanishi, "Aerosol Optical Characteristics in the Yellow Sand Events Observed in May 1982 at Nagasaki – Part II Models," *Jour. Meteorological Soc. Japan* **67**, 279–291 (1989).
- [15] R. W. Young, K. L. Carder, P. R. Betzer, D. K. Costello, R. A. Duce, G. R. Ditullio, N. W. Tindale, E. A. Laws, M. Uematsu, J. T. Merrill and R. A. Feeley, "Atmospheric Iron Inputs and Primary Productivity: Phytoplankton Responses in the North Pacific," *Global Biogeochemical Cycles* **5**, 119–134 (1991).
- [16] R. J. Charlson, S. E. Schwartz, J. M. Hales, R. D. Cess, J. A. Coakley, J. E. Hansen and D. J. Hofmann, "Climate Forcing by Anthropogenic Aerosols," *Science* **255**, 423–430 (1992).

- [17] Y. J. Kaufman, "Remote Sensing of Direct and Indirect Aerosol Forcing," in *Aerosol Forcing of Climate*, edited by R. H. Charlson and J. Heintzenberg (Wiley, New York, NY, 1995) p. 297-332.
- [18] M. Griggs, "Measurements of the Aerosol Optical Thickness Over Water Using ERTS-1 Data," *Jour. Air Poll. Contr. Assoc.* **25**, 622-626 (1975).
- [19] Y. Mekler, H. Quenzel, G. Ohring and I. Marcus, "Relative Atmospheric Aerosol Content from ErtS Observations," *Jour. Geophys. Res.* **82**, 967-970 (1977).
- [20] M. Griggs, *AVHRR Measurements of Atmospheric Aerosols Over Oceans* (NOAA National Environmental Satellite Service, Final Report Contract No. M0-A01-78-00-4092, November 1981).
- [21] M. Griggs, *Satellite Measurements of Tropospheric Aerosols* (NASA, Contractor Report 3459, August 1981).
- [22] M. Griggs, *AVHRR Aerosol Ground Truth Experiment* (NOAA National Environmental Satellite Service, Final Report Contract No. NA-83-SAC-00106, January 1984).
- [23] R. S. Fraser, "Satellite measurement of mass of Sahara dust in the atmosphere," *Applied Optics* **15**, 2471-2479 (1976).
- [24] P. Koepke and H. Quenzel, "Turbidity of the Atmosphere Determined From Satellite: Calculation of Optimum Viewing Geometry," *Jour. Geophys. Res.* **84**, 7847-7856 (1979).
- [25] P. Koepke and H. Quenzel, "Turbidity of the Atmosphere Determined From Satellite: Calculation of Optimum Wavelength," *Jour. Geophys. Res.* **86**, 9801-9805 (1981).

- [26] P. A. Durkee, D. R. Jensen, E. E. Hindman and T. H. V. Haar, "The Relationship Between Marine Aerosol Particles and Satellite-Detected Radiance," *Jour. Geophys. Res.* **91D**, 4063–4072 (1986).
- [27] C. R. N. Rao, L. L. Stowe, E. P. McClain and J. Sapper, "Development and Application of Aerosol Remote Sensing with AVHRR Data from the NOAA Satellites," in *Aerosols and Climate*, edited by P. Hobbs and M. P. McCormick (Deepak, Hampton, VA, 1988) p. 69–80.
- [28] J. R. Herman, P. K. Bhartia, O. Torres, C. Hsu, C. Seftor and E. Celarier, "Global Distribution of Absorbing Aerosols from Nimbus-7/TOMS Data," 1996, *Jour. Geophys. Res.* (Submitted).
- [29] J. E. Hansen and L. D. Travis, "Light Scattering in Planetary Atmospheres," *Space Science Reviews* **16**, 527–610 (1974).
- [30] H. R. Gordon, O. B. Brown, R. H. Evans, J. W. Brown, R. C. Smith, K. S. Baker and D. K. Clark, "A Semi-Analytic Radiance Model of Ocean Color," *Jour. Geophys. Res.* **93D**, 10909–10924 (1988).
- [31] A. Morel and L. Prieur, "Analysis of Variations in Ocean Color," *Limnology and Oceanography* **22**, 709–722 (1977).
- [32] A. Bricaud and A. Morel, "Atmospheric Corrections and Interpretation of Marine Radiances in CZCS Imagery: Use of a Reflectance Model," *Oceanologica Acta* **7**, 33–50 (1987).
- [33] A. Morel and B. Gentili, "Diffuse reflectance of oceanic waters: its dependence on Sun angle as influenced by the molecular scattering contribution," *Applied Optics* **30**, 4427–4438 (1991).
- [34] A. Morel and B. Gentili, "Diffuse reflectance of oceanic waters. II. Bidirectional aspects," *Applied Optics* **32**, 6864–6879 (1993).

- [35] A. Morel, K. J. Voss and B. Gentili, "Bidirectional reflectance of oceanic waters: A comparison of modeled and measured upward radiance fields," *Jour. Geophys. Res.* **100C**, 13,143–13,150 (1995).
- [36] A. Morel and B. Gentili, "Diffuse reflectance of oceanic waters. III. Implication of bidirectionality for the remote sensing problem," *Applied Optics* **35**, 4850–4862 (1996).
- [37] D. Tanre, M. Herman, P. Y. Deschamps and A. de Leffe, "Atmospheric modeling for space measurements of ground reflectances, including bidirectional properties," *Applied Optics* **18**, 3587–3594 (1979).
- [38] H. Yang and H. R. Gordon, 1997 , "Remote sensing of ocean color: Assessment of the water-leaving radiance bidirectional effects on the atmospheric diffuse transmittance," *Applied Optics*, (Submitted).
- [39] M. Wang and H. R. Gordon, "Estimating aerosol optical properties over the oceans with the multiangle imaging spectroradiometer: Some preliminary studies," *Applied Optics* **33**, 4042–4057 (1994).
- [40] M. Wang and H. R. Gordon, "Estimation of aerosol columnar size distribution and optical thickness from the angular distribution of radiance exiting the atmosphere: simulations," *Applied Optics* **34**, 6989–7001 (1995).
- [41] E. P. Shettle and R. W. Fenn, *Models for the Aerosols of the Lower Atmosphere and the Effects of Humidity Variations on Their Optical Properties* (Air Force Geophysics Laboratory, Hanscomb AFB, MA 01731, AFGL-TR-79-0214, 1979).

- [42] F. X. Kenizys, E. P. Shettle, W. O. Gallery, J.H.Chetwynd, L. W. Abreu, J. E. A. Selby, S. A. Clough and R. W. Fenn, *Atmospheric Transmittance/Radiance: The LOWTRAN 6 Model* (Air Force Geophysics Laboratory, Hanscomb AFB, MA 01731, AFGL-TR-83-0187, 1983) NTIS AD A137796.

Table 1: Mean values of retrieved $\omega'_0(865)$ for the seven sun-viewing geometries and each of four aerosol models (M80, C80, T80, U80). The standard deviation divided by the mean is listed in parenthesis.

	$C: \text{mg/m}^3$	0.100	0.500	1.000
M80 $\omega_0 = 0.993$	$\tau_a(865) = 0.100$	0.992 (0.43%)	0.996 (0.14%)	0.997 (0.10%)
	$\tau_a(865) = 0.200$	0.995 (0.10%)	0.995 (0.10%)	0.996 (0.05%)
	$\tau_a(865) = 0.300$	0.996 (0.05%)	0.996 (0.06%)	0.996 (0.10%)
	$C: \text{mg/m}^3$	0.100	0.500	1.000
C80 $\omega_0 = 0.988$	$\tau_a(865) = 0.100$	0.980 (0.97%)	0.972 (1.60%)	0.965 (2.26%)
	$\tau_a(865) = 0.200$	0.983 (0.53%)	0.988 (0.31%)	0.989 (0.41%)
	$\tau_a(865) = 0.300$	0.987 (0.25%)	0.987 (0.27%)	0.987 (0.37%)
	$C: \text{mg/m}^3$	0.100	0.500	1.000
T80 $\omega_0 = 0.953$	$\tau_a(865) = 0.100$	0.952 (0.78%)	0.935 (0.13%)	0.935 (0.00%)
	$\tau_a(865) = 0.200$	0.946 (0.34%)	0.936 (0.44%)	0.940 (1.41%)
	$\tau_a(865) = 0.300$	0.945 (0.31%)	0.934 (0.04%)	0.945 (1.82%)
	$C: \text{mg/m}^3$	0.100	0.500	1.000
U80 $\omega_0 = 0.748$	$\tau_a(865) = 0.100$	0.793 (4.21%)	0.761 (4.51%)	0.769 (3.36%)
	$\tau_a(865) = 0.200$	0.730 (4.76%)	0.750 (8.25%)	0.712 (7.44%)
	$\tau_a(865) = 0.300$	0.730 (5.14%)	0.784 (2.56%)	0.699 (7.34%)

Table 2: Mean values of retrieved C' for seven sun-viewing geometries and four aerosol models (M80, C80, T80, U80). The standard deviation divided by the mean is listed in parenthesis.

$C: \text{mg/m}^3$	0.100	0.500	1.000
$\tau_a(865) = 0.100$	0.100 (1.90%)	0.528 (7.30%)	1.098 (11.7%)
$\tau_a(865) = 0.200$	0.101 (4.56%)	0.547 (15.2%)	0.982 (23.9%)
$\tau_a(865) = 0.300$	0.101 (4.42%)	0.612 (24.1%)	0.947 (31.3%)

Table 3: Mean values of retrieved C' for seven sun-viewing geometries and three aerosol models (M80, C80, T80). derived using the Gordon and Wang¹¹ algorithm. The standard deviation divided by the mean is listed in parenthesis.

$C: \text{mg/m}^3$	0.10	0.47	0.91
$\tau_a(865) = 0.100$	0.101 (1.6%)	0.466 (3.4%)	0.912 (9.1%)
$\tau_a(865) = 0.200$	0.100 (3.1%)	0.470 (4.7%)	0.940 (12.8%)
$\tau_a(865) = 0.300$	0.098 (5.5%)	0.493 (15.3%)	0.936 (25.3%)

Table 4: Percentage of retrieved pigment concentration C' within certain error limits for aerosol models of M80, C80, T80, and U80.

	$\Delta C/C :$	< 5%	< 10%	< 20%	< 30%
$C = 0.1 \text{ mg/m}^3$	$\tau_a(865) = 0.100$	96%	100%	100%	100%
	$\tau_a(865) = 0.200$	89%	92%	100%	100%
	$\tau_a(865) = 0.300$	89%	92%	100%	100%

	$\Delta C/C :$	< 5%	< 10%	< 20%	< 30%
$C = 0.5 \text{ mg/m}^3$	$\tau_a(865) = 0.100$	32%	75%	92%	100%
	$\tau_a(865) = 0.200$	32%	50%	75%	89%
	$\tau_a(865) = 0.300$	25%	35%	64%	75%

	$\Delta C/C :$	< 5%	< 10%	< 20%	< 30%
$C = 1.0 \text{ mg/m}^3$	$\tau_a(865) = 0.100$	21%	50%	71%	96%
	$\tau_a(865) = 0.200$	28%	39%	57%	71%
	$\tau_a(865) = 0.300$	14%	25%	50%	60%

Table 5: Mean values of retrieved $\tau'_a(865)$ for seven sun-viewing geometries and four aerosol models (M80, C80, T80, U80). The standard deviation divided by the mean is listed in parenthesis.

$C: \text{ mg/m}^3$	0.100	0.500	1.000
$\tau_a(865) = 0.100$	0.102 (8.94%)	0.101 (10.2%)	0.102 (11.6%)
$\tau_a(865) = 0.200$	0.201 (6.31%)	0.199 (8.53%)	0.199 (8.20%)
$\tau_a(865) = 0.300$	0.300 (6.22%)	0.294 (8.79%)	0.300 (9.93%)

Appendix 2

Remote sensing of ocean color: Assessment of the water-leaving radiance bidirectional effects on the atmospheric diffuse transmittance

Haoyu Yang and Howard R. Gordon

Department of Physics

University of Miami

Coral Gables, FL 33124

Submitted to *Applied Optics*

Abstract

Two factors influence the diffuse transmittance (t) of water-leaving radiance (L_w) to the top of the atmosphere: the angular distribution of upwelling radiance beneath the sea surface (L_u); and the concentration and optical properties of aerosols in the atmosphere. We examine these factors and show (1) that the error in L_w induced by assuming L_u is uniform, i.e., in treating the subsurface reflectance by the water-body as lambertian, is significant in comparison to the other errors expected in L_w only at low phytoplankton concentration and then only in the blue region of the spectrum, (2) that when radiance ratios are used in biophysical algorithms the affect of the uniform- L_u approximation is even smaller, and (3) the diffuse transmittance is a strong function of the absorption properties of aerosol in the atmosphere, but is nearly independent of their vertical distribution. An avenue for introducing accurate computation of the uniform- L_u diffuse transmittance into atmospheric correction algorithms is presented. In an appendix the reciprocity principle for a medium in which the refractive index is a continuous function of position is derived.

1. Introduction

The feasibility of measuring marine phytoplankton concentrations from earth-orbiting sensors was demonstrated by the proof-of-concept Coastal Zone Color Scanner (CZCS)^{1,2} mission. Based on the CZCS experience, several similar instruments with a larger number of spectral bands and higher radiometric sensitivity are being prepared for launch, e.g., the sea-viewing wide-field-of-view sensor (SeaWiFS),³ the moderate resolution imaging spectroradiometer (MODIS),⁴ etc. The surrogate for measurement of the phytoplankton concentration is the concentration of the photosynthetic pigment chlorophyll *a* within the water (actually, within the plants). As chlorophyll *a* has a broad strong absorption in the blue (~ 435 nm) and a minimum of absorption in the green (~ 565 nm), the concentration within the water can be estimated from the solar radiance backscattered out of the water near these wavelengths,^{5,6} the water-leaving radiance. Unfortunately, the water-leaving radiance typically comprises at most 10% of the total radiance exiting the top of the atmosphere (TOA). Briefly, the radiance exiting the top of the atmosphere in a spectral band centered at λ_i , $L_t(\lambda_i)$, can be written

$$L_t(\lambda_i) = L_{Other}(\lambda_i) + L_w^a(\lambda_i). \quad (1)$$

where $L_{Other}(\lambda_i)$ represents the contribution to the radiance from all sources except the water-leaving radiance propagated to the TOA, $L_w^a(\lambda_i)$. Sources of L_{Other} include scattering of solar radiation in the atmosphere, specular reflection of scattered and unscattered radiation from the direct solar beam by the sea surface, and diffuse reflection from oceanic whitecaps. The atmospheric correction algorithm of Gordon and Wang^{7,8} estimates L_{Other} and removes it from the total radiance, thereby obtaining the water-leaving radiance transmitted to the top of the atmosphere, $L_w^a(\lambda_i)$. The water-leaving radiance at the top of the atmosphere is related to the water-leaving radiance at the bottom of the atmosphere (usually just called the water-leaving radiance) through the diffuse transmittance, $t(\hat{\xi}_v)$, i.e.,

$$t(\hat{\xi}_v) = \frac{L_w^a(\hat{\xi}_v)}{L_w(\hat{\xi}_v)}$$

where $\hat{\xi}_v$ is a unit vector directed from the sea surface to the sensor, and $L_w(\hat{\xi}_v)$ is the water-leaving radiance just above the surface. In addition to the attenuation of $L_w(\hat{\xi}_v)$ along the path from the

surface to the sensor, the diffuse transmittance also accounts for its augmentation by scattering of $L_w(\hat{\xi})$ into the direction $\hat{\xi}_v$, i.e., atmospheric scattering from $\hat{\xi}$ to $\hat{\xi}_v$.

The water-leaving radiance L_w can assume a range of values. Table 1 provides values of L_w at 443 nm and 550 nm with the sun near the zenith for a range of pigment concentrations⁹ (C , the sum of the concentrations of chlorophyll a and its degradation product phaeophytin a) for Case 1 waters,⁵ i.e., waters for which the optical properties are controlled by the water itself, the phytoplankton, and the phytoplankton decay products. The goal of the atmospheric correction algorithm is the derivation of L_w from L_t with an uncertainty of $< 5\%$ at 443 nm for very clear oceanic waters, e.g., the Sargasso Sea in summer (for which $C \sim 0.03 \text{ mg/m}^3$). As t is of order unity, the residual error in L_w (after removal of L_{Other} from L_t) should be $\lesssim 0.1 \text{ mW/cm}^2\mu\text{m Sr}$. The Gordon and Wang⁷ algorithm is capable of this performance at 443 nm. Clearly, at higher pigment concentrations the relative error in L_w at 443 nm will be higher, e.g., $\sim 25\%$ for $C \sim 1 \text{ mg/m}^3$ (Table 1). Furthermore, the error in the removal of L_{Other} at 550 nm is about $\frac{1}{3} - \frac{1}{4}$ that at 443 nm,¹⁰ i.e., $\sim 0.03 \text{ mW/cm}^2\mu\text{m Sr}$. Thus, even in the Sargasso Sea in Summer, the relative error in L_w at 550 nm will be $\sim 10\%$.

Table 1: Water-leaving radiance at 443 and 550 nm
as a function of the pigment concentration.

C (mg/m^3)	$L_w(443)$ ($\text{mW/cm}^2\mu\text{m Sr}$)	$L_w(550)$ ($\text{mW/cm}^2\mu\text{m Sr}$)
0.03	1.95–2.20	0.28–0.30
0.10	1.35–1.60	0.28–0.30
0.47	0.40–0.75	0.28–0.40
0.91	0.30–0.50	0.24–0.50

To retrieve the water-leaving radiance from L_w^a , we need to calculate the diffuse transmittance. However, as we shall see, the diffuse transmittance itself is a function of the water-leaving radiance, and we generally need to know the angular distribution of the water-leaving radiance in order to calculate the diffuse transmittance. The angular distribution has been shown to possess significant bidirectional structure;^{11–13} however, in the computation of t it has always been assumed that the

water-leaving radiance is nearly uniform (independent of viewing direction), i.e., that the deviation of the actual radiance distribution from uniform causes only negligible error in the computation of t . The main objective of this paper is to evaluate the validity of this assumption. As we focus on sensors with a spatial resolution of ~ 1 km designed for the open ocean, where the typical scale of variability is a few km, we assume that L_w is constant over the scene. Thus, the adjacency effect of the atmosphere^{14–16} is ignored. We compare the diffuse transmittance calculated with several realistic water leaving radiance distributions, including one from actual measurements, to that with a uniform radiance distribution. The results reveal that errors in the retrieved water leaving radiance caused by making the uniform approximation are significant compared to the error in L_{Other} only in the blue and only at low pigment concentration. We then examine the behavior of t as a function of the concentration and optical properties of the aerosol present in the atmosphere.

2. Computational procedure

For the purposes of this paper, we assume the atmosphere is divided into two layers, a molecular-scattering layer on the top and an aerosol layer at the bottom. The ocean surface is assumed to be flat.

The computation of t is straightforward: the radiative transfer equation (RTE) can be solved for the radiance exiting the top of the atmosphere (L_w^a) with the correct upwelling radiance distribution $L_u(\hat{\xi})$ incident just beneath the sea surface. Accounting for the transfer of radiance across the air-water interface,

$$t(\hat{\xi}) = \frac{L_w^a(\hat{\xi})}{L_w(\hat{\xi})},$$

where

$$L_w(\hat{\xi}) = \frac{T_f(\hat{\xi}')}{m_w^2} L_u(\hat{\xi}'),$$

$T_f(\hat{\xi}')$ is the Fresnel transmittance of the interface for radiance incident from below in the direction $\hat{\xi}'$, and m_w is the refractive index of water. $\hat{\xi}$ and $\hat{\xi}'$ are related by Snell's law. This is the direct approach to finding $t(\hat{\xi})$. However, rather than using this approach, we choose to solve the reciprocal problem and use the reciprocity principle (Appendix 1) to derive t .

In the reciprocal problem the extraterrestrial solar beam is incident on the top of the atmosphere. Let F_0 be the extraterrestrial solar irradiance, $\hat{\xi}_0$ a unit vector in the direction of propagation of the solar beam, and $L_R(\hat{\xi})$ the resulting radiance propagating downward just beneath the sea surface in the direction $\hat{\xi}$. Then, it is shown in Appendix 1 that

$$t(-\hat{\xi}_0) = \frac{1}{F_0 |\hat{\xi}_0 \bullet \hat{n}_0| T_f(\hat{\xi}_0)} \int_{\Omega_d} |\hat{\xi} \bullet \hat{n}| L_R(\hat{\xi}) \frac{L_u(-\hat{\xi})}{L_u(-\hat{\xi}'_0)} d\Omega(\hat{\xi}), \quad (2)$$

where $L_u(-\hat{\xi})$ is the upward radiance distribution incident just beneath the sea surface for which we want t , $\hat{\xi}'_0$ and $\hat{\xi}_0$ are related by Snell's law, and Ω_d indicates the integral is to be evaluated over all downward $\hat{\xi}$. If $L_u(\hat{\xi})$ is uniform, this becomes

$$t^*(-\hat{\xi}_0) = \frac{1}{F_0 |\hat{\xi}_0 \bullet \hat{n}_0| T_f(\hat{\xi}_0)} \int_{\Omega_d} |\hat{\xi} \bullet \hat{n}| L_R(\hat{\xi}) d\Omega(\hat{\xi}) = \frac{E_R(\hat{\xi}_0)}{F_0 |\hat{\xi}_0 \bullet \hat{n}_0| T_f(\hat{\xi}_0)}, \quad (3)$$

where $E_R(\hat{\xi}_0)$ is the downward irradiance just beneath the surface in the reciprocal problem.

The relative error in the retrieval of water-leaving radiance caused in making the uniform radiance approximation is

$$\frac{\Delta L_w(-\hat{\xi}_0)}{L_w(-\hat{\xi}_0)} \equiv \frac{L_w^*(-\hat{\xi}_0) - L_w(-\hat{\xi}_0)}{L_w(-\hat{\xi}_0)} = \frac{t(-\hat{\xi}_0) - t^*(-\hat{\xi}_0)}{t^*(-\hat{\xi}_0)}, \quad (4)$$

where $L_w^*(-\hat{\xi}_0)$ is computed from $L_w^a(-\hat{\xi}_0)$ using $t^*(-\hat{\xi}_0)$. Thus,

$$\frac{\Delta L_w(-\hat{\xi}_0)}{L_w(-\hat{\xi}_0)} = \frac{1}{E_R(\hat{\xi}_0)} \int_{\Omega_d} |\hat{\xi} \bullet \hat{n}| L_R(\hat{\xi}) \left[\frac{L_u(-\hat{\xi})}{L_u(-\hat{\xi}'_0)} - 1 \right] d\Omega(\hat{\xi}), \quad (5)$$

For the development of the atmospheric correction algorithm, Gordon and Wang carried out extensive simulations ($\sim 33,000$) of the reciprocal problem for a variety of aerosol models, aerosol optical thicknesses, and $\hat{\xi}_0$'s. According to Eq. (5), we can use these existing simulations to compute the error for any radiance distribution, $L_u(\hat{\xi})$, without having to carry out further radiative transfer simulations. This is the reason for using the reciprocal approach developed here.

3. Computation of the error in L_w

In order to compute the error in L_w using Eq. (5) we need the radiance backscattered toward the surface in the water. Precise computation of this requires coupling the ocean and the atmosphere

in a multiple scattering computation. However, because the radiance reflected *out* of the ocean is small (reflectance < 0.04), the probability of photons being reflected out of the ocean twice is negligible. Therefore, the coupling is not really required and the ocean and atmosphere can be treated separately.¹⁷ To further simplify the computations, we shall not consider multiple scattering in the water. Rather, we will employ the quasi-single scattering approximation^{18,19} (QSSA) to provide L_u , given the scattering phase function for the medium. For given optical properties of the ocean, the QSSA will provide an upwelling radiance distribution beneath the surface that is identical in angular distribution to that produced in single scattering, and as such, will represent the upper limit to the departure of L_u from a uniform distribution for a given phase function. The reason for this is that multiple scattering will always produce a smoother radiance distribution than single scattering.

We introduce a cartesian coordinate system at the sea surface with the z -axis pointed in the downward direction (the same direction as \hat{n} at the surface). In this system we describe the direction of $\hat{\xi}$ by the angle θ measured from the z -axis, and the azimuth angle ϕ measured from the x -axis. If $\hat{\xi}$ is directed toward increasing depth, $\theta < 90^\circ$. Thus, the direction of the solar beam $\hat{\xi}'_0$ in the water is specified by θ'_0 and ϕ'_0 , and for radiance in the water propagating upward toward the sea surface, $\theta > 90$. We take $\phi_0 = 0$, so photons that are exactly backscattered from the ocean-atmosphere system, i.e., scattered in the direction $-\hat{\xi}_0$, have $\phi = 180^\circ$.

Considering only the refracted direct solar beam in the water, in the QSSA the upwelling radiance distribution just beneath the sea surface is given by^{18,19}

$$L_u(\theta, \phi) = C(\omega_0, P) F_0 T(\theta_0) \frac{\cos \theta'_0 P(\Theta)}{\cos \theta'_0 - \cos \theta}, \quad (6)$$

where $\cos \theta < 0$ and C is a constant depending mostly on the value of the single-scattering albedo ω_0 , but also weakly on P . $P(\Theta)$ is the scattering phase function of the medium for a scattering angle Θ , given by

$$\cos \Theta = \cos \theta \cos \theta'_0 + \sin \theta \sin \theta'_0 \cos(\phi - \phi'_0).$$

When diffuse skylight refracted into the water in the direction $\hat{\xi}'$ is considered as well, an additional term

$$C(\omega_0, P) \int_{\hat{\xi}' \cdot \hat{n} > 0} L_d(\hat{\xi}') \frac{\cos \theta' P(\Theta)}{\cos \theta' - \cos \theta} d\Omega(\hat{\xi}'),$$

where $L_d(\hat{\xi}')$ is the sky radiance transmitted through the air-sea interface, and

$$\cos \Theta = \cos \theta \cos \theta' + \sin \theta \sin \theta' \cos(\phi - \phi'),$$

must be added to the right-hand-side of Eq. (6).

In general the scattering phase function for the ocean, $P(\Theta)$, will be a combination of that due to molecular scattering by the water itself (Rayleigh scattering), $P_R(\Theta)$, and that resulting from scattering by the suspended particles $P_p(\Theta)$, i.e.,

$$P(\Theta) = \frac{b_r P_R(\Theta) + b_p P_p(\Theta)}{b_r + b_p},$$

where b_r and b_p are the Rayleigh and particle scattering coefficients, respectively. In contrast to forward scattering angles for which $P_p(\Theta) \gg P_r(\Theta)$, P_p and P_r are comparable for $\Theta \gtrsim 80^\circ$, so Rayleigh scattering plays an important role in the determination of $P(\Theta)$ for $\Theta \gtrsim 80^\circ$. This is seen in Figure 1 which compares P_r with P_p measured by Petzold²⁰ in San Diego Harbor. Petzold's San Diego Harbor phase function is often taken in ocean radiative transfer simulations as characteristic of particles in ocean water.^{21–23}

The limits for $P(\Theta)$ are $P_R(\Theta)$ ($b_p \ll b_r$) and $P_p(\Theta)$ ($b_p \gg b_r$). We shall estimate the error in L_w given by Eq. (5) in these two limits. In general, the error will fall between these two limits. Figure 2 provides the upward in-water radiance distribution $L_u(-\hat{\xi})$ due to the direct solar beam alone for these two limits for $\theta_0 = 40^\circ$ and 60° . In these figures, $\pi - \theta = 0$ implies photons are traveling toward the zenith, and for $\phi = 180^\circ$ ($\pi - \phi = 0$) and $\theta = \theta'_0$ the photons are exactly backscattered. Since photons with $\pi - \theta >$ the critical angle ($\sim 48^\circ$) cannot escape the ocean when the surface is flat, the radiance distributions are truncated at $\pi - \theta = 50^\circ$. Also, they are normalized to unity at their maximum value. In the Rayleigh scattering limit, an observer looking into the water with $\theta = \theta'_0$ would observe maximum radiance for $\phi = 180^\circ$, i.e., with the sun at the

observer's back. In contrast, in the pure particle limit the maximum would be along $\phi = 0$. As we shall see, these radiance distributions lead to different values for the diffuse transmittance t .

We have applied Eq. (5) and the QSSA to compute $\Delta L_w/L_w$, the error in the recovered water-leaving radiance made by assuming that $L_u(\theta, \phi)$ is uniform (constant). To compute $L_R(\hat{\xi})$ and $E_R(\hat{\xi}_0)$ in Eq. (5) we assume as in Ref. 7 that the atmosphere can be approximated as two layers with pure molecular scattering in the upper layer and pure aerosol scattering in the lower layer. We use the Shettle and Fenn²⁴ Maritime aerosol model at 90% relative humidity (M90) to provide the aerosol optical properties. The solution of the reciprocal problem was obtained using the successive-order-of-scattering method²⁵ for solving the radiative transfer equation. The computations are provided for aerosol optical thickness $\tau_a = 0.1$ and 0.2 , and wavelengths (λ) of 443 and 555 nm, the principal spectral regions used to estimate the phytoplankton pigment concentration from L_w .⁵ These values for τ_a are typical of those in a pure maritime atmosphere.^{26–28}

We begin by examining sun-viewing geometry typical of scanning ocean color sensors: viewing in the perpendicular plane ($\phi = 90^\circ$) at the center of the scan ($\theta_v \approx 0$), and near the scan edge ($\theta_v \approx 45^\circ$), where $\theta_v = 180^\circ - \theta$, i.e., θ_v is the angle between the direction the radiometer is viewing and the nadir. The computations are performed for $\theta_0 = 0, 20^\circ, 40^\circ$, and 60° , and thus, cover the sensor's full scan as it progresses along the orbit with ever increasing solar zenith angles.

Figure 3 provides the error $\Delta L_w/L_w = (t - t^*)/t^*$ in assuming that L_w is uniform. In the case of a pure Rayleigh-scattering ocean (Figures 3a and 3b), the maximum error is $< 1\%$ for all θ_v and θ_0 . Furthermore, the error depends only weakly on the wavelength and τ_a . In contrast, in the case of a pure particle-scattering ocean (Figures 3c and 3d), errors as large as 4% are observed, along with considerable dependence on wavelength and on τ_a . The large errors are explained by the much larger range of variation in $L_u(\theta, \phi)$ for the particle-dominated ocean compared to the Rayleigh-scattering ocean (Figure 2), which increases the affect of the $L_u(-\hat{\xi})/L_u(-\hat{\xi}_0')$ in Eq. (5). The dependence on λ and τ_a is explained by the fact that as τ_a increases or as λ decreases, the sky radiance becomes more diffuse, spreading $L_R(\hat{\xi})$ in Eq. (5) over a larger range of directions ($\hat{\xi}$).

Similar results are obtained in other sun-viewing geometries. For example, Figure 4 shows $\Delta L_w/L_w$ as a function of the viewing azimuth angle for situations in which $\theta_v = \theta_0$. The resulting errors are similar to those in Figure 3, although in the case of a Rayleigh-scattering ocean, the error near $\phi_v = 0$ or 180° (the principal plane) is much greater than that near $\phi_v = 90^\circ$ (the perpendicular plane). As most ocean color instruments scan closer to the perpendicular plane than the principal plane, this is not considered important. Figure 5 provides the error as a function of the viewing angle in the perpendicular plane. The behavior is similar to that in Figure 4, although the error does not exceed 4% over the meaningful range of θ_v (0 – 60°).

We have also carried out computations of $\Delta L_w/L_w$ using actual measurements of radiance distributions made by Voss^{13,29} on the R/V *New Horizon* West of San Diego at $32^\circ 40'N$ and $121^\circ 18'W$. In this case the water itself contributed $\lesssim 1$ – 2% to the total backscattering in the blue.¹³ The radiance distributions at 450 and 500 nm are provided in Figure 6 for $\theta_0 = 60^\circ$. Note the similarity of these to those for the particle-dominated ocean (Figures 2c and 2d); however, the total variation (minimum to maximum) of the measured $L_u(\theta, \phi)$ is smaller, as would be expected in the presence of multiple scattering. Figure 7 provides the resulting $\Delta L_w/L_w$ as a function of ϕ_v with $\theta_v = \theta_0$ (Figure 7a) and as a function of θ_v in the perpendicular plane (Figure 7b) for 443 and 510 nm. For the 443 nm computations, L_u at 450 nm was used, while for 510 nm, L_u at 500 nm was used. The resulting errors are similar to those provided in Figures 4 and 5. The strikingly different behavior of the error at the two wavelengths for $\theta_v = 0$ in Figure 7a and for $\phi_v = 0$ and 60° in Figure 7b results from differences in the two radiance distributions.

Considering that the goal of atmospheric correction is recovering L_w at 443 nm to within $\pm 5\%$ in very clear ocean water, we see that the assumption that $L_u(\theta, \phi)$ is uniform can lead to significant error in L_w in such situations, i.e., errors similar in magnitude to L_{Other} , when the phase function is similar to Petzold's, or when the radiance distribution is similar to that measured on the *New Horizon*. However, in more productive waters, or in the green, the error in the recovered L_w induced by this assumption will usually be small compared to that induced by error in removing L_{Other} , i.e., the error in L_w^a itself will be considerably more than the error in L_w induced by replacing t by t^* .

Finally, most algorithms for relating L_w to water constituents involve the use of radiance ratios.⁵ For algorithms using the ratio $L_w(443)/L_w(555)$, e.g., the CZCS phytoplankton pigment algorithm, Figures 3–5 suggest that the error in this ratio induced by replacing t by t^* is $\lesssim 2\%$ with the exception of a very clear ocean (Rayleigh scattering) viewing near $\phi_v = 0$ with $\theta_v = \theta_0 = 60^\circ$, for which the error is $\sim 3\%$ (Figure 4b).

4. Dependence of t^* on atmospheric parameters

As it is clear that usually t can be replaced by t^* , it is important to understand how this quantity depends on the optical properties of the atmosphere. Assuming that the water-leaving radiance is totally diffuse and spatially uniform, the work of Tanré et al.¹⁴ provides an approximation to t^* :

$$t^*(\theta) = \exp \left[- \left(0.48\tau_r + 0.50(1 - g)\tau_a \right) / \cos \theta \right], \quad (7)$$

where τ_a is the aerosol optical thickness, and g is the cosine of the scattering angle averaged over the aerosol scattering phase function. Similarly, Gordon et al.⁶ approximated t^* by

$$t^*(\theta) = \exp \left[- \left(0.50\tau_r + (1 - \omega_a F)\tau_a \right) / \cos \theta \right], \quad (8)$$

where ω_a is the aerosol single scattering albedo, and F is defined by

$$F = \frac{1}{4\pi} \int_0^{2\pi} \int_0^1 P_a(\alpha) d\mu' d\phi',$$

where $P_a(\alpha)$ is the aerosol scattering phase function (normalized to 4π) for a scattering angle α ,

$$\cos \alpha = \mu\mu' + \sqrt{(1 - \mu^2)(1 - \mu'^2)} \cos \phi',$$

and $\mu = \cos \theta$. These formulas yield similar results for $\omega_a = 1$. Because of the typically large aerosol forward scattering, i.e., $g \sim 0.7$ and $F \sim 0.9$, the affect of aerosols on $t^*(\theta)$ is significantly less than on the direct transmittance. In the absense of aerosols, both formulas yield $t_r^* \approx \exp[-\tau_r/2 \cos \theta]$. This approximation can be shown to be exact near the single scattering limit, i.e., $t_r^*(\theta) \rightarrow 1 - \tau_r/2 \cos \theta$. The quantity t_r^* was used as an approximation to t^* in processing CZCS imagery,³⁰ i.e., τ_a was set to zero in Eq. (8).

We used Eq. (3) to compute $t^*(\theta)$ in the absence of aerosols, t_r^* . This is provided in Figure 8a at the centers of several of the SeaWiFS spectral bands. Figure 8b provides the error in Eq. (8) for the spectral band at 412 nm ($\tau_r = 0.32$). It is seen that Eq. (8) overestimates t_r^* by $\sim 1.5\%$, which is approximately the loss in radiance upon transmission through the air-sea interface at small solar zenith angles.

To investigate the influence of aerosols on t^* , we used several of the Shettle and Fenn²⁴ aerosol models. Specifically, we used their Urban model at 50% relative humidity (U50), their Tropospheric model at 50% relative humidity (T50), and their Maritime model at 90% relative humidity (M90). M90, T50, and U50 have ω_a values at 443 nm of 0.9951, 0.9643, and 0.6534, respectively, i.e., increasing amounts of absorption. As expected from Eqs. (7) and (8), the variation of $t^*(\theta)$ with θ is similar to that observed in Figure 8a. Figure 9 provides the dependence of t^* on τ_a for each aerosol model at $\theta = 20^\circ$ and 60° for 443 and 555 nm. t^* is seen to be a strong function of ω_a .

Gordon¹⁰ has shown that in the case of a strongly-absorbing aerosol, the quantity L_{Other} in Eq. (1) is a sensitive function of the vertical distribution of the aerosol. This is particularly true in the blue region of the spectrum. Thus, it is of interest to understand the influence of aerosol vertical structure on t^* . Figure 10 compares t^* at 443 nm for the U50 model (strongly absorbing) computed for a two-layer atmosphere (aerosols at the bottom) and a one-layer atmosphere in which the aerosol are uniformly mixed with Rayleigh scatterers. The results clearly demonstrate that t^* is nearly independent of aerosol vertical structure.

Examination of Figure 9 shows that the error in replacing t^* by t_r^* is typically small as long as τ_a is not too large and $\omega_a \sim 1$. For example, at τ_a as high as 0.3 the error in t^* at $\theta = 20^\circ$ is only $\sim 2 - 3\%$ for the M90 model, which is expected to be realistic over much of the open ocean. Furthermore, the error in t^* has the same sign at both wavelengths, so the error induced in radiance ratios will be even smaller. As $\tau_a = 0.3$ would be large for such areas,²⁶⁻²⁸ this approximation should be excellent for most oceanic areas. In contrast, for U50 the error under the same conditions will be as high as $\sim 15\%$, but the error in radiance ratios will still be small. These results suggest that the approximation $t^* = t_r^*$ will probably be acceptable (considering the expected error in L_{Other}) if the algorithms that use L_w 's are in the form of radiance ratios, as in the case of CZCS. For algorithms

using L_w 's in other ways, the error can be excessive unless the aerosol is included in the t^* estimate. Fortunately, the computation of t^* is simple given the aerosol model. Recall that the Gordon and Wang⁷ algorithm utilizes that variation of L_{Other} in the near infrared (NIR) to select an aerosol model, from a set of candidate models, for estimating L_{Other} in the visible. Once an aerosol model is chosen, L_{Other} in the NIR can be used to estimate τ_a at all wavelengths. An aerosol model and τ_a are all that are needed to accurately compute t^* . Given the fact that t^* depends exponentially on τ_a (Figure 9), i.e., $t^*(\theta) \approx A(\theta) \exp[-B(\theta)\tau_a]$, for a given θ only two parameters are needed to compute t^* . To effect the removal of L_{Other} , a set of lookup tables (LUTs) have been prepared that relate L_{Other} to τ_a for each candidate aerosol model, sun-viewing geometry, and wavelength, by solving the radiative transfer equation (RTE) for a two-layer atmosphere (aerosols on the bottom). These existing solutions to the RTE can be used with Eq. (3) to compute the required t^* , since t^* does not depend on the vertical structure of the aerosol (Figure 10). As the L_{Other} LUTs have been prepared for $\theta_0 = 0(2.5^\circ)80^\circ$, i.e., 33 values of θ_0 , LUTs relating t^* to τ_a with the same resolution require only 66 constants for each wavelength and candidate aerosol model of interest. In contrast, the LUTs for L_{Other} require $\sim 35,000$ constants per aerosol model per wavelength. Thus, computation of a precise value of $t^*(\theta)$ appropriate to a given candidate aerosol model is not a challenge.

5. Concluding remarks

In this paper we have examined the effects of factors influencing the diffuse transmittance of the water-leaving radiance to the top of the atmosphere: the angular distribution of upwelling radiance beneath the sea surface; and the concentration and optical properties of the aerosol in the atmosphere. Several conclusions are possible based on the analysis.

First, the error in L_w made by assuming that L_u is uniform is $\lesssim 4\%$ for viewing geometries typical of ocean color observations, and aerosol optical thicknesses typical of the open-ocean marine atmosphere. As the error in retrieving L_w^a from L_t will usually exceed 4% by a considerable amount, the departure of L_u from uniform usually can be ignored. An exception is for low values of C in the blue where L_w^a is large and its removal from L_t can be expected to be in error by $\lesssim 5\%$. Thus, for atmospheric correction over clear water in the blue, it will be necessary to estimate the

angular distribution of L_u in the computation of t in order to insure that the error in L_w remains $< 5\%$. This can be accomplished using an estimate of C , obtained with t^* , in an iterative manner as suggested by Morel and Gentili.³¹ In contrast, for sensors that are capable of viewing over a large range of azimuth angles, e.g., the polarization and directionality of earth reflectance (POLDER)³² instrument, the uniform- L_u assumption can lead to errors of more than 6% in L_w (Figure 4b) and is highly dependent on the viewing azimuth relative to the sun.

Next, when biophysical products, e.g., C , are derived from ratios of L_w at two wavelengths, the effect of replacing t by t^* is significantly smaller than the effect on L_w .

Finally, in the absence of aerosols, t^* can be computed from simple formulas with an, easily correctable (Figure 8b), error of $\lesssim 2\%$. In the presence of aerosols, t^* is a strong function of the aerosol absorption (Figure 9) but is independent of the aerosol vertical distribution (Figure 10). Given that the atmospheric correction algorithm⁷ provides candidate aerosol models, accurate computation of t^* can be made using the models chosen to remove L_{Other} .

6. Appendix: The reciprocity principle

As we were unable to find the result in the literature, we provide here a derivation of the reciprocity principle for a medium in which the refractive index m is a function of position. We then apply this to derive Eq. (2) in the text.

In the absence of internal sources, with such a medium occupying a volume V and illuminated from the outside, the radiance $L(\ell, \hat{\xi})$ along a ray is governed by the radiative transfer equation (RTE),

$$\frac{d}{d\ell} \left[\frac{L(\ell, \hat{\xi})}{m^2(\ell)} \right] = -c(\ell) \frac{L(\ell, \hat{\xi})}{m^2(\ell)} + \int_{4\pi} \beta(\ell; \hat{\xi}' \rightarrow \hat{\xi}) \frac{L(\ell, \hat{\xi}')}{m^2(\ell)} d\Omega(\hat{\xi}'), \quad (9)$$

where $\hat{\xi}$ is a unit vector tangent to the path of the ray, and ℓ is measured along the ray. In this equation, $\beta(\ell; \hat{\xi}' \rightarrow \hat{\xi})$ is the volume scattering function for scattering from $\hat{\xi}'$ to $\hat{\xi}$, $c(\ell)$ is the beam attenuation coefficient of the medium, and $d\Omega(\hat{\xi}')$ is a differential of solid angle around $\hat{\xi}'$. To derive the reciprocity principle, we imagine a given medium with two different radiance distributions incident on a volume V from the outside. We index the solution to these two problems by the indices 1 and 2. Thus, for problem 1, we have

$$\frac{d}{d\ell} \left[\frac{L_1(\ell, \hat{\xi})}{m^2(\ell)} \right] = -c(\ell) \frac{L_1(\ell, \hat{\xi})}{m^2(\ell)} + \int_{4\pi} \beta(\ell; \hat{\xi}' \rightarrow \hat{\xi}) \frac{L_1(\ell, \hat{\xi}')}{m^2(\ell)} d\Omega(\hat{\xi}'), \quad (10)$$

with a similar equation for problem 2. Now in problem 2, we reverse the sign of $\hat{\xi}$ everywhere, i.e.,

$$-\frac{d}{d\ell} \left[\frac{L_2(\ell, -\hat{\xi})}{m^2(\ell)} \right] = -c(\ell) \frac{L_2(\ell, -\hat{\xi})}{m^2(\ell)} + \int_{4\pi} \beta(\ell; \hat{\xi}' \rightarrow -\hat{\xi}) \frac{L_2(\ell, \hat{\xi}')}{m^2(\ell)} d\Omega(\hat{\xi}'), \quad (11)$$

where the minus sign on the left-hand-side is introduced so that the direction of increasing ℓ is in the direction $+\hat{\xi}$ in both problems 1 and 2. The integral term in Eq. (11) can be rearranged in the following manner: first, since the direction $\hat{\xi}'$ is an integration variable, it can be replaced by $-\hat{\xi}'$ everywhere in the integral; next, we recall that $\beta(\ell; -\hat{\xi}' \rightarrow -\hat{\xi}) = \beta(\ell; \hat{\xi} \rightarrow \hat{\xi}')$; and finally, we note that $d\Omega(-\hat{\xi}') = d\Omega(\hat{\xi}')$. Thus, the integral term in (11) can be written

$$\int_{4\pi} \beta(\ell; \hat{\xi} \rightarrow \hat{\xi}') \frac{L_2(\ell, -\hat{\xi}')}{m^2(\ell)} d\Omega(\hat{\xi}').$$

Now, multiply Eq. (10) by $L_2(\ell, -\hat{\xi})/m^2(\ell)$, and Eq. (11) by $L_1(\ell, \hat{\xi})/m^2(\ell)$, and subtract. Then multiply the result by $m^2(\ell) d\Omega(\hat{\xi}) dV$ and integrate over all $\Omega(\hat{\xi})$ and over V . The left-hand-side of the result is

$$\int_{4\pi} d\Omega(\hat{\xi}) \int_V m^2(\ell) \frac{d}{d\ell} \left[\frac{L_1(\ell, \hat{\xi})}{m^2(\ell)} \frac{L_2(\ell, -\hat{\xi})}{m^2(\ell)} \right] dV,$$

and the right-hand-side is

$$\begin{aligned} & \int_V dV \int d\Omega(\hat{\xi}) m^2(\ell) \int \beta(\ell; \hat{\xi}' \rightarrow \hat{\xi}) \frac{L_1(\ell, \hat{\xi}')}{m^2(\ell)} \frac{L_2(\ell, -\hat{\xi})}{m^2(\ell)} d\Omega(\hat{\xi}') \\ & - \int_V dV \int d\Omega(\hat{\xi}) m^2(\ell) \int \beta(\ell; \hat{\xi} \rightarrow \hat{\xi}') \frac{L_1(\ell, \hat{\xi})}{m^2(\ell)} \frac{L_2(\ell, -\hat{\xi}')}{m^2(\ell)} d\Omega(\hat{\xi}'). \end{aligned}$$

Clearly, the terms on the right-hand-side add to zero, and

$$\int_{4\pi} d\Omega(\hat{\xi}) \int_V m^2(\ell) \frac{d}{d\ell} \left[\frac{L_1(\ell, \hat{\xi})}{m^2(\ell)} \frac{L_2(\ell, -\hat{\xi})}{m^2(\ell)} \right] dV = 0$$

Now, we write $dV = dA(\hat{\xi}) d\ell$, where $dA(\hat{\xi})$ is a differential of area with normal in the direction of $\hat{\xi}$. Then using the fact that $m^2(\ell) dA(\hat{\xi}) d\Omega(\hat{\xi})$ is constant along the path of the ray,³³

$$\int_{\ell_1}^{\ell_2} \frac{d}{d\ell} \left[\int_A \int_{4\pi} \frac{L_1(\ell, \hat{\xi})}{m^2(\ell)} \frac{L_2(\ell, -\hat{\xi})}{m^2(\ell)} m^2(\ell) d\Omega(\hat{\xi}) dA(\hat{\xi}) \right] d\ell = 0$$

or

$$\int_A \int_{4\pi} \left[\frac{L_1(\ell, \hat{\xi}) L_2(\ell, -\hat{\xi})}{m^2(\ell)} d\Omega(\hat{\xi}) dA(\hat{\xi}) \right]_{\ell_1}^{\ell_2} = 0,$$

where ℓ_1 is the beginning of the path in V (the position where the ray enters V) and ℓ_2 is the end of the path (the position where the ray exits V). If \hat{n} is the outward normal to the surface of V , then $dA(\hat{\xi})$ at ℓ_1 or ℓ_2 is $\hat{\xi} \cdot \hat{n} dS$, where dS is the associated differential element of area on the surface of V , and this equation becomes

$$\int_S dS \int_{4\pi} \hat{\xi} \cdot \hat{n} \frac{L_1(\vec{\rho}, \hat{\xi}) L_2(\vec{\rho}, -\hat{\xi})}{m^2(\vec{\rho})} d\Omega(\hat{\xi}) = 0, \quad (12)$$

with $\vec{\rho}$ specifying the position of a point on the surface. This is the reciprocity principle for a medium with variable m . It can be rearranged to read

$$\int_S dS \int_{\hat{\xi} \cdot \hat{n} < 0} |\hat{\xi} \cdot \hat{n}| \left[\frac{L_1(\vec{\rho}, \hat{\xi}) L_2(\vec{\rho}, -\hat{\xi})}{m^2(\vec{\rho})} - \frac{L_1(\vec{\rho}, -\hat{\xi}) L_2(\vec{\rho}, \hat{\xi})}{m^2(\vec{\rho})} \right] d\Omega(\hat{\xi}) = 0, \quad (13)$$

where the integration over $\Omega(\hat{\xi})$ is only over directions for which $\hat{\xi} \bullet \hat{n} < 0$. When there are internal sources in the medium of intensity density $Q(\vec{r}, \hat{\xi})$, where \vec{r} specifies the position of a point in the medium, a term $Q(\vec{r}, \hat{\xi})/m^2(\vec{r})$ must be added to the right-hand-side of Eq. (9). In this case, it is easy to show that the right-hand-side of Eq. (13) becomes

$$\int_{4\pi} d\Omega(\hat{\xi}) \int_V dV \left[\frac{Q_2(\vec{r}, -\hat{\xi})L_1(\vec{r}, \hat{\xi})}{m^2(\vec{r})} - \frac{Q_1(\vec{r}, \hat{\xi})L_2(\vec{r}, -\hat{\xi})}{m^2(\vec{r})} \right].$$

It is straightforward to use this to derive Eq. (2) in the text. Consider a volume with upper surface at the top of the atmosphere, and lower surface just beneath the sea surface. Then, for problem 1 choose the incident radiance on the top of the atmosphere (TOA) to be that of the solar beam, i.e., $L_1(\rho_{\vec{T}}, \hat{\xi}) = F_0 \delta(\hat{\xi} - \hat{\xi}_0)$, where $\rho_{\vec{T}}$ is a TOA point, and $\hat{\xi}_0$ is the direction of the solar beam. We assume that there is no upward radiance incident at $\rho_{\vec{B}}$, a point just beneath the sea surface, i.e., $L_1(\rho_{\vec{B}}, \hat{\xi}) = 0$ for $\hat{\xi} \bullet \hat{n} < 0$. This is referred to in the text as the reciprocal problem. For problem 2 (the direct problem in the text), we let $L_2(\rho_{\vec{T}}, \hat{\xi}) = 0$ for $\hat{\xi} \bullet \hat{n} < 0$ (no incident radiance on the TOA), and $L_2(\rho_{\vec{B}}, \hat{\xi})$ be specified for $\hat{\xi} \bullet \hat{n} < 0$, i.e., a specified upward radiance distribution incident on the bottom surface. Then applying Eq. (13), we have

$$L_2(\rho_{\vec{T}}, -\hat{\xi}_0) = \frac{1}{F_0 |\hat{\xi}_0 \bullet \hat{n}|} \int_{\Omega_d} |\hat{\xi} \bullet \hat{n}| \frac{L_1(\rho_{\vec{B}}, \hat{\xi}) L_2(\rho_{\vec{B}}, -\hat{\xi})}{m_w^2} d\Omega(\hat{\xi}),$$

where Ω_d is the full solid angle in the downward direction, and m_w is the refractive index of water. Letting $\hat{\xi}'_0$ be the direction of the refracted solar beam in the water for a flat surface,

$$\frac{L_2(\rho_{\vec{T}}, -\hat{\xi}_0)}{L_2(\rho_{\vec{B}}, -\hat{\xi}'_0)} = \frac{1}{F_0 |\hat{\xi}_0 \bullet \hat{n}| m_w^2} \int_{\Omega_d} |\hat{\xi} \bullet \hat{n}| L_1(\rho_{\vec{B}}, \hat{\xi}) \frac{L_2(\rho_{\vec{B}}, -\hat{\xi})}{L_2(\rho_{\vec{B}}, -\hat{\xi}'_0)} d\Omega(\hat{\xi}). \quad (14)$$

In the absence of absorption and scattering in the atmosphere,

$$L_1(\rho_{\vec{B}}, \hat{\xi}) = T_f(\hat{\xi}_0) F_0 \frac{|\hat{\xi}_0 \bullet \hat{n}|}{|\hat{\xi}'_0 \bullet \hat{n}|} \delta(\hat{\xi} - \hat{\xi}'_0),$$

where $T_f(\hat{\xi})$ is the Fresnel transmittance of the interface. Equation (14) then yields

$$L_2(\rho_{\vec{T}}, -\hat{\xi}_0) = \frac{T_f(\hat{\xi}_0)}{m_w^2} L_2(\rho_{\vec{B}}, -\hat{\xi}'_0),$$

which is the familiar relationship for the propagation of radiance across the air-sea interface. If we replace $L_2(\vec{\rho}_B, -\hat{\xi}'_0)$ in Eq. (14) by $L_w(\vec{\rho}_B, -\hat{\xi}_0)$, the water-leaving radiance just *above* the sea surface, i.e.,

$$L_2(\vec{\rho}_B, -\hat{\xi}'_0) = \frac{m_w^2}{T_f(\hat{\xi}_0)} L_w(\vec{\rho}_B, -\hat{\xi}_0),$$

then, Eq. (14) becomes

$$\frac{L_2(\vec{\rho}_T, -\hat{\xi}_0)}{L_w(\vec{\rho}_B, -\hat{\xi}_0)} = \frac{1}{F_0|\hat{\xi}_0 \bullet \hat{n}|T_f(\hat{\xi}_0)} \int_{\Omega_d} |\hat{\xi} \bullet \hat{n}| L_1(\vec{\rho}_B, \hat{\xi}) \frac{L_2(\vec{\rho}_B, -\hat{\xi})}{L_2(\vec{\rho}_B, -\hat{\xi}'_0)} d\Omega(\hat{\xi}) \equiv t(-\hat{\xi}_0).$$

$t(-\hat{\xi}_0)$ is the quantity we defined as the diffuse transmittance in the text, Eq. (2).

References

- [1] W. A. Hovis, D. K. Clark, F. Anderson, R. W. Austin, W. H. Wilson, E. T. Baker, D. Ball, H. R. Gordon, J. L. Mueller, S. Y. E. Sayed, B. Strum, R. C. Wrigley and C. S. Yentsch, "Nimbus 7 coastal zone color scanner: system description and initial imagery," *Science* **210**, 60–63 (1980).
- [2] H. R. Gordon, D. K. Clark, J. L. Mueller and W. A. Hovis, "Phytoplankton pigments derived from the Nimbus-7 CZCS: initial comparisons with surface measurements," *Science* **210**, 63–66 (1980).
- [3] S. B. Hooker, W. E. Esaias, G. C. Feldman, W. W. Gregg and C. R. McClain, *SeaWiFS Technical Report Series: Volume 1, An Overview of SeaWiFS and Ocean Color* (NASA, Greenbelt, MD, Technical Memorandum 104566, July 1992).
- [4] V. V. Salomonson, W. L. Barnes, P. W. Maymon, H. E. Montgomery and H. Ostrow, "MODIS: Advanced Facility Instrument for Studies of the Earth as a System," *IEEE Geosci. Rem. Sens.* **27**, 145–152 (1989).
- [5] H. R. Gordon and A. Y. Morel, *Remote Assessment of Ocean Color for Interpretation of Satellite Visible Imagery: A Review* (Springer-Verlag, New York, 1983), 114 pp.
- [6] H. R. Gordon, D. K. Clark, J. W. Brown, O. B. Brown, R. H. Evans and W. W. Broenkow, "Phytoplankton pigment concentrations in the Middle Atlantic Bight: comparison between ship determinations and Coastal Zone Color Scanner estimates," *Applied Optics* **22**, 20–36 (1983).
- [7] H. R. Gordon and M. Wang, "Retrieval of water-leaving radiance and aerosol optical thickness over the oceans with SeaWiFS: A preliminary algorithm," *Applied Optics* **33**, 443–452 (1994).

- [8] H. R. Gordon and M. Wang, "Influence of Oceanic Whitecaps on Atmospheric Correction of SeaWiFS," *Applied Optics* **33**, 7754–7763 (1994).
- [9] H. R. Gordon, O. B. Brown, R. H. Evans, J. W. Brown, R. C. Smith, K. S. Baker and D. K. Clark, "A Semi-Analytic Radiance Model of Ocean Color," *Jour. Geophys. Res.* **93D**, 10909–10924 (1988).
- [10] H. R. Gordon, 1996, Atmospheric Correction of Ocean Color Imagery in the Earth Observing System Era, *Jour. Geophys. Res.* (In press).
- [11] A. Morel and B. Gentili, "Diffuse reflectance of oceanic waters: its dependence on Sun angle as influenced by the molecular scattering contribution," *Applied Optics* **30**, 4427–4438 (1991).
- [12] A. Morel and B. Gentili, "Diffuse reflectance of oceanic waters. II. Bidirectional aspects," *Applied Optics* **32**, 6864–6879 (1993).
- [13] A. Morel, K. J. Voss and B. Gentili, "Bidirectional reflectance of oceanic waters: A comparison of modeled and measured upward radiance fields," *Jour. Geophys. Res.* **100C**, 13,143–13,150 (1995).
- [14] D. Tanre, M. Herman, P. Y. Deschamps and A. de Leffe, "Atmospheric modeling for space measurements of ground reflectances, including bidirectional properties," *Applied Optics* **18**, 3587–3594 (1979).
- [15] Y. J. Kaufman, "Atmospheric effect on spatial resolution of surface imagery," *Applied Optics* **23**, 3400–3408 (1984).
- [16] P. Reinersman and K. L. Carder, "Monte Carlo simulation of the atmospheric point-spread function with an application to correction of the adjacency effect.," *Applied Optics* **34**, 4453–4471 (1995).

- [17] H. R. Gordon, "Radiative Transfer: A Technique for Simulating the Ocean in Satellite Remote Sensing Calculations," *Applied Optics* **15**, 1974–1979 (1976).
- [18] H. R. Gordon, "Simple Calculation of the Diffuse Reflectance of the Ocean," *Applied Optics* **12**, 2803–2804 (1973).
- [19] H. R. Gordon, "Modeling and Simulating Radiative Transfer in the Ocean," in *Ocean Optics*, edited by R. W. Spinrad, K. L. Carder and M. J. Perry (Oxford, 1994) , p. 3–39.
- [20] T. J. Petzold, "*Volume Scattering Functions for Selected Natural Waters*," 1972, Scripps Institution of Oceanography, Visibility Laboratory, San Diego, CA. 92152, SIO Ref. 72–78.
- [21] J. T. O. Kirk, "Estimation of the Scattering Coefficient of Natural Waters using Underwater Irradiance Measurements," *Aust. J. Mar. Freshwater Res.* **32**, 533–539 (1981).
- [22] J. T. O. Kirk, "The upwelling light stream in natural waters," *Limnology and Oceanography* **34**, 1410–1425 (1989).
- [23] J. T. O. Kirk, "Estimation of the absorption and scattering coefficients of natural waters by the use of underwater irradiance measurements," *Applied Optics* **33**, 3276–3278 (1994).
- [24] E. P. Shettle and R. W. Fenn, *Models for the Aerosols of the Lower Atmosphere and the Effects of Humidity Variations on Their Optical Properties* (Air Force Geophysics Laboratory, Hanscomb AFB, MA 01731, AFGL–TR–79-0214, 1979).
- [25] H. C. van de Hulst, *Multiple Light Scattering* (Academic Press, New York, 1980), 739 pp.
- [26] P. J. Reddy, F. W. Kreiner, J. J. Deluisi and Y. Kim, "Aerosol Optical Depths Over the Atlantic Derived From Shipboard Sunphotometer Observations During the 1988 Global Change Expedition," *Global Biogeochemical Cycles* **4**, 225–240 (1990).

- [27] G. K. Korotaev, S. M. Sakerin, A. M. Ignatov, L. L. Stowe and E. P. McClain, "Sun-Photometer Observations of Aerosol Optical Thickness over the North Atlantic from a Soviet Research Vessel for Validation of Satellite Measurements," *Jour. Atmos. Oceanic Technol.* **10**, 725–735 (1993).
- [28] Y. V. Villevalde, A. V. Smirnov, N. T. O'Neill, S. P. Smyshlyaev and V. V. Yakovlev, "Measurement of Aerosol Optical Depth in the Pacific Ocean and North Atlantic," *Jour. Geophys. Res.* **99D**, 20983–20988 (1994).
- [29] K. J. Voss, "Electro-optic Camera System for Measurement of the Underwater Radiance Distribution," *Optical Engineering* **28**, 241–247 (1989).
- [30] R. H. Evans and H. R. Gordon, "CZCS 'System Calibration:' A retrospective examination," *Jour. Geophys. Res.* **99C**, 7293–7307 (1994).
- [31] A. Morel and B. Gentili, "Diffuse reflectance of oceanic waters. III. Implication of bidirectionality for the remote sensing problem," *Applied Optics* **35**, 4850–4862 (1996).
- [32] P. Y. Deschamps, F. M. Bréon, M. Leroy, A. Podaire, A. Bricaud, J. C. Buriez and G. Sèze, "The POLDER Mission: Instrument characteristics and scientific objectives," *IEEE Trans. Geoscience and Remote Sensing* **32**, 598–615 (1994).
- [33] W. T. Welford, *Aberrations in Optical Systems* (Hilger, Bristol, 1986).

Figure Captions

Figure 1. Comparison of the scattering phase functions for Rayleigh scattering (dotted line) and Petzold's²⁰ turbid water measurements.

Figure 2. Subsurface upwelling radiance predicted using the Rayleigh and Petzold phase functions. The radiances are normalized to their maximum value. Panel (a) Rayleigh with $\theta_0 = 40^\circ$; Panel (b) Rayleigh with $\theta_0 = 60^\circ$; Panel (c) Petzold with $\theta_0 = 40^\circ$; Panel (d) Petzold with $\theta_0 = 60^\circ$.

Figure 3. The error in t , induced by assuming that L_u is uniform, as a function of wavelength and aerosol optical thickness at the SeaWiFS scan center and scan edge. The M90 aerosol model is used in all the computations. Panel (a) Rayleigh at the scan center; Panel (b) Rayleigh at the scan edge; Panel (c) Petzold at the scan center; Panel (d) Petzold at the scan edge.

Figure 4. The error in t , induced by assuming that L_u is uniform, as a function of wavelength, aerosol optical thickness, and viewing azimuth (ϕ_v) for $\theta_0 = \theta_v$. The M90 aerosol model is used in all the computations. Panel (a) Rayleigh with $\theta_0 = 40^\circ$; Panel (b) Rayleigh with $\theta_0 = 60^\circ$; Panel (c) Petzold with $\theta_0 = 40^\circ$; Panel (a) Petzold with $\theta_0 = 60^\circ$.

Figure 5. The error in t , induced by assuming that L_u is uniform, as a function of wavelength, aerosol optical thickness, and viewing angle (θ_v) in the perpendicular plane of the sun. The M90 aerosol model is used in all the computations. Panel (a) Rayleigh with $\theta_0 = 40^\circ$; Panel (b) Rayleigh with $\theta_0 = 60^\circ$; Panel (c) Petzold with $\theta_0 = 40^\circ$; Panel (a) Petzold with $\theta_0 = 60^\circ$.

Figure 6. Subsurface upwelling radiance distributions measured by Voss with the RADS system.^{13,29} Panel (a) $\lambda = 450$ nm, $\theta_0 = 58.2^\circ$; Panel (b) $\lambda = 500$ nm, $\theta_0 = 59.7^\circ$.

Figure 7. The error in t , induced by assuming that L_u is uniform, as a function of wavelength and aerosol optical thickness, using the Voss subsurface upwelling radiance distribution. The M90 aerosol model is used in all the computations. Panel (a) $\theta_0 = 60^\circ$ viewing in the perpendicular plane to the sun; Panel (b) $\theta_v = \theta_0 = 60^\circ$ with viewing azimuth ϕ_v .

Figure 8. Computed t^* for a pure Rayleigh-scattering atmosphere. Panel (a) Values computed using radiative transfer theory. From bottom to top the curves correspond to $\lambda = 412, 443, 490, 555, 670$, and 865 nm. Panel (b), Error in t^* resulting from using Eq. (7) in the text.

Figure 9. Value of t^* as a function of aerosol model and optical thickness τ_a . Upper curves are for $\lambda = 555$ nm, lower curves for $\lambda = 443$ nm. Panel (a) $\theta_0 = 20^\circ$; Panel (b) $\theta_0 = 60^\circ$.

Figure 10. Influence of vertical structure on t^* for the U50 aerosol model at 443 nm. Lines correspond to placing all of the aerosol in the bottom layer of a two-layer atmosphere. Dots correspond to the mixing the aerosol uniformly with gas molecules throughout the atmosphere. Curves from top to bottom are for $\theta_0 = 20^\circ, 40^\circ$, and 60° .

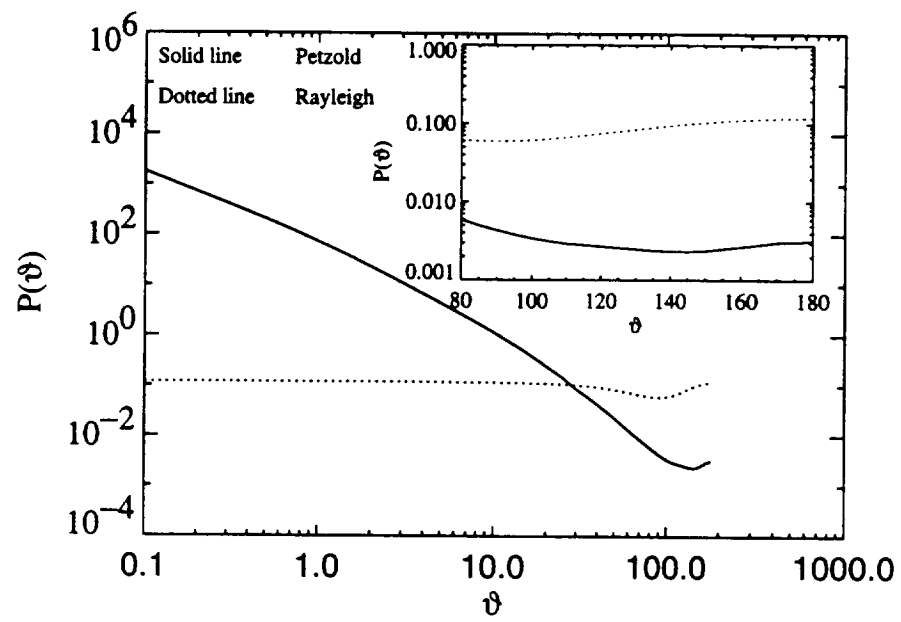
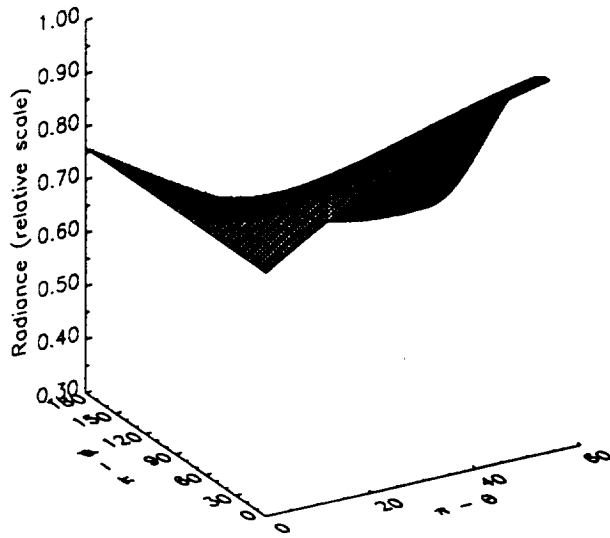
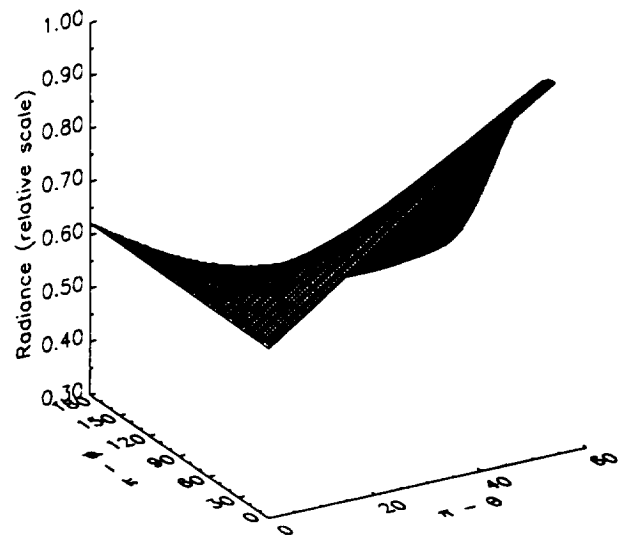


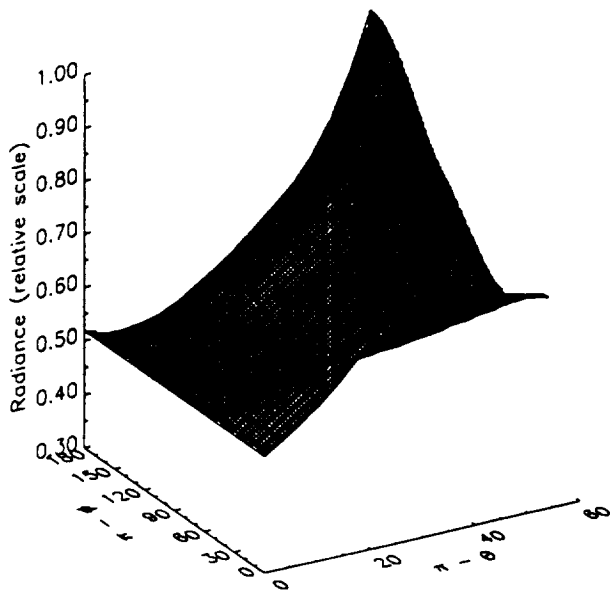
Figure 1. Comparison of the scattering phase functions for Rayleigh scattering (dotted line) and Petzold's²⁰ turbid water measurements.



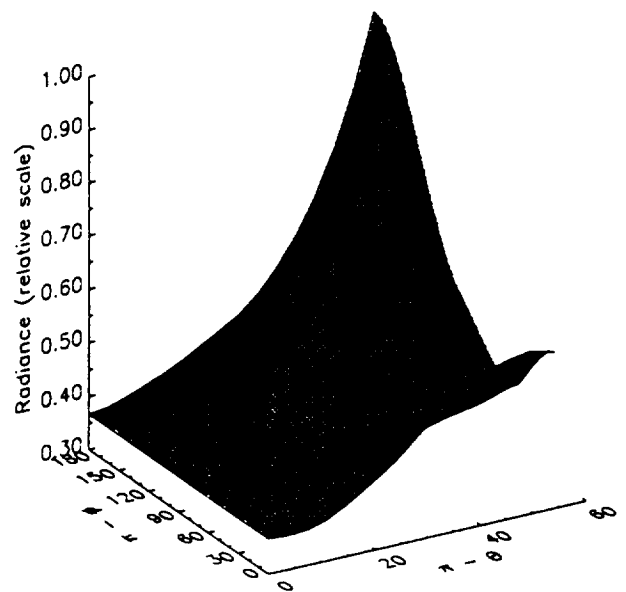
(a)



(b)

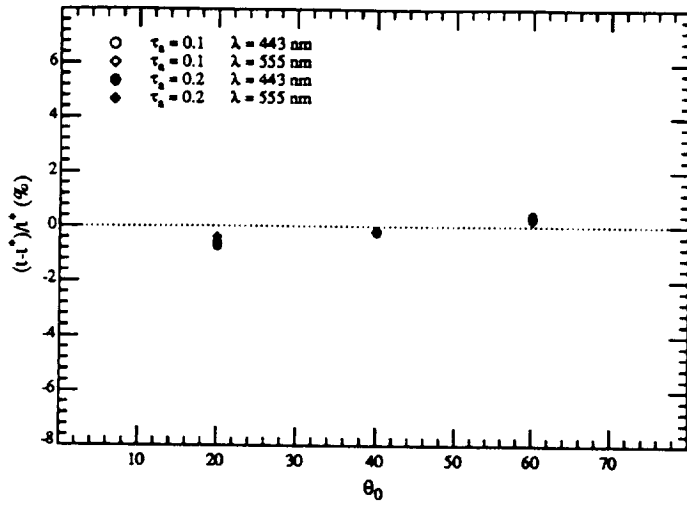


(c)

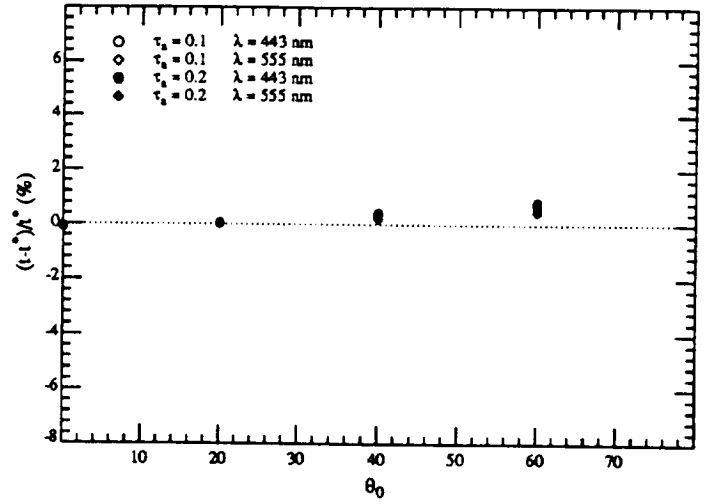


(d)

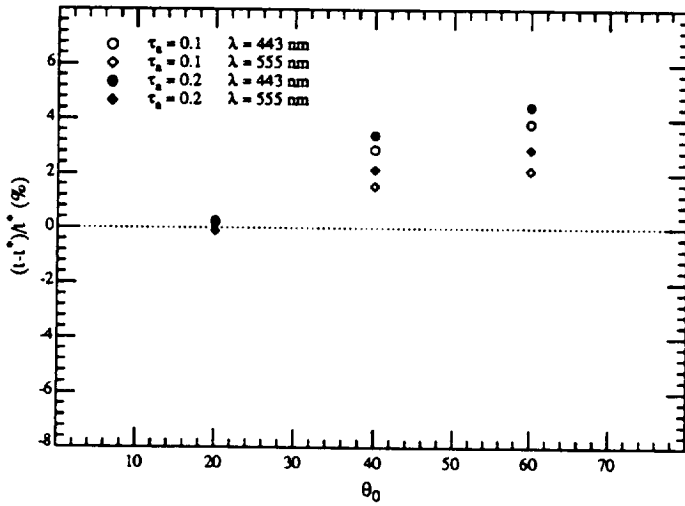
Figure 2. Subsurface upwelling radiance predicted using the Rayleigh and Petzold phase functions. The radiances are normalized to their maximum value. Panel (a) Rayleigh with $\theta_0 = 40^\circ$; Panel (b) Rayleigh with $\theta_0 = 60^\circ$; Panel (c) Petzold with $\theta_0 = 40^\circ$; Panel (d) Petzold with $\theta_0 = 60^\circ$.



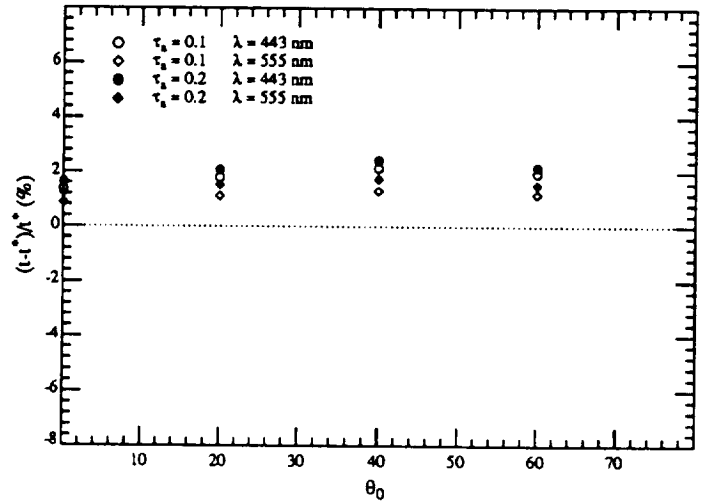
(a)



(b)

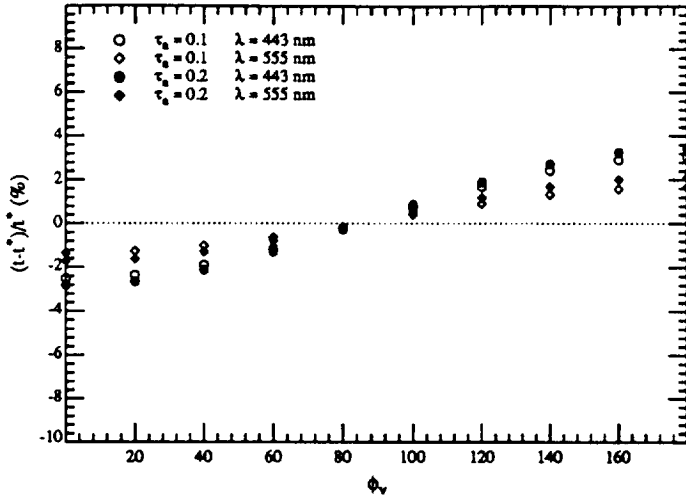


(c)

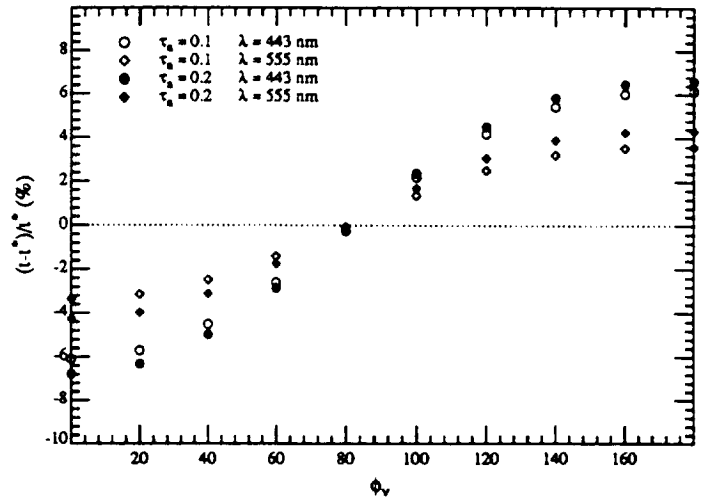


(d)

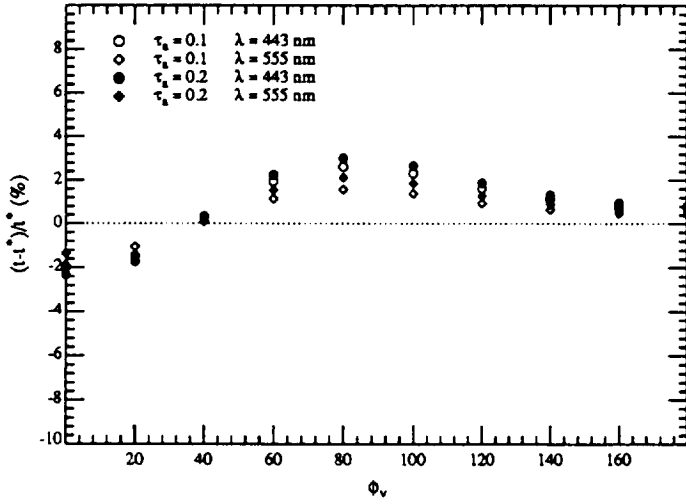
Figure 3. The error in t , induced by assuming that L_a is uniform, as a function of wavelength and aerosol optical thickness at the SeaWiFS scan center and scan edge. The M90 aerosol model is used in all the computations. Panel (a) Rayleigh at the scan center; Panel (b) Rayleigh at the scan edge; Panel (c) Petzold at the scan center; Panel (d) Petzold at the scan edge.



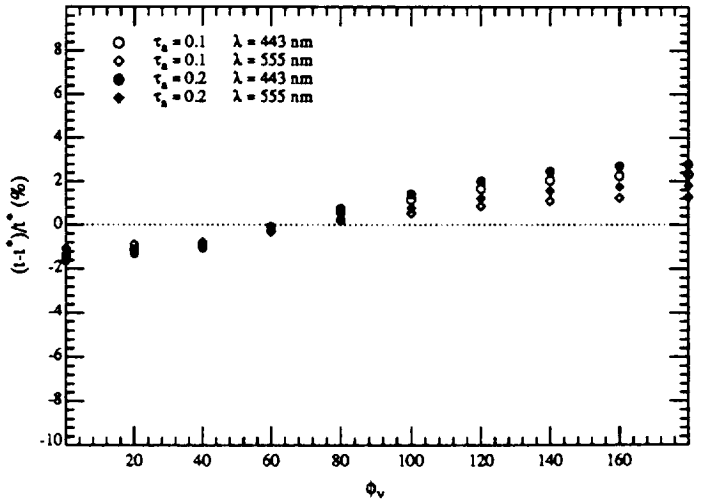
(a)



(b)

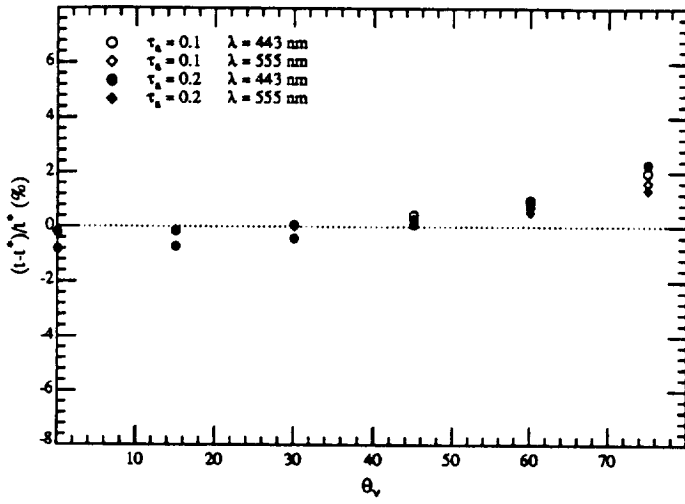


(c)

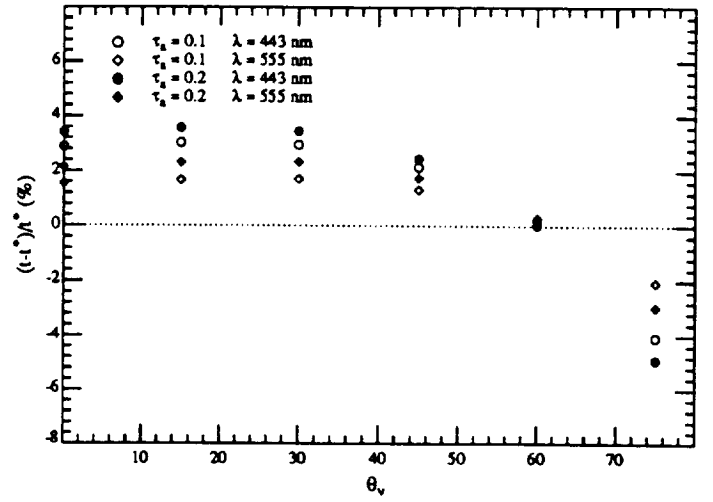


(d)

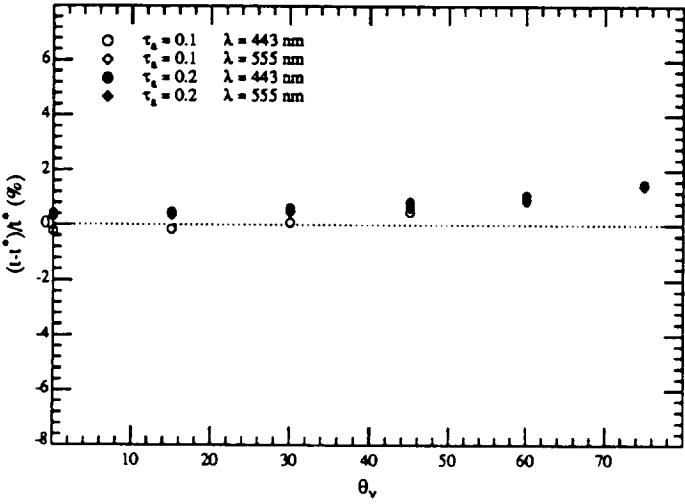
Figure 4. The error in t , induced by assuming that L_u is uniform, as a function of wavelength, aerosol optical thickness, and viewing azimuth (ϕ_v) for $\theta_0 = \theta_v$. The M90 aerosol model is used in all the computations. Panel (a) Rayleigh with $\theta_0 = 40^\circ$; Panel (b) Rayleigh with $\theta_0 = 60^\circ$; Panel (c) Petzold with $\theta_0 = 40^\circ$; Panel (d) Petzold with $\theta_0 = 60^\circ$.



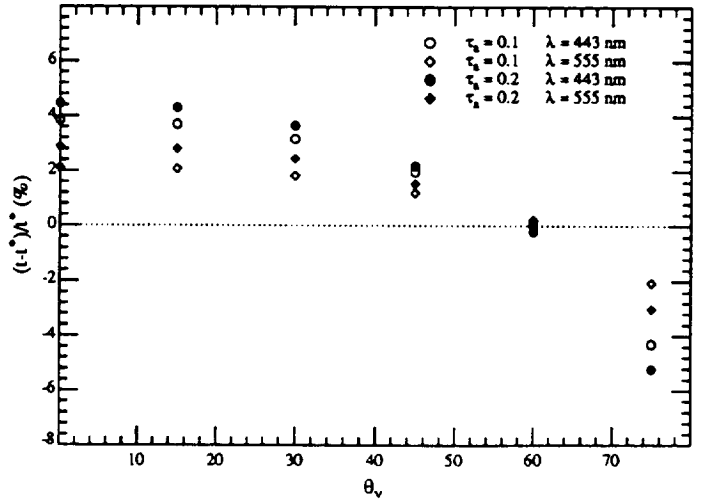
(a)



(b)

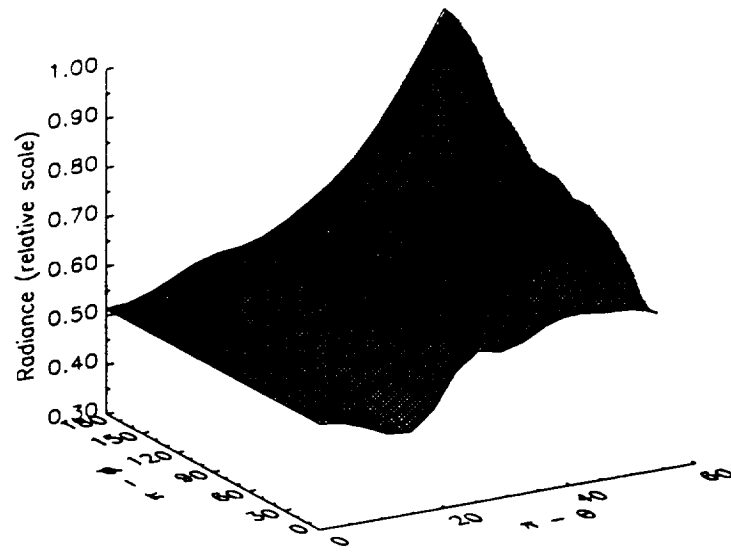


(c)

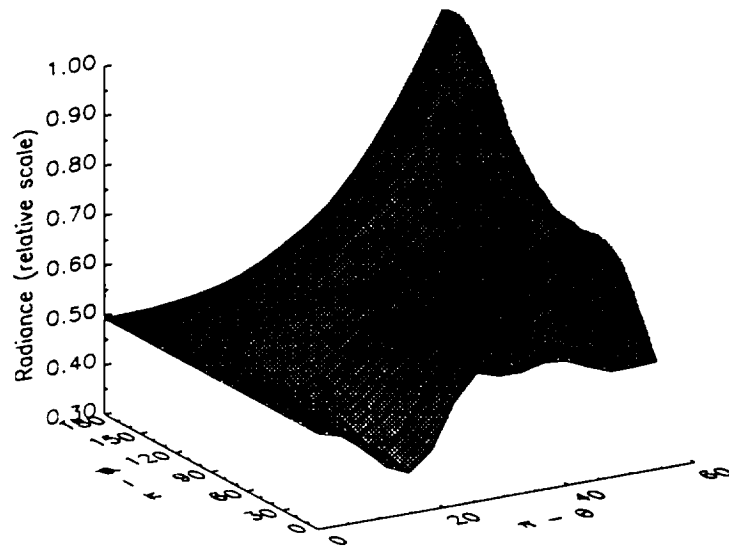


(d)

Figure 5. The error in t , induced by assuming that L_u is uniform, as a function of wavelength, aerosol optical thickness, and viewing angle (θ_v) in the perpendicular plane of the sun. The M90 aerosol model is used in all the computations. Panel (a) Rayleigh with $\theta_0 = 40^\circ$; Panel (b) Rayleigh with $\theta_0 = 60^\circ$; Panel (c) Petzold with $\theta_0 = 40^\circ$; Panel (d) Petzold with $\theta_0 = 60^\circ$.

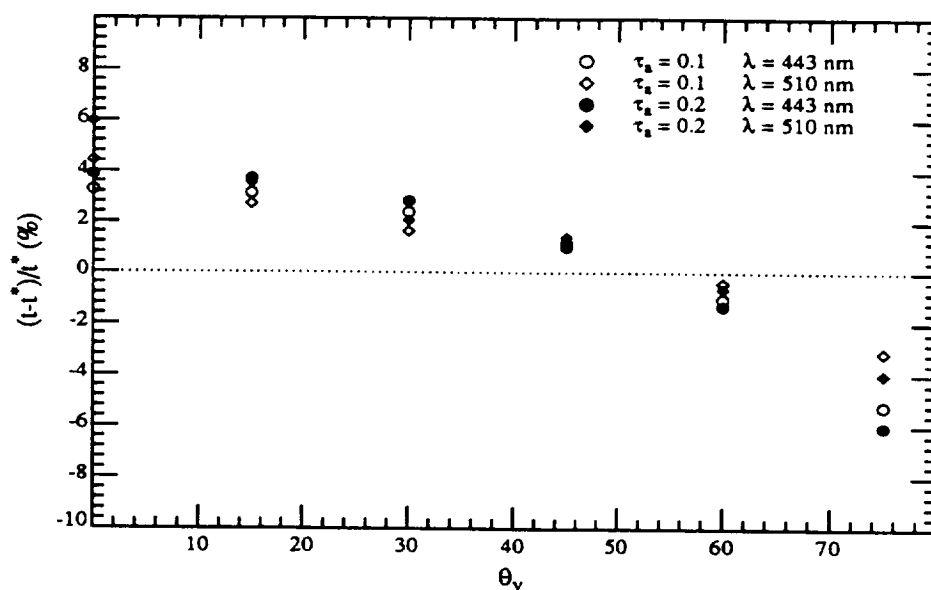


(a)

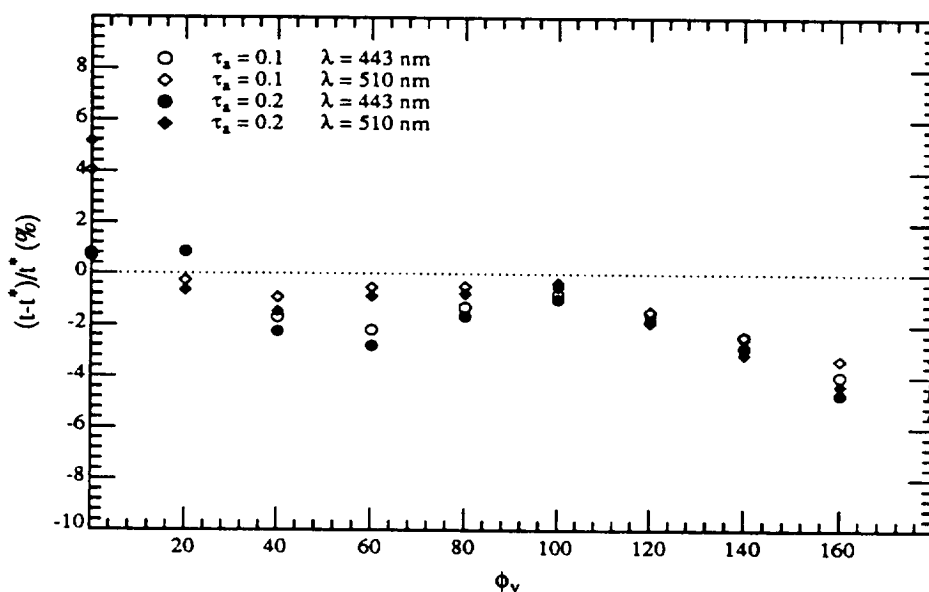


(b)

Figure 6. Subsurface upwelling radiance distributions measured by Voss with the RADS system.^{13,29} Panel (a) $\lambda = 450$ nm, $\theta_0 = 58.2^\circ$; Panel (b) $\lambda = 500$ nm, $\theta_0 = 59.7^\circ$.

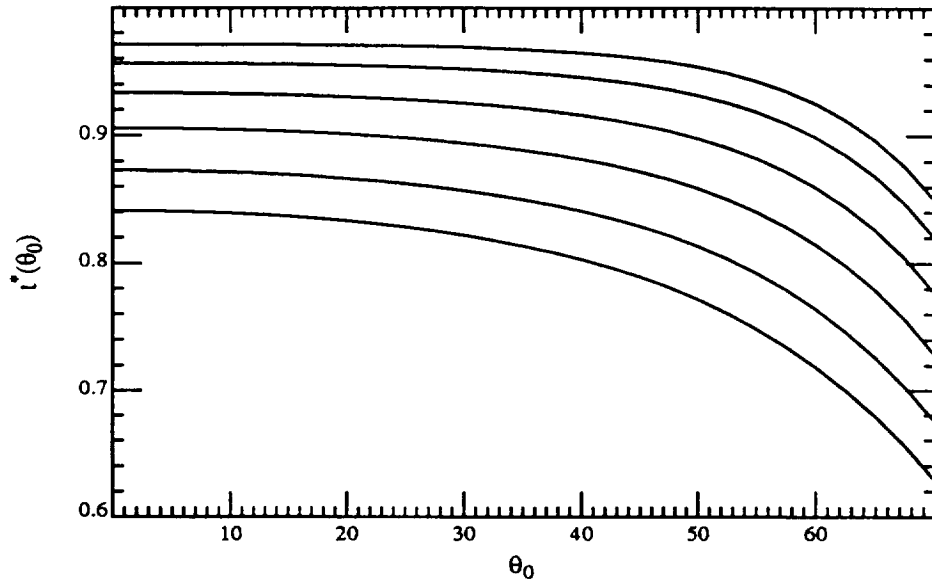


(a)

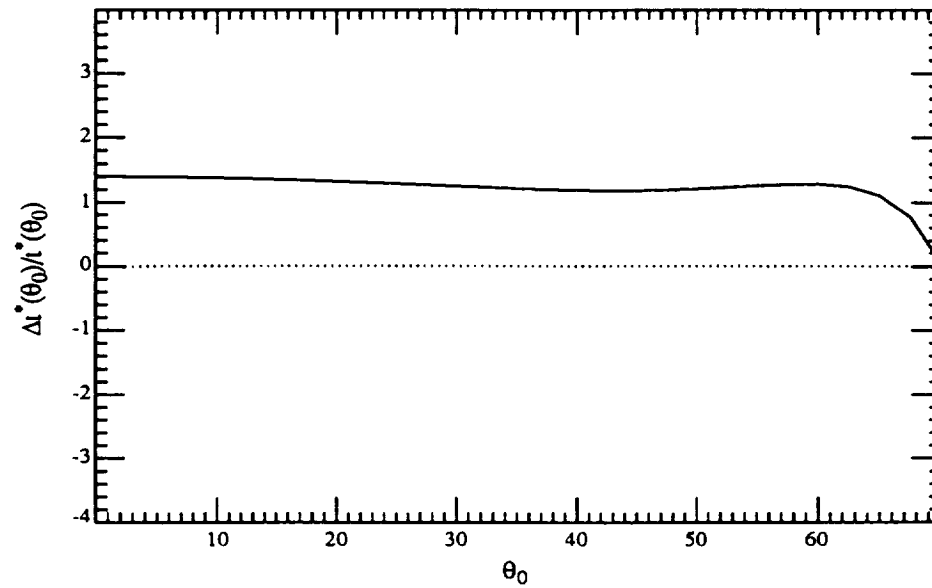


(b)

Figure 7. The error in t , induced by assuming that L_u is uniform, as a function of wavelength and aerosol optical thickness, using the Voss subsurface upwelling radiance distribution. The M90 aerosol model is used in all the computations. Panel (a) $\theta_0 = 60^\circ$ viewing in the perpendicular plane to the sun; Panel (b) $\theta_v = \theta_0 = 60^\circ$ with viewing azimuth ϕ_v .

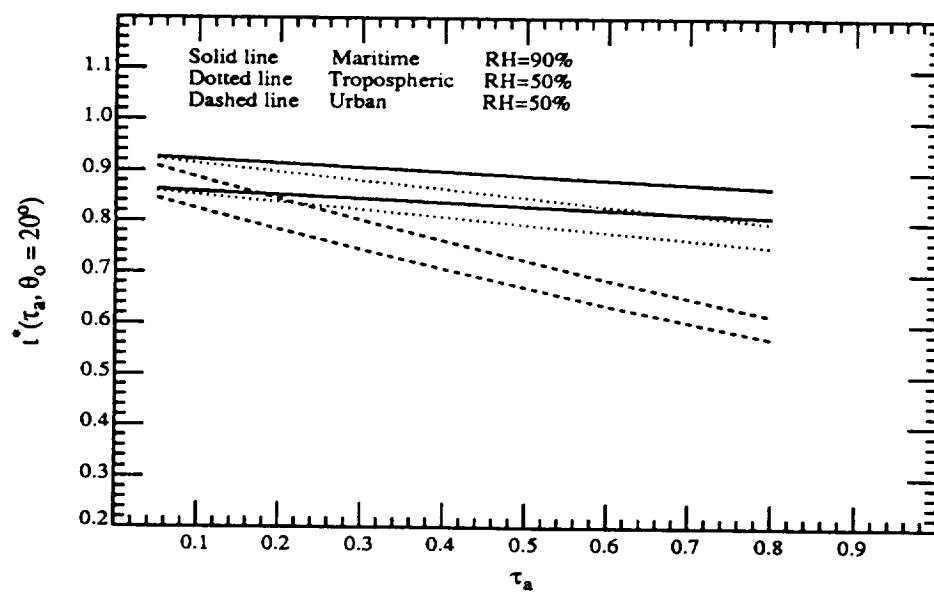


(a)

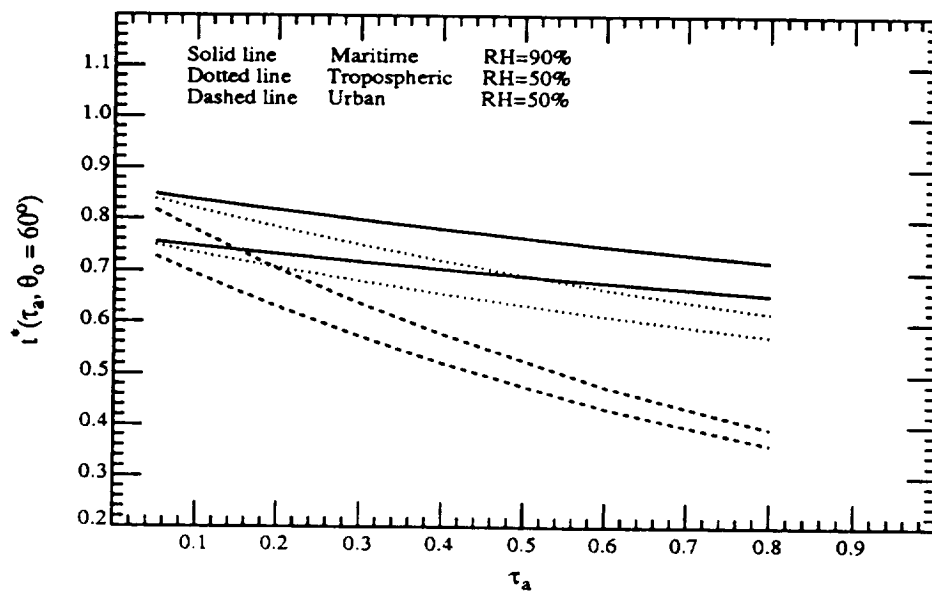


(b)

Figure 8. Computed t^* for a pure Rayleigh-scattering atmosphere. Panel (a) Values computed using radiative transfer theory. From bottom to top the curves correspond to $\lambda = 412, 443, 490, 555, 670$, and 865 nm. Panel (b), Error in t^* resulting from using Eq. (8) in the text.



(a)



(b)

Figure 9. Value of t^* as a function of aerosol model and optical thickness τ_a . Upper curves are for $\lambda = 555$ nm, lower curves for $\lambda = 443$ nm. Panel (a) $\theta_0 = 20^\circ$; Panel (b) $\theta_0 = 60^\circ$.

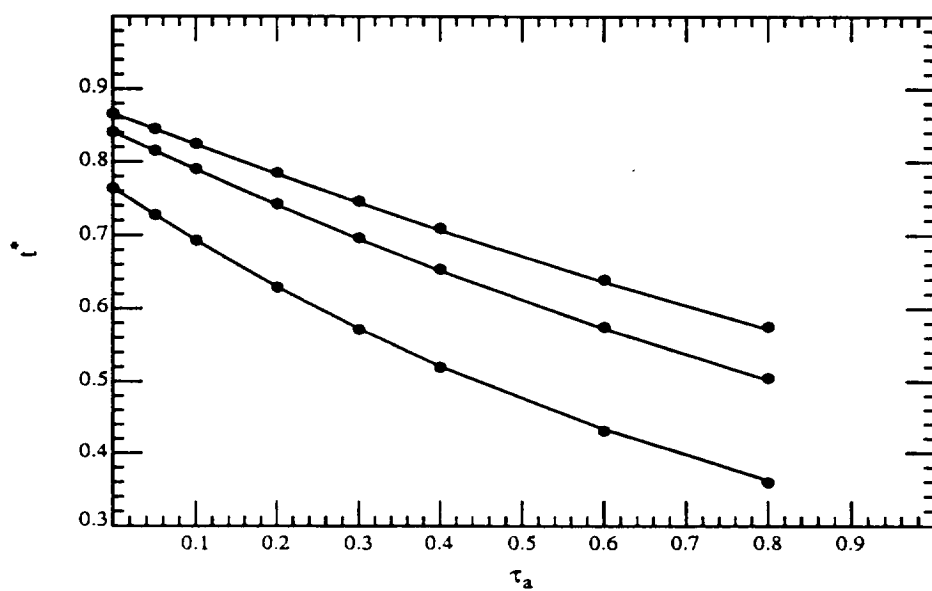


Figure 10. Influence of vertical structure on t^* for the U50 aerosol model at 443 nm. Lines correspond to placing all of the aerosol in the bottom layer of a two-layer atmosphere. Dots correspond to the mixing the aerosol uniformly with gas molecules throughout the atmosphere. Curves from top to bottom are for $\theta_0 = 20^\circ$, 40° , and 60° .

Appendix 3

Spectral Reflectance of Whitecaps: Instrumentation, Calibration and Performance in Coastal Waters.

KARL D. MOORE, KENNETH J. VOSS, HOWARD R. GORDON

Physics Dept., University of Miami, Coral Gables, FL 33124

Submitted to *Journal of Atmospheric and Oceanic Technology*

ABSTRACT

A measurement system for determining the spectral reflectance of whitecaps in the open ocean is described. The upwelling radiance is obtained from a ship by observing a small region of the water surface over time using a six channel radiometer (410, 440, 510, 550, 670 and 860 nm) extended from the bow of the ship. Downwelling irradiance is simultaneously measured and used to provide surface reflectance measurements. The system includes a TV camera mounted beside the radiometer which provides a visual reference of surface events. Air/water temperature and wind speed/direction are also measured along with global positioning system (GPS) data. Calibration procedures and radiometric characterization of the system for operation under different sky conditions and solar zenith angles is emphasized so that full advantage is taken of ship time whenever whitecap events occur. Examples of the spectral reflectance of different foam types (thick, dense, fluffy to thin residual patches) generated by the ship's bow in coastal regions are presented and found to vary spectrally. The presence of submerged bubbles in the foam measurement results in a lower reflectance at the longer wavelengths. For wavebands in the visible region, the spectral reflectance values tend to equalize with higher reflecting foam from thicker, fluffier and denser foam types.

1. Introduction

Remote sensing of the ocean by satellite requires accurate atmospheric correction. This is accomplished by measuring the upwelling radiance at a wavelength where the ocean is known to contribute very little or no radiance (Gordon and Wang, 1994a). This is typically done at wavelengths beyond 760 nm (and sometimes at 670 nm) where the absorption properties of water are particularly strong. In the presence of whitecaps, whose quantity and fractional coverage of the ocean surface varies primarily with wind speed, the ocean surface may no longer provide a negligible background for atmospheric correction at these longer wavelengths (Gordon and Wang, 1994b). An understanding of the additional or augmented spectral upwelling radiance from whitecaps must be quantified not only at the correction wavelength but at other wavelengths particularly in the visible region where spectral information provides a means of determining water content.

Previous authors have used a wavelength independent foam reflectance of 50% - 100% (Payne 1972; Gordon and Jacobs 1977; Maul and Gordon 1975) in conjunction with estimates of fractional coverage to determine the augmentation effect. Others have measured the spectral variation of foam in the laboratory using clear water and a variety of more turbid water types with various concentrations of detritus, sediment, etc. (Whitlock et al. 1982). Koepke (1984) established an efficiency factor that accounts for the diminishing reflectance and increase in area of the whitecap as it ages thus providing a smaller augmentation effect than that of other studies.

Estimates of fractional coverage of whitecaps have been carried out previously by photographic methods, either from the air (Austin and Moran 1974; Ross and Cardone 1974) or from a stationary platform over the ocean surface (Monahan 1971; Toba and Chaen 1973; Koepke 1984; Bortkovskii 1993). Spectral determination of whitecap and foam reflectance has been determined in the laboratory (Whitlock et al. 1982) and from foam generated in the surf zone (Frouin et al. 1996). Whitlock's laboratory experiments showed a decrease in reflectance with increasing wavelength beyond $\sim 0.8\mu\text{m}$. However, Frouin reported a much lower reflectance than Whitlock at the longer wavelengths with a 40% decrease at $0.87\mu\text{m}$, 50% at $1.02\mu\text{m}$ and 95% at $1.65\mu\text{m}$ relative to the reflectance at 440 nm. The difference between the laboratory and field measurements is thought to be due to the stronger absorption

properties of water at longer wavelengths acting on light reflected from submerged bubbles forced into the water by large waves.

The quantity of whitecaps covering the surface area of the ocean is detected as an augmentation in the upwelling radiance observed by the relatively low resolution of a satellite pixel. To measure the spectral influence and magnitude of whitecaps in terms of a radiometric signal, the foam-free water-leaving radiance must be differentiated from the radiance contribution of whitecaps. This entails measurement of all foam types; from thick fluffy, highly reflecting foam as the wave breaks to barely distinguishable thin, residual and fragmented patches of foam as the whitecap decays back into the ocean. To measure the spectral reflectance of these foam types, particularly within the life cycle of an individual whitecap, requires an instrument of comparably high spatial and temporal resolution. Camera images of the ocean surface can provide a varied foam assortment, but determination of the foam-free background can be complicated by variation in sky reflectance towards the extreme regions of the image. This is particularly true when the imaging system is mounted on a platform and at an angle to cover as large an area of the water surface as possible. Use of a high resolution imaging system for spectral measurements also requires a time delay between images of different wavebands, and the content of the spectral images may no longer be identical.

Using a high resolution imaging system from an airborne platform provides greater coverage and a decrease in sky reflectance variation as the height above the water surface is increased but at the cost of surface resolution. High resolution spectral data of whitecaps is more feasible to acquire from a surface platform particularly in the open ocean where flying an aircraft long distances and providing simultaneous ancillary measurements such as wind speed/direction and air/water temperature may become costly.

In this paper, a whitecap radiometer system for operation on board a ship or other surface platform is described. The spectral reflectance of the water surface is measured by a 6-channel non-imaging radiometer with a narrow field of view and wavebands at 410, 440, 510, 550, 670 and 860 nm. The radiometer is deployed from the bow of a ship along with a TV camera to provide a visual reference of the radiometrically measured surface. In conjunction with the radiometer, a deck cell (cosine

collector) monitors downwelling irradiance with matching wavebands thus providing surface reflectance measurements. By making many high spatial resolution measurements of the water surface at a fixed periodic rate, spectral data of individual whitecaps and their associated foam types (defined by their reflectance magnitude) can be analyzed and also provide an estimate of their frequency. Measurement of the frequency of different foam types provides a value of fractional coverage and the augmented spectral reflectance contribution of whitecaps to the water-leaving radiance as observed by ocean color satellites. In addition, the whitecap radiometer system acquires wind speed/direction and air/water temperature as well as global positioning system (GPS) information to provide universal time and location. Estimates of fractional coverage and augmented reflectance contribution can then be correlated to these parameters.

In this paper we describe the whitecap instrument system and give particular attention to radiometric calibration for field use under various sky conditions and solar zenith angles in order to correct for slight deviations in solid angle response of the deck cell's cosine collector and the effects of spectral filter mismatch between channels in the deck cell and radiometer. Calibration for different sky conditions provides a robust system that takes full advantage of ship time and provides confident reflectance measurements of whitecaps whenever they occur. In addition, performance of the system is discussed and foam data generated by the ship's bow in coastal waters is examined.

2. Whitecap Radiometer Instrument Description

Our strategy has been to measure whitecap reflectance from a surface platform such as a ship; either stationary or underway. The whitecap measurement system consists of a 6-channel radiometer aimed at the water surface, a downwelling irradiance cosine collector with matching wavebands, water temperature and air temperature sensors, an anemometer to determine wind speed and direction, and a global positioning system (GPS) to record location, GMT time and determine ground speed and course heading. Taking many reflectance measurements of a small area of the ocean surface over time is equivalent to capturing a large field of view with high spatial resolution at one time.

The 6-channel radiometer has wavebands at 410, 440, 510, 550, 670 and 860 nm and is aimed at the water surface with each channel covering $\sim 1^\circ$ field of view. A TV camera (Sony SSC-C350 color

CCD camera) with a greater field of view ($\sim 40^\circ$ - 50° using a 6 mm focal length video TV lens) is mounted beside the radiometer to provide a visual reference of radiometer measurements and is recorded on video tape using a video cassette recorder (Sony EV-C100). A triggerable analog switch has been implemented to allow individual TV frames to be date and time marked whenever the radiometer acquires data, thus providing a frame by frame reference.

The radiometer and TV camera assembly are extended over the bow of the ship as a unit by means of a boom. The boom is comprised of a number of segments of equal length and any number can be deployed to provide extension from ~ 1 m to ~ 10 m depending on the sea state and at the same time ensure that optical shadowing and wind sheltering ship effects are minimized.

To provide reflectance measurements of the ocean surface, downwelling irradiance is measured by the cosine collector (deck cell) at 6 matching wavebands, positioned on the ship to avoid shadowing. Wind speed and direction are measured by an anemometer placed in an unobstructed position towards the bow of the ship. Water temperature is measured with an accuracy of 0.1°C close to the surface by means of a small thermistor with signal conditioning circuitry to provide a linear and stable output. The thermistor's signal and power cable is fed down the center of a polypropylene rope with the thermistor exposed roughly 10-20 cm from the end of the rope. The buoyancy of the polypropylene rope keeps the thermistor at or near the surface and the remaining few centimeters of the rope are flayed to ensure the thermistor does not skip out of the water as the ship moves. Air temperature is measured with an identical thermistor housed in a white plastic louvered cylinder to prevent direct solar heating. It is suspended from the bow of the ship close to the water surface but at a sufficient height to prevent contact with sea spray.

The analog signals from the radiometer, deck cell, anemometer, GPS, water and air temperature sensors are sampled at a fixed periodic rate. Upwelling and downwelling radiometric data along with air/water temperature, wind speed/direction are sampled ~ 7 times a second continuously for about 30 seconds (providing 200 contiguous samples), after which GPS data; GMT time and location, are appended to file. The acquisition sequence is repeated until a time determined by the operator. With the exception of the GPS data, all parameters including radiometer and deck cell data are measured

simultaneously (within 20 μ s). Making many measurements of the reflectance from small areas of the ocean surface as the ship moves through the water allows one to estimate white water coverage as a function of wind speed and air/water temperature, as well as providing spectral information.

All cables from the various measuring components arrive at the electronics console which is essentially an interface for individual cable connections as well as providing power and receiving analog signals. The analog signals are processed through differential amplifiers, to eliminate ground fluctuations that may originate over the long lengths of cable, before being digitized. The pre-conditioned analog signals are fed to a National Instruments NB-MIO-16XL acquisition board resident in a Macintosh Power PC. This acquisition board is configured to accommodate 16 referenced single-ended inputs and provide 16 bits A/D resolution. The acquisition logic, processing sequence and storage to file is controlled by LabVIEW software. The software also provides graphing and numeric display capabilities of the data as it is acquired. Data acquisition is allowed to free run and is halted at a time determined by the operator. Data files of various sizes are subsequently read into a statistical software package (Matlab) to produce detector background corrected and radiometrically calibrated reflectance values of the ocean surface along with air/water temperature and wind speed profiles.

a. The Radiometer

Each channel of the radiometer consists of an optical tube aligned parallel to one another. Light entering each channel passes through a BK-7 window with a broadband AR coating. Behind this window, light for each channel is collected by a 25 mm diameter, 100 mm focal length achromat with a broadband AR coating. The converging light passes through a 10 nm bandpass spectral interference filter. Behind the interference filters, broadband blocking filters are included to enhance out-of-band blocking of unwanted light. The field of view for all channels ($\sim 1^\circ$) is set by a 1.8 mm pinhole aperture placed at the focal point of the lens with the active area of the detector positioned 1.5 mm behind the focal plane. The detector for each channel is a silicon photodiode (Hamamatsu S1406-04) packaged with an integrated operational amplifier. The voltage output is fed into a low noise precision opamp (Analog Devices PM-1012GP) with a gain appropriate to each channel to offset variation in photodiode spectral

response before being sent to the electronics console. Power (+/-12 VDC) sent to the radiometer is DC/DC converted and further regulated to supply +/-5 VDC to the photodetectors along with +/-12 VDC for the low noise precision opamps. Five of the six channels are arranged in a concentric fashion about the long axis of the housing with the 410 nm channel taking up the central position. The complete radiometer assembly is housed in a black anodized aluminum cylinder 30 cm in length and 11 cm diameter (See Fig. 1). These dimensions include an extension hood (5 cm in length) that is provided to prevent rain falling on the window and to reduce light that may be reflected and refracted by sea spray and salt deposits that inevitably collect on the window.

b. The Deck Cell

The deck cell is similar to the radiometer with the exception of the collection optics and its housing. The deck cell utilizes a cosine collector with a ~5 cm diameter white diffusive acrylic plastic disk (Rohm & Hass, no. 2447) protruding ~1 cm beyond a dark rigid PVC base. Moving radially outward, the base is terraced, increasing in height with radius to a diameter of 124 mm at which point the height is flush with the top of the acrylic disk. The protruding acrylic disk provides a cosine response and in conjunction with the terraced base defines a 2π field of view as well as ensuring a cosine response at the larger zenith angles.

Five of the photodiodes with interference and blocking filters are arranged in a circle and slightly angled to view the center of the acrylic disk from behind, while the sixth photodiode-filter assemblage is centered behind the acrylic disk. In this way the cosine response is common to all channels of the deck cell. The photodiodes, electronics, and optical filters are identical to the 6-channels in the radiometer but with a different gain on the precision opamps and with different optical apertures to accommodate the spectral variation of the downwelling light and detector response.

The 15 cm diameter x 13.5 cm long cylindrical housing is made from rigid PVC plastic mounted in a 2-axis gimbal. The bottom base plate of the housing is made from lead and in combination with the gimbal mount helps the cosine collector maintain a horizontal attitude despite any low frequency small amplitude rocking motion of the test platform.

3. Radiometric Calibration

a. Reflectance calibration

Laboratory radiometric reflectance calibration of the deck cell and radiometer was carried out using a calibrated 1000 Watt (FEL) quartz-halogen lamp. The deck cell was positioned 50 cm from the lamp with the surface of its cosine collector perpendicular to normal incidence. For the radiometer, a Spectralon reflectance plaque was normally illuminated by the lamp 50 cm away and viewed by the radiometer at a 45° angle. The reflectance of the plaque is 94.6 +/- 0.2% from 400 to 870 nm normally illuminated and viewed at an 45° angle. Background dark current readings were taken before and after each measurement. Absolute calibration was done in this manner before and after deployment in the field to verify radiometric stability.

b. Radiometric performance

To assess the radiometric performance of the radiometer and deck cell in determining reflectance under the variety of natural sky conditions and solar zenith angles occurring during a ship cruise, the radiometer and deck cell were tested outside the lab. The radiometer was aimed vertically downward at a Spectralon reflectance plaque with the deck cell positioned beside the plaque. The plaque surface was level and at the same height as the flat surface of the deck cell cosine collector. The radiometer was positioned to avoid direct shadowing of the plaque and the deck cell, and so that the radiometer blocked out only a small section of the sky.

Under overcast conditions with dark and bright patches of cloud passing overhead, variations in the measurement of the reflectance value of the plaque were observed. A set of reflectance data were taken around noon with sky conditions going from one extreme (very overcast - sky totally covered and no distinct shadows observed) to another (direct sunlight breaking through a large clear patch with solar elevation angle ~60°). The variation (maximum to minimum) in reflectance values observed during these conditions for each channel (410 through 860 nm) were: 0.040, 0.045, 0.039, 0.050, 0.058 and 0.063 with the mean reflectance value for each found to be 0.987, 1.022, 0.969, 0.993, 1.001 and 1.122 respectively (See Fig. 5), the reflectance variation of the reflectance plaque and correction will be

discussed later. Calibration factors determined under laboratory conditions obviously were not sufficient to measure real field conditions with a changing angular distribution of the 2π light field. These results led to a rigorous calibration and understanding of the radiometric system so that we could be confident of reflectance data acquired under many sky conditions and times of day in field measurements.

c. Linearity

The first test was to check the linearity of both the deck cell and radiometer in order to identify and eliminate any gross malfunctioning of the system. The photodiodes are reversed biased and as such should be highly linear. However, a damaged component, loose wire or bad connection could exhibit non-linearity at higher light levels that may not be seen at lower light levels of the laboratory calibration. As the gain and throughput of these instruments is specifically set for outdoor conditions, taking them into the lab where the proportion of blue light is comparatively low makes it difficult to cover the full dynamic range that might be encountered outdoors particularly for the shorter wavelength channels.

The linearity test was carried out by moving a constant light source specific distances from the instrument in question and the output signal recorded. In the case of the deck cell, the cosine collector was removed and a diffusive surface of much greater transmissivity put in its place in order to achieve an equivalent illumination intensity found outdoors on a clear day with the sun overhead. The diffusive surface was required to reduce non-uniform illumination effects observed by the off-axis channels when the lamp source (140W) was brought close to the deck cell.

The radiometer, with a narrow field of view, was tested in much the same way but required a 1000W lamp source and was tested intact without any alterations. A diffusive surface with low transmission was placed a fixed distance in front of the radiometer to provide uniform illumination as the lamp source moved position. Both the deck cell and radiometer were found to be highly linear.

d. Angular response of deck cell and plaque

From the experiment outdoors, it was noted that the measured reflectance value of the plaque would sometimes increase and at other times decrease even though the downwelling intensity remained

much the same. This suggested a possible sensitivity of the instrumentation to the angular distribution of the downwelling light field. A crude test done under a clear sky with the sun high overhead also seemed to support this view. An opaque surface sufficiently large to continually block out the direct sun incident on both the deck cell and the reflectance plaque was raised and lowered to simulate a changing angular light field. By doing this, the reflectance value of the plaque was also observed to change in a consistent manner with changing angular light field.

The angular response of the deck cell and the reflectance plaque was measured in the lab. With the lamp source (point) placed ~1.5 meters from the surface of the cosine collector of the deck cell, the deck cell was rotated in 10° increments from normal incidence to plus and minus 90° . The reflectance plaque could not be viewed from the normal due to the restrictive geometry of placing the detector in the same position as the source. Starting with the closest reasonably achievable viewing angle of 2° , subsequent measurements were taken at 5° through 85° at 5° increments. Spline curves were then fitted to these data points and the results of the angular responses for both the deck cell and the reflectance plaque are shown for the 410 nm channel in Fig. 2(a). Also included for reference is the angular response of an ideal cosine collector or Lambertian reflector. In Fig. 2(b) the angular response from 0° to 85° for both the deck cell and reflectance plaque is shown for all channels in terms of deviation from true cosine.

In most channels, the response of the deck cell and reflectance plaque are similar with slight differences becoming apparent at larger angles of incidence. Although both deviate from true cosine, they appear to be close in response to each other with the exception of the poorer deck cell performance at 860 nm. For channels 410, 440, 510 and 550 nm the deck cell appears to have an angular response that is closer to true cosine than the reflectance plaque particularly at the larger angles. The 670 nm channel of the deck cell and reflectance plaque are the most similar yet both deviate from true cosine. In the 860 nm channel the deck cell response is much lower than the reflectance plaque response. Also, the reflectance plaque appears to have a consistent angular response in all channels.

To better understand the implications of these angular response measurements, performance of the deck cell and reflectance plaque operating outdoors under 2π illumination must be addressed. To achieve this, the angular response variation in solid angle with zenith angle must be taken into account. In Fig. 3 the angular response has been weighted by $2\pi \sin\theta d\theta$ which accounts for the greater solid angle viewed with increasing zenith angle (θ). Figure 3 shows the solid angle response for the 410 nm channel of the deck cell and reflectance plaque and also for a true cosine solid angle response. These values are normalized to the ideal cosine sensitivity at 0° . The solid angle response for both the deck cell and reflectance plaque in terms of deviation from true cosine is identical to Fig. 2(b).

For the deck cell and the radiometer to measure correct reflectance of the calibrated reflectance plaque outdoors, both the deck cell and reflectance plaque must be corrected for solid angle response to the particular downwelling angular light field distribution. To measure true (correct) reflectance, R , in each channel,

$$R = \frac{\pi L_t}{E_t},$$

where L_t is true upwelling radiance from a perfect Lambertian reflector, E_t is true downwelling irradiance measured by an ideal cosine collector, and

$$L_t = L_{rad} r_{rad},$$

where L_{rad} is the radiance measured by the radiometer viewing the reflectance plaque and r_{rad} is the correction factor, due to deviation of plaque response from true Lambertian, applied to L_{rad} to yield L_t . Similarly,

$$E_t = E_{dc} r_{dc},$$

where E_{dc} is the downwelling irradiance measured by the deck cell and r_{dc} is its correction factor. Also,

$$r_{rad} = \frac{2\pi \int TC(\theta) \cdot L(\theta) \cdot \sin\theta d\theta}{2\pi \int RP(\theta) \cdot L(\theta) \cdot \sin\theta d\theta} \Rightarrow \frac{TCR}{RPR}$$

and,

$$r_{dc} = \frac{2\pi \int TC(\theta) \cdot L(\theta) \cdot \sin\theta d\theta}{2\pi \int DC(\theta) \cdot L(\theta) \cdot \sin\theta d\theta} \Rightarrow \frac{TCR}{DCR}$$

where TC is the true cosine response, RP the reflectance plaque response, DC the deck cell response, L is the downwelling radiance or sky condition and θ is the zenith angle. TCR , RPR and DCR are the true cosine, reflectance plaque and deck cell responses respectively for a particular sky condition. Therefore,

$$R = \frac{\pi L_{rad}}{E_{dc}} \cdot C_r,$$

where $C_r = \frac{DCR}{RPR}$, and the response correction factor, C_r , is dependent on sky condition $L(\theta)$. For

example, to simulate the overcast sky condition the coroidal expression, $L(\theta) = 1 + 2\cos\theta$ (where θ is zenith angle), is used. C_r in this case is the product of the angular response of the deck cell and the overcast sky distribution, integrated over all zenith angles and divided by the integrated product of the angular response of the reflectance plaque and the overcast sky profile over all zenith angles ($\theta = 0^\circ$ to 90°). This process is repeated for each waveband channel. See Table 1.

Other sky conditions have been simulated such as different solar zenith angles on a clear day. Data from principal plane measurements taken during clear sky conditions using a sun-tracking photometer (Welton, 1996), developed by CIMEL, were used to generate the radiance distribution for different solar zenith angles at 0° , 10° , 20° , 30° , 40° , 50° , 60° , 70° and 80° . Radiance measurements from the sun photometer-sky radiometer at two different wavebands (440 and 860 nm) passing through the sun at a 55° solar zenith angle were used. There was no discernible difference in the correction factors, C_r , when the two wavelengths were applied, and changing the peak solar radiance by a factor of 10 only effects the resulting correction factors shown in Table 1 by $\sim 0.1\%$.

As can be seen from Table 1, applying the laboratory calibration relationship between the deck cell and the reflectance plaque to determine reflectance under a clear sky with the sun directly overhead (solar zenith angle = 0° , i.e. 'sun 0') is not valid.

e. Filter response

In addition to characterizing the effect of the angular response mismatch of deck cell and reflectance plaque under different sky conditions, the spectral filter response must also be examined. A monochromator using a 1000W lamp source was used to determine the bandpass characteristics of each channel in both the deck cell and the radiometer. The monochromator output bandwidth was set to 1 nm to profile the nominal 10 nm bandpass of each filter assemblage. Measurement of the bandpass filters in each channel of the radiometer was a straightforward process. However, for the deck cell the amount of light passing through the diffusive acrylic material of the cosine collector was too small to afford any appreciable signal and was removed as before.

In order to normally illuminate the filter assemblages in the deck cell, the deck cell housing had to be angled with respect to the monochromatic output beam since the filter assemblages and their photodiodes (with the exception of the center photodiode-filter assembly) are purposely angled to view the center of the cosine collector. This action subsequently raised the question of the viewing angle of the interference filters inside the deck cell. The back of the cosine collector subtends a half angle of $\sim 28^\circ$

to the photodiode detectors and the field of view for each channel was established by the different sized optical apertures placed in front of the filters. They were intended originally to increase light throughput at the shorter wavelengths and reduce the throughput at the longer wavelengths. The half angle field of view for each deck cell channel was 24° , 23.5° , 18.5° , 18.4° , 16.6° and 16.6° for channels 1 through 6 (410, 440, 510, 550, 670, and 860 nm).

From these measurements it became obvious that the interference filters would possess different bandpass and transmission characteristics than measured under normal illumination conditions. As the actual bandpass profile of the deck cell channel could not be measured directly, due to insufficient light output from the monochromator with 1 nm resolution, the bandpasses were calculated. This involved accounting for the center wavelength shift to shorter wavelengths, the associated transmission drop off and bandpass broadening (Handbook of Optics, 1995). The center wavelength shift, transmission drop and bandpass broadening were weighted with the effective increase in light intensity contribution due to the increase in field of view of the back side of the uniformly illuminated cosine collector at larger angles. The photodiode spectral response was also considered.

The calibration procedure for the radiometer (viewing the plaque) and the deck cell would account for this difference in spectral response *only* if the spectral profile of the lamp source in the lab was the same as the solar spectrum. Obviously it is not, and differences in the spectral profile of the lamp and solar spectrum must be accounted for with the broader bandpass of the deck cell channels. In Fig. 4, the radiometer and deck cell bandpass profiles (calculated) for each channel are shown along with the normalized lamp source and solar spectral profiles. The difference in the estimate of reflectance will be affected by going from a laboratory calibration under the lamp source to operation outside under the different spectral weighting of the solar spectrum. In Table 2, the bandpass multiplication correction factors which have been calculated to offset the error in making reflectance measurements out of doors are provided. The bandpass correction factors, $C_{BP}(\Delta\lambda)$, have been arrived at by calculating the ratio of the integrated product of the radiometer bandpass and the solar spectrum, to the integrated product of the radiometer bandpass and lamp spectrum, divided by the ratio of the integrated product of the deck cell

bandpass and the solar spectrum, to the integrated product of the deck cell bandpass and lamp spectrum or:

$$C_{BP} = \frac{\int_{\lambda}^{\lambda+\Delta\lambda} R(\lambda) \cdot L_{solar}(\lambda) \cdot d\lambda}{\int_{\lambda}^{\lambda+\Delta\lambda} R(\lambda) \cdot L_{lamp}(\lambda) \cdot d\lambda} \bigg/ \frac{\int_{\lambda}^{\lambda+\Delta\lambda} DC(\lambda) \cdot L_{solar}(\lambda) \cdot d\lambda}{\int_{\lambda}^{\lambda+\Delta\lambda} DC(\lambda) \cdot L_{lamp}(\lambda) \cdot d\lambda},$$

where R is the bandpass response for a particular channel of the radiometer, DC the bandpass response for the same channel in the deck cell and L_{lamp} and L_{solar} are the illumination profiles over $\Delta\lambda$ for the lamp source and sun respectively.

f. Application of the correction calibration

In Fig. 5 the overcast sky and 30° solar zenith angle (sun30) correction factors are applied to the reflectance data measurements taken of the plaque outdoors (as conditions varied from being very overcast to direct sunlight breaking through with 30° solar zenith angle and then eventually to broken conditions). The filter bandwidth correction has also been included. Due to the higher gain of the radiometer which is specifically set to measure the lower upwelling water reflectance signal and foam contributions, the 860 nm channel observing the ~95% reflectance plaque saturates when the sun appears from behind the clouds. This saturation has not been included in characterizing the 860 nm reflectance variation with sky condition.

Variation in the measured reflectance persists as the real sky condition departs from the modeled sky definition. The most noticeable benefit of these correction factors is in the 860 nm channel. Regardless of the sky correction, application of the solid angle response and filter bandwidth correction results in a mean measured reflectance (over the time series shown) of 0.9944 for overcast or 1.017 for

direct sun with 30° zenith angle rather than the uncorrected mean reflectance of 1.122. [It should be noted that a reflectance plaque value of 1 has been assumed for simplicity in this analysis but its real values of 95.7%, 94.2%, 94.4%, 94.3%, 94.4% and 94.9% for channels 410 through 860 nm are applied to the field data]. The best description of an overcast sky and direct sun within the time series are shown on the figure. The application of the appropriate sky correction to the data taken under a valid sky description depicts a closer approximation to a reflectance value of 1 in all channels. The standard deviation from a reflectance of 1 for all channels is 0.0025 for the overcast condition and 0.0028 for the direct sun condition. Other regions of the time series are the result of sky conditions that are more difficult to describe and therefore to further correct. The standard deviation of variation in reflectance over the extreme sky conditions that occurred during the complete time series in Fig. 5 was 0.0081, 0.0089, 0.0086, 0.0101, 0.0127 and 0.0313 for channels 410 through 860 nm respectively.

In Table 3, the amount of correction that has been applied to the measured reflectance for each channel and for both sky conditions ('sun 30' and 'overcast') is shown. The resulting accuracy or percentage deviation from a reflectance value of 1 is given in the last two columns. For example, the 860 nm channel data is corrected by 12.77% in the overcast data to read a corrected reflectance of 0.995 (i.e. 0.005% accuracy). The direct sun data is saturated for this channel.

g. Correction of field data

To make reflectance measurements of the water surface, only the deck cell requires solid angle response correction for different sky conditions. We have:

$$R = \frac{L_{ws}}{E_i},$$

where R is the reflectance we wish to determine, L_{ws} is the upwelling radiance from the water surface (and including contributions from below the surface) received by the radiometer and E_i is the true downwelling irradiance. As before,

$$E_i = E_{dc} \cdot r_{dc},$$

where E_{dc} is the downwelling irradiance measured by the deck cell and r_{dc} is the sky correction factor that must be applied to the deck cell to have true cosine response, i.e.,

$$r_{dc} = \frac{E}{E_{dc}} = \frac{2\pi \int TC(\theta) \cdot L(\theta) \cdot \sin(\theta) d\theta}{2\pi \int DC(\theta) \cdot L(\theta) \cdot \sin(\theta) d\theta} = \frac{TCR}{DCR},$$

where,

$$R = \frac{\pi L_{wz}}{E_{dc}} \cdot C_f \quad \text{and} \quad C_f = \frac{DCR}{TCR}.$$

Table 4 shows the field correction factors, C_f , the measured reflectance must be multiplied by in order to read correct reflectance.

4. Experiment Description, Results and Discussion

The initial measurements with the whitecap radiometer system were made to evaluate its performance and ability to provide a dependable data base of air/water temperature, wind speed/direction, GPS information as well as radiometric and visual events recorded and date/time stamped onto video tape. Initially the system was deployed on the RV McGaw for a 14-day cruise off the coast of Southern California. The ship visited a number of stations located in a small area on a daily basis to collect data for other oceanographic studies. Weather conditions were far from ideal for whitecap formation, being primarily calm with mainly diffuse overcast days. However, data was taken of foam generated by the ship's bow as it moved from station to station. Also, application of the overcast correction to foam data acquired during overcast conditions is less sensitive to error than applying a clear sky correction that only approximates the true solar zenith angle and also removes the possibility of specular sun glitter in the measurements. The radiometer was mounted at different positions over the side of the ship providing a

data base for radiometric performance of the system and analysis of different stages of foam development.

The control software (LabVIEW) had originally been set to acquire all data at the same time. In this way, radiometric, air/water temperature, wind speed/direction could easily be addressed by UTC time or location during later analysis. However, the price for waiting for updated GPS data at every sample resulted in a system acquisition rate of about 0.5-1 Hz despite setting the National Instruments acquisition board to the optimal acquisition rate. In the rare moments when a whitecap did happen to form, the slow update of the system failed to provide enough samples of the event and in many cases missed the event altogether. Had the wind speeds being much stronger, yielding a good whitecap coverage, the system would have provided sufficient data.

Another factor to consider in capturing transient white water events was the integration time. The 0.5-1 Hz sampling rate of the system was not radically affected by varying the integration time due the wait period for GPS data. Although the data acquisition rate of the board was optimized (55 kHz sequential sampling frequency over 16 input channels), a set number of samples were binned at high speed (100 samples) to increase the signal-to-noise ratio, and the average value for each channel written to file. This yielded an effective integration time of the radiometer of just under 30 ms, i.e. just less than a TV video frame period so visually recorded events could be correlated to radiometric measurements with optimal signal-to-noise binning.

Figure 6 is an example of the bow foam data obtained. In this example, the radiometer samples as the ship moves to its next station and half way through this time series the ship slows to complete stop. When the ship has slowed to a speed where bow foam is no longer generated in the field of view of the radiometer, the water-leaving radiance and sky reflectance can be determined. The sky condition was completely overcast and slightly foggy, with a very calm water surface. This measurement of the foam-free water could then be subtracted from the foam reflectance to provide the spectral augmented foam reflectance contribution although the real meaning of augmented reflectance in this case is lost due to the origin of the foam.

In Fig. 7 the spectral reflectance of foam is shown in terms of different reflectance intervals relating to different foam types, i.e. thick fluffy fresh dense foam to residual thin patches, streaky foam and submerged bubbles. For this differentiation, any reflectance spectrum with a particular value at 860 nm that falls within a reflectance interval is averaged. In this example, the set reflectance intervals are 0-0.04, 0.04-0.08, 0.08-0.12, 0.12-0.16, 0.16-0.20, 0.20-0.24, 0.24-0.28, 0.28-0.32, 0.32-0.36, 0.36-0.40, 0.40-0.44, 0.44-0.48, 0.48-0.52, 0.52-0.56, 0.56-0.60, and 0.60 - 1.00. The number of spectra averaged in any one interval is also shown to give an indication of the measurement accuracy in determining the spectral profile for that reflectance level.

Foam data was also acquired under clear and sunny conditions where the effects of specular sun glitter were included. As the ship was there to service test station areas in a small grid, there was frequent changes in ship heading, making a fixed radiometric viewing angle with respect to the sun difficult to maintain. These changes in ship heading at random times of the day made the quantity of specular sun glitter more difficult to estimate. Some specular sun glitter was tolerable but depending on the illumination and viewing geometry it could at times radically affect the reflectance signal. In addition, it was difficult to avoid ship shadow particularly at lower solar zenith angles. The effects of specular sun glitter in radiometrically discriminating white water from nonwhite water events is addressed elsewhere (Moore et al. 1997). However, much of the data from this cruise was acquired under overcast sky conditions.

In Fig. 8 a collection of foam data taken at different times throughout a very overcast morning, starting with local times of 7:45 am, 10:30 am, 11:00 am and 12:00 noon (19 October 1995), was compiled into a single time series. The foam reflectance at the beginning of the time series is highest due to thicker fluffier foam layers generated by a higher ship speed. This first part of the time series is the same data used in Figs. 6 and 7, followed by starts and stops and slower ship speeds producing a varied set of foam reflectances. As before, reflectance intervals relating to different foam types (or foam thicknesses) and the foam-free water-leaving radiance and sky reflectance (referred to as the foam-free water reflectance) are shown in Fig. 9 along with the number of spectral reflectance values used in the estimation of each interval.

The pronounced drop off at the 670 and 860 nm channels is thought to be due to the strong absorbing properties of water at those wavelengths particularly on light reflected from submerged bubbles. Also of interest is the drop off in the 440 and more so in the 410 nm channels. These suppressed reflectance values at either end of the spectrum become more acute with higher reflectance values corresponding, in general, to thicker and more developed foam.

In Fig. 10 the spectral reflectance of intervals 2, 4, 7, 10 and 12 from Fig. 9 are shown. The spectral profiles are normalized at 440 nm along with the background foam-free water reflectance. The spectral variation of different foam types can be seen by normalizing their reflectances. The foam-free water spectral reflectance profile is different showing a relatively small difference between 410 and 440 nm. The foam-free water has reflectance values of 0.0431, 0.0466, 0.0509, 0.0535, 0.0370 and 0.0310 at 410, 440, 510, 550, 670 and 860 nm. The influence of the background foam-free water reflectance can be seen particularly in the lower reflectance intervals. The 550 nm value in interval 2 is slightly higher than the 510 nm value and the spectral shape appears to be somewhere between the foam-free water reflectance and that of a foam reflectance from a higher reflectance interval. While the slope between the 670 and 860 nm values for reflectance interval 2 is smaller than for the higher reflectance intervals, it is not quite as small as the foam-free water reflectance. The high 510 and 550 nm values in both the foam-free reflectance interval and interval 2 seem to eventually disappear in the higher reflectance intervals. Since the lower reflectance interval is comprised of the thinnest foam types, with patches of single-layered bubbles, measurements of the foam-free water reflectance and water-leaving radiance will inevitably be included. With thicker and denser foam types comprising the higher reflectance intervals, the measurement of foam-free contributions decreases with higher reflectance interval. The probability of including the reflectance contributions from submerged bubbles also decreases with higher reflectance intervals. On the other hand, the 410 nm values appear to remain the same regardless of reflectance interval.

In Fig. 11 the augmented reflectances for the same foam types used in Fig. 10 normalized at 440 nm are shown. The measure of augmented reflectance in this case simply means that the foam-free water reflectance has been subtracted from the foam reflectance in order to investigate spectral variation with

foam type only. Many features are similar to the reflectance profiles for these intervals shown in Fig. 10. As expected, with the removal of the foam-free water reflectance, the smallest reflectance interval no longer shows the similarity to the background foam-free water reflectance as it did in Fig. 10. All foam types are essentially identical with the exception of the 670 and 860 nm values which increase with higher reflectance interval. Once again the all foam spectra have a lower 410 nm value than the foam-free reflectance, and the 440, 510 and 550 nm values are almost equivalent, explaining the white appearance of foam. However, the values at 410 nm now appear to increase, if only very slightly, with increasing reflectance interval. Also the drop off from 440 nm to 860 nm, in these normalized spectra, can now easily be seen to decrease in a progressive manner with increasing reflectance interval and therefore of foam type; for reflectance interval 2 (with spectral augmented reflectance at 440 nm of 0.0597 taken from 357 samples with background foam-free water spectra subtracted) there is a ~62% drop, for interval 4 (spectral augmented reflectance at 440 nm of 0.252 from 94 samples) it is 57%, for interval 7 (spectral augmented reflectance at 440 nm of 0.488 from 113 samples) it is ~53%, interval 10 (spectral augmented reflectance at 440 nm of 0.620 from 48 samples) ~45% and ~41% at interval 12 (spectral augmented reflectance at 440 nm of 0.701 from a single sample).

From this data there appears to be a similar drop off trend in the blue between the 440 nm and 410 nm values. Once again the greatest drop off occurs for the lowest reflectance interval although not as large as between 440 and 860 nm. For interval 2 there is a ~20% drop off compared to the foam-free reflectance drop off of ~7%. At interval 4 a ~16% drop, interval 7 a ~13.5% drop and at intervals 10 and 12 a ~15 and 17% drop respectively. This increase in drop off in intervals 10 and 12 is possibly due to statistical lack of data.

While the very strong absorption properties of water may explain the lower reflectance values at 860 and 670 nm, the drop off at 410 nm, on the other hand, raises the question of whether the absorption properties of the water in the blue wavelengths are responsible for this effect. The absorption spectrum of pure sea water is low from about 550 nm down past 400 nm and becomes less absorbing with shorter wavelength. However, the presence of dissolved organic matter, yellow substance, detritus and phytoplankton, one or other of which is typically abundant in coastal waters, increases the

absorption qualities of the water body in the shorter wavelengths. (The spectral absorption coefficient of this water was 0.11, 0.10, 0.065, 0.08, 0.475 and 4.3 m^{-1} at the corresponding wavelengths (Roesler 1995)). In the case of absorption in the red wavelengths, it is the very strong absorption qualities of the water itself that cause the observed attenuation, and can easily outweigh the effects of any additional absorption due to particulates present in the water with the exception of high sediment amounts in turbid waters (Whitlock et al., 1982). Even so, the acute drop off at 410 nm cannot be fully explained by water absorption when considering the small absorption increase between 410 nm and 440 nm compared to the much greater absorption difference between 440 nm and 670 nm for similar values of augmented reflectance.

5. Conclusion

The whitecap system for determining the spectral reflectance of whitecaps in the open ocean has been described and calibrated for optimum use on board a ship or other over water surface platform. The calibration for different sky conditions and solar zenith angles, if not exactly represented by the real sky conditions at the time of acquisition, shows the degree of error that can be incurred without correction and indicates the degree of spectral variation that must be due to real effects in the field. In this paper we have also shown how the system works with an understanding of the possible errors that could have been incurred in going from laboratory calibration with a lamp source acting as a point source to outdoor 2π illumination under the solar spectrum.

The system has been designed to acquire spectral data of real whitecaps and their frequency rather than foam generated from the ship's bow. By taking many reflectance measurements of the water surface over time, a database of the spectral reflectance of different foam types and their frequency of occurrence can be assessed, providing estimates of fractional coverage and the augmented or extra spectral reflectance contribution of whitecaps and foam. Measurement of wind speed/direction and air/water temperature will provide additional information in correlating the augmented signal to these formation parameters.

Nevertheless, field testing the whitecap measurement system has provided interesting information on the spectral features of foam. Examples of foam reflectance, which can generally be related to different foam types and thicknesses, have been shown with interesting features that differ from the foam-free water spectral profile. The magnitude of these features are significantly greater than the error due to illumination condition and solid angle response deviation of the cosine collector, filter bandwidth mismatch or reflectance calibration of the system. Of particular interest is the drop off between the 440 nm and 860 nm values. These results are in good agreement with work reported by Frouin et al. (1996) taken in similar waters, although with lower 670 nm values (see Figs. 10 and 11) due to increased quantities of submerged bubbles generated by the ship. The greatest drop off is found for the thinnest foam layers (Fig. 11) where the majority of measurements in this reflectance interval are likely to be made of submerged bubbles. In the data acquired here, there is a greater proportion of submerged bubbles in the lower reflectance intervals due to the nature of the foam type generated by the relatively immense and hydrodynamical shape of the ship bow forcing large quantities of bubbles deep below the surface. As noted before, this drop off is considered to be due to the stronger absorption properties of water at longer wavelengths, effecting light that is reflected from submerged bubbles through a small layer of water between the bubbles and the surface. In the case of surf waves, the majority of measurements that fall within a similar reflectance interval may be from a larger proportion of thin surface foam, which produces an equivalent reflectance in the visible region to that of dense packs of submerged bubbles, but lacks the severity of the 670 and 860 nm attenuation found in ship bow foam.

The augmented reflectance for different foam types (Fig. 11) shows a distinct change in the spectra in going from the foam-free water reflectance to the thinnest foam measurement. It also shows an increasing trend in the 670 and 860 nm values with respect to the other wavebands as the foam becomes thicker and more highly reflecting. On the other hand, the reflectance of foam (Fig. 10), without the background foam-free water reflectance subtracted, shows that the water color becomes more prominent in measurement of the thinner and lower reflecting foam types. The foam-free water reflectance influences the thinner foam spectra due to the inevitable inclusion of foam-free reflectance contributions. Since the color of the foam is inextricably related to the color of the water, the use of a normalized foam

or whitecap spectrum at 440 nm to describe foam types in terms of percentage drop off may not be robust for every application. Even the use of normalized augmented reflectance, which appears to effectively remove the water color influence in these examples, can be limited when using smaller reflectance intervals to determine the thinnest foam from the foam-free water.

Acknowledgments. This research was funded by NASA / EOS -MODIS, Goddard Space Flight Center under contract NAS5-31363. We would like to thank Al Chapin for his help in the construction of the equipment, and Dr. Alan Weidemann and crew of the R/V McGaw for allowing us to participate in their oceanographic excursion.

REFERENCES

- Austin, R. W., and S. Moran, 1974: Reflectance of Whitecaps, Foam, and Spray. *Ocean Color Analysis*. Scripps Institution of Oceanography, San Diego. SIO Ref. 74-10.
- Bortkovskii, R. S., and V. A. Novak, 1993: Statistical dependencies of sea state characteristics on water temperature and wind-wave age. *J. of Marine Systems*, Vol. 4. 161-169.
- Frouin, R., M. Schwindling and P.Y. Deschamps, 1996: Spectral Reflectance of Sea Foam in the Visible and Near Infrared: In Situ Measurements and Remote Sensing Implications. *J. of Geophys. Res-Oceans*, Vol. 101, pp. 14361-14371
- Gordon, H. R., and M. M. Jacobs, 1977: Albedo of the Ocean-Atmosphere System: Influence of Sea Foam. *Applied Optics*, Vol. 16, pp. 2257-2260.
- Gordon, H. R., and M. Wang, Retrieval of water-leaving radiance and aerosol optical thickness over the oceans with SeaWiFS: A preliminary algorithm, *Applied Optics*, 33, 443-452, 1994a.
- Gordon, H. R., and M. Wang, Influence of oceanic whitecaps on atmospheric correction of SeaWiFS, *Applied Optics*, 33, 7754-7763, 1994b.
- Handbook of Optics, vol. 1, 42.89-90, McGraw Hill, Inc., 1995
- Koepke, P., 1984: Effective Reflectance of Oceanic Whitecaps. *Applied Optics*, Vol. 23, 1816-1824.
- Maul, G. A., and H. R. Gordon, 1975: On the Use of Earth Resources Technology Satellite (LANDSAT-1) in Optical Oceanography. *Remote Sensing Environment*, 4, 95.

Monahan, E. C., 1971: Oceanic whitecaps. *J. Physical Oceanogr.*, **1**, 139-144.

Moore, K.D., Voss, K.J., Gordon, H.R., 1997: Spectral reflectance of whitecaps: fractional coverage and the augmented spectral reflectance contribution to water leaving radiance. To be submitted *J. of Geophys. Res. - Oceans*, December 1996.

Payne, R. E., 1972: Albedo of the Sea Surface. *Journal of Atmospheric Physics*. Vol. **29**, pp. 959-970.

Ross, D.B., and V. J. Cardonne, 1974: Observations of oceanic whitecaps and their relation to remote measurements of surface wind speed. *J. Geophys. Res.*, Vol. **79**, pp. 444- 452.

Roesler, C., 1995: Personal communication.

Toba, Y., and M. Chaen, 1973: Quantitative expression of the breaking of wind waves on the sea surface. *Rec. Oceanogr. Works*, **12**, pp. 1-11.

Welton, J. E., 1996: Unpublished data. University of Miami, Physics Department.

Whitlock, C. H., D.S. Bartlett, and E.A. Gurganus, 1982: Sea Foam Reflectance and Influence on Optimum Wavelength for Remote Sensing of Ocean Aerosols. *Geophys. Res. Letters*, Vol. **9**, pp. 719-722.

	Channel 1 (410 nm)	Channel 2 (440 nm)	Channel 3 (510 nm)	Channel 4 (550 nm)	Channel 5 (670 nm)	Channel 6 (860 nm)
Overcast	1.0179	1.0566	1.0562	1.0420	1.0088	0.9195
Uniform	1.0243	1.0643	1.0629	1.0453	1.0088	0.9131
Sun 0	1.0063	1.0209	1.0210	1.0161	1.0038	0.9706
Sun 10	1.0034	1.0142	1.0141	1.0127	1.0085	0.9935
Sun 20	1.0069	1.0286	1.0272	1.0262	1.0135	0.9671
Sun 30	1.0061	1.0383	1.0398	1.0317	1.0093	0.9402
Sun 40	1.0014	1.0484	1.0484	1.0381	1.0035	0.9107
Sun 50	1.0046	1.0596	1.0621	1.0463	0.9996	0.8825
Sun 60	1.0163	1.0797	1.0829	1.0612	1.0061	0.8748
Sun 70	1.1061	1.1396	1.1407	1.0983	1.0493	0.8988
Sun 80	1.1140	1.1571	1.1443	1.0738	1.0207	0.8715

Table 1. Correction factors for each channel under different sky conditions due to the difference in solid angle response between deck cell and reflectance plaque.

Channel 1 (410 nm)	Channel 2 (440 nm)	Channel 3 (510 nm)	Channel 4 (550 nm)	Channel 5 (670 nm)	Channel 6 (860 nm)
1.0008	0.9278	0.9839	0.9648	0.9884	0.9640

Table 2. Correction factors for different filter bandwidths of the radiometer and deck cell in going from laboratory to outdoor illumination conditions.

Channel	Overcast - amount of correction (%)	Direct sun - amount of correction (%)	Accuracy of overcast correction (%)	Accuracy of direct sun correction (%)
410	1.8	0.7	0.51	0.25
440	2.0	3.8	0.05	0.6
510	3.8	2.3	0.63	0.37
550	0.5	0.5	0.09	0.95
670	0.29	0.24	0.17	0.37
860	12.77	saturated	0.005	saturated

Table 3. Effect of application of sky correction factor for each channel.

	Channel 1 (410 nm)	Channel 2 (440 nm)	Channel 3 (510 nm)	Channel 4 (550 nm)	Channel 5 (670 nm)	Channel 6 (860 nm)
Overcast	0.9529	0.9823	0.9809	0.9699	0.9373	0.8709
Uniform	0.9465	0.9773	0.9754	0.9624	0.9276	0.8563
Sun 0	0.9822	0.9939	0.9935	0.9894	0.9767	0.9512
Sun 10	0.9946	1.0007	1.0001	0.9988	0.9942	0.9866
Sun 20	0.9879	0.9999	0.9983	0.9959	0.9825	0.9557
Sun 30	0.9749	0.9940	0.9941	0.9874	0.9625	0.9125
Sun 40	0.9553	0.9893	0.9876	0.9791	0.9426	0.8699
Sun 50	0.9388	0.9814	0.9811	0.9694	0.9239	0.8339
Sun 60	0.9216	0.9705	0.9709	0.9539	0.9031	0.8042
Sun 70	0.9135	0.9545	0.9500	0.9246	0.8819	0.7749
Sun 80	0.8475	0.8906	0.8763	0.8382	0.7964	0.7072

Table 4. Correction factors for each channel under different sky conditions due to deviation of solid angle response of the deck cell.

Figure Captions:

Fig. 1. A schematic of the whitecap radiometer and its components.

Fig. 2(a). Angular response of the deck cell and reflectance plaque for the 410 nm channel. Ideal cosine collector response is shown for reference.

Fig. 2(b). Angular response of the deck cell and reflectance plaque in terms of deviation from true cosine response for 410, 440, 510, 550, 670 and 860 nm channels. Each interval is 50%, and each waveband is offset by 50% for separation.

Fig. 3(a). Solid angle response of deck cell and reflectance plaque for the 410 nm channel. Ideal cosine collector solid angle response is shown for reference.

Fig. 3(b). Solid angle response of the deck cell and reflectance plaque in terms of deviation from true cosine solid angle response for 410, 440, 510, 550, 670 and 860 nm channels.

Fig. 4. Normalized radiometer and deck cell bandpass profiles with lamp and solar spectra.

Fig. 5. Field test of system ability to measure a plaque reflectance, as described in text. Note that the 860 nm channel of the whitecap radiometer saturates when the plaque is illuminated by direct sun. Each interval represents a reflectance difference of 20%, and each waveband is offset by 20% to enable display.

Fig. 6. Time series of foam data generated by bow of ship. The lower trace is for 860 nm. The rest (upper trace) are for other channels.

Fig. 7. Spectral reflectance of different foam types.

Fig. 8. Longer time series of foam data generated by ship showing periods when ship slowed and came to rest.

Fig. 9. Spectral reflectance of different foam types from larger time series. I2, I4, I7, I10 and I12 refer to reflectance intervals normalized at 440 nm in Fig. 10.

Fig. 10. Normalized spectral reflectance at 440 nm for different foam types taken from data used in Figs. 8 and 9. Note the spectral influence of the background water in measurement of the thinnest foam types in interval 2.

Fig. 11. Normalized augmented spectral reflectance at 440 nm for different foam types (used in Fig. 10). Note the spectral similarity for all foam types, and the increasing 670 nm and 860 nm values with respect to 440 nm for increasing reflectance interval from thicker fluffier foam types.

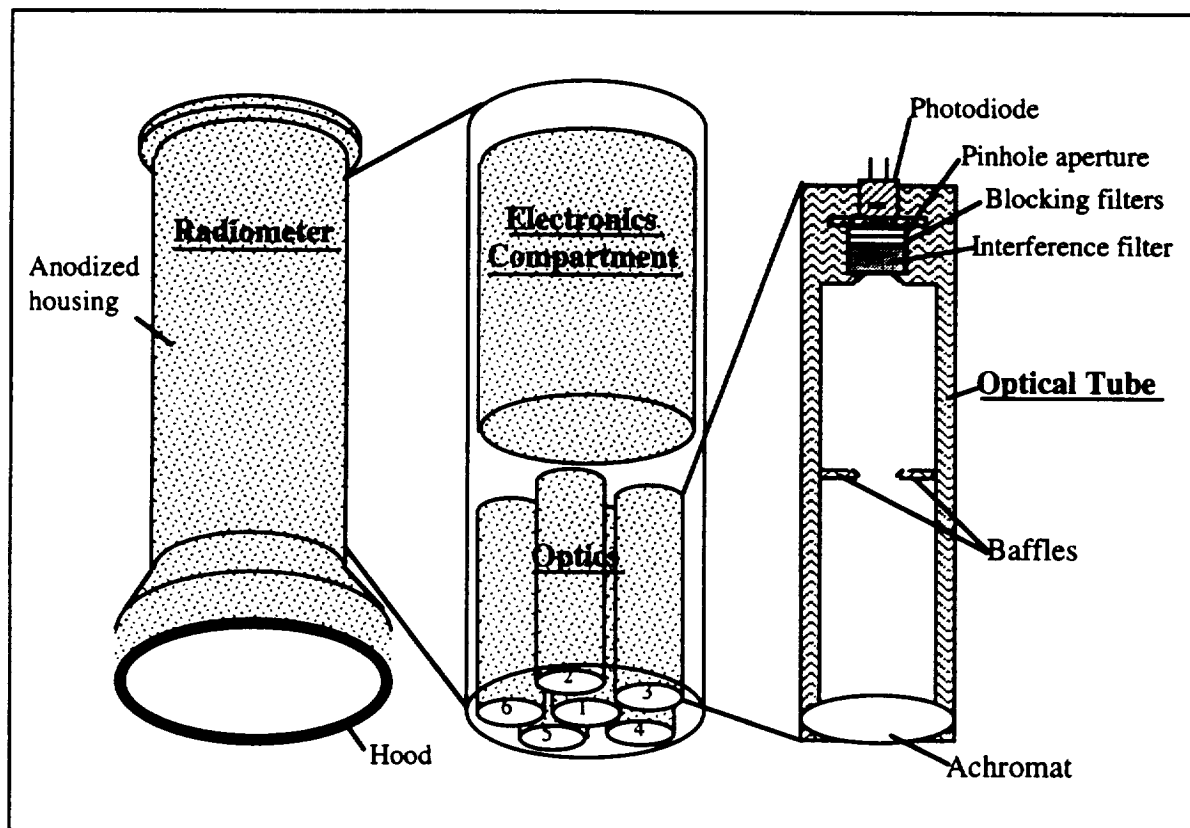


Fig. 1.

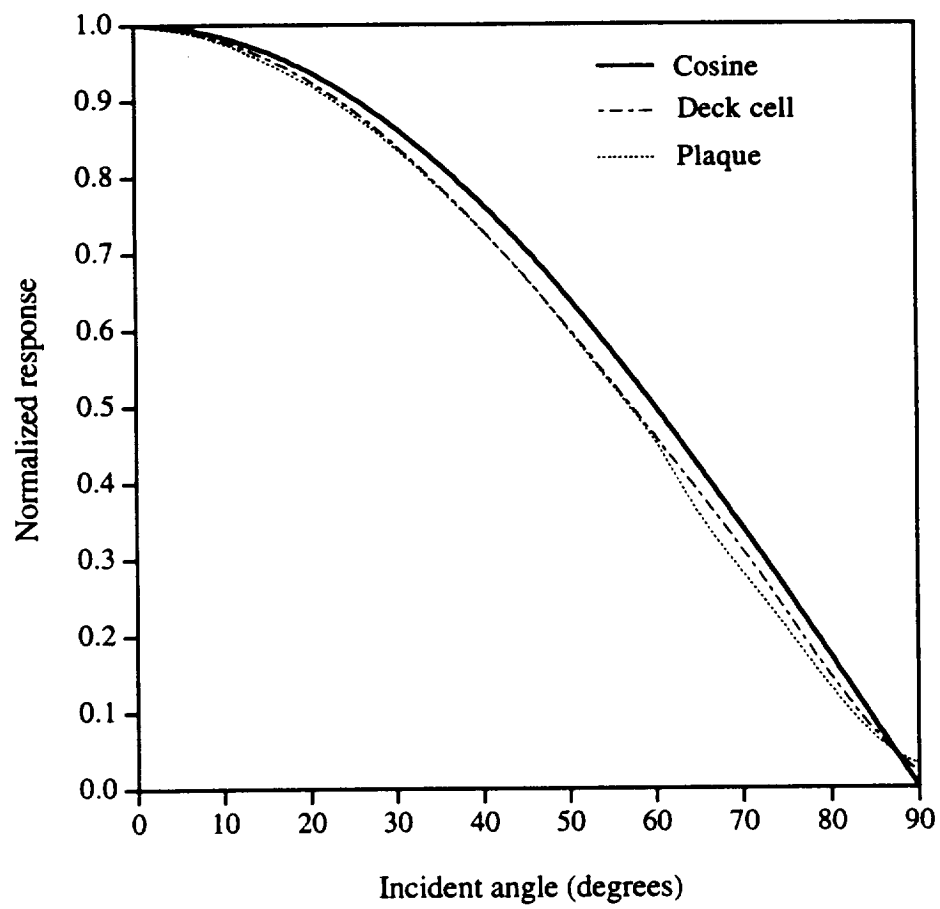


Fig. 2(a)

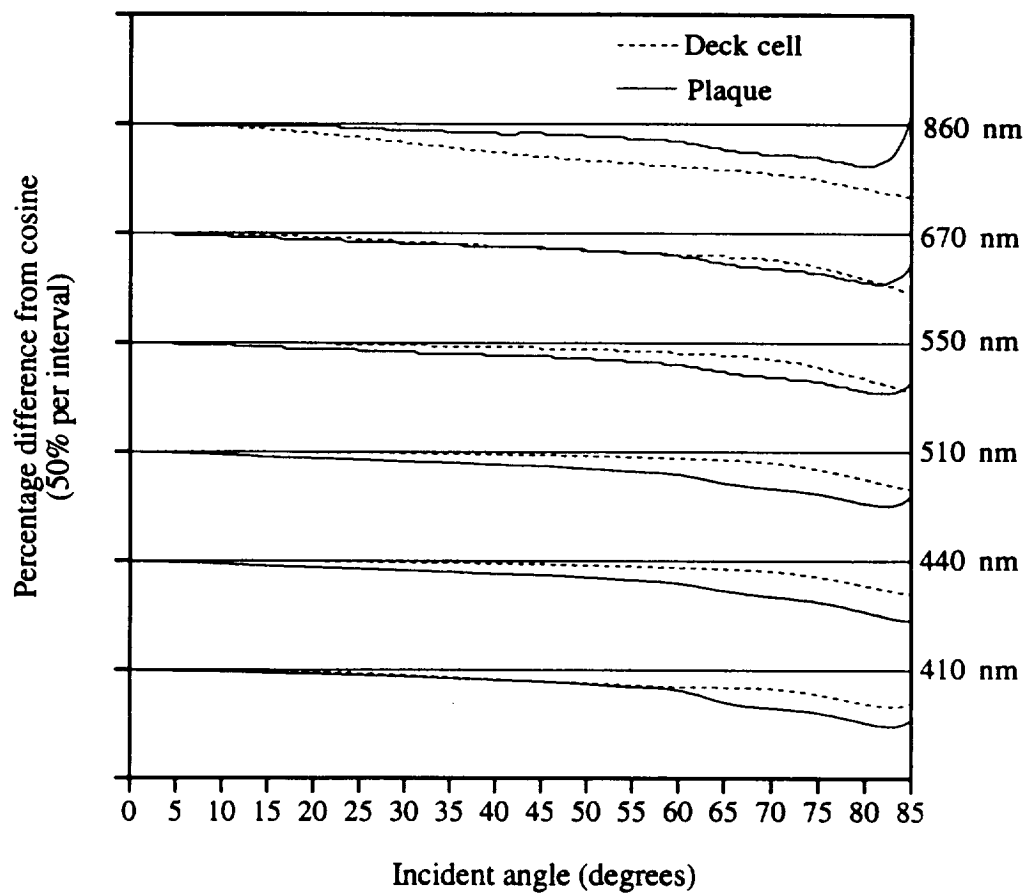


Fig. 2(b)

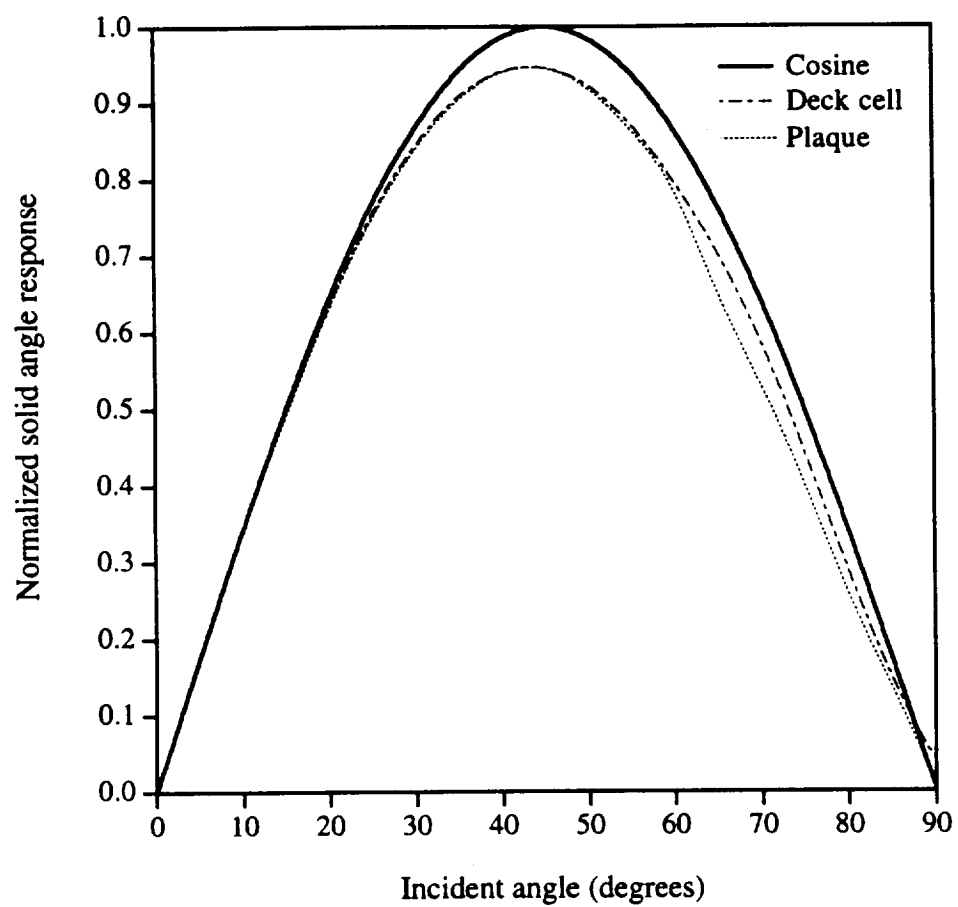


Fig. 3.

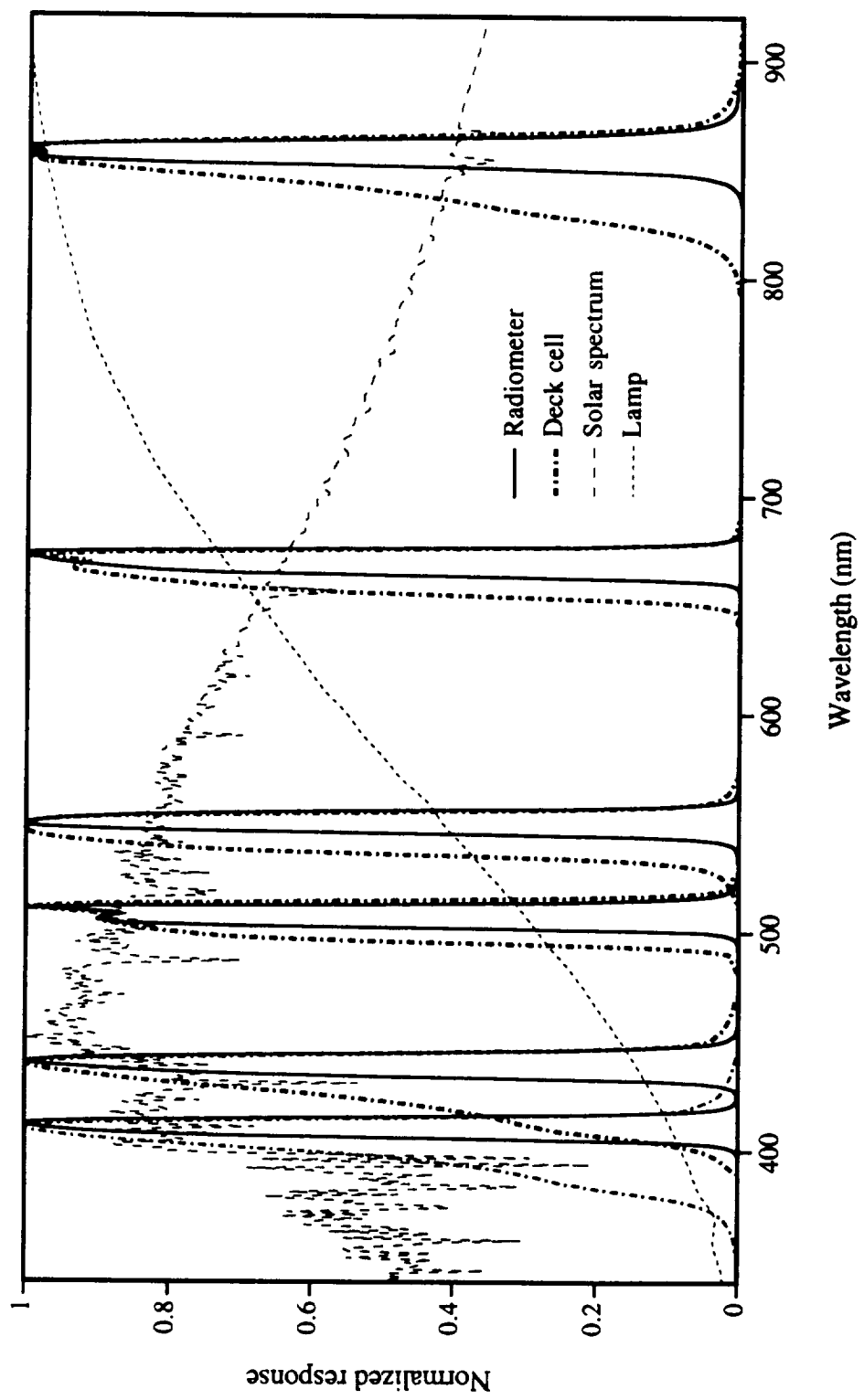


Fig. 4.

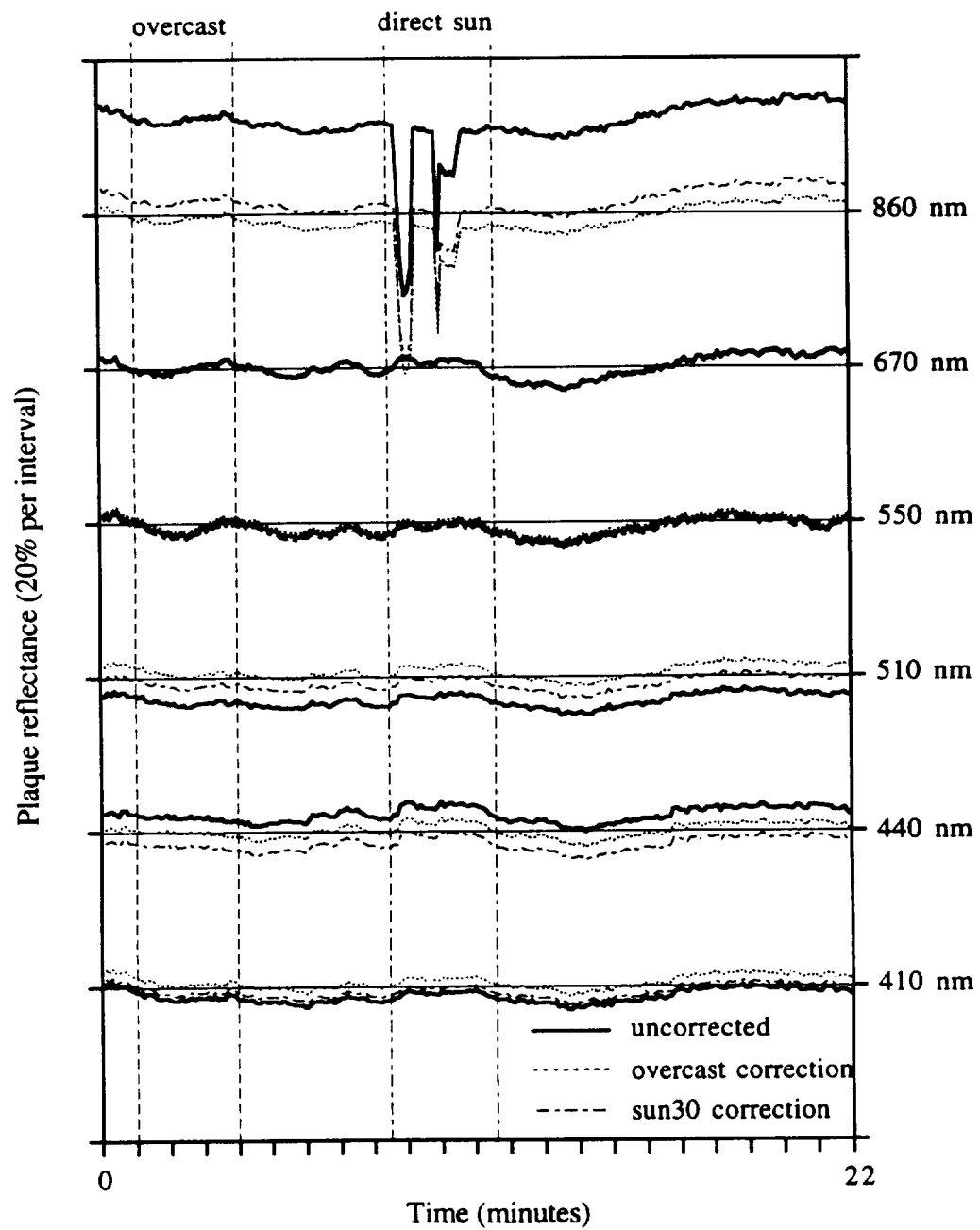


Fig. 5.

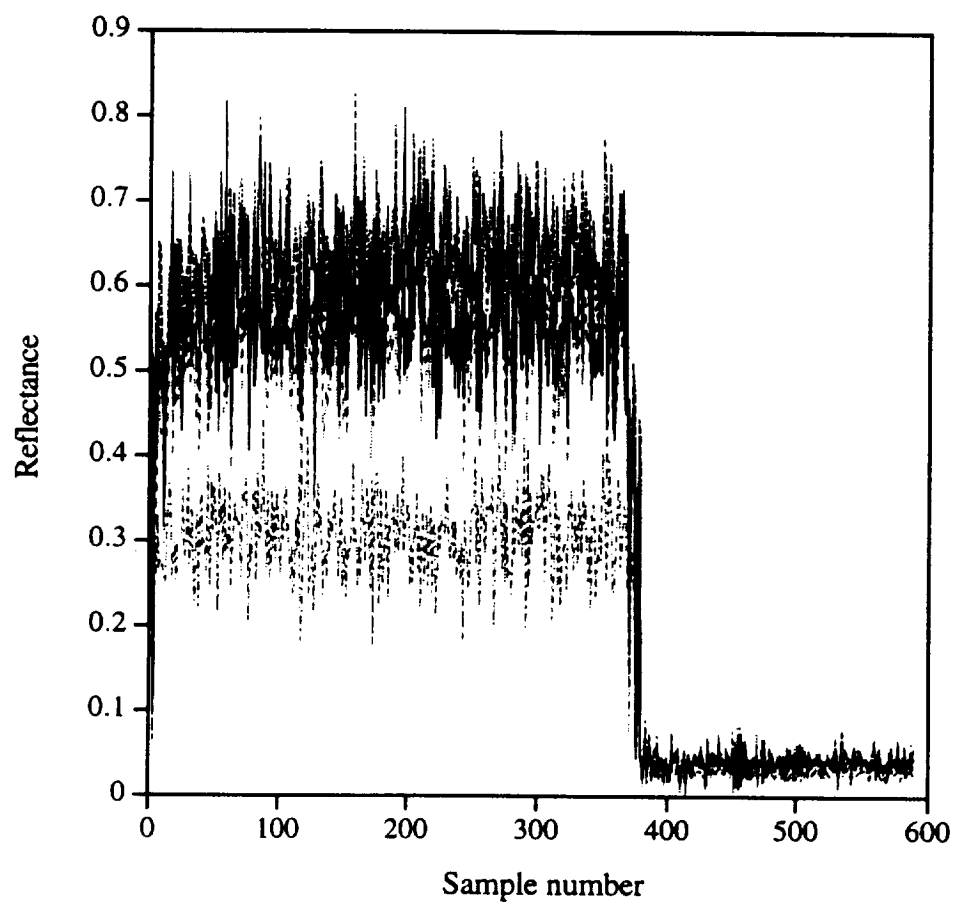


Fig.6.

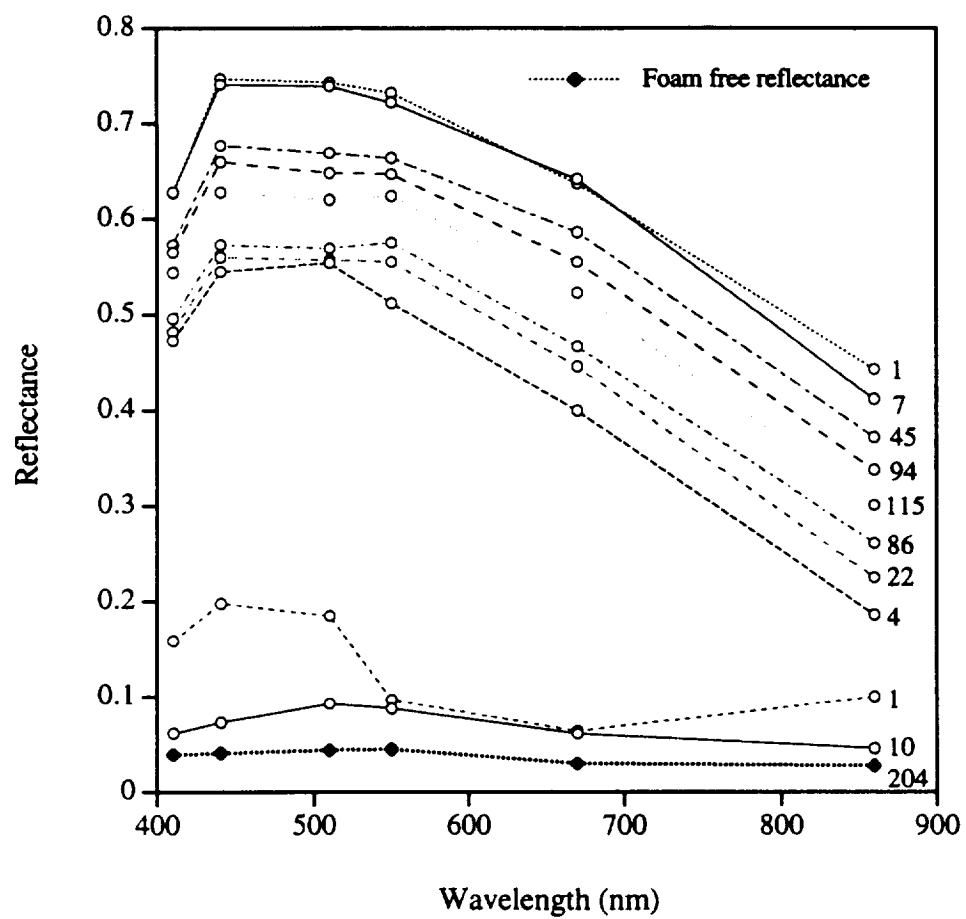


Fig.7.

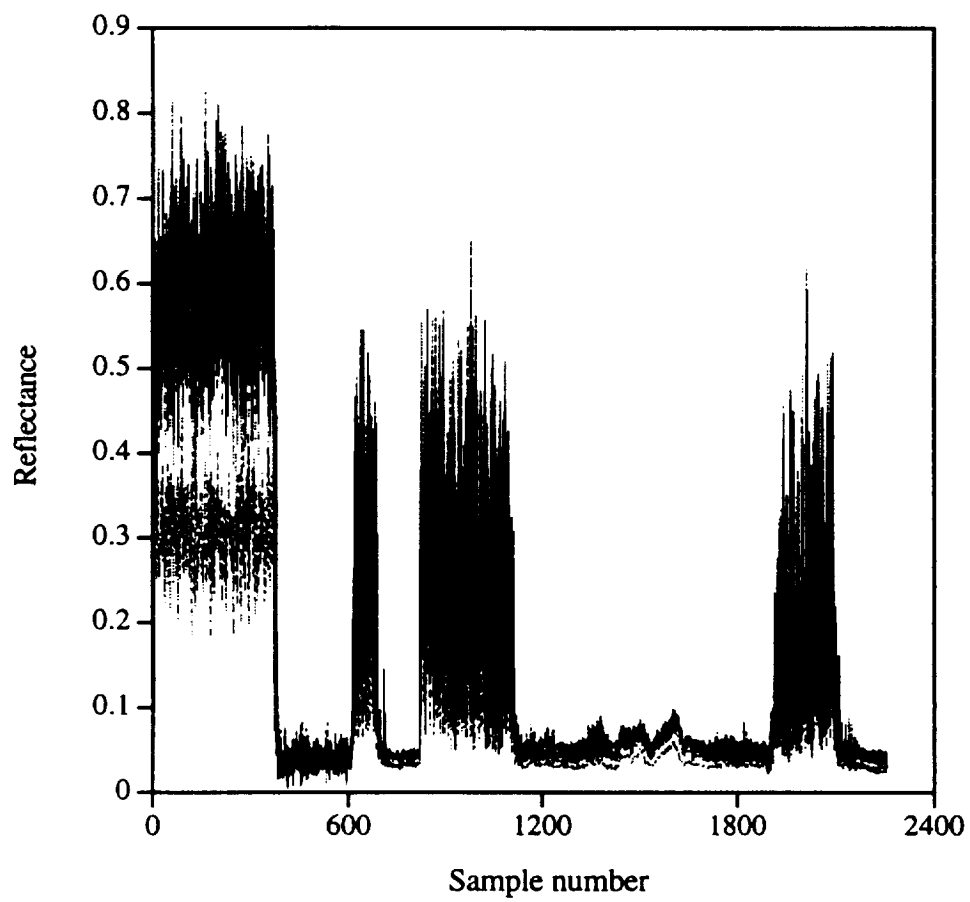


Fig. 8.

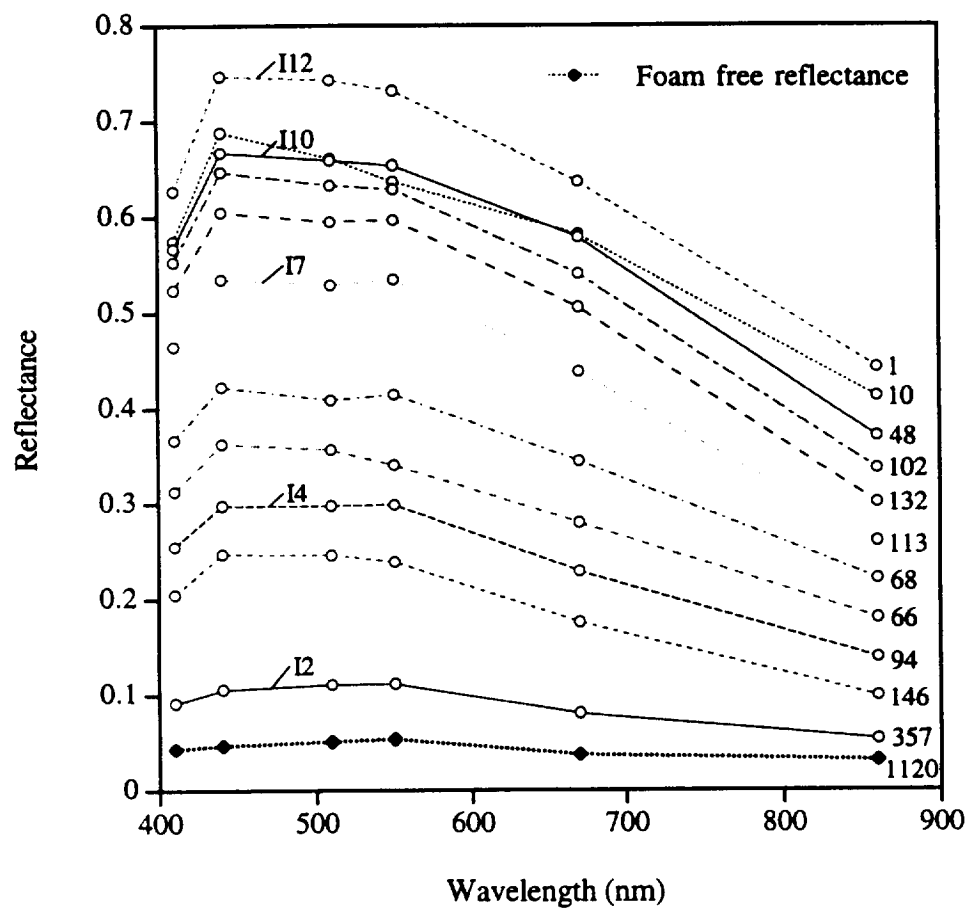


Fig. 9.

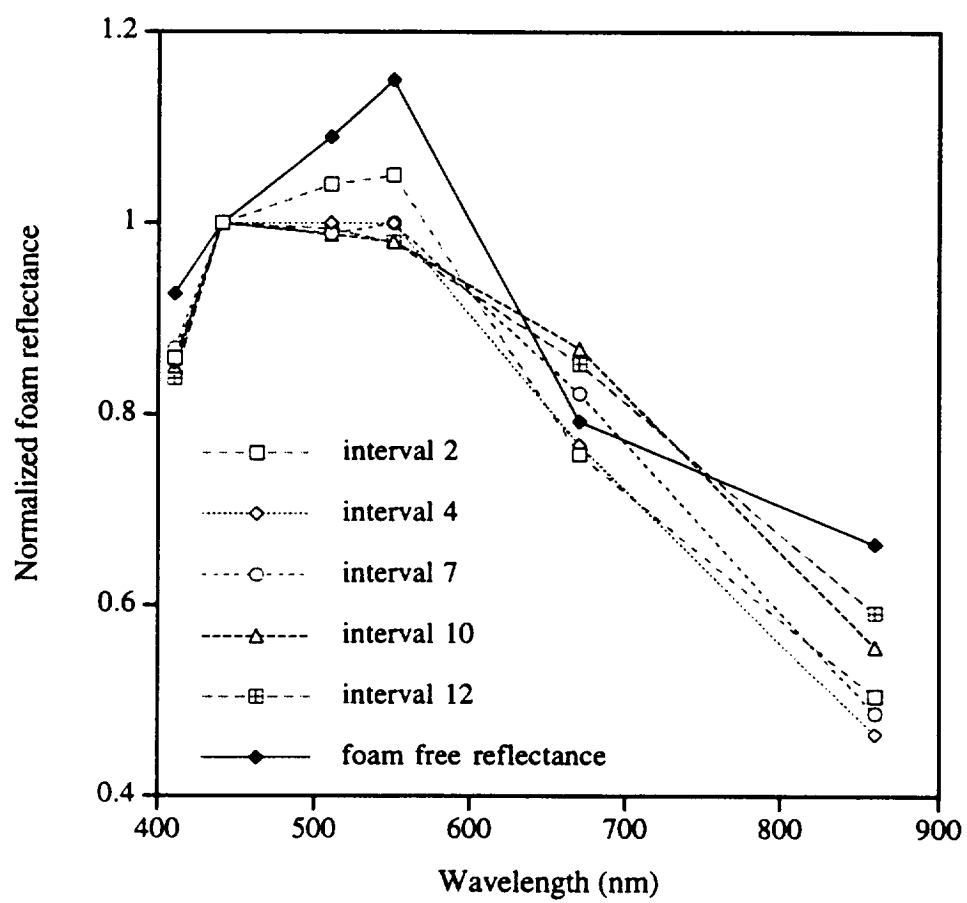


Fig. 10.

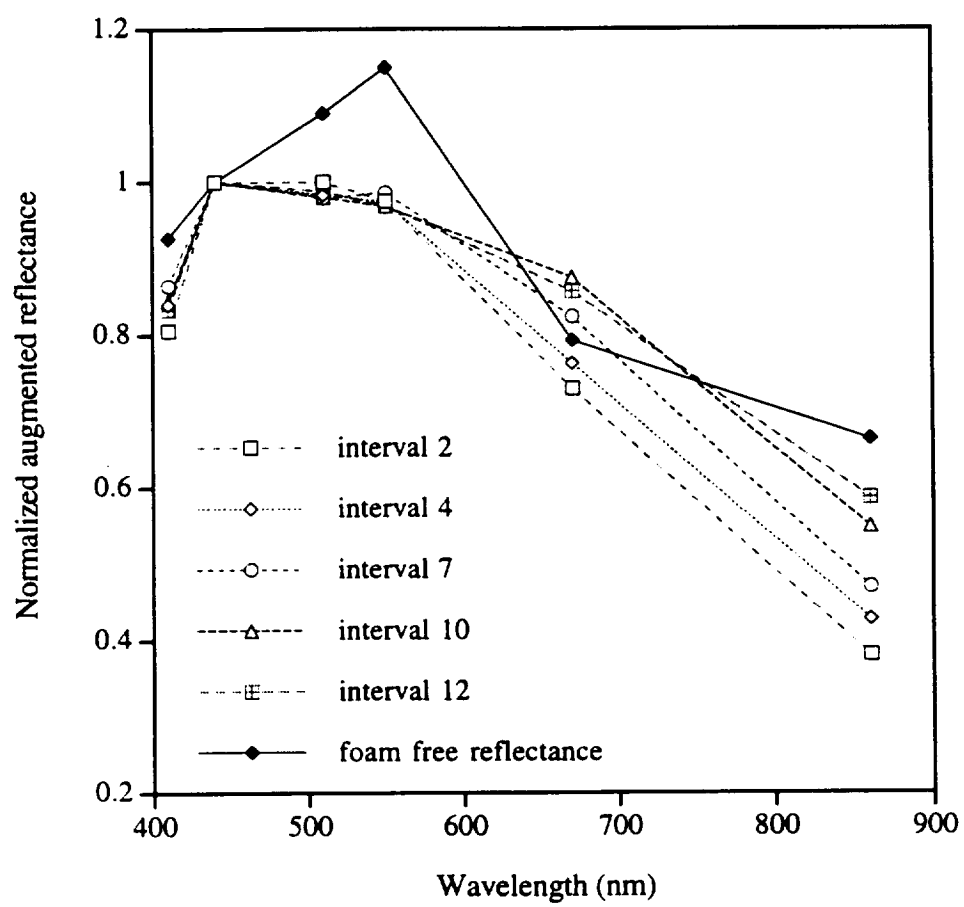


Fig. 11.

Appendix 4

Spectral Reflectance of Whitecaps: Fractional Coverage and the Augmented Spectral Reflectance Contribution to Water-Leaving Radiance

Karl D. Moore, Kenneth J. Voss, Howard R. Gordon

Physics Dept., University of Miami

Coral Gables, FL 33124

Submitted to *Journal of Geophysical Research*

Abstract. A radiometric system, deployed from a ship, is used to directly measure the optical influence of whitecaps. Estimates of the augmented reflectance contribution and fractional coverage are determined from measurements in the Gulf of Mexico and open ocean waters of the Pacific. The accuracy of these estimates are dependent on the ability to radiometrically determine the difference between white water and nonwhite water events. Subtle spectral variations in the visible are found in the augmented reflectance but are typically smaller than the error in determining the white water threshold. Sky reflectance, sky condition, specular sun glitter, wave height and wind direction can influence the spectral characteristics of the augmented reflectance particularly at low sun angles. Evidence is presented suggesting that whitecaps cannot be modeled as lambertian reflectors, particularly at low solar elevations. The augmented spectral reflectance of whitecaps measured in the open ocean is found to be 0.00031 at a wind speed of 8 m/s, 0.00058 at 10 m/s, and 0.00096 at 12 m/s for wavebands in the visible and 15% - 25% less at 860 nm.

Introduction

Due to the relatively small water-leaving radiance signal from the ocean in comparison to the total light arriving at an ocean color sensor, the quality of data depends primarily on the accuracy of atmospheric correction algorithms. Atmospheric correction over the ocean is determined by measurement of the upwelling signal arriving at the satellite at a waveband where the radiance back scattered out of the ocean is known to contribute very little or no signal [*Gordon and Wang, 1994a*]. Utilization of near infrared wavebands beyond 760 nm (and even 670 nm) can be justified in the absence of whitecaps (in case I waters) due to the strong absorption properties of liquid water at those wavelengths. In the case of an agitated sea state the presence of whitecaps occurring within a satellite image pixel augments the radiometric signal by an amount dependent on the whitecap coverage and the reflectance of whitecap foam [*Gordon and Wang, 1994b*]. This is referred to as the augmented reflectance of whitecaps. Previous researchers have used a whitecap foam reflectance of 50% - 100% [*Payne, 1972; Maul and Gordon, 1975; Gordon and Jacobs,*

1977] and have assumed it to be constant at all wavelengths. Laboratory measurements carried out by *Whitlock et al.* [1982] yield a value of ~55% in the visible part of the spectrum for dense foam in clear water and have shown that it diminishes with increasing wavelength beyond ~0.8 μm , with 5% decrease at 0.85 μm , 10% at 1.02 μm , and 50% at 1.65 μm . *Koepke* [1984] determined the effective reflectance of whitecaps, which takes into consideration the decrease in reflectance and increase in area of an individual whitecap as it ages, to be 22% in the visible. This wavelength independent estimate of the effective reflectance is then combined with the relative area covered with whitecaps as a function of wind speed [*Monahan and O'Muircheartaigh*, 1980] in order to obtain the total optical influence of whitecaps for different wind speeds. *Koepke* found that it was necessary to introduce this value of effective reflectance since the simple combination of fractional coverage with the foam reflectance values of *Whitlock*, valid for dense fresh foam (~55%), gave too high a value for the optical influence of the total whitecap.

Field measurements taken of the reflectance of foam generated by breaking waves in the surf zone [*Frouin et al.*, 1996] indicate a larger spectral variation in reflectance than reported by *Whitlock*. *Frouin* found the reflectance decreased by 40% at 0.87 μm , 50% at 1.02 μm , and 95% at 1.65 μm relative to the reflectance at 440 nm. The greater spectral variation in reflectance found in field data, unlike the laboratory foam of *Whitlock*, is thought to be due to the strong absorption properties of water at longer wavelength acting on light reflected from submerged bubbles forced into the water column by the breaking waves.

In addition to the spectral differences between foam measured in the laboratory and in the field, estimates of whitecap fractional coverage for different wind speeds are found to be quite noisy [*Blanchard*, 1971; *Monahan*, 1971; *Ross and Cardone*, 1974; *Wu*, 1979; *Toba and Chaen*, 1973; *Monahan and O'Muircheartaigh*, 1980, 1986]. Fractional coverage (W) has been typically related to wind speed (U) with the form $W = \alpha U^\beta$. The values of α and β vary with geographic location, air and sea temperature as well as wind speed range. These relationships remain noisy, despite attempts to fine tune particular data sets, due to the dynamic nature and interdependence of the many parameters involved in whitecap formation. Whitecap coverage is primarily dependent

on wind speed, but also on other factors such as fetch and duration [Cardone, 1969], water temperature [Miyake and Abe, 1948], air temperature, stability of the lower atmosphere defined by the air/water temperature differential [Monahan and O'Muircheartaigh, 1986], salinity [Monahan and Zietlow, 1969] and even surface tension variations due to the presence of organic films [Garrett, 1967]. A slightly different approach by Wu [1988] relates whitecap coverage to wind-friction velocity, being proportional to the square root of the wind stress which depends strongly on atmospheric stability conditions. Bortkovskii and Novak [1993] assessed whitecap and foam coverage with particular dependence on the sea surface temperature which effects sea water viscosity and wind friction.

In addition, defining a threshold between white water and nonwhite water events is a difficult process and usually depends on a subjective interpretation. Further complexities can arise, such as the increase in foam streak-to-whitecap ratio with wind speed above 9 m/s [Ross and Cardone, 1974]. As the foam streak approximates a single bubble layer with a low reflectance contribution that is close the threshold, a greater error can be induced in the estimate of the augmented reflectance contribution at higher wind speeds.

To date, the optical influence of whitecaps on the upwelling water-leaving radiance has been estimated by utilizing and combining the work of different researchers as described above. In this paper, a measurement system deployed from a ship is used to directly determine the augmented spectral reflectance and fractional coverage of whitecaps in the field. Our measurement system provides spectral reflectance data from individual whitecaps - as they grow and decay - and, by integrating over longer periods of time, estimates of the fractional coverage and augmented reflectance contribution to the water-leaving radiance can be determined. The principal reason we undertook the present investigation was to see if the Frouin *et al.* [1996] spectral measurements in the surf zone were applicable to real oceanic whitecaps. A secondary motivation was to validate the whitecap reflectance versus wind speed relationship proposed by Koepke [1984] [Gordon and Wang 1994b].

Instrument System

The whitecap reflectance measurement system is described in detail elsewhere [Moore *et al.*, 1997]. The system consists of a 6-channel radiometer with narrow field of view and nominal 10 nm bandpasses at 410, 440, 510, 550, 670 and 860 nm. It is held over the water surface by means of a boom extended from the bow of a ship providing an unobstructed view of the water surface. At the same time a cosine collector with matching wavebands measures downwelling irradiance so that the reflectance of the water surface can be calculated. A TV camera is mounted by the radiometer to provide a visual reference, and whenever the radiometric data is acquired the associated video frame is time and date marked and recorded onto video tape to assist in later analysis. Air and water temperature, wind speed and direction are measured simultaneously with the radiometric data at a rate of ~7 times a second continuously for about 30 seconds (providing 200 contiguous samples), after which global positioning (GPS) data, universal time, and location are recorded. This acquisition sequence is repeated until a time determined by the operator. This radiometric rate allows many sample points of an individual whitecap to be captured as well as providing an adequate data set over a time period of reasonably consistent sea state and sky conditions.

Once the system has been installed on a ship, only periodic measurements of the dark current are required. This requires bringing the radiometer in from the boom and covering both the radiometer and the deck cell with light tight caps. This is necessary only when significant temperature changes are encountered such as when conditions change from early morning to noon, or from dark, overcast, rainy conditions to bright sunshine. The radiometer can also be angled up to 20° from nadir in order to minimize the effects of specular sun glitter and bright sky reflections.

Data Description

Data from two different cruises are presented in this paper. The data acquired from the first cruise is used to introduce the data reduction process, consider the difficulties in radiometrically defining white water events and to investigate the effects that low solar elevation, wind direction,

specular sun reflection and sky conditions have on the estimate of fractional coverage and on the augmented spectral reflectance contribution. In the second cruise, data was acquired in the open ocean and is used to provide practical measurements of the augmented reflectance contribution needed for ocean color and atmospheric correction algorithms.

For the first cruise, the whitecap radiometer system was deployed in the spring of 1996 on the NOAA ship, R/V Malcolm Baldrige for a 21-day ship cruise from Miami to a test location in the Gulf of Mexico, approximately 70 miles offshore from Cedar Key (Florida) in the Apalachicola Bay. The location provided relatively warm waters ($\sim 16 - 17^{\circ}\text{C}$) with a number of cold fronts moving down off the continental mainland, resulting in variable conditions. These fronts usually lasted a couple of days bringing strong winds (sometimes as high as 18 m/s) and lowering the air temperature to about 12°C . The occurrence of an unstable atmosphere and good winds provided an interesting whitecap data set.

The second cruise involved a $\sim 6,000$ km transit through equatorial waters of the Pacific Ocean from Manzanillo, Mexico to Honolulu, Hawaii. This 13-day cruise took place in November 1996 aboard the NOAA ship R/V Ka'imimoana. Conditions were more consistent with air/water temperature and wind speed/direction changing only by a relatively small amount over time. Fetch was typically greater than 1000 km and duration could be considered unlimited. Data was acquired far from land and for the most part, water temperature was $\sim 22-23^{\circ}\text{C}$ with air temperature $\sim 20-23^{\circ}\text{C}$. Wind speeds ranged from ~ 8 m/s to ~ 13 m/s and wind direction changed from an initial northerly direction at the beginning of the transect to an easterly and southerly direction as the Trade winds were crossed. The sky conditions were mainly broken and scattered with some overcast periods.

The data used in the following section was acquired during one particular cold front passage during the first cruise in the Gulf of Mexico. The front approached in the morning with a completely overcast sky. Wind speed was initially ~ 6 m/s from the south east but at about 10:40 am the wind changed direction to the north northwest with wind speed increasing to about 15 m/s (gusting to 18 m/s) within 15 minutes. The water surface which had been relatively 'flat' with a

wave height of about 1-2 ft (30 - 60 cm) became ruffled with many small whitecaps appearing. As the day progressed the whitecaps became larger but fewer in number as the wave height increased and a swell began to develop. Although there were lull periods, the winds picked up again during the night blowing between 10 to 15 m/s and changing direction to the east as the front passed. By the next day, the wave height had increased to 2 m with a swell frequency of 7-8 seconds. The sky was clear and the ship adopted a rocking motion with the sea swell. Examples of data taken from both days with similar wind speeds but differing sea states, sky conditions, air temperatures, duration, etc. are presented in the next section.

Data Reduction

Phase I Reduction Process

One half hour of data collected at the rate described above amounts to about a 1.5 megabytes of data storage. To reduce this data, analysis software using Matlab was developed to partition and separate the data matrix into radiometric data, environmental parameters (wind speed/direction, air/water temperature) and GPS data. The radiometric data is then reduced to produce dark background-subtracted and radiometrically-corrected reflectance values from the six up- and downwelling channels. This radiometric correction process consists of three steps [Moore *et al.*, 1997] briefly reviewed here.

First, ratios of upwelling radiance to downwelling irradiance are formed from the dark subtracted signals for each channel. These six ratios are then multiplied by a calibration factor determined in the laboratory relating the channels in the radiometer to those in the deck cell in order to yield reflectance measurements. This was established using a calibrated 1000W (FEL) quartz halogen lamp source and a calibrated Spectralon reflectance plaque. The deck cell was positioned 50 cm in front of the source and measurements taken. For the radiometer, the reflectance plaque replaced the deck cell, and the radiometer viewed the plaque from a 45° angle.

For the second step, a multiplication factor is required to correct bandpass differences between the radiometer and deck cell and for differences in the light spectrum between laboratory and outdoor illumination conditions.

Thirdly, each channel of the deck cell must be corrected for solid angle response for operation outdoors under 2π illumination due to the slight deviation in angular response of the deck cell cosine collector from true cosine. Correction factors for different angular distributions of the downwelling light field are required for various sky conditions that may be encountered. A set of correction factors were established for different sky conditions such as overcast, or clear sky with different solar zenith angles, to correct solid angle response.

After applying these corrections, the corrected data are presented as a time series in blocks of 200 water surface reflectance measurements along with wind speed/direction, air/water temperature, upwelling radiance and downwelling irradiance data. The reflectance data are then grouped into reflectance intervals; any reflectance spectra whose average value falls within a predetermined reflectance interval is binned. In analysis of foam data obtained with the system in earlier work [Moore *et al.*, 1997], the value of the reflectance at 860 nm was used as the binning parameter rather than the mean spectral value used here. However, in estimating the fractional coverage and augmented spectral reflectance, it was found that it makes no difference which parameter is used.

For analysis of the data from the first cruise, the reflectances are divided into 48 intervals, with high resolution reflectance intervals of 0.0025 reserved for reflectance values between 0.005 and 0.1. (First interval is 0.0 to 0.005). Above this, the reflectance intervals are incremented by 0.1 and continue up to 1.0. As will be seen later, the high resolution intervals used for the lower reflectance values below 0.1 have been implemented in an attempt to accurately determine and discriminate between white water and nonwhite water events. Reflectance intervals above 0.1 were primarily used to analyze the spectral characteristics of different foam types which may be defined by their reflectance magnitude.

In the work by *Frouin et al.* [1996] in making spectral measurements of foam in the surf zone, reflectance intervals were also used in an attempt to determine spectral variations with foam type and thickness. The total reflectance was partitioned into 4 intervals (0 - 0.25, 0.25 - 0.4, 0.4 - 0.55, and any reflectance greater than 0.55). *Koepke* [1984] on the other hand required a threshold between nonwhite water and white water in analysis of photographic images to determine fractional coverage and the effective reflectance, which considers the drop in reflectance and increase in area as a whitecap decays. To accomplish this, the white water threshold was set at 0.1 with the maximum reflectance in a particular photograph normalized to 1. These images were acquired using a 6 cm x 6 cm Hasselbad camera angled between 45° and 60° degrees in viewing the surface from a height of 30 m. This threshold was further complicated by the increased white threshold towards the horizon due to increased Fresnel sky reflection. With the whitecap radiometer used in this paper, the effect of sky reflection variation with viewing angle is drastically reduced due to the small field of view of the radiometer optics (1°), and with 0.0025 reflectance resolution more accurate threshold information can be obtained.

After the reflectance data from each block has been grouped into reflectance intervals, these reflectance intervals are added to previous blocks of similarly reduced reflectance data, resulting in a set of reflectance intervals for the complete data matrix. UTC time is extracted and displayed at the beginning of each block so that reflectance measurements can be correlated with water surface events replayed on the VCR. The VCR (Sony EV-C100 (video Hi8)) can be advanced frame by frame in either direction with the time/date mark appearing on the bottom of the monitor approximately every third frame. In this way, individual samples from whitecaps and their different foam types can be radiometrically tracked.

Once all the data from a particular acquisition period has been reduced to this level, the spectral reflectance values and the number of samples binned in each interval are stored along with the total number of samples taken, mean air/water temperature, wind speed/direction readings and GPS data from each block (200 samples) of the original data matrix.

Phase I Examples

In Fig. 1(a) an example of a time series with two whitecaps passing under the radiometer is shown. These whitecaps were acquired during the onset of the cold front described above. The sky was overcast and the data were taken ~11:00 am. Wind speed was ~12 m/s, air temperature 16.2°C and water temperature 17°C. The 96 samples (from a block of 200) shown in Fig. 1(a) were acquired over a period of ~15 seconds. In this example, a large whitecap suddenly breaks into view of the radiometer with thick white foam (sample point 11) reaching a peak reflectance of ~55%. Six traces are plotted representing the six radiometer channels (410, 440, 510, 550, 670 and 860 nm). The lower trace (symbols) corresponds to the 860 nm reflectance. Thick foam is temporarily replaced by a region of submerged bubbles and thinner surface foam (~sample points 13, 14, 15). Thick foam comes into view again at sample point 17. At sample point 20 and 21 a thin layer of foam passes followed by some dense (not thick) older foam and stays in field of view to about sample point 35. Sample points from about 35 - 56 show the reflectance of thinning residual and fragmented surface foam. From 60 to about 75 the reflectance of the foam free water surface is shown and is suddenly followed by another whitecap of smaller magnitude (sample point 76) which continues to decay out to about sample point 96.

In Fig. 1(b) the individual reflectance samples from this sample period have been binned into reflectance intervals. The lower reflectance intervals correspond to the nonwhite water reflectance; some are higher due to Fresnel reflectance from brighter regions of the sky, others are lower due to shadowing by adjacent waves. The variation in the spectral profiles of each interval is partly due to the small number of samples used. However, a common feature that stands out is the lower 860 nm reflectance. This is attributed to reflectance from submerged bubbles modified by the strong absorption of water at 860 nm [Frouin *et al.*, 1996; Moore *et al.*, 1997]. (Other examples of phase I data reduction into reflectance levels are shown in Figs. 2(b), 3(b) and 4(b) where larger data sets of about 10,000 samples are used).

Phase II Reduction Process

In phase II, the reduced data from phase I are processed to determine fractional coverage and the augmented spectral reflectance contribution. Correlations between these estimates and the environmental conditions responsible for whitecap development can then be investigated.

Each reflectance interval, resulting from the reduction of a complete data matrix, is multiplied by the fraction of reflectance samples that have contributed to that reflectance interval. This weighted reflectance spectrum is the effective spectral reflectance contribution of that reflectance interval (i.e. the contribution of that interval to the total reflectance). Repeating this for all reflectance intervals and summing their effective reflectances together yields the total spectral reflectance. This is equivalent to the reflectance observed in a satellite image pixel mapped onto the ocean surface.

The total reflectance contains both white water and nonwhite water contributions. In order to determine only the contribution of whitecaps and foam, the background water-leaving radiance, sky reflectance, sun glitter and other nonwhite water contributions must be removed. The background water color (and sky reflection etc.) has the greatest number of samples being the most frequently measured and since the presence of foam on the surface of the water increases the overall reflectance signal, the optimal threshold must be at some reflectance interval above it. However, reflectance intervals above the reflectance interval with the most number of samples may contain both thin foam reflectance as well as sky reflectance contributions from brighter regions of the sky. Also, reflectance intervals below this may contain thin foam reflectance contributions that are in the shadow of an adjacent wave and may register as having a lower reflectance than a sky reflectance contribution from an unshadowed foam free water facet. This is true for threshold intervals near the reflectance interval with the most number of samples. This inability to distinguish between white water and nonwhite water events places a limit on the accuracy with which fractional coverage and augmented spectral reflectance contribution can be determined.

The estimate of fractional coverage and the augmented reflectance contribution is dependent on choosing a reasonable reflectance threshold. Once an appropriate threshold has been chosen, it

is subtracted from each interval above it. This difference in reflectance is assumed to be due to white water contributions only. The reflectance difference is then multiplied by the fraction of samples that have fallen into that reflectance interval to yield the effective augmented spectral reflectance of that particular reflectance interval. All the weighted reflectance intervals above the threshold are summed to yield the (total) augmented spectral reflectance contribution. Fractional coverage is estimated from the total number of white water samples divided by the total number of samples and, notably, is not weighted by the magnitude of reflectance.

In the following examples, a range of plausible thresholds are implemented to demonstrate the effects on the estimate of both fractional coverage and the augmented spectral reflectance contribution from data acquired with similar wind speeds but under different sky conditions, solar zenith angles, and sea states.

Phase II examples

Overcast Sky

Data presented in Figs. 2(a) - 2(d) were the result of 9,000 surface reflectance measurements acquired over a period of ~23 minutes as the ship covered a 4 kilometer path during the onset of the cold front described above. Mean location was 29.05°N and 83.51°W. During acquisition the mean wind speed was 11.86 m/s with a standard deviation of 3.6 m/s (gusts up to 18 m/s). The wind was from the north between 350° and 0°. Ship heading was originally ~170° during the first half of the acquisition period and then passed through a southerly direction and settled on a north westerly direction of 330°. The radiometer was nadir viewing and since conditions were overcast there was no specular sun glitter. Air temperature was 16.2°C and water temperature 17.0°C, resulting in a slightly unstable atmosphere. Other parameters taken from the ship's log were salinity (35.027 ppt), barometric pressure (1015.4 mB), and relative humidity (93%). In this example, during the onset of the cold front, many small whitecaps suddenly appeared on the relatively flat and dark water surface. Duration was limited to ~15 minutes with whitecap development and sea state measured during an abrupt transition period in weather conditions. The

resulting measurements produced high values of the augmented reflectance and fractional coverage estimates.

In Figs. 2(a) - 2(d) the more interesting portions of the output of data processed in phase II are presented. Figure 2(a) shows all the reflectance samples reduced to reflectance intervals. In Fig. 2(b) a histogram of the number of samples used to determine each reflectance interval is shown. Remember that the first 39 levels cover the mean reflectance spectral values between 0 and 0.1. Above that the reflectance intervals are incremented in 0.1 steps causing the bump at interval 40. In the histogram there seems to be no obvious distinguishing feature to identify the background from the white water, but as mentioned above, a suitable threshold must be above the reflectance interval with the most number of samples.

Figure 2(c) shows the total reflectance. The total reflectance spectrum peaks at 510 nm suggesting a blue-green color and a maximum value of ~ 0.06180 . The nonzero value at 860 nm (0.02412) is mainly due to the overcast sky being reflected at the water surface. The graphs in Fig. 2(d) show the augmented spectral reflectance contribution and an estimate of the fractional coverage for different thresholds choices.

In Fig. 2(d) a range of reflectance intervals (intervals 16 through 23 and where interval 16 contains the greatest number of samples) are used as threshold reflectance intervals between white water and nonwhite water events. In the resulting estimates of the augmented spectral reflectance, the spectral shape has changed from that of the total reflectance. The spectral shape of the augmented reflectance seems to vary somewhat from one choice of threshold interval to another with exception of a common lower 860 nm value and a relatively flat region between 440 and 670 nm. The 860 nm value, as seen in previous data, is much lower than the other wavelengths.

For threshold intervals 16, 17 and 18 the fractional coverage estimates are particularly high (37.2%, 22.5% and 14.3%) for this wind speed of 11.86 m/s. From threshold interval 19 through 23, the spectral shape has become more settled and appears to be relatively constant with the exception of the 410 nm channel which appears to decrease with increasing threshold with respect to the other spectral values. In this range of thresholds, the estimates of fractional coverage are

also more plausible (9.5%, 6.9%, 5.3%, 4.1% and 3.7%). This spectral shape continues for higher threshold intervals (not shown here) and eventually breaks down with the highest threshold intervals due to a small number of samples.

It is interesting to note that the augmented spectral reflectance for these threshold intervals (19 through 23) maintain a small peak at 510 nm although it decreases with increasing threshold. Increasing the threshold moves the analysis into higher reflectance levels and therefore into thicker whitecap foam types. Investigation of the spectral variation of different foam types with increasing reflectance [Moore *et al.*, 1997] revealed a similar trend with the 510 nm value decreasing while the 670 nm and 860 nm values increased. The 410 nm value was also observed to decrease in the foam spectra.

The 510 nm reflectance maintains the highest value and is reminiscent of the total reflectance spectrum which is predominantly comprised of non-foam water reflectance contributions. The reflectance values of the wavebands in the visible region tend to equalize with higher threshold choice. The augmented reflectance spectral profiles seem reasonable and explain the apparent whiteness of whitecaps, where the channels covering the visible region are essentially equivalent with an increasing hint of blue-green for lower reflectance intervals. This is similar to what is visually observed; white thick fresh foam and blue-green thin foam where the background water color penetrates through the thin bubble layers.

With a consistent spectral profile for the higher threshold intervals, the optimal choice becomes difficult. However, it seems that threshold interval 23 is perhaps too far into the white water realm and can be ruled out as the optimum threshold choice. Threshold interval 19 might be a reasonable choice but could contain some non-foam bright sky reflectance contributions. It also has a particularly high 410 nm value that is not present when higher threshold reflectance intervals are applied suggesting the presence of some non foam contributions. Being conservative, the optimal choice seems to be around threshold interval 20 or even 21. The augmented reflectances are 0.00315 and 0.00290 at 510 nm and 0.00169 and 0.00161 at 860 nm for thresholds 20 and 21 respectively. The fractional coverage estimates using these thresholds,

although a little high due to the inclusion of the thinnest foam types, are 6.9% and 5.3% respectively.

In the augmented spectra for thresholds 20 and 21, changing the threshold by a small reflectance of 0.0025 changes the fractional coverage estimate by 1.6% but only by ~ 0.000186 for the augmented reflectance in the visible (410 nm -550 nm), and by ~ 0.00008 for the augmented reflectance at 860 nm.

The upwelling signal, particularly in the lower threshold regions, is mixed with contributions from brighter sky reflectances, thin foam layers and fragmented foam patches. As stated before, there is no decisive definition of threshold; only a compromise between either obtaining a reasonably pure white water spectrum and underestimating the augmented reflectance contribution, or obtaining perhaps a more complete measure of the augmented reflectance contribution at the cost of including some nonwhite water contributions. It is important to include the lowest reflecting and thinnest foam types since they persevere longer than the thicker and more highly reflective foam and as result have great statistical weight in contributing to the total augmented reflectance. This threshold problem makes accurate determination difficult and somewhat subjective. However, it is comforting that the augmented reflectance is a weak function of the actual choice of the threshold.

Clear Sky

In the next example, whitecap data was taken the next day ($\sim 9:05$ am) under clear sky conditions, and as described above, with a more developed sea. Wave height was about 2 m with a periodicity of 7-8 seconds. Mean wind speed was 11.7 m/s with a standard deviation of 1 m/s coming from the north west at about 340° . The ship heading was 355° and moving through the water at 7 knots (2.6 m/s) covering a straight track of 4.3 km. Air temperature was 12°C and the water surface temperature was 16.5°C , resulting in an unstable atmosphere. Other parameters taken from the ship's log were salinity (35.0895 ppt), barometric pressure (1019.9 mB) and relative humidity (61%). This location ($\sim 29.15^\circ$ N, 84.02° W) was approximately 20 km north and 56 km west of the location where the data during overcast conditions in Fig. 2 was acquired. With

wind speed continually blowing in the 10-15 m/s range for roughly a 24 hour period, the sea had become more fully developed, producing a different whitecap morphology and foam distribution from the previous day. Reflectance measurements included a larger proportion of foam streaks and residual foam patches resulting from larger breaking waves although less frequent than in the previous 'overcast' case.

In Fig. 3(a) the reflectance measurements reduced to reflectance intervals are shown and the histogram of reflectance interval vs. number of samples is shown in Fig. 3(b). Noticeable differences from the overcast sky condition are (i) the tighter distribution of samples about the peak, and (ii) the much lower sky reflectance (~ 0.00276 at 860 nm). This is the result of a low sun angle (30° above the horizon) and the viewing angle of the radiometer. The radiometer was orientated to view the water surface at 20° from nadir in a direction opposite the sun in order to minimize specular sun glitter in the measurements. As a result, the sky reflectance signal arriving at the radiometer was from a region of the sky centered roughly 80° from the sun where the sky is dark relative to overcast conditions.

With regard to the histogram of reflectance interval vs. number of samples, it may be tempting to fit a symmetrical distribution about the mode and use the difference between the fit and the histogram to identify any augmentation. But this would assume an equal probability of darker and brighter sky reflectances contributing to the distribution from a symmetrical distribution of wave orientations of the water surface reflecting a proportionately graded sky. It is not that simple since the wind typically blows from one direction causing the waves to progress across the surface in rows creating a preference for surface angle orientation and skewing any symmetry in the distribution. In addition, in the presence of low sun angles, the distribution of reflectance intervals is further complicated by the specific illumination direction of the sun reflected from waves and whitecaps. Even if the distribution of reflectance intervals vs. number of samples were perfectly symmetric, the finite bandwidth of this distribution indicates an accuracy limitation. Within this envelop there is an indiscriminate region where sky reflectance signal overlaps with thin foam contribution thus concealing any obvious threshold.

In Fig. 3(c) the total reflectance has a peak at 510 nm but is not as prominent as in the overcast data. This is most likely due to the ship being in a slightly different body of water. In Fig. 3(d) the augmented spectral reflectance profiles are shown for thresholds 4 through 9 (threshold 4 is the mode). Following similar reasoning as in the overcast case, it seems that the profiles resulting from the application of thresholds 6 and 7 are more realistic. The augmented reflectances are 0.00097 and 0.00085 at 510 nm and 0.00071 and 0.00059 at 860 nm for thresholds 6 and 7 respectively with fractional coverage estimates of 4.8% and 3.4% respectively.

It is interesting to note the relatively higher 440 nm value appearing in the augmented reflectance spectra as it does in the total reflectance profile, whereas in the Fig. 2 data it is relatively low in both the total and augmented reflectance spectra with the application of higher thresholds. This difference is due to measurements taken in slightly different water bodies and to the inclusion of the foam free water color (sky reflection and water-leaving radiance) in measurements of the thinnest foam types and submerged bubbles.

In this example, the augmented reflectance at 670 nm using threshold 6 is marginally highest and the 860 nm has substantially increased in comparison with the overcast example. Also, the augmented reflectance contribution at 670 appears to be consistently higher than at 550 nm, whereas in the overcast example both the 550 and 670 nm values are essentially equal. The augmented reflectance profile suggests a stronger influence from the longer wavelengths. This effect is even more pronounced in the following example.

Clear Sky Low Sun

In Figs. 4(a) - 4(d), data was acquired an hour earlier (at ~7:50 am) on the same day as the data presented in Fig 3. The sun was lower in the sky at approximately 10° above the horizon and at ~80° azimuth from true north. Mean wind speed was 12.1 m/s with a standard deviation of 1.3 m/s during the acquisition period. The wind was out of the north west (325°) and the ship heading was 355°. Air temperature was 12.6°C and water surface temperature 16.55°C (unstable atmosphere). Other parameters from the ship's log were salinity (35.0445 ppt), barometric

pressure (1019.1 mB) and relative humidity (62%). As in the preceding example, the radiometer was angled 20° away from the direction of the sun to reduce the possibility of sun glitter and specular reflection. The location (29.11° N, 84.02° W) was approximately 2.7 miles due south of the location where the data in Fig. 4 was taken. During this period of ~ 18 minutes, 7,000 surface reflectance samples were taken. The whitecap development and foam distribution during this acquisition period was similar to the 'clear sky' case, only the sun elevation was smaller.

Figure 4(a) shows the reflectance intervals. In the histogram of the number of samples vs. reflectance levels in Fig. 4(b), the shape of the distribution is similar to that in Fig. 3(b). The distribution rises sharply and falls with a slight broadening towards higher reflectance. The total reflectance shown in Fig. 4(c) is somewhat higher than in Fig. 3(c) data suggesting a possible higher white water contribution. The spectral shape is similar with the exception of relatively higher 410 and 440 nm values. This can be attributed to a spectrally different angular distribution of the downwelling light field. The sky was comprised of a prominently yellow reddish maximum at high zenith angles due to the low sun, and a very rich and dark blue sky toward the zenith - typical of a clear early morning as the sun rises. Horizontal waves and waves inclined away from the low sun reflect the predominantly very blue sky and are most frequently measured by the radiometer. This bias towards more blue measurements accounts for the different shape of the total reflectance profile in this example. However, when plausible threshold reflectance intervals (Fig. 4(d)) are applied in order to estimate the augmented reflectance contribution, the opposite is observed with a bias towards the longer wavelengths.

At threshold interval 5 (mode of the histogram) in Fig. 4(d), the augmented reflectance values at the shorter wavelengths are lower with respect to the longer wavelengths than they were in the total reflectance profile. Using the same criteria from the two previous data sets, white water contribution should begin to appear above the background reflectance in the region of reflectance intervals 6, 7, 8, 9 and maybe 10. Moving up to threshold interval 6, the resulting augmented reflectance spectrum is more accentuated with even lower values towards the blue end and higher values in the red. This is the result of the low sun angle (10° above the horizon). The augmented

reflectance spectra for threshold 6 yields a 410 nm value (0.00203) that is less than that at 860 nm (0.00265), and with a maximum at 670 nm (0.00313).

Although the spectral shape of the augmented reflectance profiles from thresholds 6, 7 and 8 are somewhat similar, their fractional coverage estimates appear to be too high - 18.5%, 10.9% and 7.9%. Threshold 9 has a more reasonable fractional coverage of 6.0% with an augmented reflectance contribution ~ 0.0017 in the visible. Threshold 10 has a fractional coverage of 4.8% and an augmented reflectance of ~ 0.0015 in the visible. Comparing the fractional coverage and augmented reflectance contribution estimates with the previous example taken under similar conditions (wind speed, air/water temperature, sea state) but with higher sun angle, shows the estimates in this example are much higher; nearly 3 times the augmented reflectance and more than twice the fractional coverage using similar thresholds. These augmented reflectance profiles and their particularly high estimates of fractional coverage suggest that the higher augmented reflectance values at the longer wavelengths may include specular reflections from foam free water facets, although an additional explanation is provided below.

Comparing Figs. 3(d) and 4(d) shows that the augmented reflectance becomes relatively more enhanced in the red and near infrared for the lower solar elevation. Although whitecaps are usually modeled as lambertian reflectors, we believe that this reddening of their reflectance with reduced solar elevation provides indirect evidence of their nonlambertian nature. As the solar elevation is decreased, the contribution to the incident irradiance from the diffuse sky light is enhanced at the expense of the direct sun light. For low solar elevations, the incident irradiance in the blue is almost totally from diffuse sky light. In contrast, the reverse is true in the red, most of the incident irradiance is direct sun light. Let us assume that the whitecaps are lambertian, i.e., they have reflecting properties similar to sheets of white paper floating on the water, and that their reflectance is spectrally neutral throughout the visible. In the red, whitecaps on the side of the waves away from the sun or in the troughs of the waves receive little or no illumination, i.e., they are shadowed from the direct sun. In contrast, in the blue, where the illumination is diffuse, all whitecaps will be illuminated. Thus, in this example, the augmented reflectance would be expected

to *increase* from red to blue because fewer whitecaps are illuminated with red light. In fact, the experimental result [Fig. 4(d)] is exactly the opposite!

Further evidence of the nonlambertian character of whitecaps can be seen by comparing Figs. 3(a) and 4(a). The highest reflectance levels in these figures will be due to the thickest-youngest foam patches. In this case, removal of the ocean background is not relevant to measuring their properties. The reddening of the spectrum in the visible for these foam patches from Figs. 3(a) to 4(a) is very evident. Figure 4(a) shows a strong variation in reflectance with wavelength, a surrogate here for the variation in the angular distribution in of the incident irradiance. In contrast, Fig. 3(a) shows a much more neutral or bluer reflectance for the most-reflective whitecaps. Thus, even for the brightest whitecaps, the dependence of reflectance on the angular distribution of the incident irradiance is clear: they are nonlambertian. However, note that the measurements we have presented here cannot shed light on the actual bi-directional reflection distribution function (BRDF) of the augmented reflectance. The only conclusion we can make regarding the BRDF is that the nadir-viewing augmented reflectance spectrum for diffuse illumination [Fig. 2(d)] and for solar elevations $>$ about 30° are similar.

The nonlambertian nature of whitecaps and its relationship to the solar elevation is easy to understand. Whitecaps are isolated volume scatterers, and at low solar elevations the solar beam can enter the sides as well as the top of the whitecap and be scattered out toward the zenith. In contrast, for high elevations or for diffuse illumination relatively fewer photons will enter the sides, and this results in a lower overall reflectance.

Open Ocean Data

The data used here were acquired from a transect of the Pacific Ocean from Manzanillo, Mexico (19.03° N, 104.20° W) to Honolulu, Hawaii (21.20° N, 157.55° W). Only data which were acquired under relatively constant and overcast conditions were used to model augmented reflectance with other parameters such as wind speed etc. These data sets have a well behaved

background in terms of radiometrically determining a threshold between white water and nonwhite water events. Overcast conditions also provide a better downwelling light description for correction of the deck cell cosine collector [Moore *et al.*, 1997]. Other whitecap data were acquired during broken sky and scattered cloud conditions, but have not been included in the modeling. The threshold is more difficult to define for these data sets, due to the large variability and random nature of the downwelling light field and its effect on surface reflectance measurements.

The data used are from 4 different days and locations during the transect. Wind speed was relatively constant and remained within a range of 1-2 m/s for days at a time. Reflectance data was acquired for wind speeds between ~8 - 13 m/s. Stability of the lower atmosphere, defined by the air temperature / water temperature differential, varied from neutral to slightly unstable. Other parameters such as salinity, humidity and barometric pressure were also recorded for possible correlation.

The reflectance interval resolution was increased from the previous value of 0.0025 to 0.001. While more threshold choices were generated as result of the higher resolution, it was primarily implemented to monitor background stability by observing the distribution of reflectance intervals verses number of samples. In cases where the sun came out from behind the clouds or a cloud blocked the sun, the foam free water surface reflectance either decreased or increased. This was observed as a broadening (sometimes with bumps) in the distribution of reflectance interval vs. number of samples for given data set.

In Fig. 5 the augmented reflectance contribution from 17 data sets is presented as a function of wind speed. Each of the 17 augmented reflectance data points were acquired from an average acquisition time of 45 minutes (or ~800 m² surface area). For clarity, the augmented reflectances from wavebands 410 nm through 550 nm (ARC₄₁₀₋₅₅₀) have been averaged since their values vary only slightly with respect to one another. The augmented reflectance at 670 nm (ARC₆₇₀) which also varies only slightly with the other visible wavebands, and the augmented spectral reflectance at 860 nm (ARC₈₆₀) which is always distinctly lower than the visible wavebands are shown. To relate augmented reflectance to wind speed a power law relationship has been applied in the same

vein as previous authors have related fractional coverage to wind speed [*Blanchard*, 1971; *Ross and Cardone*, 1974; *Wu*, 1979; *Toba and Chaen*, 1973; *Monahan and O'Muircheartaigh*, 1980,1986]. For a given wind speed the augmented reflectance contribution in the 410-550 nm region can be related to the wind speed with a correlation of 0.702 by:

$$ARC_{410-550} = 9.648 \times 10^{-7} U^{2.777}$$

where $ARC_{410-550}$ is the augmented reflectance contribution as described above and U is the wind speed in meters per second. Thus, the wind speed accounts for about half of the variance in $ARC_{410-550}$. For the augmented reflectance contribution at 670 nm and 860 nm we have:

$$ARC_{670} = 1.131 \times 10^{-6} U^{2.698}$$

and

$$ARC_{860} = 1.302 \times 10^{-6} U^{2.545}$$

with correlation factors of 0.699 and 0.647, respectively. Data taken during scattered and partly cloudy conditions, although not used in determining the above relationship, are also shown in Fig.

5. These data were acquired with sun elevation greater than 50°. Reducing this data was more complex due to a variable threshold but the results are similar to the data acquired under steady overcast conditions with a well defined threshold.

In Fig. 6 the respective fractional coverage estimates are plotted as a function of wind speed. The distribution of fractional coverage estimates for a given wind speed appear to be more scattered than for augmented reflectance.

In Fig. 7 the relationship between augmented reflectance contribution ($ARC_{410-550}$) and fractional coverage can be expressed as a linear relationship with a correlation of 0.694 given by:

$$ARC_{410-550} = 9.252 \times 10^{-3} W + 0.000195$$

where W is the fractional coverage.

A scatter plot of the percentage drop in augmented reflectance from $ARC_{410-550}$ to ARC_{860} is shown in Fig. 8. A linear fit is applied between the data points to indicate an increasing trend in the drop off between $ARC_{410-550}$ and ARC_{860} with wind speed rather than to establish a model, as the correlation is very low, 0.359. However, the data indicate that for wind speeds in the range 8-12 m/s the percentage drop off between $ARC_{410-550}$ and ARC_{860} is approximately 15 - 25%.

Possible correlations between the augmented reflectance and other parameters such as water temperature, air temperature, stability of the lower atmosphere, humidity, salinity, barometric pressure, wave height, sea swell were investigated. No correlations could be established mainly due to the small variation in the parameters during the transect.

Discussion

In this paper we have shown examples of whitecap spectra of different foam types and reflectances, both from individual whitecaps and as an integrated sum over a period of time expressed as the augmented reflectance contribution and fractional coverage. From the first cruise, estimates of the augmented spectral reflectance contribution and fractional coverage have been obtained from measurements taken under different sky conditions and sea states but with similar wind speeds in order to highlight the variability of whitecap formation and the difficulties in providing accurate information on the optical influence of whitecaps. From the second cruise, estimates of augmented spectral reflectance and fractional coverage acquired during overcast skies and more consistent weather conditions with essentially unlimited fetch and duration have been derived for ocean color satellite waveband correction and atmospheric correction algorithms.

Of particular importance is the determination of the threshold required to accurately determine augmented spectral reflectance contribution and fractional coverage. Despite the application of high

resolution white water threshold reflectance intervals, the threshold choice remains difficult and somewhat subjective. Regardless of the threshold resolution that may be applied, the very wave nature of the water surface and the distribution of the downwelling light field creates an inseparable and indiscriminate region between foam and foam free contributions. As mentioned earlier, the reflectance of foam in the shadow of an adjacent wave may result in a lower reflectance than a foam free water facet reflecting a bright region of the sky. Choice of threshold is further compounded since the thinnest foam types, which are close to the threshold reflectance, are very important due to their long endurance. Without adequate discrimination of the thinner foam type, the estimation of fractional coverage and augmented spectral reflectance contribution will always incur some error. Utilization of a higher threshold resolution and the subsequent inclusion of the less reflecting and thinnest foam types results in fractional coverage estimates that are roughly 3 times higher than that reported by other researchers [*Blanchard, 1971; Ross and Cardone, 1974; Wu, 1979; Toba and Chaen, 1973; Monahan and O'Muircheartaigh, 1980,1986*]. The ratio of the augmented reflectance contributions in the visible to the fractional coverage estimates determined with this system results in an effective reflectance of $\sim 1.25\%$. This much lower effective reflectance than the 22% determined by *Koepke [1984]* gives an indication of the greater quantity of thin foam and foam streaks that have been included in these measurements.

From the data used in this paper, the fractional coverage has been observed to vary by a larger amount than the augmented reflectance contribution in going from one threshold interval choice to another. This is due to the definition of fractional coverage which is not weighted by reflectance, and as result, the thinnest foam patches are assumed equal in reflectance to the more highly reflecting thick, dense foam types. The augmented spectral reflectance contribution is the more meaningful measurement for satellite observations whereas fractional coverage must be combined with reflectance data to achieve the same result.

Examples from the first cruise in the Gulf of Mexico reveal the dependence of whitecap formation on parameters other than the wind speed measured at the time of observation. The examples described from the first cruise all had similar wind speeds. Changing weather conditions

such as during the onset of a cold front produced higher values of augmented reflectance and fractional coverage ('overcast') than when conditions had been consistent for a longer period of time ('clear sky', 'clear sky low sun'). For the 'overcast' example, the lower atmosphere was essentially neutral ($\Delta T = T_{\text{air}} - T_{\text{water}} = -0.8^{\circ}\text{C}$) and produced high augmented reflectance and fractional coverage estimates. By the next day, the sea state under the influence of conditions of greater duration produced augmented reflectance and fractional coverage estimates that were roughly 1/3 those obtained during the onset of the cold front, despite the atmosphere being unstable (i.e. $\Delta T = T_{\text{air}} - T_{\text{water}} = \sim -4^{\circ}\text{C}$). The whitecaps visually appeared different to those in the 'overcast' case with large breaking waves, although less frequent, and with more residual foam patches and foam streaks that were essentially absent in the 'overcast' case. Nevertheless, one would expect the opposite result with greater whitecap influence during unstable atmospheric conditions and less during neutral conditions. On the other hand, the augmented reflectance and fractional coverage for the 'clear sky low sun', which had similar whitecap and foam conditions to the 'clear sky' case, produced values roughly twice the 'clear sky' values due to the effects of the low sun. The dependence on sea state, wind variations with rising or falling trend, change in wind direction, minimal fetch and duration along with specular sun reflections, whitecap BRDF effects, and low sun angles are responsible for these differences in fractional coverage and augmented spectral reflectance for similar wind speeds. The data from the Gulf of Mexico was taken roughly 110 km offshore which is an adequate fetch for 12 m/s wind speeds [*Ross and Cardone*, 1974]. The estimate of the augmented reflectance from the 'clear sky' case, which was acquired under sea state conditions with adequate fetch and duration, and under illumination conditions that were not particularly extreme (sun elevation of 30°), produced similar results to the open ocean data taken in the Pacific.

Another interesting aspect resulting from these examples is the spectral change in the upwelling signal during low sun angle. The spectral variation in estimates of the augmented reflectance contribution seems to be dependent on sea state and the whitecap morphology. In Fig. 2(d) the decrease from the 440 nm to the 860 nm value is $\sim 41\%$ from observation of many small

whitecaps and very few residual and fragmented foam patches. From Fig. 3(d) the drop in augmented reflectance from 440 nm to 860 nm is ~28% from observation of a few large whitecaps but mostly residual and patchy foam. We attribute the significant change in the spectral variation of whitecap reflectance from the 'clear sky' to the 'clear sky low sun' examples to the nonlambertian nature of the whitecaps (the BRDF effect). This effect could also influence the magnitude the drop from 440 to 860 nm.

Since the low sun has this influence on the augmented reflectance (and fractional coverage), the wind direction with respect to the sun becomes an important consideration. The longitudinal axis of waves (and whitecaps) are more or less perpendicular to the direction of the wind. In the 'clear sky low sun' case, the wind is from the north-west at 325° with the sun at 80° azimuth with respect to true north. This results in whitecaps and the crests of waves being illuminated at ~25° incident angle (azimuth). One might expect a maximum effect if the wind had been from the west at 260° or perhaps from the east at 80° azimuth and a minimal effect with the wind from the north at 350° or south at 170° azimuth.

The goal of this study is to determine the augmented reflectance contribution from whitecaps as viewed from satellites and, in particular, its spectral dependence. Useful satellite data of the ocean is taken around solar noon and from cloud free regions. The low sun angle examples (10° and 30° above the horizon) used here can be considered extreme conditions and are not frequently encountered. However, it brings attention the effect low sun angle has on the augmented reflectance contribution. This effect may have particular importance for higher latitude waters both north and south of the equator where, during the winter months or even in higher latitudes in the summer months, the sun maintains a low angle above the horizon at around midday. For higher sun elevation, the BRDF effect (although substantially reduced) may still exist. These high latitude waters are particularly prolific as regards phytoplankton blooms, triggered by seasonal nutrient rich cold upwellings. They are often windy areas with an abundance of whitecaps and a bias of the reflectance towards the yellow-red end of the visible spectrum, with low sun angle, brings attention to the 670 nm waveband near the phytoplankton fluorescence peak at 685 nm. The

Moderate Resolution Imaging Spectroradiometer (MODIS) sensor [Salmonson, 1989] will be capable of estimating this phytoplankton fluorescence signal [Letelier and Abbott, 1996]. This fact adds to the importance whitecaps may play in these higher latitudes. And of course, the high values at 670 and 860 nm at lower sun angles, from a combination of whitecaps and foam free waves, could complicate atmospheric correction algorithms unless adequately characterized.

The spectral characteristics of the augmented reflectance found in both the Gulf of Mexico and from the Pacific Ocean seem to possess some spectral characteristics that are related to the water color properties in which they were formed. In Fig. 9 examples of the nonwhite water spectral profiles and their augmented reflectances from both water bodies are shown. Both examples were taken under overcast sky conditions. For Gulf of Mexico waters, the augmented reflectance from threshold interval 20 in the 'overcast' case is used and the augmented reflectance and the nonwhite water spectrum have distinctly lower 410 nm values than their respective 440 nm values. For the very blue and clear Pacific Ocean waters, the 410 nm value is higher than the 440 nm value in both the augmented reflectance and nonwhite water spectral profiles.

The augmented reflectance profile in Fig. 9 for the Pacific Ocean has been compiled by averaging the normalized augmented reflectance of each of the 17 data samples used in earlier modeling. The difference between each channel of the mean augmented reflectance profile shown and the mean $ARC_{410-550}$ is +2.9%, -6.0%, +6.1%, -3.1%, -2.4% and -21.6%. The standard deviation for each waveband over the 17 data points is typically less than, or about equal to, the size of the symbols in Fig. 9. For the augmented reflectance from the Gulf of Mexico the difference between each channel and its $ARC_{410-550}$ is -4.5%, -1.8%, +7.0%, -0.8%, -2.1% and -42.2%.

In both cases, the augmented reflectances are similar with the exception of the 410 and 860 nm values. The 860 nm value is lower in the Gulf of Mexico example due to a different type of wave breaking (many small whitecaps suddenly appeared at the onset of a cold front yielding very high augmented reflectance and fractional coverage estimates). Although the 410 nm value of the augmented reflectance seems to be related to the water in which it was formed, the 510 nm value

does not and would appear to be independent of water color type. A similarly low 410 nm value was observed in foam data generated by a ship's wake in coastal waters off the coast of Southern California [Moore *et al.*, 1997]. The low 410 nm value may be influenced by the higher absorption properties of coastal waters at the shorter wavelengths, but the enhanced absorption alone cannot explain this effect. Initially it was thought that this coupling between the augmented reflectance and the water type in which the white water is formed might be explained by the inclusion of very thin foam types where a good proportion of the background water color is also measured. But this does not explain the apparent indifference of wavebands above 410 nm (and perhaps 440 nm) to the foam free background water color.

Although most of our open ocean analysis utilized only data acquired during overcast conditions (to facilitate more accurate estimation of the background water reflectance threshold, and to eliminate sun glint, which is easy to mistake for thin foam), some data for partly cloudy and clear skies were examined. This partly cloudy/clear sky data possessed an augmented reflectance spectrum similar to the overcast cases, as well as similar values of $ARC_{410-550}$ (Fig. 5). Thus, we believe that our ARC results should be reasonably representative of clear sky situations, and thus useful for estimating the whitecap contribution to the reflectance measured by ocean color sensors.

Conclusions

To summarize, spectral characteristics found in the augmented reflectance can be influenced by a number of factors such as sky condition (e.g. bright horizon and overcast sky), solar elevation, sea state; type of wave breaking and direction of wave breaking (particularly at low solar elevation). The spectral profile of the augmented reflectance contribution may even be dependent on the color properties of the water body in which the whitecap forms, since the detection of very thin foam types include upwelling water-leaving radiance contributions. Despite the inaccuracies in determining the white water threshold, the spectral profile of the augmented reflectance remains consistent over a large number of reasonable threshold choices. Threshold determination is inherently complicated and subject to some error due to the overlap of white water and nonwhite

water reflectance contributions. For most applications, any subtle spectral characteristics found in the estimates of the augmented reflectance, besides the distinctive lower 860 nm value, are overshadowed by the inaccuracy in determining the correct white water to nonwhite water threshold.

We have determined the augmented reflectance contribution in the open ocean for the 410 - 550 nm range to be 0.00031 at a wind speed of 8 m/s, 0.00058 at 10 m/s and 0.00096 at 12 m/s with a standard deviation of 0.000108. These results are somewhat lower than previously derived values of whitecap optical influence [Koepke, 1984; Gordon and Wang, 1994b]. Using Koepke's effective reflectance of 22% and the fractional coverage determined by wind speed for water temperature above 14°C [Monahan and O'Muircheartaigh, 1980] yields values that are greater than 4 times our values at 12 m/s and roughly 3 times at 8 m/s. Applying the fractional coverage relationship which takes into account atmospheric stability [Monahan and O'Muircheartaigh, 1986], our results are still lower even when assuming a very stable atmosphere. Also the 860 nm value, which may be an indicator of the type of wave breaking responsible for the amount and depth of bubbles forced into the water column, is found to be 15%-20% lower than the optical influence of whitecaps in the visible for wind speeds 8 - 12 m/s in the open ocean, i.e., half of that observed by Frouin *et al.* [1996] in the surf zone. We have ascertained the augmented reflectance contribution at 860 to be 0.00026 at wind speed of 8 m/s, 0.00046 at 10 m/s and 0.00073 at 12 m/s. This implies a lower contribution from whitecaps at 860 nm (~5.6 times lower for wind speeds at 12 m/s and ~3.8 times lower for wind speeds of 8 m/s using the Koepke [1984] effective reflectance of 22% and the Monahan and O'Muircheartaigh [1980] wind speed to fractional coverage relationship).

Koepke [1984] concluded that the optical influence of oceanic whitecaps was in fact less important than had been previously assumed since his effective reflectance reduced the optical influence of whitecaps by a factor of 2. Certainly from our direct measurements of the optical influence of whitecaps and foam in the 8 - 12 m/s wind speed range suggest that whitecap optical influence can be considered to be even less important than Koepke's optimistic conclusion.

Notation

$ARC_{410-550}$	mean augmented reflectance contribution from values at 410, 440, 510 and 550 nm.
ARC_{670}	augmented reflectance contribution at 670 nm.
ARC_{860}	augmented reflectance contribution at 860 nm.
T_{air}	air temperature
T_{water}	water surface temperature
ΔT	temperature differential ($\Delta T = T_{air} - T_{water}$);
U	wind speed in meters per second
W	fractional coverage of whitecaps and foam

Acknowledgments. This research was funded by NASA / EOS - MODIS, Goddard Space Flight Center under contract #NAS5-31363. We would like to thank Al Chapin for his help in the design and construction of the equipment. Also our thanks to Dr. Rik Wanninkhof (NOAA/AOML) and Dr. Gary Hitchcock (RSMAS/University of Miami) for allowing us to participate in their oceanographic excursion on the R/V Malcolm Baldrige in the Gulf of Mexico. We would like to thank the NOAA personnel: CMDR Mark Koehn, LCDR Tim Wright (TAO Operations Manager) and Lt. John Herring for allowing us to join their transit of the Pacific Ocean aboard the R/V Ka'imimoana.

References

- Blanchard, D. C., Whitecaps at sea. *J. Atmos. Sci.*, 28, 645, 1971.
- Bortkovskii, R. S., and V. A. Novak, Statistical dependencies of sea state characteristics on water temperature and wind-wave age. *J. of Marine Systems*, 4, 161-169, 1993.
- Cardone, V. J., Specification of the wind field distribution in the marine boundary layer for wave forecasting. *Rep. TR 69-1*, Geophys. Sci. Lab., New York Univ., New York, December 1969.
- Frouin, R., M. Schwindling and P. Y. Deschamps, Spectral Reflectance of Sea Foam in the Visible and Near Infrared: In Situ Measurements and Remote Sensing Implications. *J. Geophys. Res.*, 101C, 14361-14371, 1996.
- Garrett, W. D., The influence of surface-active material on the properties of air bubbles at the air/sea interface. *Rep. Naval Research Lab.*, 6545, Washington D.C., 14 pp., 1967.
- Gordon, H. R., and M. M. Jacobs, Albedo of the Ocean-Atmosphere System: Influence of Sea Foam. *Applied Optics*, 16, 2257-2260, 1977.
- Gordon, H. R., and M. Wang, Retrieval of water-leaving radiance and aerosol optical thickness over the oceans with SeaWiFS: A preliminary algorithm, *Applied Optics*, 33, 443-452, 1994a.
- Gordon, H. R., and M. Wang, Influence of oceanic whitecaps on atmospheric correction of SeaWiFS, *Applied Optics*, 33, 7754-7763, 1994b.

Koepke, P., Effective Reflectance of Oceanic Whitecaps. *Applied Optics*, 23, 1816-1824, 1984

Letelier, R. M., and M. R. Abbott, An analysis of chlorophyll fluorescence algorithm for the moderate resolution imaging spectroradiometer (MODIS), *Remote Sensing Environment*, 58, 215-223, 1996.

Maul, G. A., and H. R. Gordon, On the Use of Earth Resources Technology Satellite (LANDSAT-1) in Optical Oceanography. *Remote Sensing Environment*, 4, 95, 1975.

Miyake, Y., and T. Abe, A study on the foaming of sea water. *J. Marine Res.*, 7, 67-73, 1948.

Monahan, E. C., and C. R. Zietlow, Laboratory comparisons of fresh-water and salt-water whitecaps. *J. Geophys. Res.*, 74, 6961-6966, 1969.

Monahan, E. C., Oceanic whitecaps. *J. Physical Oceanogr.*, 1, 139-144, 1971.

Monahan, E. C., and I. G. O'Muircheartaigh, Optimal power-law description of oceanic whitecap coverage dependence on wind speed. *J. Phys. Oceanogr.*, 10, 2094-2099, 1980.

Monahan, E. C., and I. G. O'Muircheartaigh, Whitecaps and passive remote sensing of the ocean surface. *Int. J. Remote Sens.*, 7, 627-642, 1986.

Moore, K. D., Voss, K. J., Gordon, H. R., 1997: Spectral reflectance of whitecaps: Instrumentation, calibration and performance in coastal waters. Submitted *J. Atmospheric and Oceanic Technology*. December 1996.

- Payne, R. E., Albedo of the Sea Surface. *J. Atmospheric Physics*, 29, 959-970, 1972.
- Ross, D. B., and V. J. Cardone, Observations of oceanic whitecaps and their relation to remote measurements of surface wind speed. *J. Geophys. Res.*, 79, 444-452, 1974.
- Salmonson, V. V., W. L. Barnes, P. W. Maymon, E. H. Montgomery and H. Ostrow, MODIS: Advanced facility instrument for studies of the earth as a system, *IEEE Geosci. Rem. Sens.*, 27, 145-152, 1989.
- Toba, Y., and M. Chaen, Quantitative expression of the breaking of wind waves on the sea surface. *Rec. Oceanogr. Works*, 12, 1-11, 1973.
- Whitlock, C. H., D. S. Bartlett, and E. A. Gurganus, Sea foam reflectance and influence on optimum wavelength for remote sensing of ocean aerosols. *Geophys. Res. Letters*, 9, 719-722, 1982.
- Wu, J., Oceanic whitecaps and sea state. *J. Phys. Oceanogr.*, 9, 1064-1068, 1979.
- Wu, J., Variation of whitecap coverage with wind stress and water temperature. *J. Phys. Oceanogr.*, 18, 1448-1453, 1988.

Figure Captions

Fig. 1(a). Time series of the reflectance of two whitecaps and their foam types passing in view of the radiometer.

Fig. 1(b). Reflectance spectra of the two whitecaps of Fig. 1(a) reduced to reflectance intervals.

Fig. 2(a). Reflectance spectra of ~9,000 water surface reflectance samples from 'overcast' data reduced to reflectance intervals.

Fig. 2(b). Histogram of the number of reflectance samples per reflectance interval for 'overcast' data.

Fig. 2(c). Total reflectance of 'overcast' data (the sum of all weighted reflectance intervals). This is equivalent to the upwelling signal detected by a satellite assuming no atmospheric contribution.

Fig. 2(d). Augmented spectral reflectance contribution for a range of reflectance interval threshold choices. The fractional coverage estimate for each augmented reflectance profile is shown. For higher threshold choices the contributions in the visible region equalize with the exception of the 410 nm and 860 nm contributions.

Fig. 3(a). Reflectance spectra of ~10,000 water surface reflectance samples from 'clear sky' data (sun elevation of ~30° above horizon) reduced to reflectance intervals.

Fig. 3(b). Histogram of the number of reflectance samples per reflectance interval for 'clear sky' data.

Fig. 3(c). Total reflectance of 'clear sky' data (the sum of all weighted reflectance intervals). This is equivalent to the upwelling signal detected by a satellite assuming no atmospheric contribution.

Fig. 3(d). Augmented spectral reflectance contribution for a range of reflectance interval threshold choices. The fractional coverage estimate for each augmented reflectance profile is shown. Note the higher 670 nm and 860 nm values due to the influence of the longer wavelengths from a low sun.

Fig. 4(a). Reflectance spectra of ~7,000 water surface reflectance samples from 'clear sky low sun' data (sun elevation of ~10° above horizon) reduced to reflectance intervals.

Fig. 4(b). Histogram of the number of reflectance samples per reflectance interval for 'clear sky low sun' data.

Fig. 4(c). Total reflectance of 'clear sky low sun' data (the sum of all weighted reflectance intervals). This is equivalent to the upwelling signal detected by a satellite assuming no atmospheric contribution.

Fig. 4(d). Augmented spectral reflectance contribution for a range of reflectance interval threshold choices. The fractional coverage estimate for each augmented reflectance profile is shown. Note the much higher 670 nm and 860 nm and lower 410 nm values due to the influence of the longer wavelengths from a low sun. The 410 nm value is lower than the 860 nm value for all threshold choices.

Fig. 5. Augmented reflectance contribution for different wind speeds from open ocean data taken in the equatorial Pacific. Data points of the augmented reflectance from different waveband regions and their power law relationships with wind speed are shown. $ARC_{410-550}$ is the mean

augmented reflectance of wavebands 410, 440, 510 and 550 nm. ARC_{670} and ARC_{860} are the augmented reflectance for the 670 and 860 nm wavebands respectively. $ARC_{410-550} PC /$ scattered is for data taken under partly cloudy and scattered conditions (solar elevations $\sim 50^\circ$) and not used in establishing power law relationship.

Fig. 6. Fractional coverage vs. wind speed for same data used in Fig. 5. A power law relationship is applied although the fractional coverage values are more varied for a given wind speed.

Fig. 7. Fractional coverage vs. mean augmented reflectance of 410, 440, 510 and 550 nm values. A linear fit is applied with a reasonable correlation of 0.694. Wind speed is shown for each data point.

Fig. 8. Percentage drop in the augmented reflectance between $ARC_{410-550}$ and ARC_{860} for wind speeds in the 8 - 12 m/s range. The linear fit indicates an increasing trend with higher wind speed.

Fig. 9. Augmented and nonwhite water reflectance profiles normalized at 510 nm (not to scale) are shown for data taken in the Pacific Ocean and the Gulf of Mexico. The augmented reflectance for the Pacific Ocean is compiled from all data presented in this paper used to estimate the optical influence of whitecaps. Note the similarities in augmented reflectance profiles regardless of the water color in which the whitecaps form. The 410 nm value seems to be the exception and mimics the nonwhite water reflectance in both cases. The 860 nm value, which may be used to indicate the type of wave breaking, is lower in the Gulf of Mexico data due to type of whitecaps formed by the sudden arrival of a cold front.

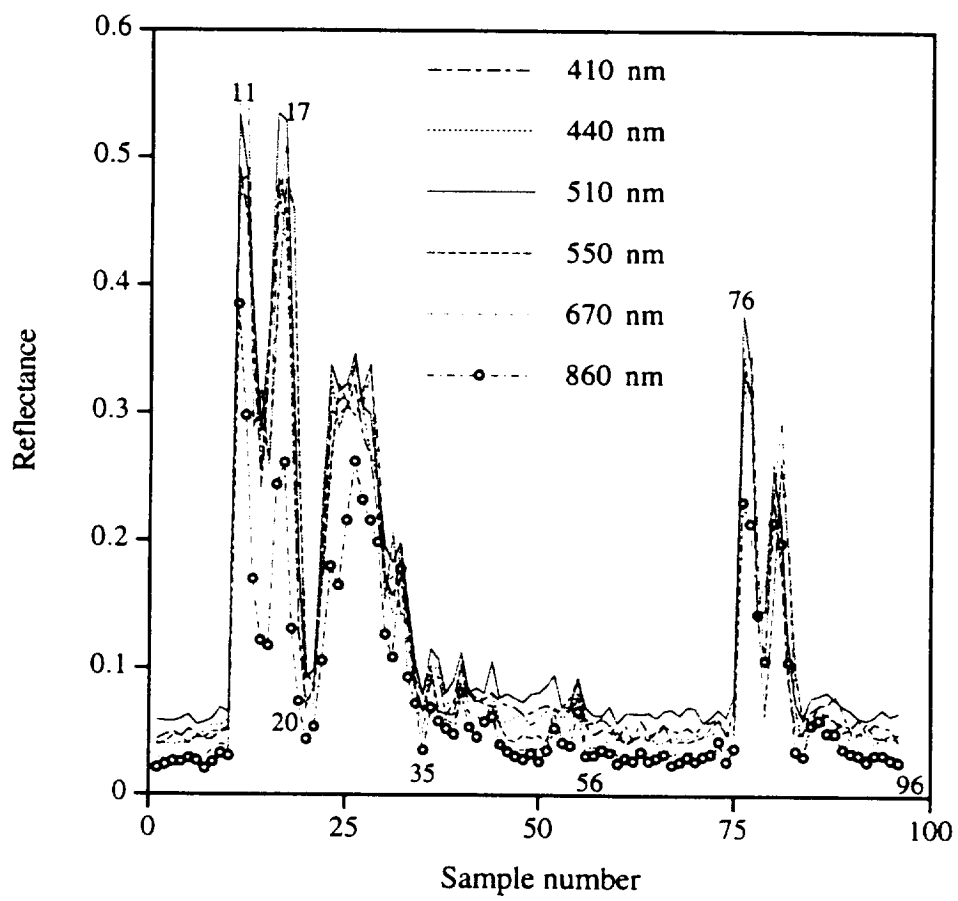


Fig.1(a)

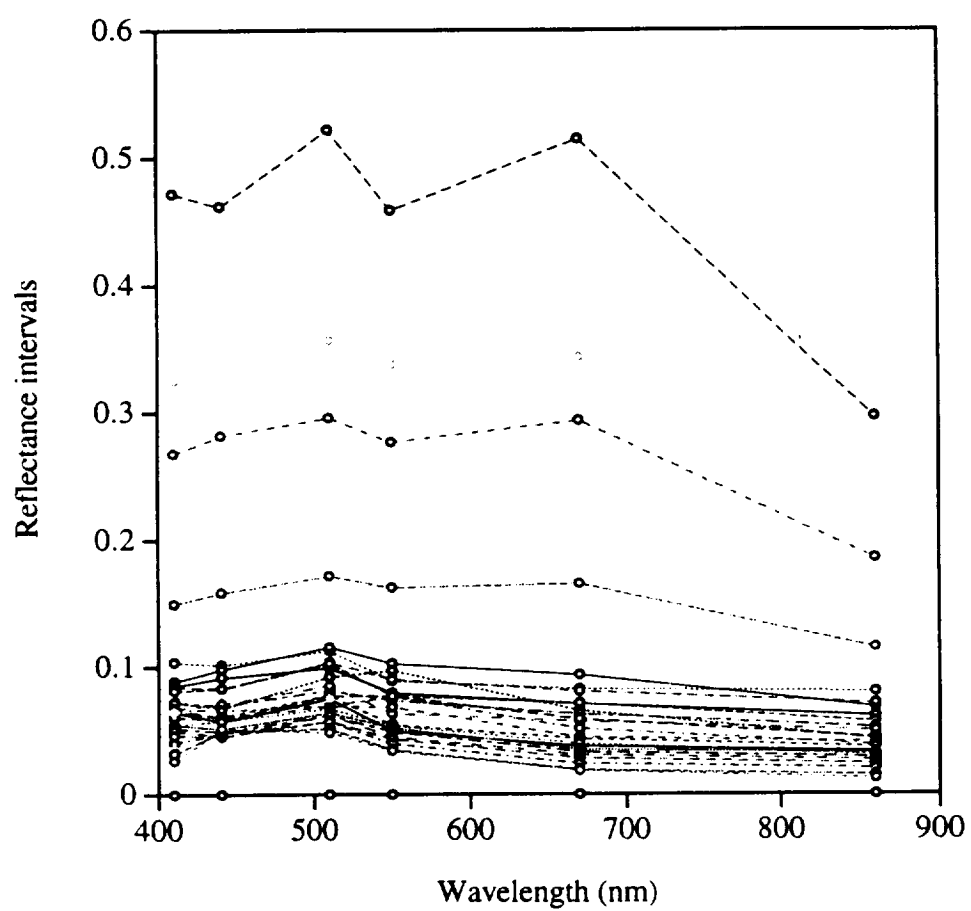


Fig. 1(b)

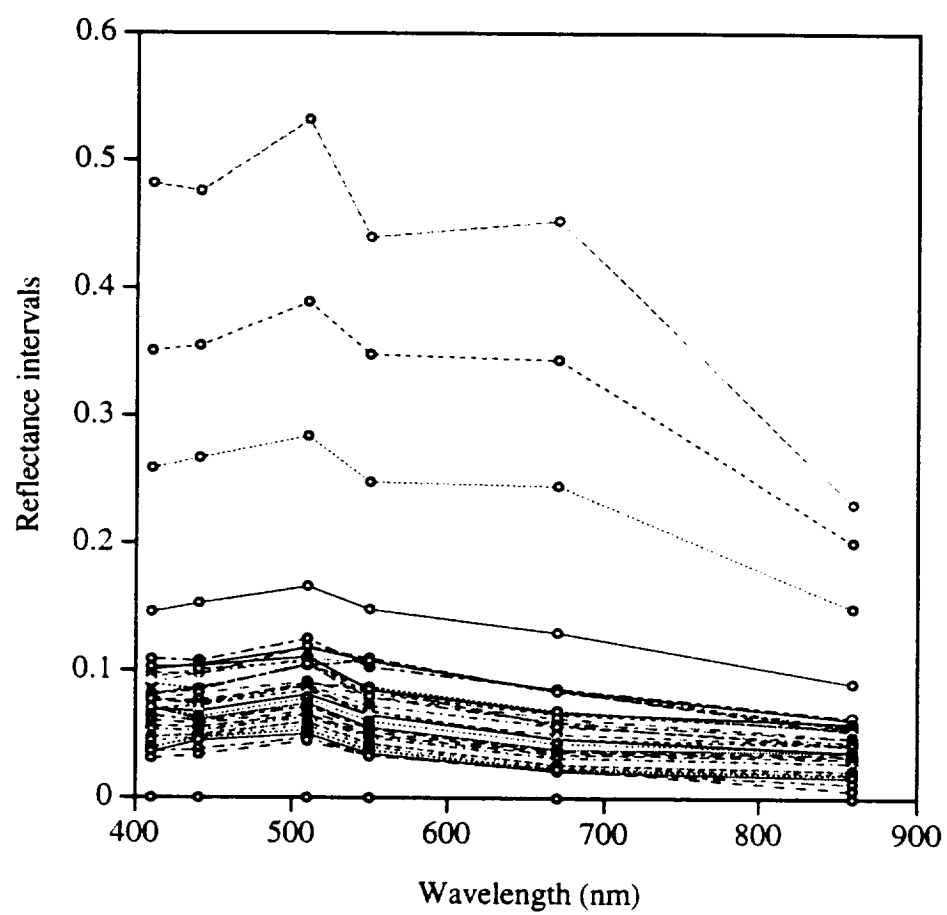


Fig. 2(a)

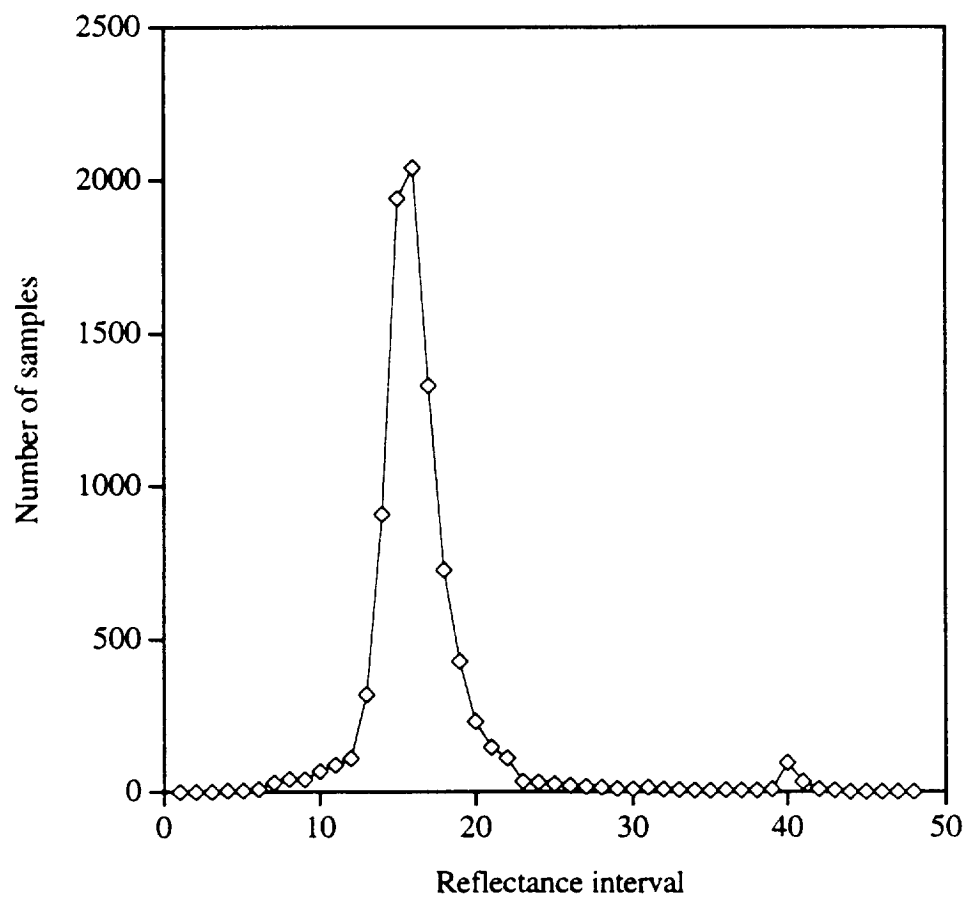


Fig.2(b)

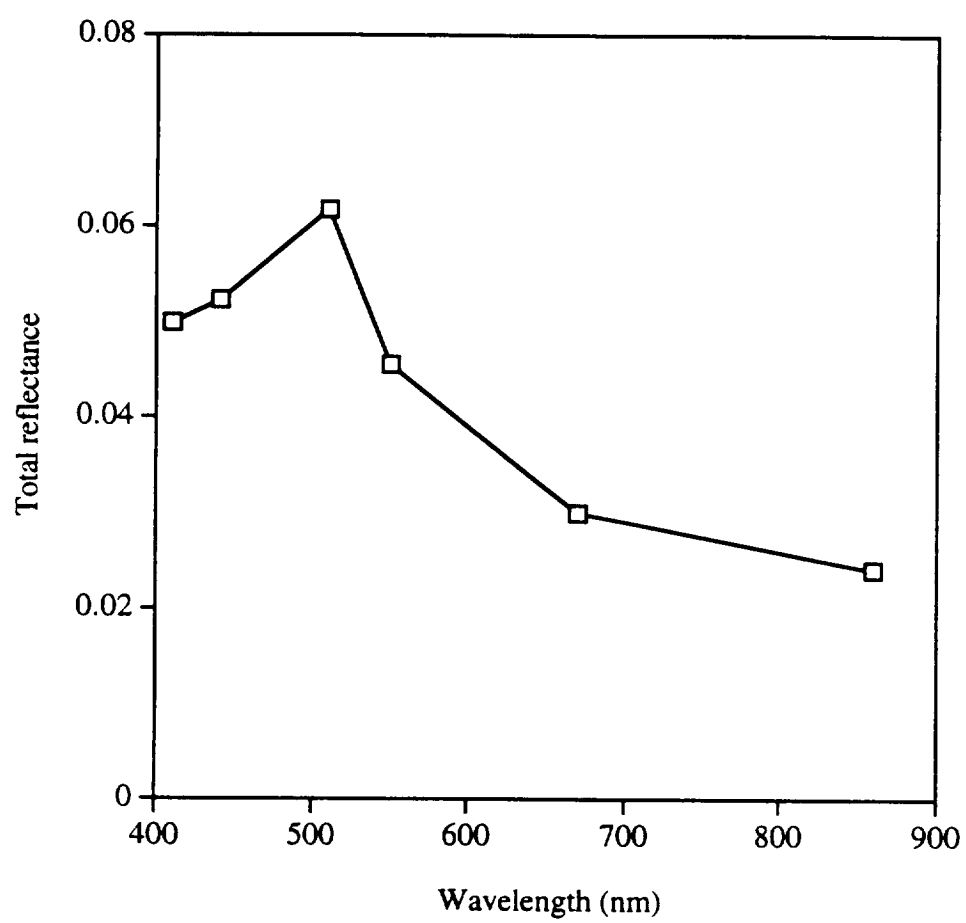


Fig. 2(c)

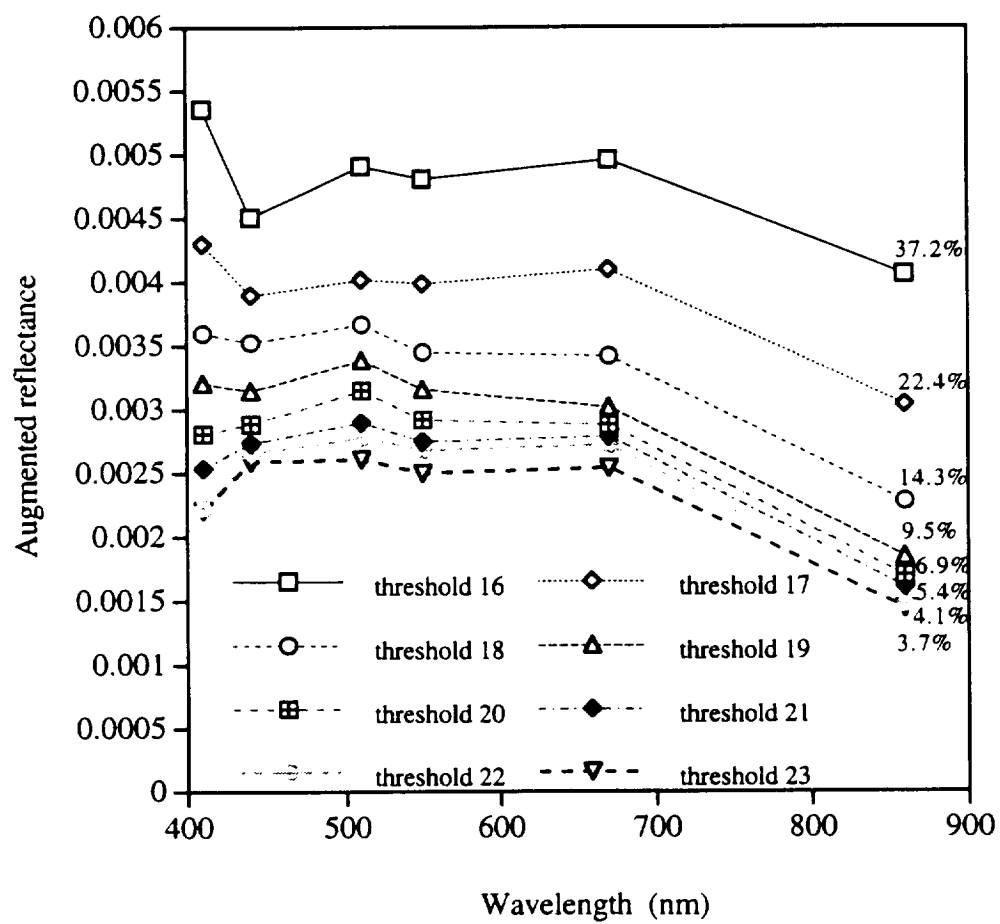
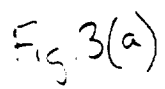


Fig. 2(d)



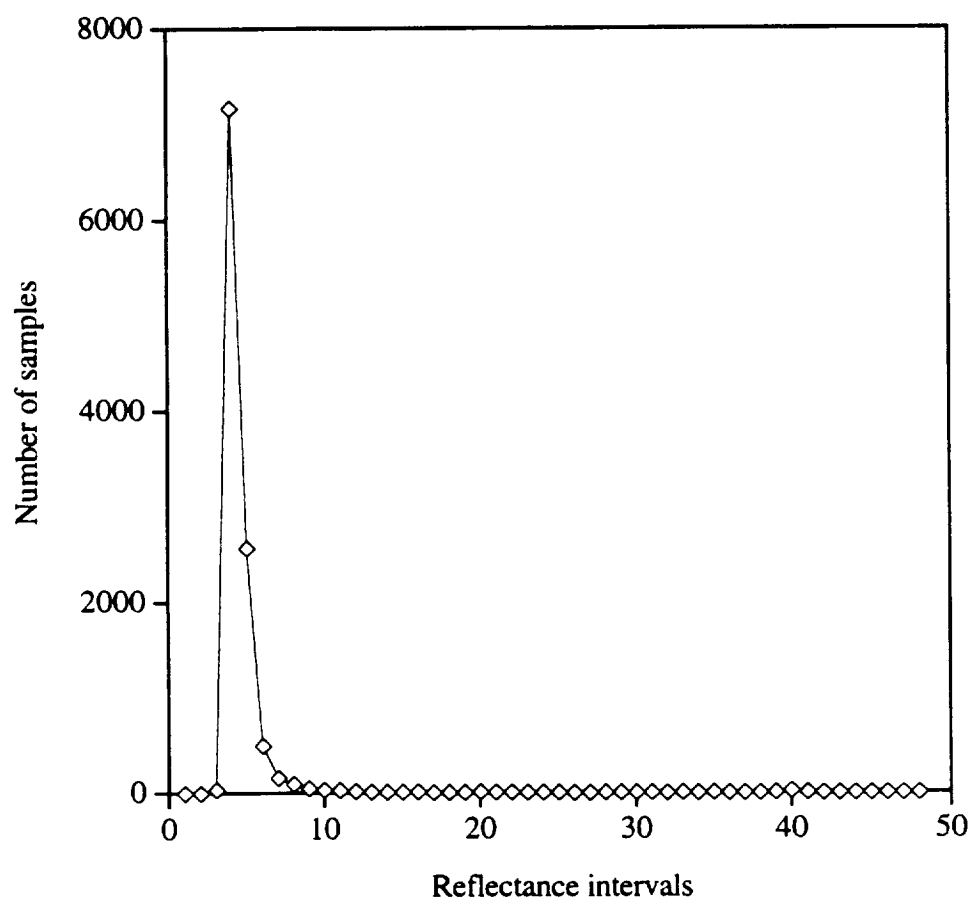


Fig. 3(b)

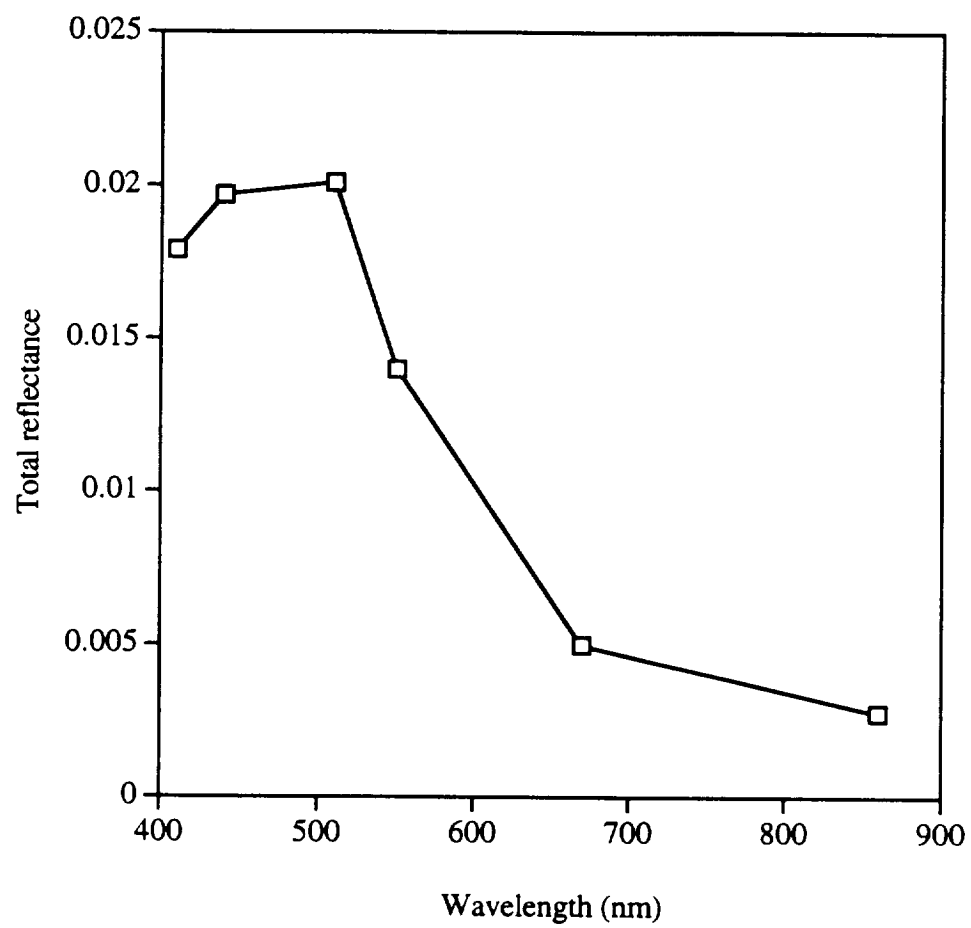


Fig. 3(c).

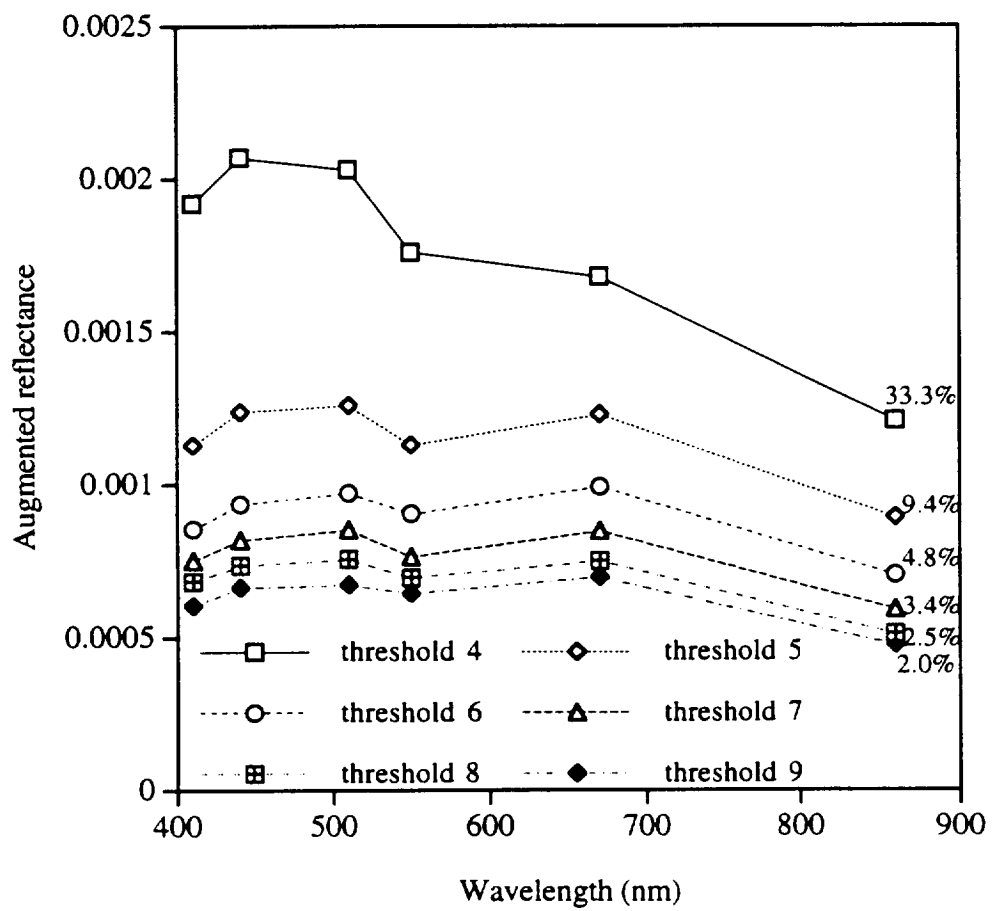


Fig. 3(d).

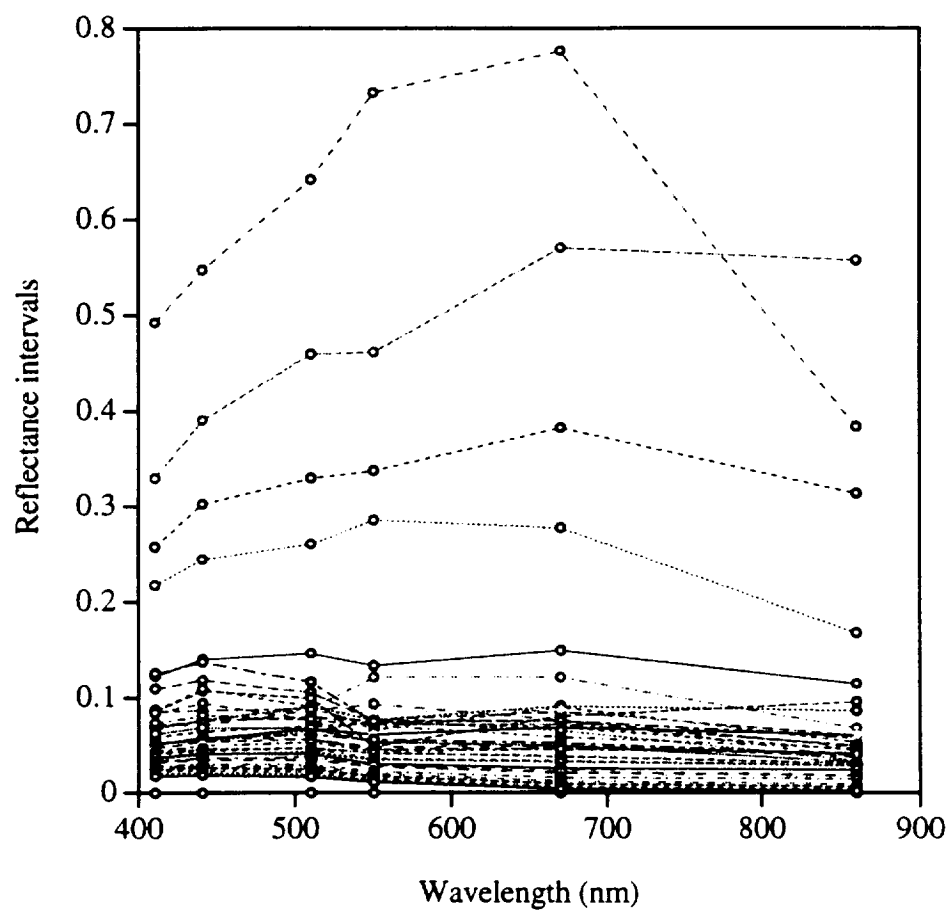


Fig. 4(a).

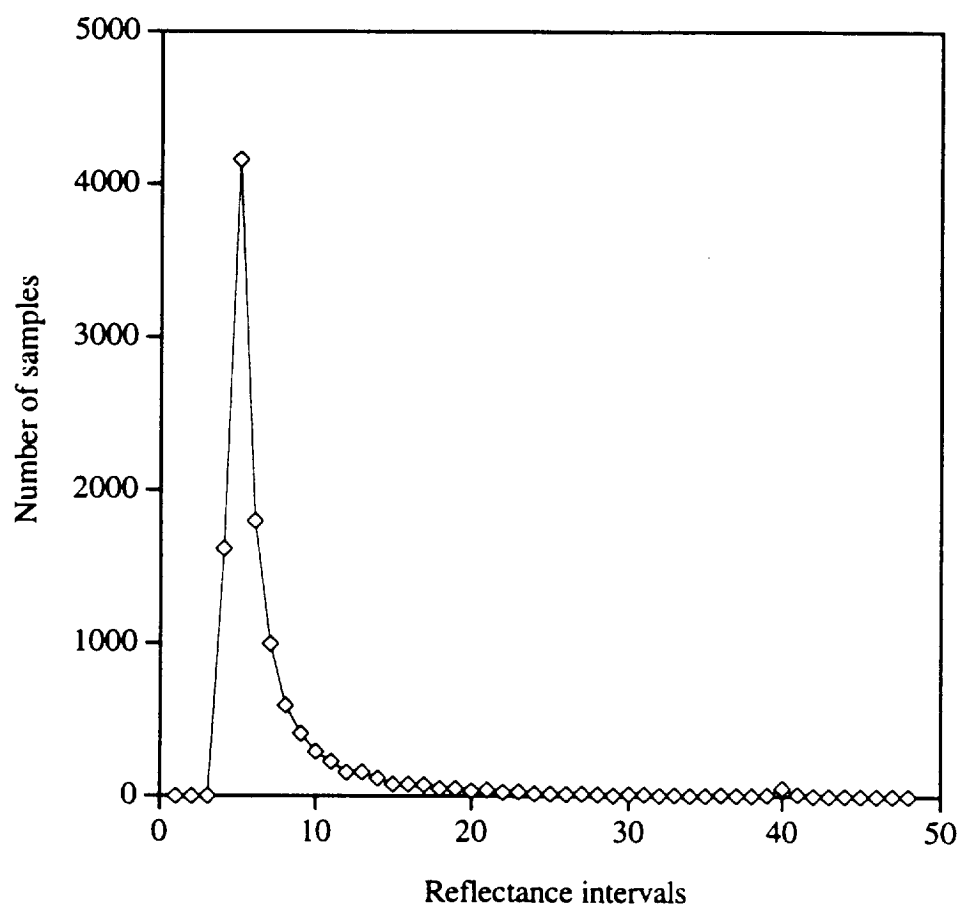


Fig. 4(b).

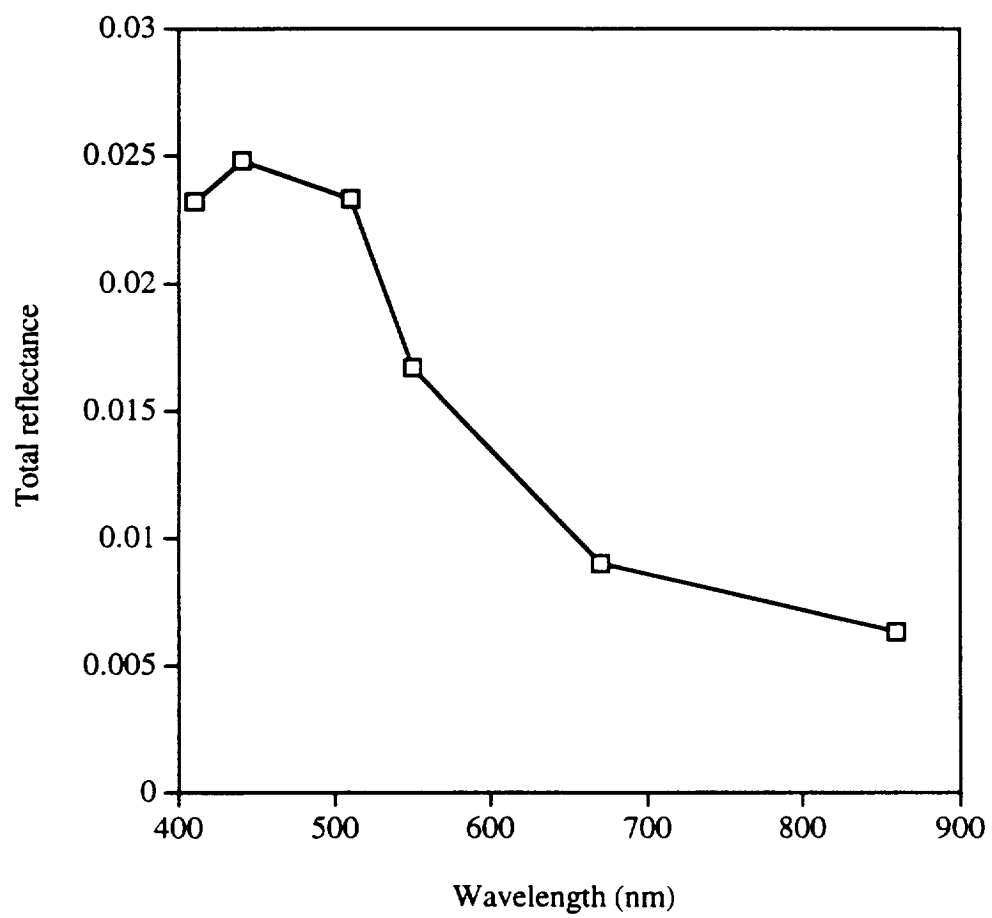


Fig. 4(c).

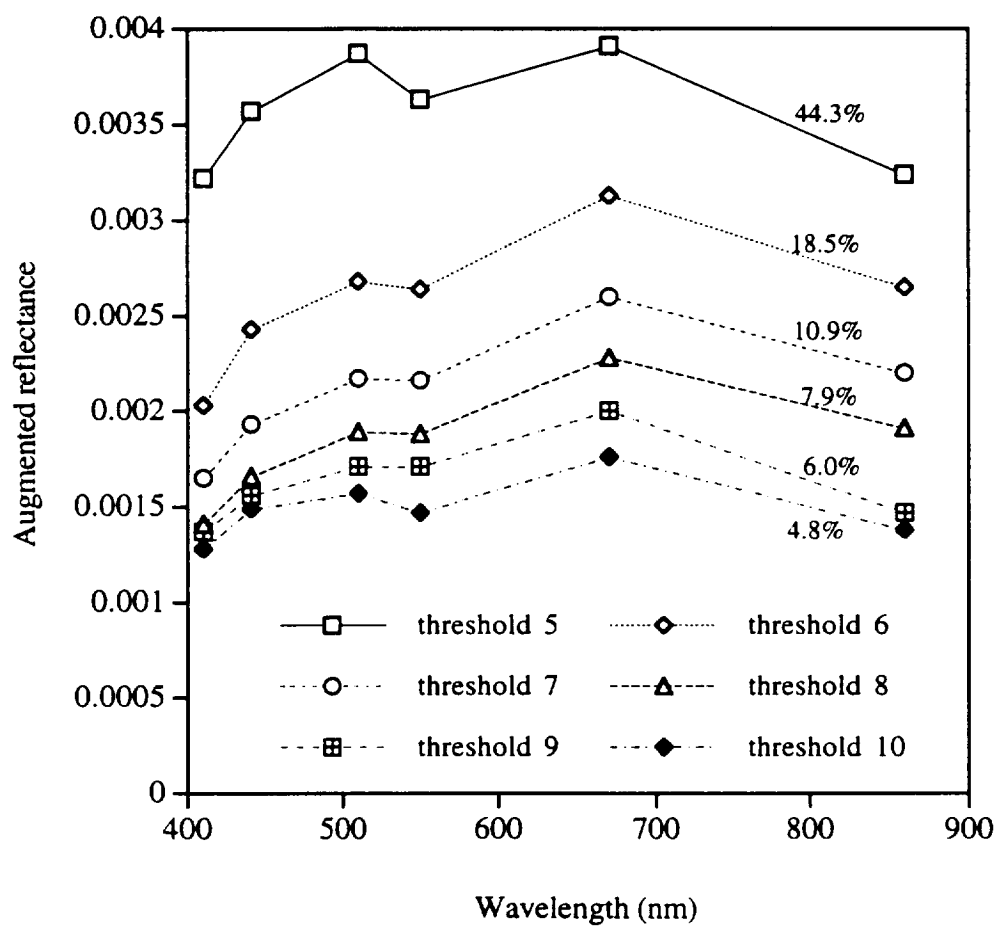


Fig. 4(d).

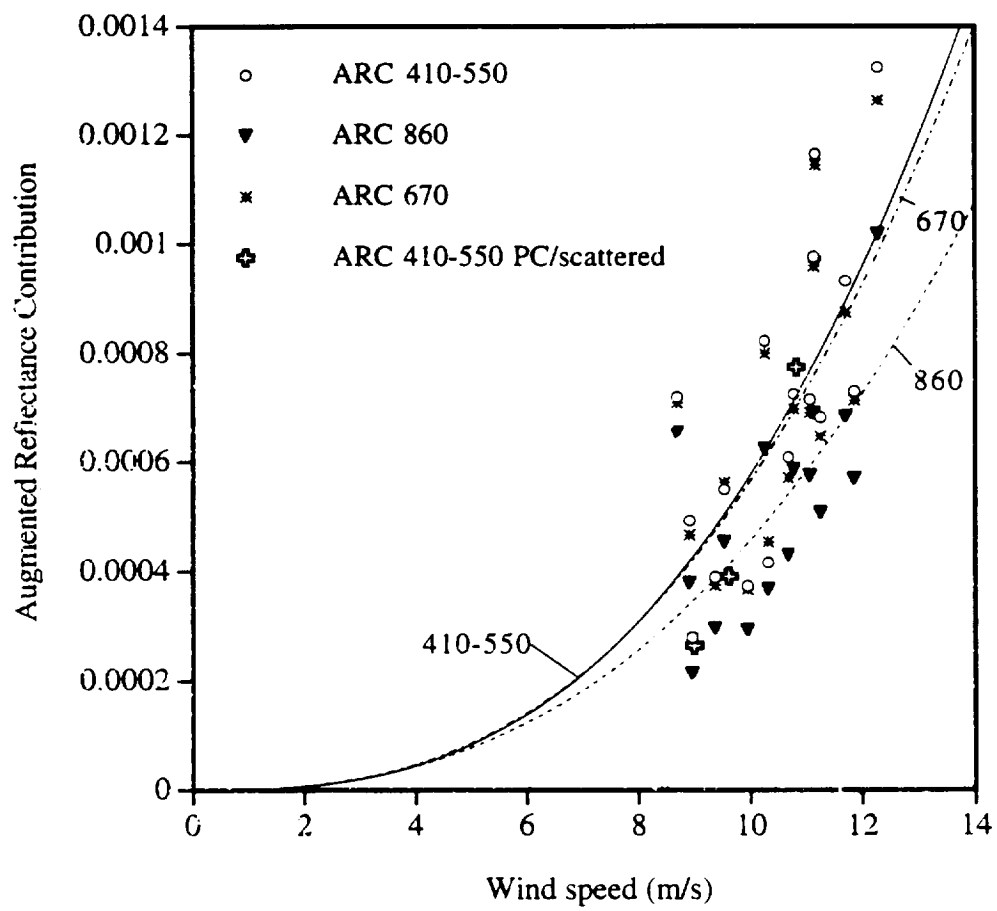


Fig. 5.

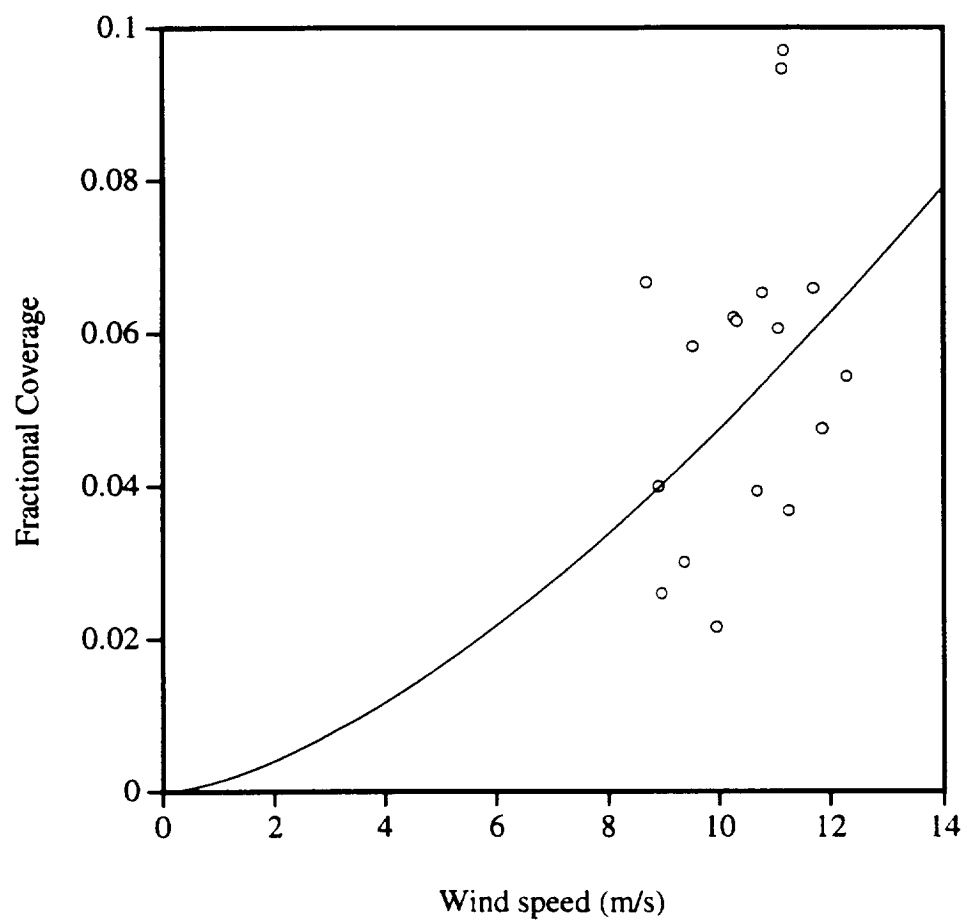


Fig. 6.

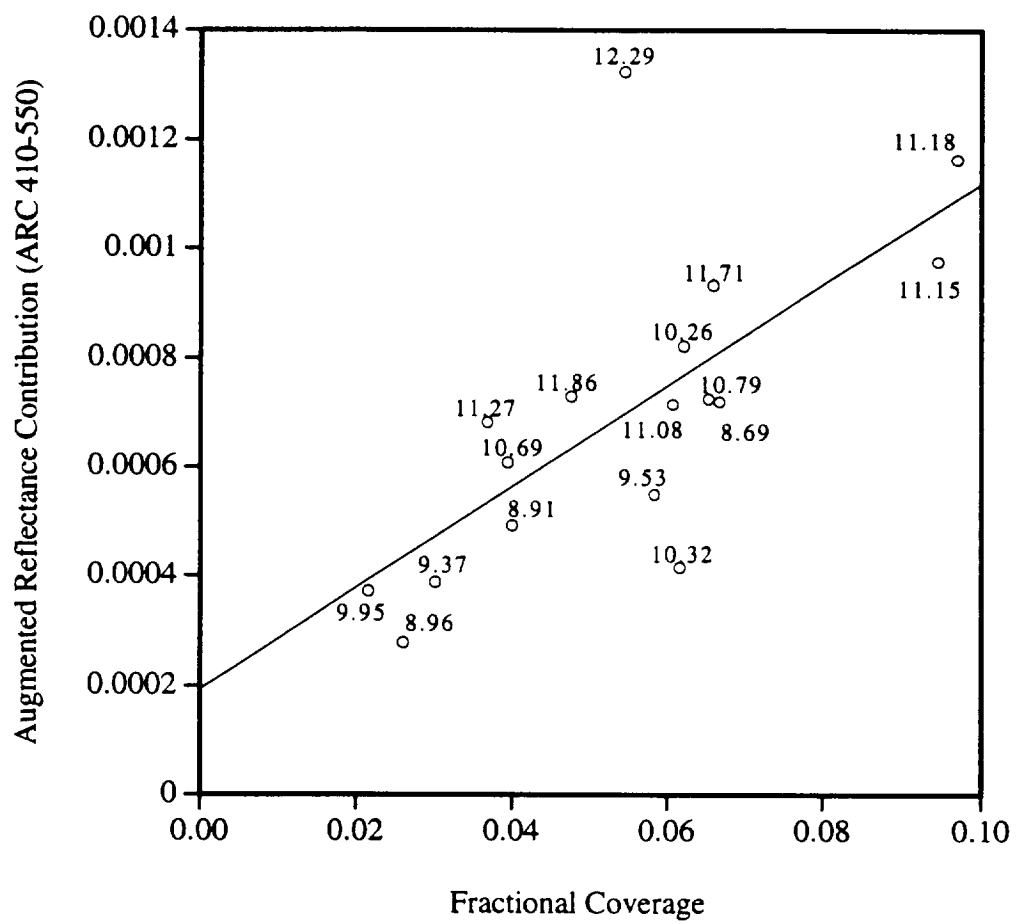


Fig. 7.

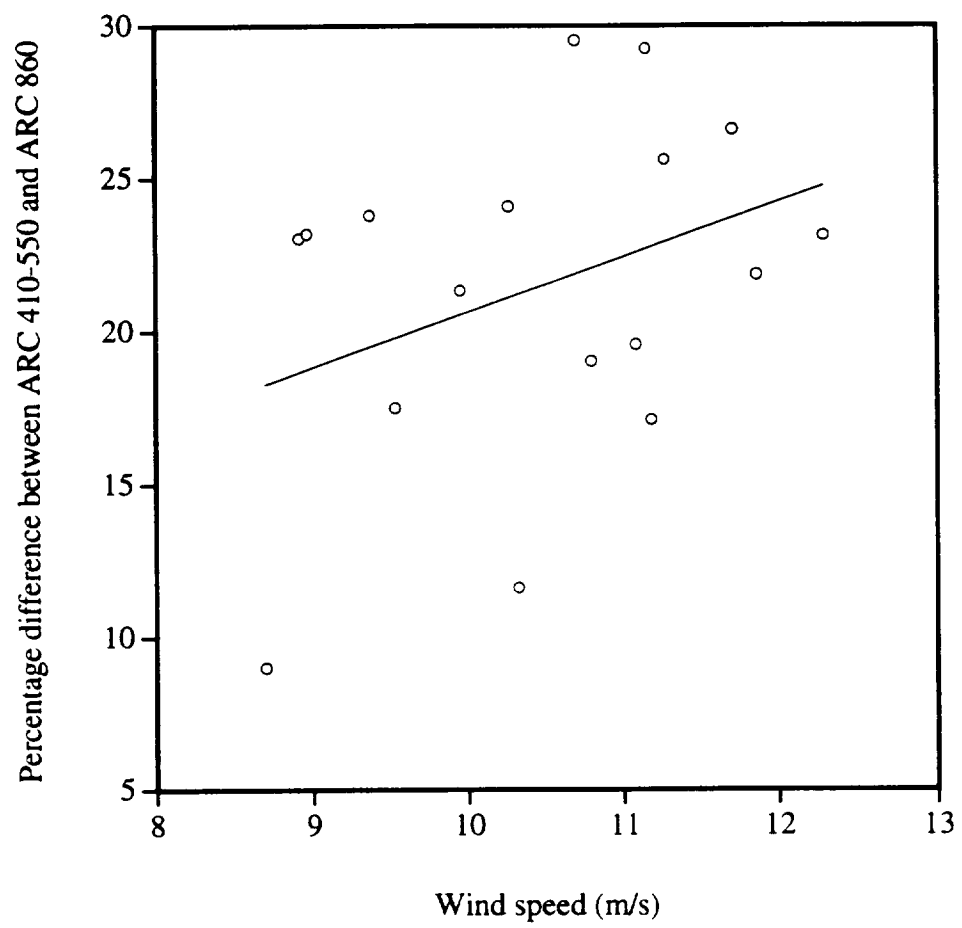


Fig. 8.

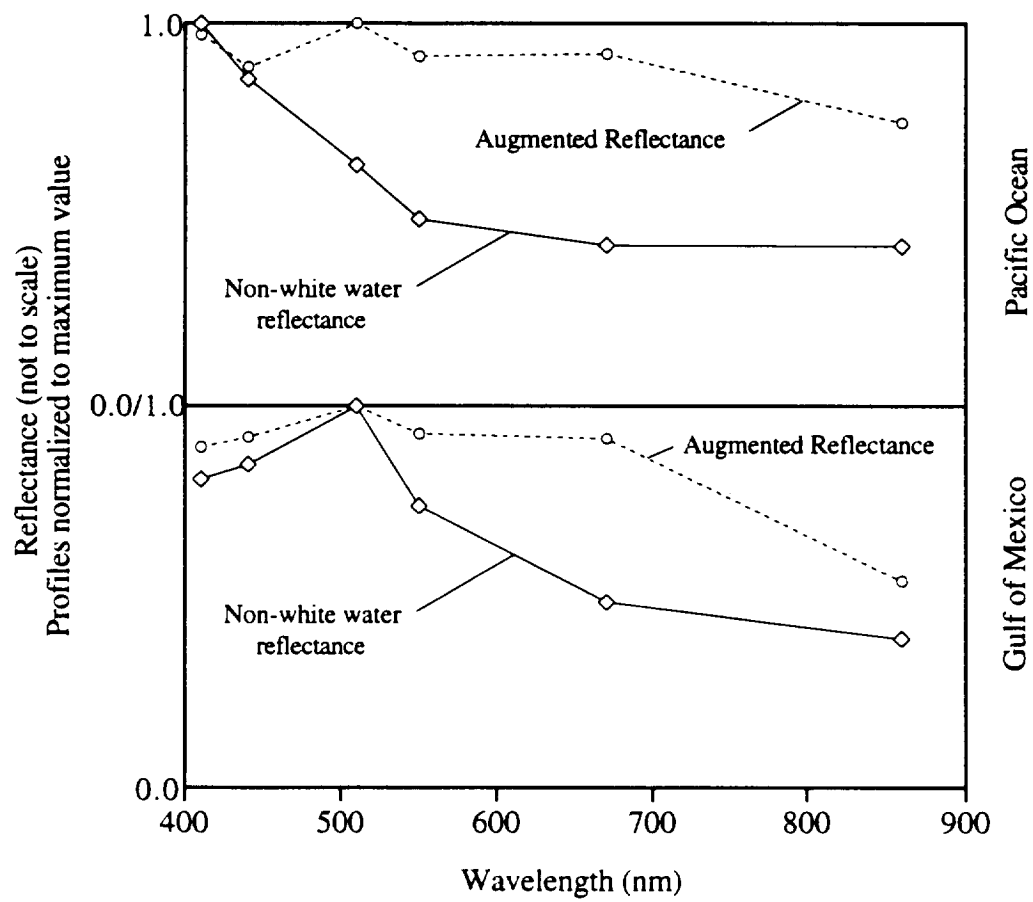


Fig. 9.

Appendix 5

Atmospheric Correction of Ocean Color Sensors: Analysis of the Effects of Residual Instrument Polarization Sensitivity

By

Howard R. Gordon, Tao Du, and Tianming Zhang

Department of Physics

University of Miami

Coral Gables, FL 33124

Submitted to *Applied Optics*

Abstract

We provide an analysis of the influence of instrument polarization sensitivity on the radiance measured by space-borne ocean-color sensors. Simulated examples demonstrate the influence of polarization sensitivity on the retrieval of the water-leaving reflectance (ρ_w). A simple method for partially correcting for polarization sensitivity — replacing the linear polarization properties of the top-of-atmosphere reflectance by that from a Rayleigh-scattering atmosphere — is provided and its efficacy evaluated. It is shown that it improves ρ_w retrievals as long as the polarization sensitivity of the instrument does not vary strongly from band to band. Of course, a complete polarization-sensitivity characterization of the ocean-color sensor is required to implement the correction.

Introduction

The spectral reflectance of the ocean atmosphere system is modified by the concentration of marine phytoplankton, microscopic plants that constitute the first link in the marine food chain.¹ The component of the spectral reflectance that is due to photons backscattered *out* of the ocean (the water-leaving reflectance) is usually termed the ocean color. The flight of the Coastal Zone Color Scanner (CZCS)^{2,3} on the satellite NIMBUS-7 proved the feasibility of measuring the concentration of the photosynthetic pigment chlorophyll *a* (a surrogate for the concentration of phytoplankton in the water) on a global scale. Based on the CZCS success, several follow-on ocean color missions have been planned, e.g., the sea-viewing wide-field-of-view sensor (SeaWiFS),⁴ and the moderate resolution imaging spectroradiometer (MODIS).⁵

The contribution of the water-leaving reflectance, ρ_w , to the reflectance of the ocean-atmosphere system, ρ_t , is $\lesssim 10\%$, the remainder being due to photons scattered by the atmosphere and reflected from the sea surface. Extraction of ρ_w from ρ_t is referred to as atmospheric correction. As ρ_w is a small component of ρ_t , adequate atmospheric correction can only be effected if ρ_t is accurately measured, e.g., a 5% error in ρ_t translates into \sim a 50% error in ρ_w in the blue in waters with low phytoplankton concentrations, and a larger error in waters with higher concentrations. The goal set for SeaWiFS and MODIS is the retrieval of ρ_w in such waters with an uncertainty of $\pm 5\%$.

In ocean color remote sensing, it has been assumed implicitly that the sensor is able to accurately measure (subject to calibration limitations⁶) the radiance exiting the top of the atmosphere (TOA). However, the radiance reflected from the ocean-atmosphere system can be strongly polarized.⁷ Since all radiometers display some sensitivity to the polarization state of the radiance they intend to measure, generally a biased measurement will be obtained. Although the ocean-viewing radiometers are generally designed to have low polarization sensitivity, e.g., for SeaWiFS and MODIS it was specified that the response vary by $< 2\%$ for all linear polarization states of the incident radiance, some may not meet the design requirements. Others, e.g., the Spectroscopic Imagers (SPIM) on the Midcourse Space Experiment (MSX),⁸ were not specifically designed to

examine strongly polarized sources, and may be quite sensitive to polarization. Because of this, it is of interest to understand the influence of residual instrument polarization sensitivity on the retrieved products, and to devise a method to minimize it. This is the focus of the present paper.

We begin by reviewing the measurements required to specify the polarization sensitivity of a radiometer, show how the “measured” TOA radiance depends on the polarization state of the light, and provide examples of the polarization properties of the TOA radiance. Next, we review the atmospheric correction algorithm and use it to derive the desired water-leaving radiance by operating it with the radiance measured by the sensor if the instrument’s polarization sensitivity is ignored. Finally, we propose a simple algorithm for making an approximate correction for the effects of residual instrument polarization sensitivity, and provide some examples of its efficacy.

2. Polarization Sensitivity

2A. Sensor polarization sensitivity

We assume that the radiometer can be modeled as an optical system, which responds in a manner dependent on the state of polarization of the radiance to be measured, and a detector with a response that is independent of the state of polarization of the radiance. The radiance is specified by the column vector \mathbf{I} , the Stokes vector,^{9–12}

$$\begin{pmatrix} I \\ Q \\ U \\ V \end{pmatrix},$$

where

$$\begin{aligned} I &= \langle E_t E_t^* + E_r E_r^* \rangle, \\ Q &= \langle E_t E_t^* - E_r E_r^* \rangle, \\ U &= \langle E_t E_r^* + E_r E_t^* \rangle, \\ V &= i \langle E_t E_r^* - E_r E_t^* \rangle, \end{aligned} \tag{1}$$

E_t and E_r are the components of the electric field in any two orthogonal directions normal to the direction of propagation, the superscript $*$ indicates the complex conjugate, and the angle bracket denotes the average over time. The first element of the Stokes vector, I , is the radiance that would

be measured with a detector that is insensitive to the polarization state of the field. We refer to it here as the *radiance*. The polarization state of the radiation is determined by the other components of \mathbf{I} , for example, the degree of polarization of the radiation is

$$P = \frac{\sqrt{Q^2 + U^2 + V^2}}{I}, \quad (2)$$

where $0 \leq P \leq 1$. The limit $P = 0$ corresponds to a completely unpolarized radiation field, while $P = 1$ corresponds to a completely polarized radiation field. Radiation fields with intermediate values of P are partially polarized. Any field with a degree of polarization P can be represented as a linear combination of an unpolarized field of radiance $(1 - P)I$ and a completely polarized field of radiance PI , i.e.,

$$\mathbf{I} = \begin{pmatrix} I \\ Q \\ U \\ V \end{pmatrix} = \begin{pmatrix} (1 - P)I \\ 0 \\ 0 \\ 0 \end{pmatrix} + \begin{pmatrix} PI \\ Q \\ U \\ V \end{pmatrix}.$$

Fields for which $V = 0$ are said to be linearly polarized.

The action of the optical system on \mathbf{I} is to produce a new Stokes vector \mathbf{I}_m , given by

$$\mathbf{I}_m = \mathbf{M}\mathbf{I},$$

where \mathbf{M} is a 4×4 matrix (the Mueller matrix). The measured radiance, I_m , is the top element of the column vector \mathbf{I}_m . The transform matrix \mathbf{M} describes the action of the instrument on \mathbf{I} . It follows from the action of the instrument on the fields,

$$\begin{pmatrix} E_r \\ E_l \end{pmatrix}_m = \mathbf{A} \begin{pmatrix} E_r \\ E_l \end{pmatrix} = \begin{pmatrix} A_1 & A_4 \\ A_3 & A_2 \end{pmatrix} \begin{pmatrix} E_r \\ E_l \end{pmatrix}, \quad (3)$$

where E_r and E_l are the electric field components of the beam in the directions perpendicular and parallel to a reference plane, respectively. This reference plane is arbitrary. It is defined using the basis vectors \hat{l} and \hat{r} , respectively, parallel and perpendicular to the reference plane. The plane itself is formed by \hat{l} and the direction of propagation of the radiance, $\hat{r} \times \hat{l}$. Starting from the Eq. (3) and the definition of I , Q , U , and V in terms of the fields, the derivation of \mathbf{M} from \mathbf{A} is straightforward.^{9,13} In what follows we will omit the explicit dependence of \mathbf{I} and \mathbf{M} on wavelength λ for simplicity.

Viewing the earth, the sensor responds to the Stokes vector \mathbf{I}_t exiting the top of the atmosphere (TOA). It is defined with respect to a reference plane determined by the propagation direction of the light (specified by the polar angles θ , ϕ) and the vertical, with $\hat{\ell}_t$ and \hat{r}_t , respectively parallel and perpendicular to this plane. However, the transformation matrix \mathbf{M} is defined relative to a reference plane ($\hat{\ell}$ and \hat{r}) fixed with respect to the instrument. If these two reference planes are not coincident, then a transformation (rotation) of the Stokes vector from one reference plane to the other has to be made. Letting $\hat{\ell}_t \bullet \hat{\ell} = \cos \alpha$, we have¹³

$$\mathbf{I}_m = \mathbf{M}\mathbf{R}(\alpha)\mathbf{I}_t, \quad (4)$$

where

$$\mathbf{R}(\alpha) \equiv \begin{pmatrix} 1 & 0 & 0 & 0 \\ 0 & \cos 2\alpha & \sin 2\alpha & 0 \\ 0 & -\sin 2\alpha & \cos 2\alpha & 0 \\ 0 & 0 & 0 & 1 \end{pmatrix},$$

with α measured clockwise from $\hat{\ell}_t$ to $\hat{\ell}$ looking toward the source. Assuming that the detector itself is not sensitive to the polarization state of the light, Eq. (4) shows that the “measured” radiance I_m is related to the components of the “true” stokes vector \mathbf{I}_t by

$$I_m = M_{11}I_t + M_{12}(\cos 2\alpha Q_t + \sin 2\alpha U_t) + M_{13}(-\sin 2\alpha Q_t + \cos 2\alpha U_t) + M_{14}V_t, \quad (5)$$

where M_{11} , M_{12} , M_{13} and M_{14} are the elements of the first row of the matrix \mathbf{M} . For the radiance backscattered to the top of the atmosphere, $V_t \approx 0$ (refer to Subsection 2B), so I_m in Eq. (5) can be rewritten as

$$I_m = M_{11}I_t + M_{12}(\cos 2\alpha Q_t + \sin 2\alpha U_t) + M_{13}(-\sin 2\alpha Q_t + \cos 2\alpha U_t) \quad (6)$$

Clearly, the measured radiance I_m is not I_t , I_m depends on the characteristics of the instrument (M_{11} , M_{12} and M_{13}) and the characteristics of the radiation (I_t , Q_t and U_t). Of course, it is desirable to have an ideal instrument with \mathbf{M} being a unit matrix ($M_{12} = M_{13} = 0$ and $M_{11} = 1$), i.e., an instrument having no polarization sensitivity. However, this is not practical. All instruments, unavoidably, have some polarization sensitivity. On the other hand, if the degree of polarization of the radiance received by the instrument is zero ($Q_t = U_t = V_t = 0$), the measured radiance I_m will be the true radiance I_t . But, as the upwelling radiance we intend to measure is polarized, I_m will never be I_t .

In order to study the effect of the polarization sensitivity of the instrument, we need to know only three elements, M_{11} , M_{12} and M_{13} , in the transform matrix \mathbf{M} . We now describe a series of hypothetical experiments to determine M_{11} , M_{12} and M_{13} of the instrument. First, choose a reference plane for the instrument, with basis vectors \hat{l} and \hat{r} parallel and perpendicular to this reference plane, respectively, and $\hat{r} \times \hat{l}$ in the propagation direction of the beam. Then illuminate the instrument with linearly polarized radiance ($P = 1$) of radiance I_0 in the following ways [here, to conserve space, we write \mathbf{I} as a row vector, $\mathbf{I} = (I, Q, U, V)$]:

(1) with the oscillation direction (plane) of the electric vector along \hat{l} , so the incident Stokes vector is $\mathbf{I}_{in} = I_0(1, 1, 0, 0)$, for which the instrument records a radiance $I_{\hat{l}}$, and from Eq. (6) with $\alpha = 0$ (since M_{11} , M_{12} and M_{13} are defined on this reference plane) we have

$$I_{\hat{l}} = (M_{11} + M_{12})I_0;$$

(2) with the oscillation direction along \hat{r} , i.e., $\mathbf{I}_{in} = I_0(1, -1, 0, 0)$, for which the instrument records a radiance $I_{\hat{r}}$,

$$I_{\hat{r}} = (M_{11} - M_{12})I_0;$$

(3) with its oscillation direction along the line which bisecting the angle between \hat{l} and \hat{r} , i.e., $\mathbf{I}_{in} = I_0(1, 0, 1, 0)$, for which the instrument records a radiance $I_{\hat{lr}}$,

$$I_{\hat{lr}} = (M_{11} + M_{13})I_0.$$

From these experimental results, M_{11} , M_{12} and M_{13} can be found easily:

$$\begin{aligned} M_{11} &= \frac{I_{\hat{l}} + I_{\hat{r}}}{2I_0}, \\ M_{12} &= \frac{I_{\hat{l}} - I_{\hat{r}}}{2I_0}, \\ M_{13} &= \frac{I_{\hat{lr}}}{I_0} - M_{11}. \end{aligned}$$

Considering that M_{11} can be determined during instrument calibration using an unpolarized source, we use $M_{11} = 1$ in this paper. Upon defining q_t and u_t as

$$q_t = \frac{Q_t}{I_t},$$

$$u_t = \frac{U_t}{I_t},$$

Eq. (6) can be rewritten

$$I_m = I_t [1 + m_{12}(\cos 2\alpha q_t + \sin 2\alpha u_t) + m_{13}(-\sin 2\alpha q_t + \cos 2\alpha u_t)] \quad (7)$$

with m_{12} and m_{13} defined by

$$m_{12} = \frac{M_{12}}{M_{11}},$$

$$m_{13} = \frac{M_{13}}{M_{11}}.$$

Even if I_0 is unknown in the above experiment, we can still obtain the polarization sensitivity of instrument by finding m_{12} and m_{13} from the following equations

$$m_{12} = \frac{I_i - I_r}{I_i + I_r},$$

$$m_{13} = \frac{2I_{ir}}{I_i + I_r} - 1.$$

2B. Polarization properties of I_t

To examine the influence of the instrument polarization sensitivity, we need to know the polarization characteristics of the radiance exiting the top of the atmosphere. For remote sensing of ocean color, in general I_t can be written as

$$I_t = I_r + I_a + I_{ra} + tI_w, \quad (8)$$

where I_r is the contribution from the Rayleigh scattering, I_a is the contribution from the aerosol scattering, I_{ra} is the contribution from the interaction between molecular and aerosol scattering, tI_w is the water leaving radiance diffused transmitted (t) to the top of the atmosphere. This yields

$$I_t = I_r + I_a + I_{ra} + tI_w.$$

The water-leaving component tI_w is at most (in the blue) $\sim 10\%$ of the total I_t , and considering the incident light field on the top of the atmosphere from the sun is completely unpolarized, the polarization state of I_t is mainly governed by the atmospheric scattering contribution. For

Rayleigh scattering, its polarization state is well known and easy to determine. But for aerosols, their scattering properties, and the polarization state of the scattered light, are generally unknown, as they strongly depend on their particle size distributions and refractive indexes.

Consider a spherical coordinate system with origin at the TOA, z axis directed downward, and x axis directed away from the sun (sun's rays are in the x - z plane). Let the direction of propagation of a photon be specified by the polar and azimuth angles, θ and ϕ , in this system. The solar beam has $\theta = \theta_0$ and $\phi = 0$. Photons exiting the TOA have $\theta > 90^\circ$. Using τ to represent the optical depth measured from the TOA, the propagation of \mathbf{I} at a wavelength λ is governed by the vector radiative transfer equation (VRTE)

$$\cos \theta \frac{d\mathbf{I}(\lambda, \tau, \theta, \phi)}{d\tau} = -\mathbf{I}(\lambda, \tau, \theta, \phi) + \omega_0 \int_{4\pi} \mathbf{R}(\alpha) \mathbf{P}(\lambda, \tau, \theta', \phi' \rightarrow \theta, \phi) \mathbf{R}'(\alpha') \mathbf{I}(\lambda, \tau, \theta', \phi') d\Omega', \quad (9)$$

where \mathbf{P} is the phase matrix, and \mathbf{R} is the rotation matrix. As mentioned in Subsection 2A, the reference plane for \mathbf{I} is defined by the direction of propagation and the z axis, i.e., the reference plane is perpendicular to the ocean surface. It should be noted that there are two rotations among three reference planes whenever a scattering occurs,¹⁰ since the phase matrix is defined on the scattering plane (determined by the incident light and the scattered light). One must first rotate the incident reference plane to the scattering plane, then apply phase matrix \mathbf{P} , and finally, rotate the scattering plane to the scattered reference plane. The boundary condition at the top of the atmosphere is

$$\mathbf{I}(0; \theta, \phi) = \begin{pmatrix} F_0 \\ 0 \\ 0 \\ 0 \end{pmatrix} \delta(\cos \theta - \cos \theta_0) \delta(\phi - \phi_0), \quad \theta_0 < \pi/2.$$

The boundary condition at the (assumed flat) sea surface is given by

$$\mathbf{I}(\tau_1; \theta_r, \phi_r) = \mathbf{F}(\theta_i) \mathbf{I}(\tau_1; \theta_i, \phi_i), \quad (10)$$

where the Fresnel reflection Mueller matrix \mathbf{F} is

$$\mathbf{F}(\theta_i) = \begin{pmatrix} \rho_+(\theta_i) & \rho_-(\theta_i) & 0 & 0 \\ \rho_-(\theta_i) & \rho_+(\theta_i) & 0 & 0 \\ 0 & 0 & \rho_{33}(\theta_i) & 0 \\ 0 & 0 & 0 & \rho_{33}(\theta_i) \end{pmatrix}, \quad (11)$$

with $\theta_r = \pi - \theta_i$ and $\phi_r = \phi_i$. The factors $\rho_\pm(\theta_i)$ and $\rho_{33}(\theta_i)$ are given by

$$\rho_\pm(\theta_i) = \frac{1}{2} \left(\frac{\cos \theta_i - \sqrt{n^2 - \sin^2 \theta_i}}{\cos \theta_i + \sqrt{n^2 - \sin^2 \theta_i}} \right)^2 \left[\left(\frac{\sin^2 \theta_i - \cos \theta_i \sqrt{n^2 - \sin^2 \theta_i}}{\sin^2 \theta_i + \cos \theta_i \sqrt{n^2 - \sin^2 \theta_i}} \right)^2 \pm 1 \right],$$

$$\rho_{33}(\theta_i) = \left(\frac{\cos \theta_i - \sqrt{n^2 - \sin^2 \theta_i}}{\cos \theta_i + \sqrt{n^2 - \sin^2 \theta_i}} \right)^2 \left(\frac{\sin^2 \theta_i - \cos \theta_i \sqrt{n^2 - \sin^2 \theta_i}}{\sin^2 \theta_i + \cos \theta_i \sqrt{n^2 - \sin^2 \theta_i}} \right).$$

The aerosol scattering phase matrix has the following form for spherical particles:

$$\mathbf{P}_a(\Theta) = \begin{pmatrix} P_{11} & P_{12} & 0 & 0 \\ P_{12} & P_{11} & 0 & 0 \\ 0 & 0 & P_{33} & P_{34} \\ 0 & 0 & -P_{34} & P_{33} \end{pmatrix}, \quad (12)$$

where P_{11} , P_{12} , P_{33} and P_{34} are functions of the scattering angle Θ . For the aerosol models used in this study, the phase matrices are computed by using the Mie theory. The Rayleigh phase matrix, \mathbf{P}_r , is

$$\mathbf{P}_r(\Theta) = \frac{3}{16\pi} \begin{pmatrix} 1 + \cos^2 \Theta & -\sin^2 \Theta & 0 & 0 \\ -\sin^2 \Theta & 1 + \cos^2 \Theta & 0 & 0 \\ 0 & 0 & 2 \cos \Theta & 0 \\ 0 & 0 & 0 & 2 \cos \Theta \end{pmatrix}, \quad (13)$$

where Θ is the scattering angle. Note that the depolarization factor¹⁴ has been set to zero.

The VRTE can be solved by the Successive Order Method and the Monte-Carlo Method, in a similar way used for solving the scalar radiative transfer equation (SRTE). However, instead of solving a single equation in the SRTE approximation, we have to solve four coupled equations.

Although the upwelling radiance I_t at the TOA is not the result of just single scattering, we gain some understanding by examining the Rayleigh and aerosol single scattering contributions to I_t . From single scattering theory, with the incident light on top of the atmosphere completely unpolarized, the upwelling radiance exiting the top of the atmosphere by direct molecular or aerosol scattering (i.e., without considering the reflection from the ocean surface) is given by¹⁴

$$\begin{pmatrix} I_t \\ Q_t \\ U_t \\ V_t \end{pmatrix} = \frac{F_0 \cos \theta_0 \omega_0}{\cos \theta_0 - \cos \theta} \left[1 - \exp\left(\frac{\tau_1}{\cos \theta} - \frac{\tau_1}{\cos \theta_0}\right) \right] \begin{pmatrix} P_{11}(\Theta) \\ P_{12}(\Theta) \cos 2\alpha \\ -P_{12}(\Theta) \sin 2\alpha \\ 0 \end{pmatrix}, \quad (14)$$

where ω_0 is the single scattering albedo, τ_1 is the optical thickness of the molecules or aerosols, and Θ is the scattering angle. It can be seen that there is no contribution to V_t from single Rayleigh scattering or single aerosol scattering. Observing that there is no P_{34} term in Rayleigh scattering phase matrix, there is no contribution to V_t from pure Rayleigh multiple scattering either. The term V_t is the result of multiple aerosol scattering (including the aerosol and Rayleigh interaction terms) because of the existence of element P_{34} in the scattering phase matrix of aerosols, or the

result of single scattering followed or preceded by reflection from the sea surface. Our simulation results agree with the computations of Kattawar *et al.*,^{15,16} that $V_t \approx (V_a + V_{ra}) \sim 10^{-3} I_t$. This is why we can assume $V_t \approx 0$ in Eq. (6). It means circular polarization effects are ignored.

From Eq. (14) we can also see that, in the case of single scattering, Q and U (or the degree of polarization) are introduced mainly because of the existence of the scattering phase matrix element P_{12} for Rayleigh and aerosol scattering. Figure 1 provides P_{12} for Rayleigh scattering and aerosol scattering as a function of scattering angle Θ . The aerosol models used in the figure are the Shettle and Fenn¹⁷ Maritime and Tropospheric models at 80% relative humidity, labeled as M80 and T80 respectively. It is observed from Figure 1 that P_{12} for the aerosol is usually small compared to that for Rayleigh scattering, and that this element for Rayleigh scattering is a strong function of the scattering angle Θ . In the backward directions ($90^\circ < \Theta \leq 180^\circ$), when Θ is greater than $\sim 160^\circ$, the P_{12} elements for Rayleigh and aerosol scattering are comparable. In contrast, when $90^\circ < \Theta \leq 150^\circ$ Rayleigh scattering has a very strong effect on the polarization state. Thus, when single scattering dominates, the degree of polarization will be small for large scattering angle Θ ($\Theta > 160^\circ$), while when Θ is less than 150° , strong polarization effects will be encountered, caused largely by Rayleigh scattering.

By employing the aerosol models described in Gordon and Wang,¹⁸ the Stokes vector \mathbf{I}_t can be computed by solving the VRTE. Using a two-layer atmosphere model with molecules confined in the upper layer, and aerosols confined in the lower layer, bounded by a flat Fresnel-reflecting ocean surface, the VRTE was solved using a Monte-Carlo code to provide a pseudo radiance vector \mathbf{I}_t received by the sensor at the top of the atmosphere. The simulations we present were carried out for the M80 and T80 aerosol models in three wavebands (443, 765, and 865 nm), and the aerosol optical thickness for $\lambda = 865$ nm was taken to be 0.2 [$\tau_a(865) = 0.2$].

As the error in I_m [Eq. (7)] is determined by q_t and u_t , the ratios of Q_t/I_t and U_t/I_t computed for M80 at three wavelengths are plotted in Figure 2 as a function of the viewing angle of the sensor, $\theta_v \equiv \pi - \theta$, for $\phi = 90^\circ$. The T80 aerosol model yields similar curves. It should be noted that U_t changes sign on crossing the principal plane ($\phi = 0$). In the figure, we plot U_t for the side of the principal plane for which it is negative. In contrast, Q_t is symmetric with respect to

reflection across the principal plane. These computations show that (1) the degree of polarization, P , generally increases with increasing θ_0 and θ_v ; (2) P can be as large as ~ 0.5 - 0.6 ; (3) Q_t and U_t both contribute significantly to P (Q_t for small θ_v and U_t for large θ_v); and the polarization properties at 765 and 865 nm are similar, but show significantly less polarization than at 443 nm.

These computations can be used to obtain a coarse estimate of the error in I_t induced by the polarization sensitivity. Choose $\hat{\ell}$ and \hat{r} so that $m_{13} = 0$. Then,

$$\frac{\Delta I_t}{I_t} \equiv \frac{I_m - I_t}{I_t} = m_{12}(q_t \cos 2\alpha + u_t \sin 2\alpha).$$

It is easy to show that the maximum value of $(q_t \cos 2\alpha + u_t \sin 2\alpha)$ is $P_t \equiv \sqrt{q_t^2 + u_t^2}$. Thus

$$\frac{\Delta I_t}{I_t} \leq m_{12} P_t.$$

As P_t can be as large as 0.5-0.6, we see that the error in I_t is potentially as large as $\sim 0.5m_{12}$. For $m_{12} \leq 0.02$, the error is at most 1%. In contrast if $m_{12} = 0.10$ the error could be as large as 5%. Gordon¹⁹ has shown that errors of 1% can be tolerated in atmospheric correction as long as the error has the same sign throughout the spectrum, however, errors $\sim 5\%$ cannot be tolerated.

3. Effects of sensor polarization sensitivity on atmospheric correction

In the absence of strongly-absorbing aerosols and instrument polarization sensitivity, the Gordon and Wang atmospheric correction algorithm works well.¹⁹ The error in the retrieved water-leaving reflectance at 443nm $\Delta\rho(443) = t(443)\Delta\rho_w(443)$, where the reflectance $\rho_w \equiv \pi I_w / F_0 \cos \theta_0$, is about $\sim \pm 0.001$ to ± 0.002 . This meets the requirements of MODIS and SeaWiFS. However, since the instrument has a residual polarization sensitivity, and the upwelling radiance I_t we intend to measure is polarized, we cannot be provided with the true I_t . Instead, we will have the biased I_m . Therefore, it is necessary to assess the influence of polarization sensitivity on the Gordon and Wang atmospheric correction algorithm.

We employed simulated I_m pseudo data to study the influence of the polarization sensitivity of the instrument on the performance of the Gordon and Wang atmospheric correction algorithm. Briefly, I_t was computed for the M80 and T80 aerosol models with aerosol optical thickness at 865

nm, $\tau_a(865) = 0.2$. This value of $\tau_a(865)$ is somewhat higher than observed over regions with a pure maritime atmosphere, i.e., not subjected to anthropogenic aerosol or mineral dust transported over the oceans.^{20–22} The water-leaving radiance was taken to be zero. The simulations were carried out for $\theta_0 = 0, 20^\circ, 40^\circ$, and 60° , both at the center, $\theta_v \approx 1^\circ$, and the edge, $\theta_v \approx 45^\circ$, of the SeaWiFS scan with $\phi = 90^\circ$. The combination $\theta_0 = 0$ and $\theta_v \approx 1^\circ$ is omitted because it would be near the center of the sun's glitter pattern. These seven geometries approximately cover the full range of sun-view geometries encountered in progressing along a polar orbit from the equator to a latitude of 60° at the equinox.

The Stokes vector I_t was then introduced into Eq. (7) and I_m computed given the polarization sensitivity of the sensor. A rotation of the reference plane used to define m_{12} and m_{13} does not change $\sqrt{m_{12}^2 + m_{13}^2}$, it only reallocates polarization sensitivity between m_{12} and m_{13} , i.e., it simply changes the definition of the angle α . Thus, for simplicity we set m_{13} equal to zero, and present the results of our study as a function of α .

The Gordon and Wang algorithm¹⁸ uses the SeaWiFS bands at 765 and 865 nm (where $\rho_w = 0$, except in turbid coastal water) to provide atmospheric correction for the visible. Here, we examine the error in the water-leaving reflectance, $t\Delta\rho_w \equiv \Delta\rho$, at 443 nm. To demonstrate the effect of the polarization sensitivity, we examined six sets of values of m_{12} in the three wavebands 443, 765 and 865 nm. The six sets of m_{12} [written $(m_{12}(443), m_{12}(765), m_{12}(865))$] were $m_{12} = (0.10, 0.10, 0.10)$, $m_{12} = (0.05, 0.05, 0.05)$, $m_{12} = (0.05, 0.03, 0.03)$, $m_{12} = (0.02, 0.02, 0.02)$, $m_{12} = (0.05, -0.05, -0.05)$, and $m_{12} = (0.02, -0.02, -0.02)$. As mentioned above $m_{13} = (0, 0, 0)$ for each set. Note that setting m_{13} to zero at all three wavebands, implies that when the plane of polarization of radiation (of constant radiance) entering the sensor is rotated through 360° , the sinusoidal responses (in $2\times$ the rotation angle) of the detectors for the three bands will be either in phase or exactly out of phase with each other. This is not a necessity for the development we present, it is used only to simplify the analysis.

Sample results for the errors in the retrieved water-leaving reflectance at 443 nm are presented in Figure 3, for viewing at the scan edge with $\phi = 90^\circ$, as a function of α . For this fixed viewing geometry, α would be constant; however here, varying α is identical to varying the fraction of

the polarization sensitivity allocated to m_{12} and m_{13} . The solid line connecting the solid dots on the figure provides the error in $t\rho_w$ in the absence of polarization sensitivity, i.e., the result of operating the algorithm with the correct input, I_t not I_m . The simulation results in Figure 3 suggest that (1) large instrument m_{12} causes large errors when polarization state is considered; (2) for m_{12} as small as 0.02, the polarization sensitivity effects are not a problem in most sun-viewing geometries (error $< \pm 0.002$) as long as the m_{12} has the same sign in all band; (3) retrieval errors for $m_{12} = (0.05, 0.05, 0.05)$ are about same as that for $m_{12} = (0.05, 0.03, 0.03)$, and retrieval errors for $m_{12} = (0.05, -0.05, -0.05)$ are about same as that for $m_{12} = (0.10, 0.10, 0.10)$, suggesting that when the m_{12} 's are wavelength dependent, the retrieval errors are larger than that when they are wavelength independent.

It is clear that the performance of the Gordon and Wang algorithm is degraded in the presence of sensor polarization sensitivity. Thus, a method to remove the errors induced by the instrument polarization sensitivity is required.

4. Removal of instrument polarization sensitivity

To completely remove the instrument polarization sensitivity, the polarization properties of the upwelling radiance vector I_t are needed. As aerosol scattering is highly variable, measuring only the upwelling radiance I_t can not provide any information regarding its polarization characteristics. Fortunately, the polarization state of the upwelling radiance I_t is mainly determined by Rayleigh scattering (Figure 1). Figure 4 provides a comparison of Q/I and U/I between Rayleigh scattering (without aerosols) and total scattering (Rayleigh plus aerosols) for $\theta_0 = 60^\circ$. Associated with Q/I and U/I , the subscript “r” refers to Rayleigh scattering and “t” for total scattering. Figure 4 shows that, generally in the blue Q_r/I_r is close to Q_t/I_t , and U_r/I_r is close to U_t/I_t , with $|Q_r/I_r| > |Q_t/I_t|$ and $|U_r/I_r| > |U_t/I_t|$. This can be explained as the aerosol-scattering contribution to Q_t and U_t is generally smaller than its contribution to I_t , which means the existence of the aerosol reduces the degree of polarization, due to pure Rayleigh scattering, in the upwelling radiance vector I_t . For the short wavelength (Figure 4a), the Rayleigh scattering dominates, and there is little difference between Q_r/I_r and Q_t/I_t , and between U_r/I_r and U_t/I_t . For the long wavelengths,

aerosol scattering significantly reduces the degree of polarization of the upwelling radiance.

Observing that a significant portion of q_t and u_t is contributed by Rayleigh scattering, and noting that the Rayleigh scattering properties of the air are well known, we would expect that a significant amount of the polarization-induced error in $t\rho_w(443)$ could be removed by replacing q_t and u_t in Eq. (7) by their Rayleigh-scattering counterparts, Q_r/I_r and U_r/I_r . When q_r close to q_t and u_r close to u_t , the corrected radiance should be close to the true radiance I_t . Using the upwelling radiance at the top of the atmosphere corrected in this manner, instead of the biased I_m , we applied Gordon and Wang atmospheric correction algorithm to the same pseudo data used in Figure 3. The retrieved errors in water-leaving reflectance at 443 nm are presented in Figure 5. It can be observed from the simulations that: (1) generally, the polarization correction works better for smaller m_{12} ; (2) when m_{12} is not dependent on wavelength, it works very well, even for m_{12} as large as (0.1, 0.1, 0.1); (3) when m_{12} is dependent on wavelength, it does not work as well as in (1); (4) when values of m_{12} have different signs in different wavebands, even for m_{12} as small as 2%, it cannot perform well (Figures 5e and 5f). Similar results were obtained for the T80 aerosol model with $\tau_a = 0.2$, although the residual error in $t\rho_w$ was larger. For the purpose of removing the effects of polarization sensitivity, these simulations show the importance of designing instruments for which m_{12} does not depend significantly on wavelength.

We have tried to improve on this polarization-sensitivity correction by accounting for the presence of aerosols, which cause the difference between the q_r - u_r pair and the q_t - u_t pair (Figure 4). However, as the polarization properties of the aerosol cannot be known prior to atmospheric correction, some assumption must be made in this regard. Figure 1 suggests that a reasonable assumption would be that aerosol single scattering completely depolarizes incident radiance, i.e., that the only nonzero element of $\mathbf{P}_a(\Theta)$ is at the top left of the matrix. In the single-scattering approximation to the TOA radiance, this would correspond to replacing the actual q_t by Q_r/I_t and u_t by U_r/I_t . Such a replacement would effect a first-order correction for the depolarization by aerosols. As I_t is unknown, we tried replacing I_t by I_m , the radiance measured without regard for the polarization sensitivity, i.e., in Eq. (7) we replaced q_t and u_t by Q_r/I_m and U_r/I_m , respectively. The results were disappointing, there was no improvement in the polarization correction, and in

many cases the error after correction was larger than that shown in Figure 5 (but less than that in Figure 3). Thus, we rejected this method in favor of replacing q_t and u_t in Eq. (7) by q_r and u_r , respectively.

5. Concluding remarks

We have presented simulations demonstrating the effect of sensor polarization sensitivity on the atmospheric correction of ocean color sensors (Figure 3). In addition, we provided a simple method — substituting the polarization properties of I_t those of a pure Rayleigh-scattering atmosphere — for partially correcting the error induced by polarization sensitivity. This correction method was shown to be effective (even for relatively large polarization sensitivities) as long as the polarization sensitivity of the instrument does not vary strongly from band to band (Figures 5a-d). An attractive feature of this polarization correction is the simplicity of its implementation as part of the overall atmospheric correction algorithm. The possible error in the retrieved values of $t\rho_w$ without polarization correction (Figure 3), underscores the importance of a complete characterization of the polarization sensitivity of an ocean-color sensor prior to launch so that the polarization-sensitivity correction can be applied.

References

- [1] H. R. Gordon and A. Y. Morel, *Remote Assessment of Ocean Color for Interpretation of Satellite Visible Imagery: A Review* (Springer-Verlag, New York, 1983), 114 pp.
- [2] W. A. Hovis, D. K. Clark, F. Anderson, R. W. Austin, W. H. Wilson, E. T. Baker, D. Ball, H. R. Gordon, J. L. Mueller, S. Y. E. Sayed, B. Strum, R. C. Wrigley and C. S. Yentsch, "Nimbus 7 coastal zone color scanner: system description and initial imagery," *Science* **210**, 60-63 (1980).
- [3] H. R. Gordon, D. K. Clark, J. L. Mueller and W. A. Hovis, "Phytoplankton pigments derived from the Nimbus-7 CZCS: initial comparisons with surface measurements," *Science* **210**, 63-66 (1980).
- [4] S. B. Hooker, W. E. Esaias, G. C. Feldman, W. W. Gregg and C. R. McClain, *SeaWiFS Technical Report Series: Volume 1, An Overview of SeaWiFS and Ocean Color* (NASA, Greenbelt, MD, Technical Memorandum 104566, July 1992).
- [5] V. V. Salomonson, W. L. Barnes, P. W. Maymon, H. E. Montgomery and H. Ostrow, "MODIS: Advanced Facility Instrument for Studies of the Earth as a System," *IEEE Geosci. Rem. Sens.* **27**, 145-152 (1989).
- [6] H. R. Gordon, "Calibration Requirements and Methodology for Remote Sensors Viewing the Oceans in the Visible," *Remote Sensing of Environment* **22**, 103-126 (1987).
- [7] G. W. Kattawar, G. N. Plass and J. A. Guinn, "Monte Carlo Calculations of the Polarization of Radiation in the Earth's Atmosphere-Ocean System," *Journal of Physical Oceanography* **3**, 353-372 (1973).

- [8] J. D. Mill, R. R. O'Neil, S. Price, G. J. Romick, O. M. Uy, E. M. Gaposchkin, G. C. Light, W. W. M. Jr., T. L. Murdock and A. T. S. Jr., "Midcourse Space Experiment: Introduction to the Spacecraft Instruments, and Scientific Objectives," *Journal of Spacecraft and Rockets* **31**, 900–907 (1994).
- [9] H. C. van de Hulst, *Light Scattering by Small Particles* (Wiley, New York, 1957), 470 pp.
- [10] H. C. van de Hulst, *Multiple Light Scattering* (Academic Press, New York, 1980), 739 pp.
- [11] S. Chandrasekhar, *Radiative Transfer* (Oxford University Press, Oxford, 1950), 393 pp.
- [12] W. A. Shurcliff, *Polarized Light* (Harvard University Press, Cambridge, MA, 1962), 207 pp.
- [13] C. F. Bohren and D. R. Huffman, *Absorption and Scattering of Light by Small Particles* (Wiley, New York, 1983), 530 pp.
- [14] J. E. Hansen and L. D. Travis, "Light Scattering in Planetary Atmospheres," *Space Science Reviews* **16**, 527–610 (1974).
- [15] G. W. Kattawar, G. N. Plass and S. J. Hitzfelder, "Multiple scattered radiation emerging from Rayleigh and continental haze layers. 1: Radiance, polarization, and neutral points," *Applied Optics* **15**, 632–647 (1976).
- [16] G. N. Plass, G. W. Kattawar and S. J. Hitzfelder, "Multiple scattered radiation emerging from Rayleigh and continental haze layers. 2: Ellipticity and direction of polarization," *Applied Optics* **15**, 1003–1011 (1976).
- [17] E. P. Shettle and R. W. Fenn, *Models for the Aerosols of the Lower Atmosphere and the Effects of Humidity Variations on Their Optical Properties* (Air Force Geophysics Laboratory, Hanscomb AFB, MA 01731, AFGL-TR-79-0214, 1979).

- [18] H. R. Gordon and M. Wang, "Retrieval of water-leaving radiance and aerosol optical thickness over the oceans with SeaWiFS: A preliminary algorithm," *Applied Optics* **33**, 443–452 (1994).
- [19] H. R. Gordon, 1996, Atmospheric Correction of Ocean Color Imagery in the Earth Observing System Era, *Jour. Geophys. Res.* (In press).
- [20] P. J. Reddy, F. W. Kreiner, J. J. Deluisi and Y. Kim, "Aerosol Optical Depths Over the Atlantic Derived From Shipboard Sunphotometer Observations During the 1988 Global Change Expedition," *Global Biogeochemical Cycles* **4**, 225–240 (1990).
- [21] Y. V. Villevalde, A. V. Smirnov, N. T. O'Neill, S. P. Smyshlyaev and V. V. Yakovlev, "Measurement of Aerosol Optical Depth in the Pacific Ocean and North Atlantic," *Jour. Geophys. Res.* **99D**, 20983–20988 (1994).
- [22] G. K. Korotaev, S. M. Sakerin, A. M. Ignatov, L. L. Stowe and E. P. McClain, "Sun-Photometer Observations of Aerosol Optical Thickness over the North Atlantic from a Soviet Research Vessel for Validation of Satellite Measurements," *Jour. Atmos. Oceanic Technol.* **10**, 725–735 (1993).

Figure Captions

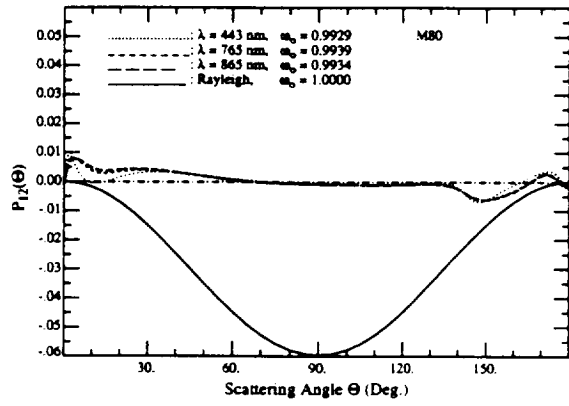
Figure 1. Scattering phase matrix element P_{12} for aerosols at 443, 765 and 865 nm, and Rayleigh (solid line): (a) M80 aerosol model; (b) T80 aerosol model.

Figure 2. Ratios Q_t/I_t and U_t/I_t as a function of θ_v for the M80 aerosol model with $\phi = 90^\circ$: (a) $\theta_0 = 20^\circ$; (b) $\theta_0 = 60^\circ$.

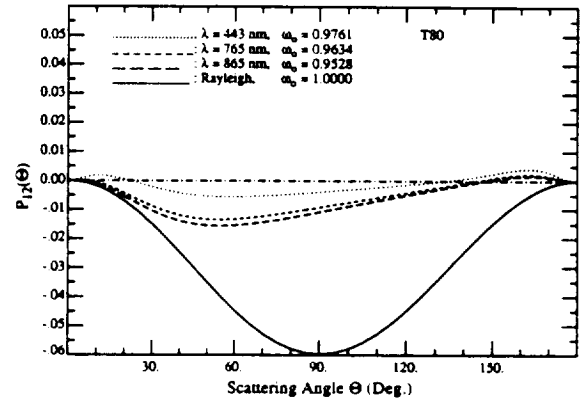
Figure 3. Retrieved error $t\Delta\rho_w$ at 443 nm as a function of θ_0 for the M80 aerosol model with $\tau_a(865) = 0.2$, in the presence of polarization sensitivity, for viewing at the edge of the scan with (a) $m_{12} = (0.10, 0.10, 0.10)$; (b) $m_{12} = (0.05, 0.05, 0.05)$; (c) $m_{12} = (0.05, 0.03, 0.03)$; (d) $m_{12} = (0.02, 0.02, 0.02)$; (e) $m_{12} = (0.05, -0.05, -0.05)$; (f) $m_{12} = (0.02, -0.02, -0.02)$.

Figure 4. Ratios Q/I and U/I for Rayleigh scattering and total scattering as a function of viewing zenith angle θ_v for the M80 aerosol model with $\tau_a(865) = 0.2$ and $\theta_0 = 60^\circ$: (a) $\lambda = 443$ nm; (b) $\lambda = 765$ nm; (c) $\lambda = 865$ nm.

Figure 5 Retrieved error $t\Delta\rho_w$ at 443 nm as a function of θ_0 for the M80 aerosol model with $\tau_a(865) = 0.2$, after applying the removal algorithm, for viewing at the edge of the scan with (a) $m_{12} = (0.10, 0.10, 0.10)$; (b) $m_{12} = (0.05, 0.05, 0.05)$; (c) $m_{12} = (0.05, 0.03, 0.03)$; (d) $m_{12} = (0.02, 0.02, 0.02)$; (e) $m_{12} = (0.05, -0.05, -0.05)$; (f) $m_{12} = (0.02, -0.02, -0.02)$.

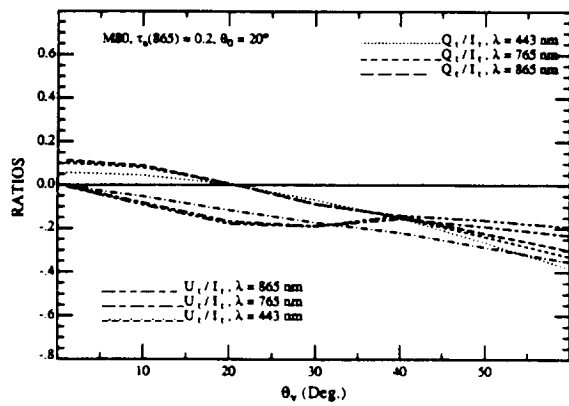


(a)

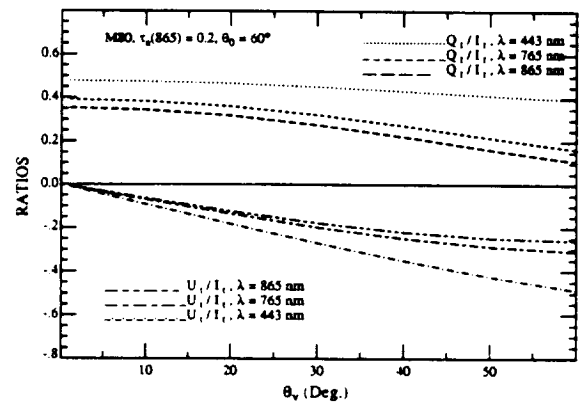


(b)

Figure 1. Scattering phase matrix element P_{12} for aerosols at 443, 765 and 865 nm, and Rayleigh (solid line): (a) M80 aerosol model; (b) T80 aerosol model.



(a)



(b)

Figure 2. Ratios Q_t/I_t and U_t/I_t as a function of θ_v for the M80 aerosol model with $\phi = 90^\circ$: (a) $\theta_0 = 20^\circ$; (b) $\theta_0 = 60^\circ$.

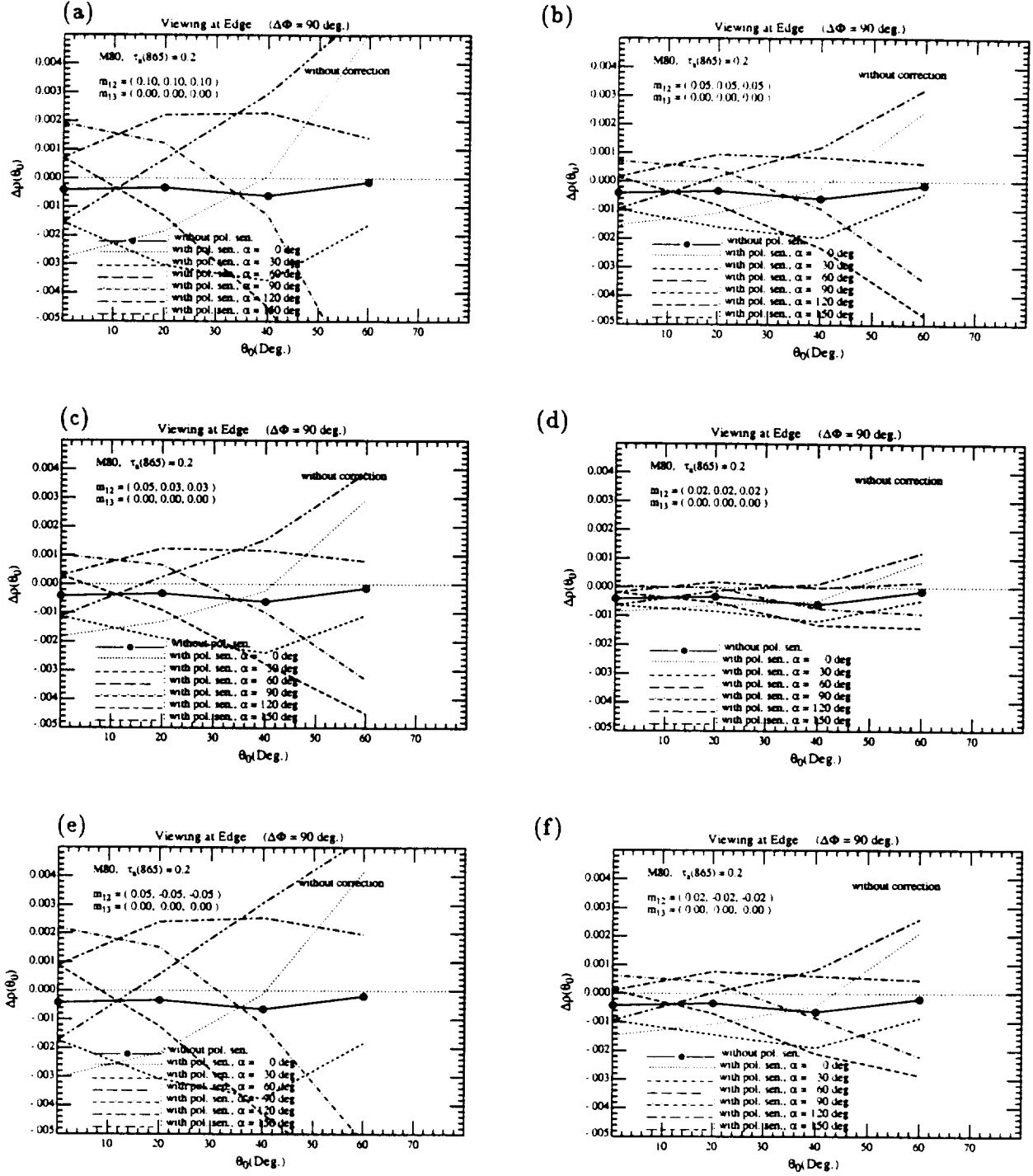


Figure 3. Retrieved error $t\Delta\rho_w$ at 443 nm as a function of θ_0 for the M80 aerosol model with $\tau_a(865) = 0.2$, in the presence of polarization sensitivity, for viewing at the edge of the scan with (a) $m_{12} = (0.10, 0.10, 0.10)$; (b) $m_{12} = (0.05, 0.05, 0.05)$; (c) $m_{12} = (0.05, 0.03, 0.03)$; (d) $m_{12} = (0.02, 0.02, 0.02)$; (e) $m_{12} = (0.05, -0.05, -0.05)$; (f) $m_{12} = (0.02, -0.02, -0.02)$.

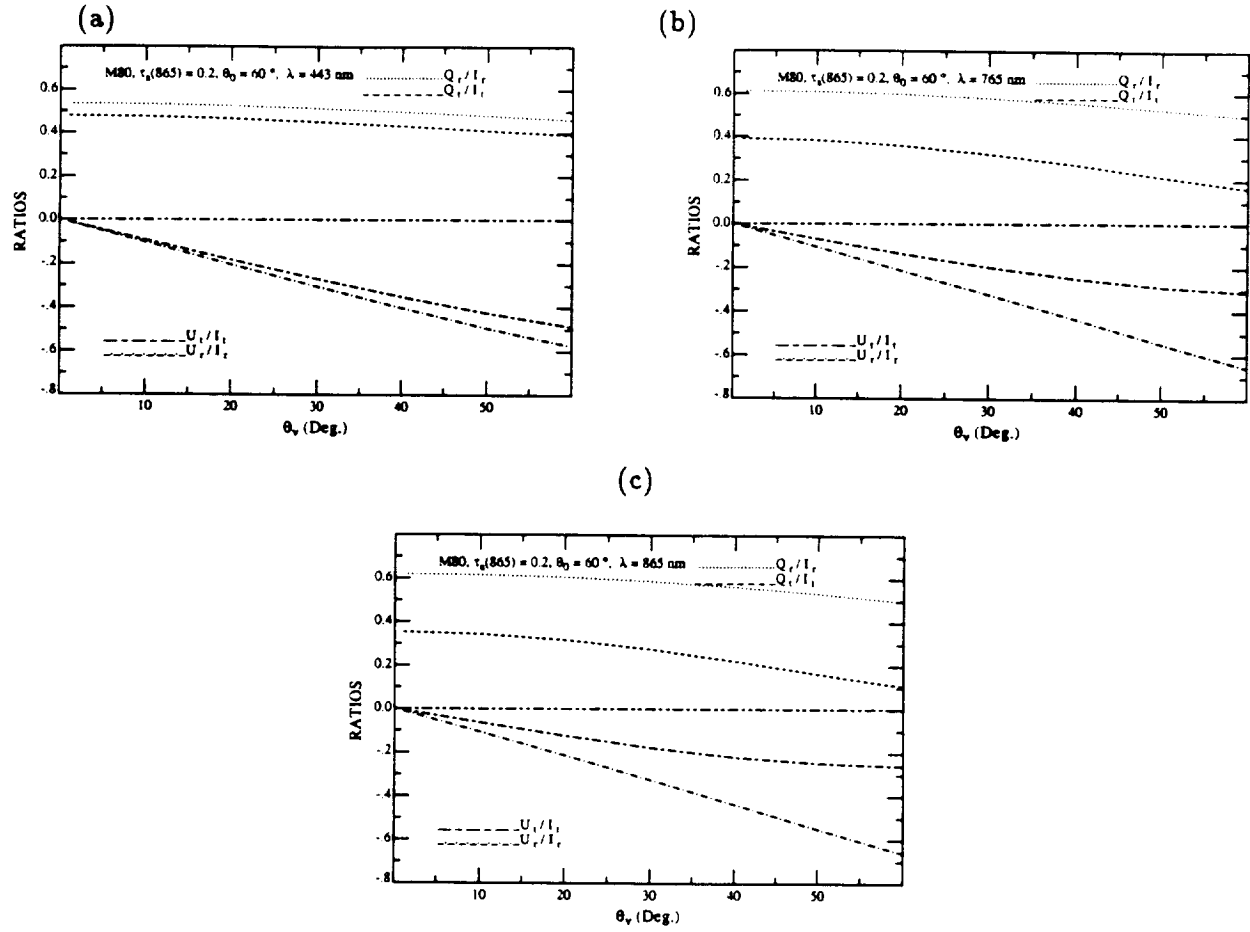


Figure 4. Ratios Q/I and U/I for Rayleigh scattering and total scattering as a function of viewing zenith angle θ_v for the M80 aerosol model with $\tau_a(865) = 0.2$ and $\theta_0 = 60^\circ$: (a) $\lambda = 443$ nm; (b) $\lambda = 765$ nm; (c) $\lambda = 865$ nm.

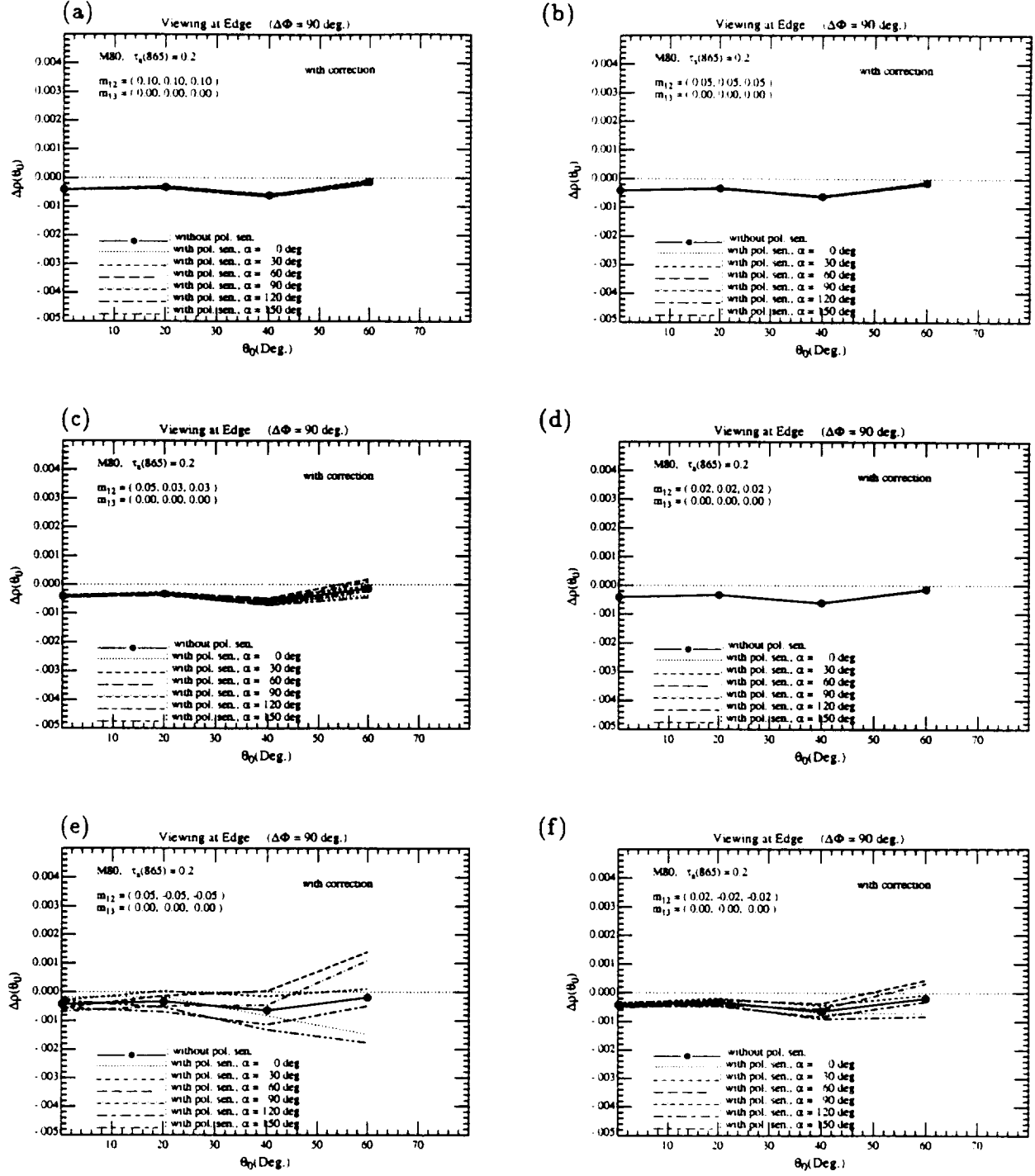


Figure 5 Retrieved error $t\Delta\rho_w$ at 443 nm as a function of θ_0 for the M80 aerosol model with $\tau_a(865) = 0.2$, after applying the removal algorithm, for viewing at the edge of the scan with (a) $m_{12} = (0.10, 0.10, 0.10)$; (b) $m_{12} = (0.05, 0.05, 0.05)$; (c) $m_{12} = (0.05, 0.03, 0.03)$; (d) $m_{12} = (0.02, 0.02, 0.02)$; (e) $m_{12} = (0.05, -0.05, -0.05)$; (f) $m_{12} = (0.02, -0.02, -0.02)$.